Numerical Limit Analysis of Precast Concrete Structures

A framework for effcient design and analysis

Herfelt, Morten Andersen; Poulsen, Peter Noe; Hoang, Linh Cao; Jensen, Jesper Frøbert

Publication date:
2017

Document Version
Publisher's PDF, also known as Version of record

Numerical Limit Analysis of Precast Concrete Structures

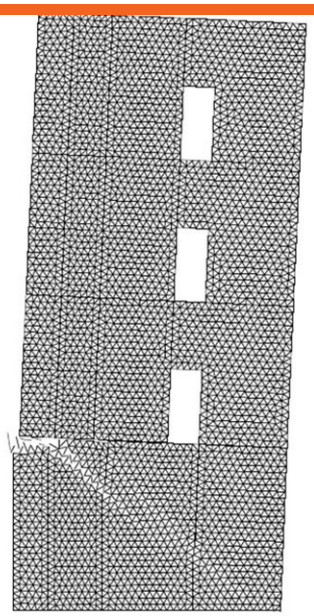

Morten Andersen Herfelt

PhD Thesis

Department of Civil Engineering
2017

DTU Civil Engineering Report 383

DTU Civil Engineering
Department of Civil Engineering

Numerical limit analysis of pre-cast concrete structures

- A framework for efficient design and analysis

Morten Andersen Herfelt

Ph.D. Thesis

Department of Civil Engineering
Technical University of Denmark

2017

Supervisors:

Associate professor Peter Noe Poulsen, DTU Civil Engineering
Professor Linh Cao Hoang, DTU Civil Engineering
Expert Jesper Frøbert Jensen, ALECTIA A/S

Assessment Committee:

Professor Henrik Stang, Ph.D., DTU Civil Engineering, Denmark
Permanent Researcher Jérémy Bleyer, Ph.D., Ecole des Ponts ParisTech, France
Project Manager Bent Steen Andreasen, Lic.Techn., Hoffmann, Denmark

Numerical limit analysis of precast concrete structures
-A framework for efficient design and analysis

Printed by DTU-Tryk
Department of Civil Engineering
Technical University of Denmark
ISBN: 9788778774583
ISSN: 1601-2917

Preface

This thesis is submitted as a partial fulfilment of the requirements for the Danish Ph.D. degree. The thesis is divided into two parts. The first part introduces the theoretical background and motivation of the research. A presentation of the research conducted is given and the major findings are concluded. The second part comprises four papers, which present the most important work conducted during the study.

Copenhagen, the 23$^{\text{rd}}$ of January 2017

Morten Andersen Herfelt

Acknowledgements

I gratefully acknowledge the financial support from the ALECTIA foundation and Innovation Fund Denmark (grant no. 1355-00157B).

I would like to thank my main supervisor, Peter Noe Poulsen, for his guidance and his invaluable advise throughout the project. I would also like to thank my co-supervisor, Linh Cao Hoang, for his knowledgeable guidance on concrete mechanics and structural understanding as a whole. I am grateful to my co-supervisor Jesper Frøbert Jensen, who skilfully kept the project focused on practical engineering problems. I would also like to thank Kristian Krabbenhøft for his guidance during my stay at the University of Newcastle.

I would to express my gratitude to my colleagues at ALECTIA for their support and interest in my research during the last three years. I offer particular thanks to Jesper Gath, Mads Nicolai Jensen, Lars Zenke Hansen, and Marianne Pia Pedersen.

My Ph.D. colleagues at the Technical University of Denmark, Jesper Harrild Sørensen, Sebastian Andersen, Asmus Skar, and Anders Bau Hansen provided an amazing and inspiring working environment as well as countless interesting discussions. For that I would like to express my sincerest thanks.

Last, but not least, I would like to thank my girlfriend Stani, family, and friends for their support during the last three years.

Abstract

Precast concrete elements are widely used in the construction industry as they provide a number of advantages over the conventional in-situ cast concrete structures. Joints cast on the construction site are needed to connect the precast elements, which poses several challenges. Moreover, the current practice is to design the joints as the weakest part of the structure, which makes analysis of the ultimate limit state behaviour by general purpose software difficult and inaccurate.

Manual methods of analysis based on limit analysis have been used for several decades. The methods provide excellent tools for engineers, however, the results are very dependent on the skill and intuition of the design engineer. Increasingly complex structures and the extensive use of computer-aided design on other aspects of civil engineering push for more accurate and efficient tools for the analysis of the ultimate limit state behaviour. This thesis introduces a framework based on finite element limit analysis, a numerical method based on the same extremum principles as the manual limit analysis. The framework allows for efficient analysis and design in a rigorous manner by use of mathematical optimisation.

The scope is to be able to model entire precast concrete structures while accounting for the local behaviour of the joints. The in-situ cast joints are crucial to the capacity of precast concrete structures, however, the behaviour of joints is in practice assessed by simple, empirical design formulas. A detailed study of in-situ cast joints in two-dimensions is conducted using finite element limit analysis, and the findings are used in the development of a two-dimensional multiscale joint finite element, which can represent the complex behaviour of the joints to a satisfactory degree.

Analysis of three-dimensional structures is rather difficult, especially by manual methods, however, considering three-dimensional nature of structures will generally increase the capacity. The two-dimensional joint element is therefore generalised to three-dimensions in order to be able to account for the influence of the joints.

The strength and efficiency of the presented framework are demonstrated

by two real size examples, a two-dimensional precast shear wall and a three-dimensional precast concrete stairwell. The analysis shows that the framework is capable of modelling complex precast concrete structures efficiently. Moreover, the influence and local behaviour of the joints are accounted for in the global model.

The results of the two examples demonstrate the potential of a framework based on finite element limit analysis for practical design. The use of mathematical optimisation ensures an optimised design, and the optimisation problems are solved efficiently using state-of-the-art solvers. It is concluded that the framework and developed joint models have the potential to enable efficient design of precast concrete structures in the near future.

Resumé

Præfabrikerede betonelementer bruges i stor grad i byggeindustrien, da de har mange fordele frem for konventionelle pladsstøbte betonkonstruktioner. Fuger støbt på byggepladsen er dog nødvendige for at samle de præfabrikerede elementer, hvilket medfører store udfordringer for både entreprenør og rådgiver. Den nuværende praksis er at designe fugerne som de svageste led i konstruktionen, hvilket gør analyse med gængse computerværktøjer besværligt og unøjagtigt.

I praksis har håndberegningsmetoder baseret på brudstadieanalyse været brugt i adskillige årtier. Metoderne giver de rådgivende ingeniører værdifulde og effektive værktøjer, men kvaliteten af resultaterne afhænger meget af den enkelte ingeniørs færdigheder. Konstruktioner bliver stadig mere komplekse, hvilket, sammen med den stigende brug af computerstøttet design i andre dele af bygningsingeniørfaget, giver et behov for effektive og nøjagtige værktøjer til analyse af konstruktionens opførsel i brudgrænsetilstanden. Denne afhandling introducerer en beregningsmetode kaldet numerisk brudstadieanalyse, som er baseret på de samme grundprincipper som håndberegningsmetoderne. Ved brug af matematisk optimering, muliggør beregningsmetoden effektiv analyse og design i en stringent manér.

Målet er at kunne modellere hele betonelementkonstruktioner og samtidig tage fugernes lokale opførsel med i regning. De pladsstøbte fuger er essentielle for den overordnede kapacitet af betonelementkonstruktioner, men fugerne bliver ikke desto mindre dimensioneret ved brug af empiriske formler. Et detaljeret studie af pladsstøbte betonfuger ved brug af numerisk brudstadieanalyse er gennemført, og resultaterne er brugt til at udvilke et to-dimensionelt multiskala fugeelement, som kan repræsentere fugernes komplekse virkemåde tilstrækkeligt præcist.

Tre-dimensionelle konstruktioner er generelt svære at analysere, specielt med håndberegningsmetoder. Ikke desto mindre vil det ofte give en større bæreevne at betragte hele den tre-dimensionelle konstruktion frem for blot et to-dimensionelt udsnit. Det to-dimensionelle fugeelement er generaliseret til tre-dimensioner for at gøre det muligt at tage fugernes virkemåde med i

regning ved analyse af betonelementkonstruktioner i tre dimensioner.

To eksempler, en to-dimensionel stabiliserende betonelementvæg og en trappeskakt af betonelementer betragetet i 3D, demonstrerer styrken og effektiviteten ved den præsenterede beregningsmetode. Analysen viser at beregningsmetoden kan håndtere komplekse konstruktioner effektivt i både 2D og 3D, samtidig med at de pladsstøbte fuger håndteres på en fornuftig måde.

Potentialet for praktisk design ved brug af numerisk brudstadieanalyse illustreres tydeligt ved resultaterne for de to eksempler. Brugen af matematisk optimering sikre et optimeret design, og selve optimeringsproblemerne kan løses hurtigt og effektivt ved brug af moderne løserer. Det kan konkluderes, at det nærværende forskningsarbejde har potentiale til at muliggøre effektivt og optimeret design af betonelementkonstruktioner i en nær fremtid.

Contents

Part I

Introduction and summary

Chapter 1

Introduction

1.1 Precast concrete

Concrete as a material has been known and used by humans for millennia. The Romans used a cement based on quicklime and volcanic ash, also known as pozzolana. When mixed with aggregates, e.g. rock pieces or ceramic tiles, the final product was a durable concrete that the Romans used for aqueducts, bridges, arches, and domes (Delatte, 2001). The Pantheon in Rome (built under emperor Hadrian about 126 AD) is still to this day the largest unreinforced concrete dome in the world. The Roman concrete was unreinforced in a modern sense, however, it was known that adding horse hair to the mixture would reduce cracking induced by shrinkage.

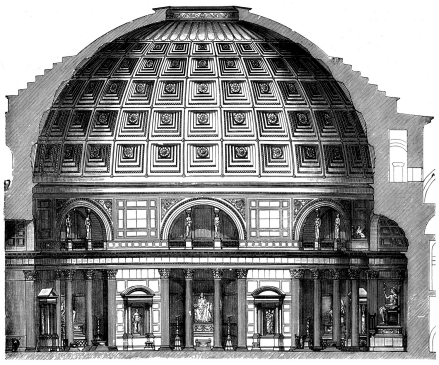

Figure 1.1*: Sketch of the cross section of the Pantheon: The spherical dome has an inner diameter of 43.3 metres (image from wikipedia.org).*

Modern concrete uses Portland cement, which was patented in 1824 by the British cement manufacturer Joseph Aspin and further developed by his

son William Aspin. However, it was not until the second half of the 19th century that metal reinforcement was added to the concrete. The ability to create such cheap composite materials capable of carrying both tension and compression quickly became essential.

During the rebuild of many European cities after the Second World War, reinforced concrete became widely used in the construction industry. Denmark also faced an increased demand for residential and industrial buildings, hence, a more rational and efficient method of construction was needed. Moreover, a shortage of masons accelerated this process.

Precast concrete was used as early as the Romans, however, in a modern context the method was developed in the early 20th century, but not adopted in a larger scale until after the Second World War. In Denmark, the earliest attempts at using precast concrete elements took place in the beginning of the 1950s. The transformation from the traditional building methods to the industrialised building methods can be seen as a transition from craftsmanship to mass production - something which many industries had already undergone before the 1950s (Nissen, 1961). During the 1950s and 60s, the industrialisation made it possible to increase the production of the Danish construction industry several times, and the use of precast concrete provided a technique that could remedy a massive shortage of housing. Several systems for precast concrete elements were developed during the 1950s and 60s, which made the Danish precast industry one of the leading players in the market, and many of the systems as well as methods developed in that time are still used today.

1.1.1 Practice and challenges

Precast concrete is cast and cured in a controlled environment, which allows for increased quality control and, therefore, makes it possible to decrease many of the tolerances. Moreover, precasting enables parallel production which increases the speed of production considerably. The commonly used techniques for precast concrete elements are described in *fib* bulletin 43 (2008) amongst other publications.

The most widely used precast component is perhaps the hollow core slab (often abbreviated HCS). The voids of the hollow core slab decrease the weight of the structure significantly, while the moment capacity of the element is practically unaffected. Both the compressive capacity of the concrete and the tensile strength of the reinforcement are exploited in the hollow core slabs. The slabs typically have a width of 1.2 metres and the joints between them are reinforced in the longitudinal direction.

The shear capacity of the HCS is somewhat limited as the slabs usually

do not have shear reinforcement. In order to increase the capacity, the voids are sometimes filled with mortar near the supports, however, experiments show that this have little to no effect.

Joints cast on the construction site are needed to connect the precast elements. These joints are often crucial to the overall behaviour and capacity of the structure, however, the design and construction techniques have developed little over the last 60 years. Several different types of joints are used, e.g. slab-to-beam joints, beam-to-column joints, panel-to-panel joints.

The panel-to-panel joints are usually reinforced with loop reinforcement, e.g. U-bars or wire loops, and the interfaces are often indented. In case of U-bars, the loops are often pre-bend by the manufacturer and, following a vertical lowering of the precast element on the construction site, the U-bar loops are straightened manually within the rather narrow gap between the precast elements. Subsequently, the void is filled with a mortar with low size aggregates.

The technique shown in Figure 1.2 poses several issues. It is almost impossible to ensure that the void of the joint is filled sufficiently with mortar. Moreover, the procedure of pre-bending and straightening the U-bars back again affects the position of the U-bars, and the quality of the joint will depend on the skill of the workers to a large degree. The current procedure means that there is no guarantee that the U-bars are placed closely together, which is assumed for the design calculations. Further more, it imposes some ductility requirements on the steel used for the U-bars, hence, high-strength steel cannot necessarily be used.

An important property of the joints is the ductility. It has been shown that the current design with U-bar loops displays some ductility, but experience a decrease capacity after the first peak load (Sørensen et al., 2016). It is therefore necessary to consider this when designing the joints.

Many of the current design methods used in Denmark for the ultimate limit state are based on the theory of rigid plastic materials, which will be introduced in Section 1.2. Lower bound methods, e.g. the stringer method, are frequently used as design tools. Advanced numerical methods such as non-linear finite element analysis are, on the other hand, rarely used for design of the ultimate limit state for precast concrete structures. Such methods require expert knowledge by the user, are often time consuming, and are prone to numerical instability.

Design of joints according to the Eurocode 2

The Eurocode 2 (European Committee for Standardization, 2008) is the current standard for design of structural concrete in most of Europe, including

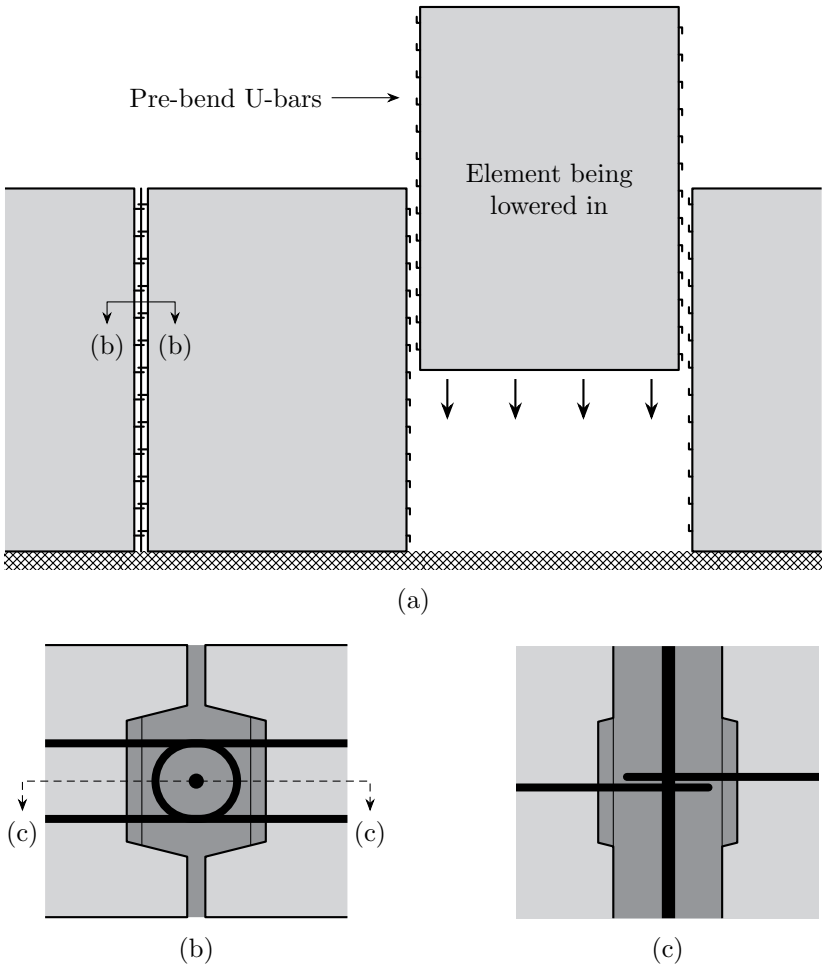

***Figure 1.2**: a) Assembly of the precast panels on the construction site, b) horizontal cross section, and c) vertical cross section of a panel-to-panel joint (adapted from Sørensen et al., 2016)*

Denmark. The design approach comprises a single criterion, namely a shear-friction criterion for the interface for concrete cast at different times, such as the interface between the precast element and the joint concrete. An upper limit for the shear capacity is also given:

$$v_{Rdi} = cf_{ctd} + \mu\sigma_n + \rho f_{yd}\left(\mu \sin\alpha + \cos\alpha\right) \leq 0.5\nu f_{cd}$$

where cf_{ctd} can be interpreted as a contribution to the shear capacity from the cohesion, and $\mu\sigma_n$ is the contribution to the capacity from external normal stresses on the joint σ_n (compression positive). The angle α is in practice always 90° (U-bar reinforcement perpendicular to the joint), hence, the contribution to the friction from the transverse reinforcement is reduced to $\mu\rho f_{yd}$,

where ρ is given as the reinforcement area A_s divided by the considered area of the interface A_i. The values of c and μ depend on the type of interface, and four types are defined according to the Eurocode 2:

- Very smooth: $c = 0.025$ to 0.10 and $\mu = 0.5$
- Smooth: $c = 0.20$ and $\mu = 0.6$
- Rough: $c = 0.40$ and $\mu = 0.7$
- Indented (keyed): $c = 0.50$ and $\mu = 0.9$

For keyed joints, it is assumed that the transfer of stresses only occurs over the area of the keys. This does not affect the contribution from the friction since the normal and shear stresses are scaled proportionally, however, it affects the contribution from the cohesion cf_{ctd} and the upper limit $0.5\nu f_{cd}$. Keyed joints will therefore often display a lower capacity than rough joints, see Figure 1.3.

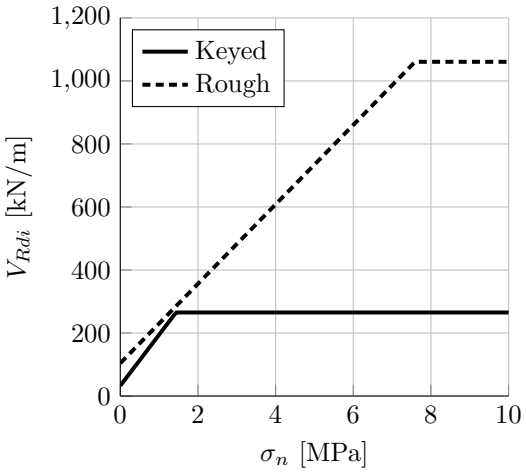

***Figure 1.3**: Shear force capacity for unreinforced keyed and rough joints as a function of the transverse confinement σ_n for typical material parameters and geometric quantities according to the Eurocode 2.*

The interfaces for the keyed joints will often be smooth, however, $\mu = 0.9$ can be used to account for the effect of the indentation. Moreover, it was found by Dahl (1994) that the friction coefficient for smooth interfaces can be taken as 0.75. The term representing the formal cohesion, cf_{ctd}, is clearly an empirical expression as the usual Coulomb friction model gives no link between the uniaxial tensile strength and the cohesion. According to Nielsen and Hoang (2010), the cohesion of an uncracked interface can be taken as

$0.55\sqrt{f_c}$, however, cracking due to e.g. shrinkage will more or less always occur at the interface, which reduces the cohesion considerably.

According to the Eurocode 2, the characteristic, 5 % fractile tensile strength can be taken as:

$$f_{ctk;0.05} = 0.21 f_{ck}^{2/3}$$

If the interface is subjected to external tension, the contribution cf_{ctd} should be set to zero.

1.2 Limit analysis of concrete

The method of limit analysis is widely used in both the industry and academia. The assumption of a rigid-plastic material behaviour leads to a simple and elegant framework for assessing the capacity and behaviour of structures. The term *limit analysis* covers a wide variety of methods including the well-known yield line method (Johansen, 1962).

Studies of plastic behaviour of materials can be traced back as far as the 17th century. However, it was not until the 20th century that a general formulation of the theory for rigid plastic materials was given by Gvozdev in 1936 (see Gvozdev, 1960, for the English translation). Gvozdev's work remained unknown in the Western world until the 1950s, but a similar theory was developed independently, mainly by Prager and Drucker (see e.g. Prager, 1952; Drucker et al., 1952). The formulation of the theory of rigid-plasticity also included precise definitions of three crucial theorems, namely the *lower bound theorem*, the *upper bound theorem*, and the *uniqueness theorem*.

Several Danish researchers have contributed to the field of limit analysis and concrete plasticity. One of the first, Ingerslev, worked in the 1920s and 30s on a calculation method for reinforced concrete slabs, which would later be known as the yield line method (Ingerslev, 1921, 1923). It is worth noting that this work was done before the precise formulations of the theorems of limit analysis were given, however, it was known by intuition that the developed method was an upper bound method (Nielsen and Hoang, 2010). Johansen continued the work of Ingerslev, and in Johansen's work (Johansen, 1931, 1932, 1962) the so-called yield lines are given a statical and geometrical interpretation as lines with constant bending moment where internal work (i.e. rotations) can take place at the collapse load. An upper bound to the load carrying capacity can then be calculated by use of the work equation. As the name indicates, upper bound solutions will give an upper bound to the exact capacity and will therefore be unsafe.

Lower bound methods are generally more desirable for design, as they give a safe estimate of the load carrying capacity (within the assumptions of the model). Several different methods have been developed, e.g. the stringer method (Kærn, 1979; Damkilde et al., 1994) or the strip method (Hillerborg, 1960). Lower bound models, however, might underestimate the capacity of the given structure considerably as it can be difficult to guess a decent estimate of the optimal stress field. Therefore, the quality of the solution will depend on the experience and engineering intuition of the structural engineer. The same can be said about upper bound solutions, but it is generally easier to guess the exact collapse mechanism (for simple structures).

A large portion of the knowledge and understanding of limit analysis of concrete structures comes from the work of M. P. Nielsen (Nielsen and Hoang, 2010). Nielsen and Hoang present the general formulation, yield criteria, and the exact analytical solutions to several common problems. The topics of punching shear, joints, and debonding are also treated in the same work within the framework of limit analysis.

1.2.1 Material model

Limit analysis assumes a rigid, perfectly plastic material with, in principle, unlimited deformation capacity. The material displays no deformations until a specific stress level has been reached and the material starts yielding, allowing for plastic deformations. Such materials do not, of course, exist in reality, however, it is a reasonable assumption when the elastic deformations of the given structure are insignificant compared to the plastic deformations. Commonly used materials like mild steel as well as reinforced concrete can be modelled as rigid, perfectly plastic with a reasonable degree of accuracy.

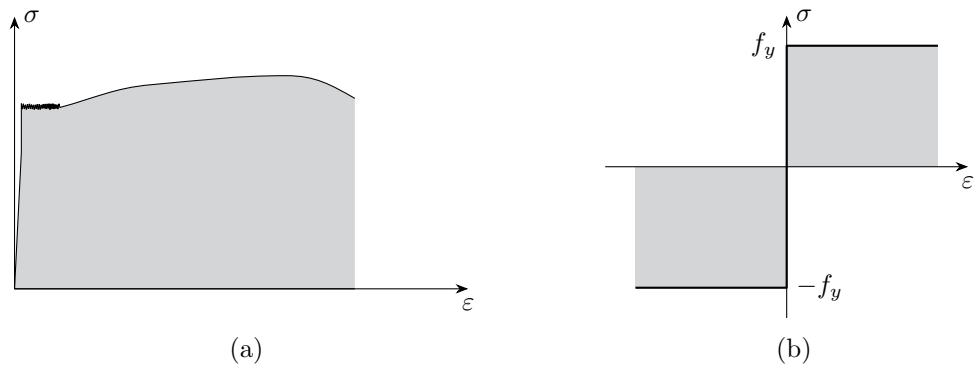

***Figure 1.4**: a) Sketch of a typical stress-strain curve for mild steel loaded in uniaixial tension, b) rigid plastic stress-strain curve.*

All materials will display some degree of elastic deformations before yielding, however, for both mild and cold formed steel, the elastic deformations are insignificant compared to the plastic deformation capacity, see Figure 1.4. The area under the curves indicates the work done and for the rigid-plastic stress-strain curve, Figure 1.4(b), the plastic work.

Figure 1.4(a) shows a typical stress-strain curve for mild steel loaded in uniaxial tension: A linear elastic part is followed by a *yield plateau*, hardening, and finally necking and failure. Figure 1.4(b) shows the stress-strain curve for a rigid, perfectly plastic material where plastic deformations initiate when the yield strength f_y has been reached.

Concrete displays behaviour far from the rigid plastic stress-strain curve. In tension, the behaviour is characterised by a steep drop in the capacity after the peak stress has been reached as illustrated in Figure 1.5 (first quadrant). The material will behave linear elastic at first until microcracks start forming which reduces the stiffness of the material. At the peak stress, f_t, the microcracks localise into discrete macrocracks which causes softening of the material (Karihaloo, 1995).

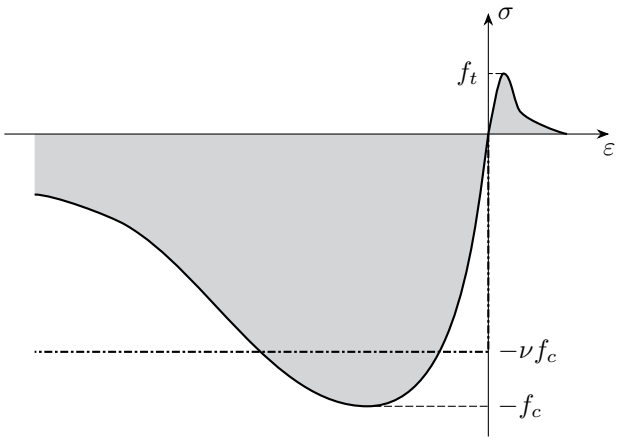

***Figure 1.5**: Sketch of a typical stress-strain curve for unreinforced concrete under uniaxial loading. Thick, dashed line indicate a rigid, perfectly plastic stress-strain curve based on the effective strength νf_c.*

In compression, the concrete will typically display the same elastic stiffness as in tension, however, the loss of stiffness occurs at a higher level of stress and the stress can still be increased considerably until the peak stress, f_c, has been reached. After the peak stress, the material will display softening until failure by crushing occurs.

Steel and concrete are often combined, and the resulting composite material exploits the tensile strength of the steel and the compressive strength

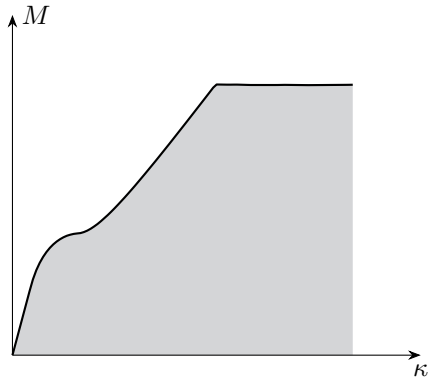

***Figure 1.6**: Typical moment-curvature relation of a normally reinforced concrete beam: The plateau marks the point where the reinforcement starts yielding.*

of the concrete. Moreover, the composite material will display a ductile behaviour which is much closer to the rigid-plastic material model than unreinforced concrete provided a reasonable amount of reinforcement, see the moment-curvature relation shown in Figure 1.6.

Figure 1.5 also shows a rigid plastic stress-strain curve which uses the effective strength νf_c, where ν is the so-called effectiveness factor which accounts for both microcracking and softening behaviour. The magnitude of the effectiveness factor depends on the stress conditions of the material and the reinforcement layout amongst other factors. Standards, e.g. the Eurocode 2, give recommendations for the value of ν to be used in different cases, e.g. for beam shear problems:

$$\nu = 0.6\left(1 - \frac{f_c}{250\ \text{MPa}}\right) \qquad (f_c \text{ in MPa})$$

An effectiveness factor of unity may be used for lower bound problems depending on the model (Nielsen and Hoang, 2010). Exner (1979) suggested an effectiveness factor for beams of $\nu = 3.2/\sqrt{f_c}$ (f_c in MPa) based on a theoretical stress-strain function. Exner also mentioned that the effectiveness factor increases with the amount of reinforcement. For upper bound solutions, which by definition is on the unsafe side, an effectiveness factor below unity should be used. As mentioned, the effectiveness factor accounts for several phenomena and, in principle, for calibration of ν for a given problem the exact rigid-plastic solution has to be used.

1.2.2 Extremum principles for rigid-plastic materials

Within the framework of limit analysis, the yield strength, f_y for steel, νf_c for concrete, describes the largest allowable stress level in the given material for uniaxial loading. For a general stress state $\boldsymbol{\sigma}$, such criteria can be stated as:

$$f(\boldsymbol{\sigma}) \leq 0 \tag{1.1}$$

where f is the so-called yield function which depends on the material and type of modelling. Plastic strains can only develop for stress states which are on the yield surface, i.e. when $f(\boldsymbol{\sigma}) = 0$. For stress states that fulfil $f(\boldsymbol{\sigma}) < 0$, no strains develop due to the assumption of a rigid plastic material. The yield function f is generally assumed to be a convex, non-linear function. A number of yield functions for materials commonly used in structural engineering will be presented in details in Section 3.3.

The relation between the general stresses $\boldsymbol{\sigma}$ which are on the yield surface, i.e. $f(\boldsymbol{\sigma}) = 0$, and the rate of general plastic strains $\boldsymbol{\varepsilon}$ can be written as

$$\boldsymbol{\varepsilon}_p = \lambda_p \frac{\partial g(\boldsymbol{\sigma})}{\partial \boldsymbol{\sigma}} \tag{1.2}$$

where g is the plastic potential function, and $\lambda_p \geq 0$ is the so-called plastic multiplier. Equation (1.2) is the flow rule, which links the stresses and the strain rates. The associated flow rule is commonly used meaning that g is identical to the yield function f, and the strain rates $\boldsymbol{\varepsilon}_p$ will be normal to the yield surface, i.e.:

$$\boldsymbol{\varepsilon}_p = \lambda_p \frac{\partial f(\boldsymbol{\sigma})}{\partial \boldsymbol{\sigma}} \tag{1.3}$$

If the stresses are inside the yield surface, the plastic multiplier will be zero as no strains occur. If the stresses are on the yield surface, λ_p can be either zero or positive depending on whether or not the given point is active, i.e. if plastic displacements occur. This can be stated as

$$\lambda_p f(\boldsymbol{\sigma}) = 0 \tag{1.4}$$

and is commonly referred to as the *complementarity condition*. For a rigid plastic material, no elastic strains will occur and, therefore, at the very onset of failure the total strains will be equal to the plastic strain rates $\boldsymbol{\varepsilon}_p$. In the literature, the term *plastic strain rates* is therefore often replaced by *plastic strains*.

We now consider a body subjected to a generalised load $\boldsymbol{P}$ which gives rise to the generalised, work-conjugate displacements $\boldsymbol{u}$. Moreover, the stress

and strain fields of the body are described by the generalised stresses $\boldsymbol{\sigma}$ and the generalised, work-conjugate strains $\boldsymbol{\varepsilon}$. The external work is given as

$$W_{\text{ext}} = \boldsymbol{u}^T \boldsymbol{P},$$

and the internal work of the body is given as

$$W_{\text{int}} = \int_\Omega \boldsymbol{\varepsilon}^T \boldsymbol{\sigma} \mathrm{d}\Omega$$

where Ω is the domain of the body. Equating the external and the internal work gives the work equation:

$$W_{\text{ext}} = \boldsymbol{u}^T \boldsymbol{P} = \int_\Omega \boldsymbol{\varepsilon}^T \boldsymbol{\sigma} \mathrm{d}\Omega = W_{\text{int}} \tag{1.5}$$

The rigid plastic constitutive model means that internal work is only produced by stresses, $\boldsymbol{\sigma}$, that are on the yield surface, i.e. $f(\boldsymbol{\sigma}) = 0$. The yield surface is assumed to be convex and contain the origin ($\boldsymbol{\sigma} = 0$), hence, given a set of stresses $\boldsymbol{\sigma}$ and corresponding strain rates $\boldsymbol{\varepsilon}$ according to the associated flow rule (1.3), any other stress state $\boldsymbol{\sigma} + \boldsymbol{\delta\sigma}$ will contribute equally or less to the internal work through the same plastic strains $\boldsymbol{\varepsilon}$:

$$\int_\Omega \boldsymbol{\varepsilon}^T \left(\boldsymbol{\sigma} + \boldsymbol{\delta\sigma}\right) \mathrm{d}\Omega = \int_\Omega \left(\boldsymbol{\varepsilon}^T \boldsymbol{\sigma} + \boldsymbol{\varepsilon}^T \boldsymbol{\delta\sigma}\right) \mathrm{d}\Omega \leq \int_\Omega \boldsymbol{\varepsilon}^T \boldsymbol{\sigma} \mathrm{d}\Omega \tag{1.6}$$

The convexity of the yield surface implies that the scalar product $\boldsymbol{\varepsilon}^T \boldsymbol{\delta\sigma}$ is non-positive, see Figure 1.7. The load on the structure is given as $\lambda \boldsymbol{P}$, where λ is a load factor. The exact collapse load of the rigid plastic body can be stated as $\boldsymbol{P}^* = \lambda^* \boldsymbol{P}$ with λ^* being the exact load factor.

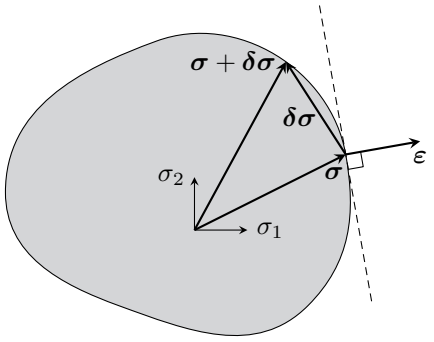

Figure 1.7*: Two stress states illustrated in a convex yield envelope: The product $\boldsymbol{\varepsilon}^T \boldsymbol{\delta\sigma}$ will be negative.*

Lower bound theorem

The lower bound theorem states that if a given stress field $\boldsymbol{\sigma}$ is statically admissible and safe, i.e. it fulfils the equilibrium conditions, balances the external loads $\lambda \boldsymbol{P}$, and satisfies the yield function in any point, the load will be a lower bound to the exact collapse load $\lambda^* \boldsymbol{P}$. Assuming the exact displacement field $\boldsymbol{u}^*$ and strain rates $\boldsymbol{\varepsilon}^*$, the work equation (1.5) gives

$$\lambda (\boldsymbol{u}^*)^T \boldsymbol{P} = \int_\Omega (\boldsymbol{\varepsilon}^*)^T \boldsymbol{\sigma} \mathrm{d}\Omega \tag{1.7}$$

From (1.6) it follows that the work of the stresses $\boldsymbol{\sigma}$ will be less than or equal to the work by the exact stress field, $\boldsymbol{\sigma}^*$:

$$\lambda (\boldsymbol{u}^*)^T \boldsymbol{P} = \int_\Omega (\boldsymbol{\varepsilon}^*)^T \boldsymbol{\sigma} \mathrm{d}\Omega \leq \int_\Omega (\boldsymbol{\varepsilon}^*)^T \boldsymbol{\sigma}^* \mathrm{d}\Omega = \lambda^* (\boldsymbol{u}^*)^T \boldsymbol{P} \tag{1.8}$$

From (1.8) it is clear that $\lambda \leq \lambda^*$. Lower bound method can therefore be used to establish safe stress fields, which gives a rigorous lower bound to the exact limit load.

Upper bound theorem

The upper bound theorem states that given a kinematically admissible displacement field $\boldsymbol{u}$ and the corresponding strain rates $\boldsymbol{\varepsilon}$, an upper bound to the exact limit load can be found by equating the internal and external work. Given a kinematically admissible collapse mode described by the displacement field $\boldsymbol{u}$ and the strains $\boldsymbol{\varepsilon}$ as well as the corresponding stresses $\boldsymbol{\sigma}$ (according to the flow rule, Equation 1.3) which balances the external load $\lambda \boldsymbol{P}$, the work equation reads

$$\lambda \boldsymbol{u}^T \boldsymbol{P} = \int_\Omega \boldsymbol{\varepsilon}^T \boldsymbol{\sigma} \mathrm{d}\Omega \tag{1.9}$$

We now assume that the exact, optimal stress field is described by $\boldsymbol{\sigma}^*$ which balances the exact collapse load $\lambda^* \boldsymbol{P}$.

The work done by the stresses $\boldsymbol{\sigma}$ corresponding the strains $\boldsymbol{\varepsilon}$ will larger than or equal to the work by any other set of stresses inside or at the yield surface including the exact stresses $\boldsymbol{\sigma}^*$ illustrated in Figure 1.8. The following must therefore be true,

$$\lambda \boldsymbol{u}^T \boldsymbol{P} = \int_\Omega \boldsymbol{\varepsilon}^T \boldsymbol{\sigma} \mathrm{d}\Omega \geq \int_\Omega \boldsymbol{\varepsilon}^T \boldsymbol{\sigma}^* \mathrm{d}\Omega = \lambda^* \boldsymbol{u}^T \boldsymbol{P}, \tag{1.10}$$

and it follows directly from (1.10) that the load factor λ for the kinematically admissible collapse mode will be an upper bound, i.e. $\lambda \geq \lambda^*$.

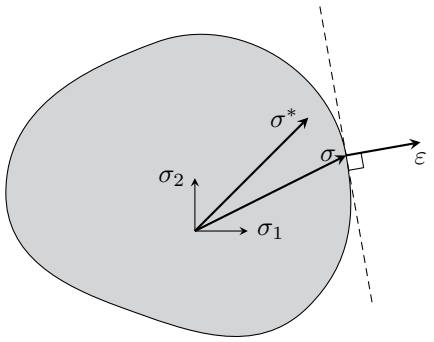

***Figure 1.8**: Convex yield envelope showing the strain rates $\boldsymbol{\varepsilon}$ and stresses $\boldsymbol{\sigma}$ corresponding to the kinematically admissible collapse mode as well as the optimal stresses $\boldsymbol{\sigma}^*$.*

Uniqueness theorem

Finally, the uniqueness theorem states that given a statically admissible and safe stress field $\boldsymbol{\sigma}$ as well as a kinematically admissible displacement field $\boldsymbol{u}$ and the corresponding strain rates $\boldsymbol{\varepsilon}$ which satisfy the flow rule, the load factor λ will be equal to the exact load factor λ^*.

This follows directly from the upper and lower bound theorems: A statically admissible and safe stress field will give a lower bound of the load factor, while a kinematically admissible collapse mode, i.e. displacements and strains, will give an upper bound, hence, for the two to be equal, the determined load factor must be the exact.

1.3 Finite element limit analysis

Several manual methods have been developed within the framework of limit analysis. These methods provide excellent tools for assessment of the ultimate load carrying capacity of structures and bound the exact limit load in a rigorous manner. For simple structures, manual methods, e.g. the yield line theory, will often provide a decent estimate of the capacity. As structures increase in complexity, however, it becomes increasingly difficult to determine an adequate estimate of the stress fields or displacement fields by hand, hence, numerical methods are needed.

The finite element method is a numerical method for solving boundary value problems for differential equations. The method was developed in the 1950s and 60s and quickly gained popularity (see e.g. Zienkiewicz and Taylor, 1977; Cook et al., 2001). The method was originally developed for structural

and mechanical engineering, however, it is used in a wide variety of fields today as the method is applicable to any differential equation. The main idea of the method is to divide a given domain into sub-domains called elements. Each element represents some variation of the unknown variables and the accuracy of the solution depends on how well the variations of the elements approximate the exact solution.

The simplest version of the finite element method used in the field of structural engineering assumes a linear elastic material behaviour as well as small deformations. The resulting mathematical problem is a linear system of equations. More advanced types of the method that incorporate plasticity or large deformations are widely used in academia, however, they only see somewhat limited use outside. Non-linear finite element analysis gives a non-linear system of equations, where the stiffness of the structure depends on the current state of stresses and deformations. It is therefore necessary to deploy an iterative approach where the forces (or deformations) are applied gradually. This makes the calculations computationally heavy and (possibly) numerically unstable. Moreover, for practical design where the ultimate load carrying capacity is the main result of interest, an iterative approach is undesirable. Non-linear finite element analysis does have a number of advantages, e.g. it is possible to capture the post-peak behaviour which can be relevant in some cases.

Finite element limit analysis can be considered as a special case of the general finite element method. It uses an element discretisation and assumes a rigid plastic material behaviour similarly to the manual limit analysis discussed in Section 1.2. The research in the field began in the late 1960s and several papers on the topic were published in the early 70s. Some of the first were Belytschko and Hodge (1970) who used quadratic stress elements to obtain strict lower bound solutions for several problems, however, sophisticated methods were necessary to ensure that the stress fields of the elements satisfied the yield criterion. Later, elements with linear stress fields became favoured (see e.g. Sloan, 1988). Anderheggen and Knöpfel (1972) presented the general formulation as well as equilibrium elements for solids and plates. The formulation of Anderheggen and Knöpfel was based on linear programming, i.e. linear optimisation, and the chosen yield criterion had to be linearised to fit the format. During the 1980s and 90s, several researchers contributed to the field of finite element limit analysis for two-dimensional problems (Christiansen, 1986; Sloan, 1989; Krenk et al., 1994; Andersen and Christiansen, 1995; Poulsen and Damkilde, 2000). Linear programming was still the choice of optimisation, however, there were some attempts of developing algorithms capable of handling non-linear constraints (Zouain et al., 1993; Borges et al., 1996; Christiansen and Andersen, 1999; Andersen et al., 2000;

Krabbenhoft and Damkilde, 2002). In the 2000s, primal-dual interior point methods for second-order cone programming and semidefinite programming - generalisations of linear programming - became established technologies and several papers on finite element limit analysis using second-order cone programming were published (Krabbenhøft et al., 2007; Makrodimopoulos and Martin, 2006, 2007). Many yield criteria commonly used for structural engineering can be cast as either second-order cones or semidefinite cones (Bisbos and Pardalos, 2007), e.g. the von Mises criterion has the shape of a conic section. A brief introduction to the field of mathematical programming will be given in Chapter 2, and the commonly used yield criteria and their conic form will be presented in Section 3.3.

Numerical limit analysis is still primarily used in academia, however, some commercial programs for geotechnical engineering are available. The commercial software LimitState, which uses discontinuity layout optimisation and is capable of handling both geotechnical problems and slabs, has been developed by a research group at the University of Sheffield (Gilbert et al., 2014; Smith et al., 2014). Moreover, the software OptumCE developed by researchers as the University of Newcastle incorporates finite element limit analysis for modelling of geotechnical problems (Krabbenhøft and Lyamin, 2014).

1.4 Relevance for the industry

The gap between researchers working in the field of numerical methods and practitioners in the field of structural engineering is substantial. Countless sophisticated material models including damage, cracking and so on, have been developed for the finite element method. These models are capable of predicting the behaviour of experimental tests accurately under certain assumptions, however, they have little practical use. Moreover, such models often require material constants which are not readily available and experimental testing are necessary to determine the required material parameters. Numerical non-linear finite element analysis in general requires expert knowledge and the results are difficult to verify and perform quality assurance on due to the various material models used by commercial software and the black box nature of the solvers and algorithms.

Manual limit analysis has been used in academia for about a century. The methods provide efficient tools for assessment of the ultimate load carrying capacity in an intuitive manner, which can easily be checked for errors. Today, many of the calculations based on these methods are automated using e.g. spreadsheets, which speed up the design process to some extent. For

the overall load distribution in structures, the quality of the solution depends heavily on the engineering intuition of the design engineer, hence, suboptimal solutions are unavoidable.

A framework based on finite element limit analysis will provide an excellent tool for optimisation of the overall load distribution and capacity of structures. As mentioned in Section 1.3, the method is based on the same basic principles as the manual limit analysis and the solutions will in most cases be intuitive and easily checked. One of the key components of precast concrete structures is the in-situ cast joints connecting the precast elements. The capacity and behaviour of these joints are today assessed using empirical expressions, see Section 1.1.1, and the overall distribution of forces does not consider the joints. Development of a framework based on finite element limit analysis capable of handling in-situ cast joints will not only lead to a more accurate load distribution in the structure, but also significant material savings. Moreover, the framework will make the design process more efficient, which is crucial to consulting engineering companies in today's market.

The material savings will benefit the environment as well. Cement, one of the key components of concrete, is responsible for approximately 7 % of the global CO_2 emissions, and the production of cement has been increasing annually by about 2.5 %. From an environmental perspective, optimisation of concrete structures will therefore be a valuable tool in reducing the emissions from the construction industry in general.

1.5 Objectives of the thesis

As discussed, the industry predominately uses automated manual methods based on the assumption of a rigid plastic material behaviour for the ultimate limit state design. Linear elastic finite element analysis is widely used in the serviceability limit state and to some extend in the ultimate limit state. More advanced types of numerical analyses, however, are rarely used for practical design and analysis in the industry.

The primary scope of the present thesis is to develop a general framework based on finite element limit analysis for design of precast concrete structures. The focus of the study will be on the in-situ cast joints which are crucial to the overall capacity and behaviour of precast structures. The objectives can be listed as follows:

- Identification of the critical mechanisms of two-dimensional shear joints.
- Development of a simplified model for use in a generalised numerical framework.

- Extension of the findings to the three-dimensional case.

In addition to these objectives, several finite elements for the framework are developed and presented in the thesis. The developed models are validated by comparison to experimental results found in the literature as well as the current standards. Moreover, real size examples are analysed using the developed framework and the findings are discussed.

1.6 Overview of the thesis

The thesis comprises two parts: Introduction and Summary (Part I) and Appended Papers (Part II). The content of the two parts overlaps to some extent as Part I will attempt to tell the complete story of the study including the research and findings presented in the papers.

After the introduction, Chapter 2 will present the basics of mathematical programming as well as a brief overview of an interior point algorithm for second-order cone programming. Chapter 3 gives a detailed description of the mathematical formulation of finite element limit analysis and the commonly used yield criteria used in structural engineering.

Chapter 4 presents the main findings of the study. This includes

- the detailed analysis of shear joints, presented in Paper I (Herfelt et al., 2016),
- the development of a simplified mechanical model for two-dimensional joints, presented in Paper II (Herfelt et al., 2017a),
- the development of a generalised plane stress element for modelling of shear walls, presented in Paper III (Herfelt et al., 2017c), and
- the generalisation of the joint model to the three-dimensional case, presented in Paper IV (Herfelt et al., 2017b).

Chapter 5 will present examples of real size structures analysed using the developed models and framework. In addition to the core work of the present study given in Chapter 4, several finite elements have been developed and their formulations are given in Chapter 6. Finally, conclusions and recommendations for future work will be given in Chapter 7.

Chapter 2

Convex optimisation

2.1 Introduction

Mathematical optimisation is used in many fields of research. The formulation of finite element limit analysis (FELA), discussed in Section 1.3, is an optimisation problem as well. The first formulations of FELA were based on linear optimisation, however, efficient solution methods for many types of non-linear, convex optimisation problems have become established technologies, and non-linear, convex optimisation is widely used in the field of FELA today. In this chapter, the basics of mathematical optimisation are introduced and the formulations of linear programming (LP), second-order cone programming (SOCP), and semidefinite programming (SDP) - all formulations used for FELA - will be presented.

In many fields of engineering, the distinction between easy and hard problems is whether or not the given problem is linear, e.g. linear differential equations are considered easy to solve. This is not the case in the field of optimisation where the distinction between easy and hard problems should be drawn between convexity and non-convexity rather than linearity and non-linearity (Boyd and Vandenberghe, 2004). Convex problems are considered easy to solve due to the fact that any local minimum must be the global minimum, while general non-linear optimisation problems with more than a few variables are extremely difficult to solve due to the possible existence of multiple local minima and saddle points.

The general mathematical optimisation problem can be stated as:

$$\begin{array}{ll} \text{minimise} & f_0(\boldsymbol{x}) \\ \text{subject to} & f_i(\boldsymbol{x}) \leq 0, \qquad i = 1, \ldots, m \end{array} \tag{2.1}$$

where $\boldsymbol{x} \in \mathbb{R}^n$ is the variable vector of the optimisation problem, and the

scope of the optimisation problem (2.1) is to minimise the objective function $f_0(\boldsymbol{x})$, while satisfying the constraints $f_i(\boldsymbol{x}) \leq 0$ for all i. Whether or not (2.1) is a convex optimisation problem depends on the convexity of the functions f_i. Generally, a function $f(\boldsymbol{x})$ is convex if it satisfies the inequality

$$f(\alpha \boldsymbol{x}_1 + (1-\alpha)\boldsymbol{x}_2) \leq \alpha f(\boldsymbol{x}_1) + (1-\alpha) f(\boldsymbol{x}_2), \tag{2.2}$$

for all $(\boldsymbol{x}_1,\ \boldsymbol{x}_2) \in \mathbb{R}^n$ and $\alpha \in [0;1]$. If the objective function as well as the constraints fulfil (2.2), the optimisation problem (2.1) is a convex optimisation problem.

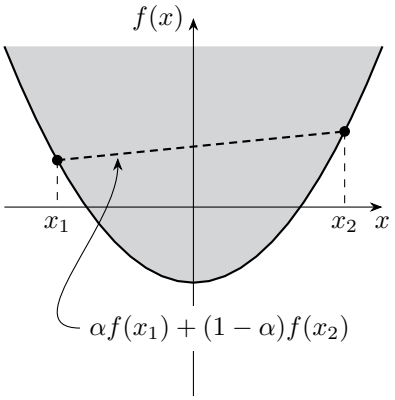

***Figure 2.1**: An example of a convex function, $f(x) = ax^2 + b$, $a \geq 0$.*

If the second derivative $f''(x)$ is non-negative for all x, the function $f(x)$ is considered convex as well. Figure 2.1 shows an example of such a function, namely $f(x) = ax^2 + b$, which has the second derivative $f''(x) = 2a$, hence, the function is convex for $a \geq 0$. Other examples of convex functions are listed below:

- $f(x) = |x|$
- $f(x) = ke^x$
- $f(x) = x^3$ for $x \geq 0$
- $f(x) = x^{-1}$ for $x > 0$, and $f(x) = -x^{-1}$ for $x < 0$

Linear functions are considered both convex and concave since they satisfy

$$f(\alpha \boldsymbol{x}_1 + (1-\alpha)\boldsymbol{x}_2) = \alpha f(\boldsymbol{x}_1) + (1-\alpha) f(\boldsymbol{x}_2)$$

which is a stricter version of (2.2).

Introducing a slightly more general version of the optimisation problem (2.1), which also includes equality constraints:

$$\begin{array}{lll} \text{minimise} & f(\boldsymbol{x}) & \\ \text{subject to} & g_i(\boldsymbol{x}) = 0, & i = 1, \ldots, m \\ & h_i(\boldsymbol{x}) \geq 0, & i = 1, \ldots, p \end{array} \tag{2.3}$$

For the problem (2.3), we now introduce the Lagrange function (also called the Lagrangian), which is defined as

$$\mathcal{L}(\boldsymbol{x}, \boldsymbol{y}, \boldsymbol{s}) = f(\boldsymbol{x}) - \sum_{i=1}^{m} y_i g_i(\boldsymbol{x}) - \sum_{i=1}^{p} s_i h_i(\boldsymbol{x}) \tag{2.4}$$

where the vector $\boldsymbol{y}$ is the Lagrange multipliers for the equality constraints of (2.3), and the vector $\boldsymbol{s}$ is the Lagrange multipliers for the inequality constraints. The Lagrangian is closely linked to the optimality criteria, which will be presented later in this section. Moreover, the Lagrangian links the original problem (2.3), denoted the primal problem, to a dual problem, which provides a lower bound to the primal minimisation problem.

2.2 Linear programming

One of the simplest subclasses of convex optimisation is linear optimisation, where the objective function and constraints are linear functions. Solving linear optimisation problems (also called linear programs or LP) with more than a few variables by hand is rather difficult. However, such problems can be solved very efficiently numerically. It is often convenient to use a so-called standard form of the problem when dealing with numerical solvers: Every linear program can be recast to fit the standard form by rearranging the constraints and introducing additional variables. The standard form for LP is given as:

$$\begin{array}{ll} \text{minimise} & \boldsymbol{c}^T \boldsymbol{x} \\ \text{subject to} & \mathbf{A}\boldsymbol{x} = \boldsymbol{b} \\ & \boldsymbol{x} \geq 0 \end{array} \tag{2.5}$$

where a linear combination of the non-negative problem variables $\boldsymbol{x}$ is sought to be minimised while fulfilling the linear equality constraints $\mathbf{A}\boldsymbol{x} = \boldsymbol{b}$. (2.5) is the primal problem and has a corresponding dual problem, which is linked via the Lagrange function, $\mathcal{L}$, see (2.4):

$$\mathcal{L}(\boldsymbol{x}, \boldsymbol{y}, \boldsymbol{s}) = \boldsymbol{c}^T \boldsymbol{x} - \boldsymbol{y}^T (\mathbf{A}\boldsymbol{x} - \boldsymbol{b}) - \boldsymbol{s}^T \boldsymbol{x} \tag{2.6}$$

where $\boldsymbol{y}$ and $\boldsymbol{s}$ are the Lagrange multipliers associated with the equality constraints and the non-negativity constraints, respectively. The vectors $\boldsymbol{y}$ and $\boldsymbol{s}$ are also the variables of the dual problem, which provides a lower bound for the primal problem. Rearranging the terms of the Lagrangian gives:

$$\mathcal{L}(\boldsymbol{x}, \boldsymbol{y}, \boldsymbol{s}) = \boldsymbol{b}^T\boldsymbol{y} + \left(\boldsymbol{c} - \mathbf{A}^T\boldsymbol{y} - \boldsymbol{s}\right)^T \boldsymbol{x} \tag{2.7}$$

Similar to $\boldsymbol{x}$, the Lagrange multipliers for the non-negativity constraints, $\boldsymbol{s}$, are required to be non-negative, and the dual problem can now be stated as an maximisation problem to obtain the largest lower bound to the primal problem:

$$\begin{aligned} &\text{maximise} \quad \inf_{\boldsymbol{x}} \mathcal{L}(\boldsymbol{x}, \boldsymbol{y}, \boldsymbol{s}) = \boldsymbol{b}^T\boldsymbol{y} + \inf_{\boldsymbol{x}} \left(\boldsymbol{c} - \mathbf{A}^T\boldsymbol{y} - \boldsymbol{s}\right)^T \boldsymbol{x} \\ &\text{subject to} \quad \boldsymbol{s} \geq 0 \end{aligned} \tag{2.8}$$

where $\inf_{\boldsymbol{x}}$ is the infimum with respect to $\boldsymbol{x}$, i.e. the greatest lower bound. The term, $\left(\boldsymbol{c} - \mathbf{A}^T\boldsymbol{y} - \boldsymbol{s}\right)^T \boldsymbol{x}$, is a linear function of $\boldsymbol{x}$, thus, for the Lagrange function to be bounded from below, $\left(\boldsymbol{c} - \mathbf{A}^T\boldsymbol{y} - \boldsymbol{s}\right)$ is required to be zero. The dual problem (2.8) can therefore be stated as:

$$\begin{aligned} &\text{maximise} \quad \boldsymbol{b}^T\boldsymbol{y} \\ &\text{subject to} \quad \mathbf{A}^T\boldsymbol{y} + \boldsymbol{s} = \boldsymbol{c} \\ &\qquad\qquad\quad \boldsymbol{s} \geq 0 \end{aligned} \tag{2.9}$$

The primal problem (2.5) and dual problem (2.9) are closely linked together by the Lagrangian and are solved simultaneously. The Lagrangian will also be used to derive the first-order optimality conditions, which is sufficient to prove optimality for convex problems. Morten er dum.

2.3 Second-order cone programming

Second-order cone programming (SOCP) is a generalisation of linear programming and a subclass of semidefinite programming (SDP), which will be discussed in the following section. The many yield criteria commonly used for finite element limit analysis can be formulated as quadratic constraints, and the resulting problem will fit the format of second-order cone programming. SOCP also has application in many other fields of engineering, physics, and chemistry (Lobo et al., 1998). For an in-depth introduction to the topic of second-order cone programming, the reader is referred to Alizadeh and Goldfarb (2003) and Antoniou and Lu (2007).

First and foremost, the second-order cone in 1, 2, 3, and k dimensions is introduced:

$$\begin{array}{ll} x_1 \geq 0, & \text{for } x \in \mathbb{R}^1 \\ x_1 \geq |x_2|, & \text{for } \boldsymbol{x} \in \mathbb{R}^2 \\ x_1 \geq \sqrt{x_2^2 + x_3^2} = \|\boldsymbol{x}_{2:3}\|_2, & \text{for } \boldsymbol{x} \in \mathbb{R}^3 \\ x_1 \geq \sqrt{\boldsymbol{x}_{2:k}^T \boldsymbol{x}_{2:k}} = \|\boldsymbol{x}_{2:k}\|_2, & \text{for } \boldsymbol{x} \in \mathbb{R}^k \end{array} \tag{2.10}$$

where $\|\boldsymbol{x}\|_2$ is the Euclidean norm. The second-order cone is also commonly known as the quadratic cone or the Lorentz cone.

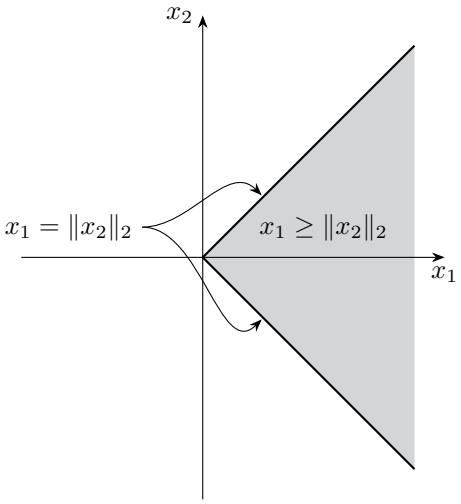

***Figure 2.2**: Two-dimensional second-order cone: The interior of the set is indicated with gray.*

The set of vectors that are in the k-dimensional cone (2.10) is defined as follows:

$$\mathcal{Q}_k = \left\{ \boldsymbol{x} \mid \boldsymbol{x} \in \mathbb{R}^k,\ x_1 \geq \|\boldsymbol{x}_{2:k}\|_2 \right\} \tag{2.11}$$

It is observed that the one-dimensional cone $\mathcal{Q}_1$ will be a non-negativity constraint. The notation $\boldsymbol{v} \in \mathcal{Q}_k$ is therefore equal to

$$\boldsymbol{v} \in \mathcal{Q}_k \quad \Leftrightarrow \quad v_1 \geq \|\boldsymbol{v}_{2:k}\|_2 \tag{2.12}$$

We also define $\mathcal{Q}$ as the Cartesian product of second-order cones:

$$\mathcal{Q} = \mathcal{Q}_{k_1} \times \mathcal{Q}_{k_2} \times \cdots \times \mathcal{Q}_{k_q},$$

hence,

$$\boldsymbol{x} \in \mathcal{Q} \quad \Leftrightarrow \quad \boldsymbol{x}_1 \in \mathcal{Q}_{k_1}, \quad \boldsymbol{x}_2 \in \mathcal{Q}_{k_2}, \ldots, \boldsymbol{x}_q \in \mathcal{Q}_{k_q}, \tag{2.13}$$

where $\boldsymbol{x}_i$ are subsets of $\boldsymbol{x}$ associated with the ith cone.

The standard form of the primal second-order cone program is given as

$$\begin{aligned} &\text{minimise} && \boldsymbol{c}^T\boldsymbol{x} \\ &\text{subject to} && \mathbf{A}\boldsymbol{x} = \boldsymbol{b} \\ & && \boldsymbol{x} \in \mathcal{Q} \end{aligned} \tag{2.14}$$

where $\boldsymbol{x}$ is the problem variables. The problem (2.14) is similar to the primal LP problem (2.5), and if all cones have a size of one, (2.14) is in fact a linear program. The primal problem has of course also a dual problem, which can be stated as follows:

$$\begin{aligned} &\text{maximise} && \boldsymbol{b}^T\boldsymbol{y} \\ &\text{subject to} && \mathbf{A}^T\boldsymbol{y} + \boldsymbol{s} = \boldsymbol{c} \\ & && \boldsymbol{s} \in \mathcal{Q} \end{aligned} \tag{2.15}$$

which again is similar to the LP dual problem (2.9). The dual problem (2.15) can be derived from the Lagrangian of the primal problem and visa versa.

Several problems that arise in finite element limit analysis, e.g. Johansen's criterion for plates given in Section 6.3.3, will require constraints of the following type:

$$2v_1v_2 \geq \boldsymbol{v}_{3:k}^T\boldsymbol{v}_{3:k}, \quad (v_1, v_2) \geq 0, \tag{2.16}$$

i.e. the vector $\boldsymbol{v}$ is in a set defined as

$$\mathcal{Q}_k^r = \left\{\boldsymbol{x} \mid \boldsymbol{x} \in \mathbb{R}^k,\ 2x_1x_2 \geq \boldsymbol{x}_{3:k}^T\boldsymbol{x}_{3:k},\ (x_1, x_2) \geq 0\right\},$$

which is denoted a rotated quadratic cone. The rotated quadratic cone can be transformed into a quadratic cone (2.11) to fit the standard form of SOCP. Introducing a matrix $\mathbf{K}$ defined as

$$\mathbf{K} = \begin{bmatrix} 1/\sqrt{2} & 1/\sqrt{2} & \mathbf{0}^T \\ 1/\sqrt{2} & -1/\sqrt{2} & \mathbf{0}^T \\ \mathbf{0} & \mathbf{0} & \mathbf{I} \end{bmatrix}$$

where $\mathbf{I}$ is an identity matrix of appropriate dimension. If a vector $\boldsymbol{v}$ is in a rotated quadratic cone $\mathcal{Q}_k^r$, the vector $\bar{\boldsymbol{v}} = \mathbf{K}\boldsymbol{v}$ will be in a quadratic cone $\mathcal{Q}_k$.

2.4 Semidefinite programming

The yield criteria used for finite element limit analysis may take the form of a semidefinite cone. This is the case for the general Mohr-Coulomb criterion,

which is given in terms of the principal stresses, i.e. the eigenvalues of the stress tensor. A matrix $\mathbf{M}$ is said to be positive semidefinite if it fulfils the following criterion:

$$\boldsymbol{x}^T\mathbf{M}\boldsymbol{x} \geq 0 \quad \text{for all} \quad \boldsymbol{x} \in \mathbb{R}^n \tag{2.17}$$

If the product $\boldsymbol{x}^T\mathbf{M}\boldsymbol{x}$ is strictly larger than zero, the matrix $\mathbf{M}$ is positive definite. A curved inequality sign $\succeq$ is often used to indicate that a matrix is positive semidefinite, e.g. $\mathbf{M} \succeq 0$.

The semidefinite optimisation problem can be stated in several different ways, and different authors use different notation. Vandenberghe and Boyd (1996) use the following, compact notation:

$$\begin{array}{ll} \text{minimise} & \boldsymbol{c}^T\boldsymbol{x} \\ \text{subject to} & \mathbf{F}(\boldsymbol{x}) \succeq 0 \end{array} \tag{2.18}$$

with

$$\mathbf{F}(\boldsymbol{x}) = \mathbf{F}_0 + \sum_{i=1}^{m} \mathbf{F}_i x_i$$

where $\mathbf{F}_i$ are symmetric matrices, and x_i is the ith element of $\boldsymbol{x}$. $\mathbf{F}(\boldsymbol{x}) \succeq 0$ is a so-called linear matrix inequality and defines a convex set of allowable vectors $\boldsymbol{x}$. Antoniou and Lu (2007) use a slightly different form of the semidefinite program which are closer to the standard form of LP and SOCP:

$$\begin{array}{ll} \text{minimise} & \mathbf{C} \cdot \mathbf{X} \\ \text{subject to} & \mathbf{A}_i \cdot \mathbf{X} = \boldsymbol{b}_i, \quad i = 1, 2, \ldots, m \\ & \mathbf{X} \succeq 0 \end{array} \tag{2.19}$$

where $\mathbf{C}$, $\mathbf{X}$, and $\mathbf{A}_i$ for all i are symmetric matrices of size n. The inner product, denoted by "$\cdot$", of two matrices is given as:

$$\mathbf{A} \cdot \mathbf{X} = \sum_{i=1}^{n} \sum_{j=1}^{n} a_{ij} x_{ij}$$

If $\mathbf{C}$ and all $\mathbf{A}_i$ are diagonal matrices, i.e.

$$\mathbf{C} = \text{diag}(\boldsymbol{c}), \quad \mathbf{A} = \text{diag}(\boldsymbol{a}),$$

the original semidefinite program (2.19) is reduced to the standard form of LP.

2.5 Optimality and algorithms

As mentioned, the Lagrangian can be used to establish the first-order optimality conditions. For the general, non-linear optimisation problem (2.3), we have the Lagrangian:

$$\mathcal{L}(\boldsymbol{x}, \boldsymbol{y}, \boldsymbol{s}) = f(\boldsymbol{x}) - \sum_{i=1}^{m} y_i g_i(\boldsymbol{x}) - \sum_{i=1}^{p} s_i h_i(\boldsymbol{x}) \tag{2.20}$$

Utilising the partial derivatives of the Lagrangian, the first-order optimality conditions (also called the Karush-Kuhn-Tucker, or KKT, conditions) can be stated as follows:

$$\nabla_{\boldsymbol{x}} \mathcal{L}(\boldsymbol{x}, \boldsymbol{y}, \boldsymbol{s}) = \nabla f(\boldsymbol{x}) - \sum_{i=1}^{m} y_i \nabla g_i(\boldsymbol{x}) - \sum_{i=1}^{p} s_i \nabla h_i(\boldsymbol{x}) = 0 \tag{2.21a}$$

$$\nabla_{\boldsymbol{y}} \mathcal{L}(\boldsymbol{x}, \boldsymbol{y}, \boldsymbol{s}) = g_i(\boldsymbol{x}) = 0, \quad i = 1, 2, \ldots, m \tag{2.21b}$$

$$\nabla_{\boldsymbol{s}} \mathcal{L}(\boldsymbol{x}, \boldsymbol{y}, \boldsymbol{s}) = h_i(\boldsymbol{x}) \geq 0, \quad i = 1, 2, \ldots, p \tag{2.21c}$$

$$s_i \geq 0, \quad i = 1, 2, \ldots, p \tag{2.21d}$$

$$s_i h_i(\boldsymbol{x}) = 0, \quad i = 1, 2, \ldots, m \tag{2.21e}$$

where ∇ is a differential operator and $\nabla_{\boldsymbol{x}}$ indicates the partial derivative with respect to $\boldsymbol{x}$. Any point $(\boldsymbol{x}^*, \boldsymbol{y}^*, \boldsymbol{s}^*)$ that fulfil (2.21) will be a solution to the primal problem and the dual problem. For convex optimisation problems, any local minimum must be the global minimum, hence, any point that fulfil the KKT conditions will be solution to both the dual and the primal problem. The condition(2.21e) is the complementarity condition, which will link the dual and primal solutions.

For linear programming we have the following KKT conditions:

$$\begin{aligned} &\mathbf{A}\boldsymbol{x} - \boldsymbol{b} = \mathbf{0} \\ &\mathbf{A}^T\boldsymbol{y} + \boldsymbol{s} - \boldsymbol{c} = \mathbf{0} \\ &\boldsymbol{x} \geq 0 \\ &\boldsymbol{s} \geq 0 \\ &x_i s_i = 0, \quad i = 1, 2, \ldots, n \end{aligned} \tag{2.22}$$

It is seen that the KKT conditions (2.22) comprise the constraints of the primal problem (2.5) and the dual problem (2.9).

For second-order cone programming, the KKT conditions are similar to

the linear case (2.22):

$$\begin{aligned}
&\mathbf{A}\boldsymbol{x} - \boldsymbol{b} = \mathbf{0} \\
&\mathbf{A}^T\boldsymbol{y} + \boldsymbol{s} - \boldsymbol{c} = \mathbf{0} \\
&\boldsymbol{x} \in \mathcal{Q} \\
&\boldsymbol{s} \in \mathcal{Q} \\
&\mathbf{arw}(\boldsymbol{x}_i)\mathbf{arw}(\boldsymbol{s}_i)\boldsymbol{e}_i = \mathbf{0}, \quad i = 1, 2, \ldots, q
\end{aligned} \tag{2.23}$$

where q is the number of conic constraints, and $\boldsymbol{e}_i$ is the first basis vector of appropriate dimension. The notation $\mathbf{arw}(\boldsymbol{v})$ denotes an arrowhead operation on the vector $\boldsymbol{v} \in \mathbb{R}^n$,

$$\mathbf{arw}(\boldsymbol{v}) = \begin{bmatrix} v_1 & \boldsymbol{v}_{2:n}^T \\ \boldsymbol{v}_{2:n} & v_1\mathbf{I} \end{bmatrix},$$

where v_1 is the first element in $\boldsymbol{v}$ and the notation $\boldsymbol{v}_{2:n}$ denotes the remaining $n-1$ elements of $\boldsymbol{v}$. Even for linear programming, the KKT conditions (2.22) represent a non-linear system of equations due to the complementarity condition with some additional non-negativity constraints on the variables.

Interior point methods

Optimisation problems are rarely solved by hand, and since the 1940s solution methods for optimisation problems have been an active field of research. One of the most well-known algorithms is the simplex algorithm first published by G. B. Dantzig in 1947 (see e.g. Dantzig, 1998). The method was used for linear programming and follows a simple scheme where it moves from vertex to vertex by updating the set of active constraints. The simplex method works remarkably well in practice, however, it has an exponential worst-case complexity, i.e. in the worst case scenario, the time required to solve the problem grows exponential with the problem size. This was shown by Klee and Minty (1972) who devised a problem where the simplex algorithm visited every single vertex before finding the optimum.

Karmarkar (1984) proposed an algorithm for linear programming with a polynomial worst-case complexity. Karmarkar's publication marked the beginning of a new era for mathematical programming. The algorithm lead to a class of algorithms, which today is known as interior point methods. It was shown by Nesterov and Nemirovsky (1988) that interior point methods could be extended to handle convex optimisation while maintaining the polynomial time complexity. Furthermore, Nesterov and Nemirovsky (1988) showed that interior point methods can solve general convex optimisation problems as efficiently as linear problems.

Mehrotra (1992) suggested an extension of Karmarkar's algorithm, namely a so-called predictor-corrector method, where two search directions are calculated every iteration. The same factorisation of the equation system can be used for both search directions, hence, the method only requires a marginally additional computational effort. The predictor-corrector is widely used today and implemented in many state-of-the-art solvers (see e.g. Wright, 1997; Roos et al., 1997; Nocedal and Wright, 2006; Terlaky, 2013).

Several methods and tricks, which increase the stability and speed of the algorithms, have been developed. Amongst those, the homogeneous model can be mentioned (Sturm, 1997; Nesterov et al., 1999), where the original problem is embedded in a slightly larger problem in order to detect infeasibility and ill-posed problems.

State-of-the-art commercial solvers for second-order cone programming also use scaling to increase the speed and accuracy of the algorithms. The non-linear system of equations is solved using the Newton's method in a scaled space, where a unique solution always is ensured (Nesterov and Todd, 1997; Kuo and Mittelmann, 2004). It has been proven that interior point algorithms based on scaling has a polynomial time complexity (Tsuchiya, 1999; Monteiro and Tsuchiya, 2000).

The mathematical optimisation problem of finite element limit analysis will generally feature extremely sparse problem matrices. This can be exploited by state-of-the-art solvers, and the computational time be a polynomial of a low order. In the following chapters, the computational time for various problems will be analysed and discussed.

Chapter 3

Finite element limit analysis

3.1 Introduction

A brief introduction to the field of finite element limit analysis was given in Section 1.3, and the historical development of the method as a whole was discussed. Like the manual counterpart, numerical limit analysis poses an optimisation problem, however, the types of problems are different. For manual limit analysis, the optimisation variables are typically angles of yield lines or geometric parameters, and the resulting mathematical optimisation problem are highly non-linear and non-convex (see e.g. the upper bound model by Joergensen and Hoang, 2013).

For finite element limit analysis, the domain is discretised using finite elements, hence, the geometry of the problem is given in advance, and the optimisation variables are the discretised stress and displacement fields. Provided a convex yield function, the resulting mathematical optimisation problem will be convex and, therefore, easy to solve in a mathematical sense. The type of optimisation problem depends on the yield criterion, however, the yield functions can often be approximated using e.g. linear constraints, which was a widely used technique before second-order cone programming and semidefinite programming became established technologies (Olsen, 1998, 1999; Poulsen and Damkilde, 2000).

Equivalently to manual limit analysis discussed in Section 1.2, finite element limit analysis can be formulated as either strict lower bound or upper bound problems which makes it possible to bound the exact limit load in a rigorous manner. A third formulation commonly called mixed problems can be considered as something in-between the lower and upper bound problems. Mixed formulations provide neither a statically admissible stress field nor a kinematically admissible collapse mode, however, the calculated collapse

load will be typically closer to the exact limit load than an equivalent lower or upper bound solution. Mixed finite elements will be discussed in Chapter 6.

3.2 Problem formulation

The scope of the basic lower bound formulation is to maximise the load acting on a given structure while ensuring a statically admissible and safe stress field, i.e. a stress field that satisfies the equilibrium conditions and does not violate the yield functions in any point. The problem variables of the lower bound problem is the discretised stress field, however, additional variables usually called auxiliary variables are typically needed in order to cast the yield function as either a second-order cone or a semidefinite cone.

The scope of the upper bound formulation is to minimise the load acting on a given structure while ensuring a kinematically admissible collapse mode. The primary variables of the upper bound problem are the discretised displacement field as well as the plastic multipliers.

Triangular elements with linear stress fields and quadratic displacement fields are generally favoured (Sloan, 1988, 1989; Makrodimopoulos and Martin, 2006). The stress fields of such elements are defined by stress vectors in the vertexes, and the state of stress in any point within the element can be stated as a linear combination of the stress vectors. Linear stress fields in combination with triangular elements means that it is only necessary to check the yield function in the vertexes to ensure a statically admissible stress field of the element. Moreover, for lower bound elements, traction continuity can likewise be ensure by enforcing the conditions near the vertexes of a given element boundary.

Example: Bar with quadratic displacement field

In order to illustrate some of the principles of finite element limit analysis, a simple example is presented. We now consider a bar element with a quadratic displacement field and a linear stress field, see Figure 3.1. The upper bound formulation of the bar element will now be derived. The quadratic displacement field and corresponding strain field are discretised and denoted $\hat{\boldsymbol{u}}$ and $\hat{\boldsymbol{\varepsilon}}$, respectively. Similarly, the stress field and external loading are discretised and denoted $\hat{\boldsymbol{\sigma}}$ and $\hat{\boldsymbol{P}}$, respectively.

$$\hat{\boldsymbol{u}} = \begin{bmatrix} u_1 \\ u_2 \\ u_3 \end{bmatrix}, \quad \hat{\boldsymbol{\varepsilon}} = \begin{bmatrix} \varepsilon_1 \\ \varepsilon_2 \end{bmatrix}, \quad \hat{\boldsymbol{\sigma}} = \begin{bmatrix} \sigma_1 \\ \sigma_2 \end{bmatrix}, \quad \hat{\boldsymbol{P}} = \begin{bmatrix} P_1 \\ P_2 \\ P_3 \end{bmatrix}.$$

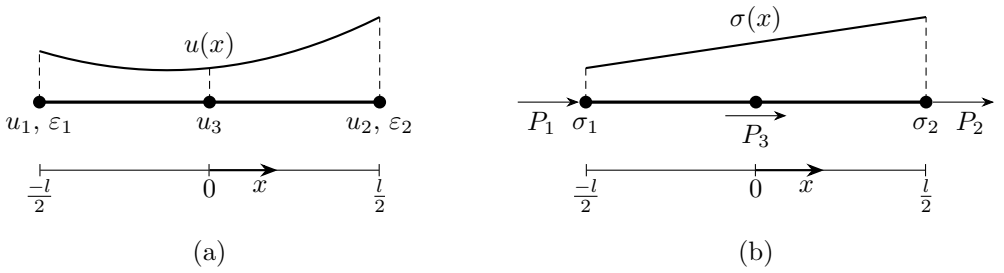

Figure 3.1*: a) The discretised displacements and strains for the bar, b) the discretised stresses and external loads.*

The displacement in a point x can be stated as

$$\boldsymbol{u} = \mathbf{N}_u \hat{\boldsymbol{u}} = \begin{bmatrix} 2s^2 - s, & 2s^2 + s, & -4s^2 + 1 \end{bmatrix} \hat{\boldsymbol{u}}$$

where $s = x/l$ is a length coordinate. The relationship between the displacements and strains is given as

$$\boldsymbol{\varepsilon} = \frac{\partial \boldsymbol{u}}{\partial x} = (\boldsymbol{\nabla} \mathbf{N}_u)\, \hat{\boldsymbol{u}} = \mathbf{B} \hat{\boldsymbol{u}}$$

where $\boldsymbol{\nabla}$ is a differential operator and $\mathbf{B}$ is given as

$$\mathbf{B} = \boldsymbol{\nabla} \mathbf{N}_u = \frac{1}{l} \begin{bmatrix} 4s - 1, & 4s + 1, & -8s \end{bmatrix}$$

The linear stress field can be expressed in terms of linear shape functions and the discretised stress field:

$$\boldsymbol{\sigma} = \mathbf{N}_\sigma \hat{\boldsymbol{\sigma}} = \begin{bmatrix} \frac{1}{2} - s, & \frac{1}{2} + s \end{bmatrix} \hat{\boldsymbol{\sigma}}$$

The work equation (1.5) for the bar can now be stated as follows using discretised quantities:

$$\hat{\boldsymbol{u}}^T \hat{\boldsymbol{P}} = \int_\Omega \boldsymbol{\varepsilon}^T \boldsymbol{\sigma} \mathrm{d}\Omega = \int_\Omega \hat{\boldsymbol{u}}^T \mathbf{B}^T \mathbf{N}_\sigma \hat{\boldsymbol{\sigma}} \mathrm{d}\Omega \tag{3.1}$$

All the discretised quantities are independent from the coordinates of the considered domain, hence, we obtain

$$\hat{\boldsymbol{u}}^T \hat{\boldsymbol{P}} = \hat{\boldsymbol{u}}^T \left[\int_\Omega \mathbf{B}^T \mathbf{N}_\sigma \mathrm{d}\Omega \right] \hat{\boldsymbol{\sigma}} = \hat{\boldsymbol{u}}^T \left[\int_{-l/2}^{l/2} \mathbf{B}^T \mathbf{N}_\sigma \mathrm{d}x \right] (A \hat{\boldsymbol{\sigma}})$$

where A is the cross sectional area of the bar. Eliminating $\hat{\boldsymbol{u}}^T$ and defining $\hat{\mathbf{B}}^T$ for the bar as

$$\hat{\mathbf{B}}^T = \int_{-l/2}^{l/2} \mathbf{B}^T \mathbf{N}_\sigma \mathrm{d}x = \begin{bmatrix} -5/6 & -1/6 \\ 1/6 & 5/6 \\ 4/6 & -4/6 \end{bmatrix},$$

we arrive at the following relation between the stress field (or normal forces) and external forces:

$$\hat{\boldsymbol{P}} = \begin{bmatrix} P_1 \\ P_2 \\ P_3 \end{bmatrix} = \begin{bmatrix} -5/6 & -1/6 \\ 1/6 & 5/6 \\ 4/6 & -4/6 \end{bmatrix} \begin{bmatrix} A\sigma_1 \\ A\sigma_2 \end{bmatrix} = \hat{\mathbf{B}}^T \hat{\boldsymbol{n}} \tag{3.2}$$

where $\hat{\boldsymbol{n}}$ is the discretised normal force vector. Equation (3.2) has the shape of equilibrium equations which relates the stresses (or section forces) to the external loads, however, (3.2) does not ensure a statically admissible stress field. The equations are derived from the relation between the displacements and the strains, hence, (3.2) ensures a kinematically admissible collapse mode.

For lower bound solutions, it is often more convenient to establish $\hat{\mathbf{B}}^T$ directly from the necessary requirements to equilibrium for the considered domain. For the bar shown in Figure 3.1, the three necessary relations between the external loads and stresses can easily be established:

$$\begin{aligned} P_1 &= -A\sigma_1 \\ P_2 &= A\sigma_2 \\ P_3 &= A\left(\sigma_1 - \sigma_2\right) \end{aligned}$$

or equivalently in matrix form:

$$\hat{\boldsymbol{P}} = \begin{bmatrix} P_1 \\ P_2 \\ P_3 \end{bmatrix} = \begin{bmatrix} -1 & 0 \\ 0 & 1 \\ 1 & -1 \end{bmatrix} \begin{bmatrix} A\sigma_1 \\ A\sigma_2 \end{bmatrix} = \hat{\mathbf{B}}^T \hat{\boldsymbol{n}} \tag{3.3}$$

The set of equations (3.3) ensures equilibrium, but not a kinematically admissible collapse mode.

General lower bound formulation

The procedure described for the bar example is general in some ways. For the general case, we also define the discretised quantities, i.e. the discretised displacement field $\hat{\boldsymbol{u}}$, the discretised external load $\hat{\boldsymbol{P}}$, the discretised

stress field $\hat{\boldsymbol{\sigma}}$, and the discretised strain field $\hat{\boldsymbol{\varepsilon}}$. Shape functions define the relationship between the continuous and discretised fields:

$$\boldsymbol{\sigma} = \mathbf{N}_\sigma \hat{\boldsymbol{\sigma}}, \quad \boldsymbol{\varepsilon} = \mathbf{N}_\varepsilon \hat{\boldsymbol{\varepsilon}}, \quad \boldsymbol{u} = \mathbf{N}_u \hat{\boldsymbol{u}} \tag{3.4}$$

The stress and strain fields will often use the same shape functions, i.e. $\mathbf{N}_\sigma = \mathbf{N}_\varepsilon$. The strain field is defined as the derivative of the displacement field:

$$\boldsymbol{\varepsilon} = \frac{\partial \boldsymbol{u}}{\partial \boldsymbol{x}} = \frac{\partial \mathbf{N}_u}{\partial \boldsymbol{x}} \hat{\boldsymbol{u}} = \mathbf{B} \hat{\boldsymbol{u}} \tag{3.5}$$

where $\mathbf{B}$ is the strain-interpolation matrix. The work equation (1.5) now reads

$$\hat{\boldsymbol{u}}^T \hat{\boldsymbol{P}} = \int_\Omega \boldsymbol{\varepsilon}^T \boldsymbol{\sigma} \mathrm{d}\Omega \tag{3.6}$$

where $\boldsymbol{\varepsilon}$ and $\boldsymbol{\sigma}$ are continuous quantities and functions of the coordinates of the domain Ω. The continuous quantities in (3.6) can be replaced by shape functions and the discretised quantities according to (3.4) and (3.5):

$$\hat{\boldsymbol{u}}^T \hat{\boldsymbol{P}} = \int_\Omega \left(\mathbf{B} \hat{\boldsymbol{u}}\right)^T \left(\mathbf{N}_\sigma \hat{\boldsymbol{\sigma}}\right) \mathrm{d}\Omega \tag{3.7}$$

The quantities $\hat{\boldsymbol{u}}$ and $\hat{\boldsymbol{\sigma}}$ are not functions of the coordinates of domains, hence, (3.7) can be restated as

$$\hat{\boldsymbol{u}}^T \hat{\boldsymbol{P}} = \hat{\boldsymbol{u}}^T \left[\int_\Omega \mathbf{B}^T \mathbf{N}_\sigma \mathrm{d}\Omega \right] \hat{\boldsymbol{\sigma}} \tag{3.8}$$

Elimitating the displacements $\hat{\boldsymbol{u}}^T$ from the equation and defining $\hat{\mathbf{B}}$ as

$$\hat{\mathbf{B}}^T = \int_\Omega \mathbf{B}^T \mathbf{N}_\sigma \mathrm{d}\Omega,$$

we obtain the discretised equilibrium equations:

$$\hat{\boldsymbol{P}} = \hat{\mathbf{B}}^T \hat{\boldsymbol{\sigma}} \tag{3.9}$$

As shown for the bar, (3.9) does not necessarily ensure equilibrium despite the name of the system of equations. Whether or not equilibrium is ensured depends on $\hat{\mathbf{B}}^T$.

The discretised stress field $\hat{\boldsymbol{\sigma}}$ approximates the exact stress field and fulfils the yield functions in the chosen check points,

$$f(\hat{\boldsymbol{\sigma}}_i) \leq 0, \; i = 1, 2, \ldots, m \tag{3.10}$$

where m is the number of check points, and $\hat{\boldsymbol{\sigma}}_i$ is a subset of the discretised stress field $\hat{\boldsymbol{\sigma}}$. The total load $\hat{\boldsymbol{P}}$ is assumed to comprise a constant part $\hat{\boldsymbol{p}}_0$ and a scalable part $\hat{\boldsymbol{p}}\lambda$ where λ is the load factor, which is sought to be maximised while ensuring a statically admissible stress field. The resulting optimisation problem can now be stated as

$$\begin{array}{lll} \text{maximise} & \lambda & \\ \text{subject to} & \hat{\mathbf{B}}^T\hat{\boldsymbol{\sigma}} = \hat{\boldsymbol{p}}\lambda + \hat{\boldsymbol{p}}_0 & \\ & f(\hat{\boldsymbol{\sigma}}_i) \leq 0, & i = 1, 2, \ldots, m \end{array} \tag{3.11}$$

which combines (3.9) and (3.10). Provided that $\hat{\mathbf{B}}^T$ is defined such that equilibrium is ensured, the solution to (3.11) will be a lower bound solution since the discretised stress field $\hat{\boldsymbol{\sigma}}$ will be statically admissible and safe.

General upper bound formulation

For the upper bound formulation, the yield function f is linearised around a point $\tilde{\boldsymbol{\sigma}}$ which satisfies $f(\tilde{\boldsymbol{\sigma}}) \leq 0$. This gives

$$\left(\boldsymbol{\nabla} f(\tilde{\boldsymbol{\sigma}})\right)^T \boldsymbol{\sigma} \leq k \tag{3.12}$$

with

$$k = \left(\boldsymbol{\nabla} f(\tilde{\boldsymbol{\sigma}})\right)^T \tilde{\boldsymbol{\sigma}}$$

which follows from the associated flow rule (1.3) and the assumed convexity of the yield function. k will in the general case depend on the stress $\tilde{\boldsymbol{\sigma}}$, however, for commonly used yield functions, e.g. the Mohr-Coulomb criterion, k will be a constant. The associated flow rule gives the following relation:

$$\boldsymbol{\varepsilon} = \lambda_p \frac{\partial f(\boldsymbol{\sigma})}{\partial \boldsymbol{\sigma}} = \lambda_p \boldsymbol{\nabla} f(\boldsymbol{\sigma}),$$

where $\lambda_p \geq 0$ are the plastic multiplier. The linearised yield function is now introduced, and we obtain

$$\boldsymbol{\varepsilon} = \lambda_p \boldsymbol{\nabla} f(\tilde{\boldsymbol{\sigma}}),$$

where $\boldsymbol{\nabla} f(\tilde{\boldsymbol{\sigma}})$ is a constant vector. The discretised version of the flow rule can be derived from the internal work, which can be stated as:

$$W_{\text{int}} = \int_\Omega \boldsymbol{\sigma}^T \boldsymbol{\varepsilon} \mathrm{d}\Omega = \int_\Omega \boldsymbol{\sigma}^T \left(\lambda_p \boldsymbol{\nabla} f(\tilde{\boldsymbol{\sigma}})\right) \mathrm{d}\Omega \tag{3.13}$$

Defining the discretised plastic multipliers using shape functions,

$$\lambda_p = \mathbf{N}_\lambda \hat{\boldsymbol{\lambda}}_p,$$

and introducing the discretised quantities into the integral of (3.13) gives the following relation ship between the discretised displacements and plastic multipliers:

$$\int_\Omega \left(\mathbf{N}_\sigma \hat{\boldsymbol{\sigma}}\right)^T \left(\mathbf{B}\hat{\boldsymbol{u}}\right) \mathrm{d}\Omega = \int_\Omega \left(\mathbf{N}_\sigma \hat{\boldsymbol{\sigma}}\right)^T \left(\boldsymbol{\nabla} f(\tilde{\boldsymbol{\sigma}}) \mathbf{N}_\lambda \hat{\boldsymbol{\lambda}}_p\right) \mathrm{d}\Omega \tag{3.14}$$

The discretised quantities are independent of the coordinates of the domain, hence, (3.14) can be restated as

$$\hat{\boldsymbol{\sigma}}^T \left[\int_\Omega \mathbf{N}_\sigma^T \mathbf{B} \mathrm{d}\Omega\right] \hat{\boldsymbol{u}} = \hat{\boldsymbol{\sigma}}^T \left[\int_\Omega \mathbf{N}_\sigma^T \boldsymbol{\nabla} f(\tilde{\boldsymbol{\sigma}}) \mathbf{N}_\lambda \mathrm{d}\Omega\right] \hat{\boldsymbol{\lambda}}_p \tag{3.15}$$

The stress field can be eliminated from the equation and we arrive at the discretised flow rule,

$$\hat{\mathbf{B}}\hat{\boldsymbol{u}} = \hat{\mathbf{F}}(\tilde{\boldsymbol{\sigma}})\hat{\boldsymbol{\lambda}}_p, \tag{3.16}$$

where $\hat{\mathbf{B}}$ and $\hat{\mathbf{F}}(\tilde{\boldsymbol{\sigma}})$ is given as

$$\hat{\mathbf{B}} = \int_\Omega \mathbf{N}_\sigma^T \mathbf{B} \mathrm{d}\Omega$$

and

$$\hat{\mathbf{F}}(\tilde{\boldsymbol{\sigma}}) = \int_\Omega \mathbf{N}_\sigma^T \boldsymbol{\nabla} f(\tilde{\boldsymbol{\sigma}}) \mathbf{N}_\lambda \mathrm{d}\Omega$$

An expression for the load factor, which is sought to be minimised, can be derived in a similar manner. An upper bound to the internal work can now be stated using the linearised yield function:

$$\int_\Omega \left(\lambda_p \boldsymbol{\nabla} f(\tilde{\boldsymbol{\sigma}})\right)^T \boldsymbol{\sigma} \mathrm{d}\Omega \leq \int_\Omega \lambda_p k \mathrm{d}\Omega \tag{3.17}$$

Introducing the discretised plastic multipliers $\hat{\boldsymbol{\lambda}}$ and shape functions gives

$$W_{\text{int}} = \int_\Omega \lambda_p k \mathrm{d}\Omega = \int_\Omega k \mathbf{N}_\lambda \hat{\boldsymbol{\lambda}} \mathrm{d}\Omega = \left[k \int_\Omega \mathbf{N}_\lambda \mathrm{d}\Omega\right] \hat{\boldsymbol{\lambda}}_p = \hat{\boldsymbol{k}}^T \hat{\boldsymbol{\lambda}}_p \tag{3.18}$$

which also defined $\hat{\boldsymbol{k}}$ implicitly. The work done by external loads, $\hat{\boldsymbol{p}}\lambda + \hat{\boldsymbol{p}}_0$, is given as

$$W_{\text{ext}} = \hat{\boldsymbol{u}}^T \left(\hat{\boldsymbol{p}}\lambda + \hat{\boldsymbol{p}}_0\right) \tag{3.19}$$

Equating the internal work (3.18) and the external work (3.19) gives an expression of the load factor λ:

$$\lambda = \frac{\hat{\boldsymbol{k}}^T \hat{\boldsymbol{\lambda}}_p - \hat{\boldsymbol{u}}^T \hat{\boldsymbol{p}}_0}{\hat{\boldsymbol{u}}^T \hat{\boldsymbol{p}}} \tag{3.20}$$

which can be reduced to a linear expression by scaling the denominator, i.e. $\hat{\boldsymbol{u}}^T\hat{\boldsymbol{p}} = 1$. The optimal upper bound solution is the lowest load which satisfies $\hat{\boldsymbol{u}}^T\hat{\boldsymbol{p}} = 1$ as well as (3.16):

$$\begin{array}{ll} \text{minimise} & \hat{\boldsymbol{k}}^T\hat{\boldsymbol{\lambda}}_p - \hat{\boldsymbol{u}}^T\hat{\boldsymbol{p}}_0 \\ \text{subject to} & \hat{\mathbf{B}}\hat{\boldsymbol{u}} = \hat{\mathbf{F}}(\tilde{\boldsymbol{\sigma}})\hat{\boldsymbol{\lambda}}_p \\ & \hat{\boldsymbol{u}}^T\hat{\boldsymbol{p}} = 1 \\ & \hat{\boldsymbol{\lambda}}_p \geq 0 \end{array} \tag{3.21}$$

The approach of (3.21) is rather impractical, and - as already discussed - upper bound problems can be implemented using the same formulation as for lower bound problems (see also Krabbenhoft et al., 2005; Makrodimopoulos and Martin, 2007). The upper bound formulation (3.21) has the dual problem,

$$\begin{array}{ll} \text{maximise} & \lambda \\ \text{subject to} & \hat{\mathbf{B}}^T\hat{\boldsymbol{\sigma}} = \hat{\boldsymbol{p}}\lambda + \hat{\boldsymbol{p}}_0 \\ & \left(\hat{\mathbf{F}}(\tilde{\boldsymbol{\sigma}})\right)^T\hat{\boldsymbol{\sigma}} \leq \hat{\boldsymbol{k}} \end{array}$$

which is a linearised version of the lower bound formulation (3.11). $\hat{\boldsymbol{\sigma}}$ and λ are the Lagrange variables associated with the flow rule condition and the scaling ($\hat{\boldsymbol{u}}^T\hat{\boldsymbol{p}} = 1$), respectively. The inequalities,

$$\left(\hat{\mathbf{F}}(\tilde{\boldsymbol{\sigma}})\right)^T\hat{\boldsymbol{\sigma}} \leq \hat{\boldsymbol{k}}$$

represent the discretised linearised yield function, which can be replaced by the original, non-linear function to obtain

$$\begin{array}{ll} \text{maximise} & \lambda \\ \text{subject to} & \hat{\mathbf{B}}^T\hat{\boldsymbol{\sigma}} = \hat{\boldsymbol{p}}\lambda + \hat{\boldsymbol{p}}_0 \\ & f(\hat{\boldsymbol{\sigma}}_i) \leq 0, \quad i = 1, 2, \ldots, m \end{array}$$

Again, the equilibrium matrix $\hat{\mathbf{B}}^T$ determines whether or not the particular problem is a lower bound, upper bound, or mixed problem. As discussed in Chapter 2, the primal and dual problems are solved simultaneously. This means that a stress field is determined when solving the upper bound problem, but the stress field is most likely not statically admissible. Similarly, a collapse mode is determined when solving the lower bound problem, however, the collapse mode is most likely not kinematically admissible. Nevertheless, the upper bound stress field and lower bound collapse mode hold some information and can be used to analyse the behaviour of the considered structure.

In the following sections and chapters, the discretised quantities are referred to without the hat for convenience, e.g. $\boldsymbol{\sigma}$ will refer to the discretised stress field.

Optimality conditions for finite element limit analysis

The formulation of finite element limit analysis (3.21) represent a convex optimisation problem, thus, the first-order optimality conditions (KKT conditions) will be sufficient to prove optimality for the problem. The problem (3.21) can be rewritten as

$$\begin{aligned} \text{maximise} \quad & \begin{bmatrix}\mathbf{0}^T & 1\end{bmatrix}\begin{bmatrix}\boldsymbol{\sigma}\\ \lambda\end{bmatrix} \\ \text{subject to} \quad & \begin{bmatrix}\mathbf{B}^T & -\boldsymbol{p}\end{bmatrix}\begin{bmatrix}\boldsymbol{\sigma}\\ \lambda\end{bmatrix} = \boldsymbol{p}_0 \\ & -f(\boldsymbol{\sigma}_i) \geq 0, \quad i = 1, 2, \ldots, m \end{aligned} \tag{3.22}$$

The Lagrangian to the problem (3.22) is given as

$$\mathcal{L}\left(\boldsymbol{\sigma}, \lambda, \boldsymbol{u}, \boldsymbol{\lambda}_p\right) = \begin{bmatrix}\mathbf{0}^T & 1\end{bmatrix}\begin{bmatrix}\boldsymbol{\sigma}\\ \lambda\end{bmatrix} - \boldsymbol{u}^T\left(\begin{bmatrix}\mathbf{B}^T & -\boldsymbol{p}\end{bmatrix}\begin{bmatrix}\boldsymbol{\sigma}\\ \lambda\end{bmatrix} - \boldsymbol{p}_0\right) + \sum_{i=1}^{m}\lambda_p^{(i)} f(\boldsymbol{\sigma}_i) \tag{3.23}$$

where $\boldsymbol{u}$ is the discretised displacement field and the Lagrange variables associated with the equality constraints of the optimisation problem (3.22). The notation $\lambda_p^{(i)}$ denotes the ith element in the plastic multiplier vector $\boldsymbol{\lambda}_p$ which is the Lagrange variables associated with the inequality constraints. The KKT conditions can now be stated as follows:

$$\nabla_{\boldsymbol{\sigma}}\mathcal{L} = -\mathbf{B}\boldsymbol{u} + \boldsymbol{\lambda}_p \boldsymbol{\nabla} f(\boldsymbol{\sigma}) = 0 \tag{3.24a}$$
$$\nabla_{\lambda}\mathcal{L} = 1 - \boldsymbol{p}^T\boldsymbol{u} = 0 \tag{3.24b}$$
$$\nabla_{\boldsymbol{u}}\mathcal{L} = \mathbf{B}^T\boldsymbol{\sigma} - \boldsymbol{p}\lambda - \boldsymbol{p}_0 = 0 \tag{3.24c}$$
$$\nabla_{\boldsymbol{\lambda}_p}\mathcal{L} = -f(\boldsymbol{\sigma}_i) \geq 0, \quad i = 1, 2, \ldots, m \tag{3.24d}$$
$$\lambda_p^{(i)} \geq 0, \quad i = 1, 2, \ldots, m \tag{3.24e}$$
$$\lambda_p^{(i)} f(\boldsymbol{\sigma}_i) = 0, \quad i = 1, 2, \ldots, m \tag{3.24f}$$

The KKT conditions (3.24) include the equality constraints of the lower and upper bound problems (using the general, non-linear yield function), hence, any solution $\left(\boldsymbol{\sigma}^*, \lambda^*, \boldsymbol{u}^*, \boldsymbol{\lambda}_p^*\right)$ which satisfies (3.24) will fulfil the primal and dual problems of finite element limit analysis. Moreover, the link between the primal and dual problems, (3.24f), is recognised as the complementarity condition introduced in Section 1.2, see Equation (1.4).

Lower bound material optimisation

Material optimisation can be considered as a special case of the lower bound problem. The scope is not to maximise the external load but rather to minimise the weighted cost of the materials for a given load case. The yield function now takes an additional input, namely the vector $\boldsymbol{\phi}$ which contains the material parameters:

$$f(\boldsymbol{\sigma}_i, \boldsymbol{\phi}) \leq 0, \ i = 1, 2, \ldots, m$$

The resulting optimisation problem can be stated as

$$\begin{aligned} &\text{maximise} && \boldsymbol{w}^T \boldsymbol{\phi} \\ &\text{subject to} && \mathbf{B}^T \boldsymbol{\sigma} = \boldsymbol{p}_0 \\ & && f(\boldsymbol{\sigma}_i, \boldsymbol{\phi}) \leq 0, \quad i = 1, 2, \ldots, m \end{aligned} \tag{3.25}$$

where $\boldsymbol{w}$ is the weight vector which depends on the cost of the given material and the particular areas or volumes associated with the material parameter. Material optimisation has a considerable potential in regards to design and analysis of new structures, however, the work presented in this thesis is primarily concerned with the lower bound load optimisation problem (3.11).

Multiple load cases

Structures have to be designed to withstand a number of different load cases prescribed by the standards, e.g. wind from different directions combined with snow, dead load, and imposed loads. When assuming a linear elastic material, the multiple load cases can be handled with a marginally additional computational effort, however, this is not the case if plasticity is considered and the stiffness of the system depends on the stress field.

A given structure is subjected to N load cases each described by the load vectors $\boldsymbol{p}_0^i$ and $\boldsymbol{p}^i$, $i = 1, 2, \ldots, N$. The lower bound problem (3.11) can be expanded to obtain

$$\begin{aligned} &\text{maximise} && \lambda \\ &\text{subject to} && \begin{bmatrix} \mathbf{B}^T & & & \\ & \mathbf{B}^T & & \\ & & \ddots & \\ & & & \mathbf{B}^T \end{bmatrix} \begin{bmatrix} \boldsymbol{\sigma}^1 \\ \boldsymbol{\sigma}^2 \\ \vdots \\ \boldsymbol{\sigma}^N \end{bmatrix} = \begin{bmatrix} \boldsymbol{p}^1 \\ \boldsymbol{p}^2 \\ \vdots \\ \boldsymbol{p}^N \end{bmatrix} \lambda + \begin{bmatrix} \boldsymbol{p}_0^1 \\ \boldsymbol{p}_0^2 \\ \vdots \\ \boldsymbol{p}_0^N \end{bmatrix} \\ & && f(\boldsymbol{\sigma}_i^1) \leq 0, \quad i = 1, 2, \ldots, m \\ & && f(\boldsymbol{\sigma}_i^2) \leq 0, \quad i = 1, 2, \ldots, m \\ & && \vdots \\ & && f(\boldsymbol{\sigma}_i^N) \leq 0, \quad i = 1, 2, \ldots, m \end{aligned} \tag{3.26}$$

The stress fields $\boldsymbol{\sigma}^i$ are independent and only the critical load case affects the load factor, hence, the combined optimisation problem (3.26) can be split into N problems and the critical load factor can be determined as the lowest load factor:

$$\lambda = \min\left(\lambda^1, \ldots, \lambda^N\right)$$

It is generally more efficient to solve many small problems rather than one large problem, hence, it is advantageous to split the combined problem (3.26) into N smaller problems.

In the case of material optimisation, the stress fields are linked together by the material parameter vector $\boldsymbol{\phi}$ via the yield functions. The resulting optimisation problem is given as

$$\begin{aligned}
&\text{maximise} && \boldsymbol{w}^T\boldsymbol{\phi} \\
&\text{subject to} && \begin{bmatrix} \mathbf{B}^T & & & \\ & \mathbf{B}^T & & \\ & & \ddots & \\ & & & \mathbf{B}^T \end{bmatrix} \begin{bmatrix} \boldsymbol{\sigma}^1 \\ \boldsymbol{\sigma}^2 \\ \vdots \\ \boldsymbol{\sigma}^N \end{bmatrix} = \begin{bmatrix} \boldsymbol{p}_0^1 \\ \boldsymbol{p}_0^2 \\ \vdots \\ \boldsymbol{p}_0^N \end{bmatrix} \\
& && f(\boldsymbol{\sigma}_i^1, \boldsymbol{\phi}) \leq 0, \quad i = 1, 2, \ldots, m \\
& && f(\boldsymbol{\sigma}_i^2, \boldsymbol{\phi}) \leq 0, \quad i = 1, 2, \ldots, m \\
& && \vdots \\
& && f(\boldsymbol{\sigma}_i^N, \boldsymbol{\phi}) \leq 0, \quad i = 1, 2, \ldots, m
\end{aligned} \tag{3.27}$$

where the external load cases are given by the vectors $\boldsymbol{p}_0^i$. The problem (3.27) cannot be split into smaller problems since the stress fields are not independent, and the combined problem has to be solved. Specialised solvers may be able to exploit the structure of the problem (3.27), however, to the best knowledge of the author papers on such algorithms have not been published.

3.3 Commonly used yield criteria

In this section, the commonly used yield criteria for structural engineering and their conic formulation will be presented. The conic formulations of many yield functions are presented by Bisbos and Pardalos (2007). Krabbenhøft et al. (2007), Krabbenhøft et al. (2008) and Makrodimopoulos and Martin (2008) present the conic formulation of the Mohr-Coulomb criterion, which is commonly used for soil. As discussed in Section 1.2, yield functions are generally non-linear but convex and can be stated as

$$f(\boldsymbol{\sigma}) \leq 0$$

where f is the yield function and $\boldsymbol{\sigma}$ is the given stress state. In most cases, some auxiliary variables are necessary to recast the yield function in a format which fit the chosen scheme of optimisation.

The Mohr-Coulomb criterion

The Mohr-Coulomb criterion can be used to describes materials prone to sliding failure. This includes soils, rock, and concrete. The basic material constants are the cohesion c and the internal angle of friction θ or the friction coefficient $\mu = \tan\theta$. For some materials, the sliding failure criterion is combined with a criterion for separation failure which bounds the tensile stresses by the tensile strength f_t. For concrete, the uniaxial compressive strength f_c is often used, which can be expressed in terms of the cohesion and a friction parameter k:

$$f_c = 2\,c\,\sqrt{k}$$

with

$$k = \left(\sqrt{1+\mu^2} + \mu\right)^2$$

where μ is the friction coefficient and θ is the internal angle of friction. For normal strength concrete, $k = 4$ corresponding to $\mu = 3/4$ and $\theta \approx 37°$ is commonly used. The Mohr-Coulomb criterion is typically formulated in terms of the principal stresses. In three-dimensions, the criterion reads

$$\sigma_1 \leq f_t \tag{3.28a}$$

$$k\,\sigma_1 - \sigma_3 \leq f_c \tag{3.28b}$$

where $\sigma_1 \leq f_t$ constitutes the separation criterion and $k\,\sigma_1 - \sigma_3 \leq f_c$ the sliding criterion. σ_1 and σ_3 are the largest and smallest principal stresses, respectively.

The yield envelope has a rather simple form illustrated in Figure 3.2. The criterion (3.28) is based on the principal stresses, which are the eigenvalues of the stress tensor, hence, (3.28) can be modelled exactly using semidefinite cones, which makes it possible to impose constraints on the eigenvalues of symmetric matrices (Krabbenhøft et al., 2008; Makrodimopoulos and Martin, 2008; Larsen, 2010). The formulation $\mathbf{F} \succeq 0$ indicates that the lowest eigenvalue of $\mathbf{F}$ must be non-negative, while $-\mathbf{F} \succeq 0$ indicates that the largest eigenvalue of F must be non-positive.

Introducing the concrete stress tensor $\boldsymbol{\sigma}_c$, which has the eigenvalues $\sigma_1 \geq \sigma_2 \geq \sigma_3$, the separation criterion (3.28a) can then be rewritten as

$$-\,\boldsymbol{\sigma}_c + f_t\mathbf{I} \succeq 0 \tag{3.29}$$

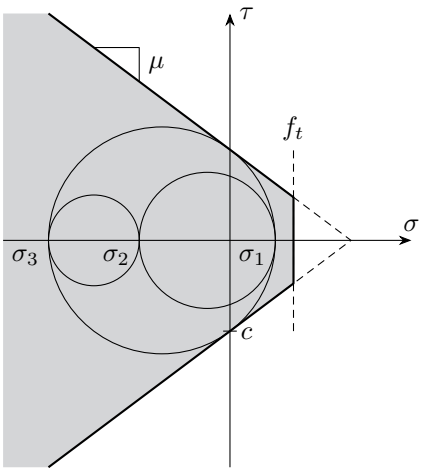

***Figure 3.2**: The Mohr-Coulomb yield envelope including separation criterion. Mohr's circle for a triaxial stress state is shown inside the envelope.*

where $\mathbf{I}$ is the identity matrix. The sliding criterion (3.28b) uses two principal stresses, hence, it is necessary to introduce an auxiliary variable α_1 to obtain

$$\begin{aligned} -\sigma_1 + \alpha_1 &\geq 0 \\ \sigma_3 - k\,\alpha_1 + f_c &\geq 0 \end{aligned} \tag{3.30}$$

Using the concrete stress tensor σ_c, (3.30) can be rewritten as

$$-\boldsymbol{\sigma}_c + \alpha_1 \mathbf{I} \succeq 0 \tag{3.31a}$$

$$\boldsymbol{\sigma}_c + (f_c - k\,\alpha_1)\,\mathbf{I} \succeq 0 \tag{3.31b}$$

The equations (3.29) and (3.31) comprise three linear matrix inequalities, however, they can be reduced to two by introducing an additional variable α_2 which fulfils:

$$\alpha_2 \leq f_t \qquad \text{and} \qquad \alpha_2 \leq \alpha_1$$

The Mohr-Coulomb criterion can now be stated as:

$$\begin{aligned} -\boldsymbol{\sigma}_c + \alpha_2 \mathbf{I} &\succeq 0 \\ \boldsymbol{\sigma}_c + (f_c - k\,\alpha_1)\,\mathbf{I} &\succeq 0 \\ \alpha_2 - \alpha_1 &\leq 0 \\ \alpha_2 - f_t &\leq 0 \end{aligned} \tag{3.32}$$

The Mohr-Coulomb criterion for plane stress

For plane stress, the principal stresses are given as $\sigma_1 \geq \sigma_2$. The Mohr-Coulomb criterion (3.28) now reads

$$\begin{aligned} \sigma_1 &\leq f_t \\ k\,\sigma_1 - \sigma_2 &\leq f_c \\ -\sigma_2 &\leq f_c \end{aligned} \tag{3.33}$$

where the principal stresses σ_1 and σ_2 are calculated as

$$\left.\begin{matrix} \sigma_1 \\ \sigma_2 \end{matrix}\right\} = \frac{\sigma_x + \sigma_y}{2} \pm \sqrt{\left(\frac{\sigma_x - \sigma_y}{2}\right)^2 + \tau_{xy}^2} \tag{3.34}$$

The expression (3.34) comprises the square root of the sum of two squares, hence, the Mohr-Coulomb criterion for plane stress can be formulated for second-order cone programming (Makrodimopoulos and Martin, 2006; Krabbenhøft et al., 2007; Nielsen, 2014). Introducing three auxiliary variables

$$p_m = -\frac{\sigma_x + \sigma_y}{2}, \quad \sigma_d = \frac{\sigma_x - \sigma_y}{2}, \quad \varphi \geq \sqrt{\sigma_d^2 + \tau_{xy}^2}, \tag{3.35}$$

the principal stresses (3.34) can now be written as

$$\begin{aligned} \sigma_1 &\leq -p_m + \varphi, \\ -\sigma_2 &\leq p_m + \varphi, \end{aligned}$$

and the Mohr-Coulomb criterion (3.33) can be stated as

$$\begin{aligned} -p_m + \varphi &\leq f_t \\ (1-k)\,p_m + (k+1)\,\varphi &\leq f_c \\ p_m + \varphi &\leq f_c \end{aligned} \tag{3.36}$$

The rewritten Mohr-Coulomb criterion (3.36) fits the format of second-order cone programming as the definition of φ (3.35) has the shape of a quadratic cone.

The von Mises criterion

The von Mises criterion is commonly used for metals and is based on the second stress invariant J_2. It can be considered as a special case of the Drucker-Prager criterion with an internal angle of friction of zero. In terms of J_2, the von Mises criterion can be stated as

$$\sqrt{3J_2} \leq f_y \tag{3.37}$$

where f_y is the yield strength. J_2 is given as

$$J_2 = \frac{(\sigma_x - \sigma_y)^2}{6} + \frac{(\sigma_y - \sigma_z)^2}{6} + \frac{(\sigma_z - \sigma_x)^2}{6} + \tau_{xy}^2 + \tau_{yz}^2 + \tau_{zx}^2, \tag{3.38}$$

hence, the yield function (3.37) comprise the square root of a sum of squares, and the criterion can be cast for second-order cone programming (Bisbos and Pardalos, 2007). Introducing six auxiliary variables,

$$\alpha_1 = \frac{\sigma_x - \sigma_y}{\sqrt{2}}, \quad \alpha_2 = \frac{\sigma_y - \sigma_z}{\sqrt{2}}, \quad \alpha_3 = \frac{\sigma_z - \sigma_x}{\sqrt{2}},$$

$$\alpha_4 = \sqrt{3}\,\tau_{xy}, \qquad \alpha_5 = \sqrt{3}\,\tau_{yz}, \qquad \alpha_6 = \sqrt{3}\,\tau_{zx},$$

into (3.38), the yield criterion (3.37) can then be stated as

$$\sqrt{\alpha_1^2 + \alpha_2^2 + \alpha_3^2 + \alpha_4^2 + \alpha_5^2 + \alpha_6^2} \leq f_y \tag{3.39}$$

which has the shape of quadratic cone. In principal stress space, the yield surface has the shape of a circular tube along the hydrostatic axis.

The von Mises criterion for plane stress

In plane stress, the second stress invariant J_2 is reduced to

$$J_2 = \frac{(\sigma_x - \sigma_y)^2}{6} + \frac{\sigma_y^2}{6} + \frac{\sigma_x^2}{6} + \tau_{xy}^2 \tag{3.40}$$

Three unique stress components exist in plane stress, hence, three auxiliary variables are sufficient to represent the criterion as a quadratic cone, however, their definitions are not as straight forward as the general, three-dimensional case. Defining

$$\alpha_1 = \frac{\sqrt{3}}{2}(\sigma_x - \sigma_y), \quad \alpha_2 = \frac{1}{2}(\sigma_x + \sigma_y), \quad \alpha_3 = \sqrt{3}\,\tau_{xy},$$

the yield criterion (3.37) can now be stated as

$$\sqrt{\alpha_1^2 + \alpha_2^2 + \alpha_3^2} \leq f_y \tag{3.41}$$

which again has the shape of a quadratic cone. In principal stress space, the plane stress version of the von Mises criterion has the shape of an ellipse, which is a conic section, see Figure 3.3.

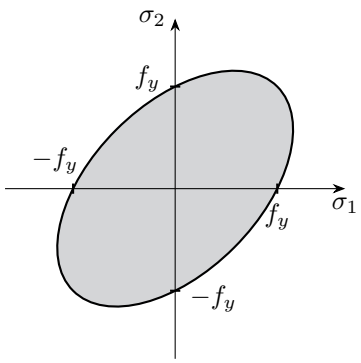

***Figure 3.3**: The von Mises yield envelope for plane stress illustrated in principal stress space.*

The yield functions presented in this section can be considered as material yield functions. The framework of finite element limit analysis makes it possible to formulate advanced yield functions which e.g. consider the behaviour of composite materials. In the following chapters, so-called submodel yield functions will be introduced which comprise semi-analytical mechanical models. The stress field and forces of the considered submodel are then checked against the appropriate material yield function, e.g. the Mohr-Coulomb criterion for concrete.

Chapter 4

Modelling precast structures

4.1 Modelling shear panels

Many of the methods and the general concept of modern precast concrete were developed in the 1950s and 60s. The calculation method and design equations have evolved to some extent, and in the serviceability limit state numerical analysis, such as linear elastic finite element analysis, is commonly used in practice. More advanced numerical methods are, however, rarely used in the ultimate limit state for practical design. Instead, methods based on manual limit analysis are favoured and many have been automated using spreadsheets.

Many of the components of the precast concrete structures are rather simple, e.g. simply supported beams. These components can be treated independently and designed analytically in both the serviceability limit state and the ultimate limit state, and effects such as cracking, yielding, and anchor slip of pre- and post-tensioned strands can be accounted for in a simple manner. For shear walls, however, it is necessary to consider the wall including shear joints as a whole. Analytical methods are still used, but it is in an approximative manner. Lower bound methods, e.g. the stringer method, are typically favoured for design.

Precast concrete structures are typically designed with shear walls as the main load carrying component. Beams and columns are of course to some degree responsible for distributing vertical forces, e.g. gravity loads. However, little is gained from a full rigid-plastic analysis due to their rather simple behaviour and support conditions.

The shear walls ensure the lateral stability of the structure, however, shear walls as structural components are rather complex. Various methods have been developed for manual design of shear walls (Nielsen, 1971; Nielsen and

Hoang, 2010; Muttoni et al., 1997, 2015). The stringer method is commonly used in practice in Denmark as it provides a rigorous lower bound and makes it possible to design for a specific shear capacity of the considered panels.

4.1.1 Plane stress lower bound element

Design and analysis of shear walls can be handled efficiently within the framework of finite element limit analysis. Shear walls are considered to be in plane stress, thus, plane stress finite elements will be the obvious choice for numerical modelling of such structures.

Several researchers have worked with plane stress and plane strain elements within the field of finite element limit analysis. Sloan (1988, 1989) presented lower bound and upper bound plane strain elements, however, the equilibrium equations are identical for plane strain and plane stress elements. From a design perspective, lower bound elements are generally more desirable as they ensure a safe design (within the assumption of rigid-plasticity). Analysis by upper bound elements determines an unsafe design, but it can be used to bound the exact limit load. Mixed elements which will be discussed in Section 6 provide neither. However, the capacity obtained using a mixed formulation will generally be closer to the exact limit load than both the upper and lower bound solutions.

Poulsen and Damkilde (2000) presented a triangular lower bound plane stress element using a linearised yield criterion due to the limitation of linear programming. The element uses a linear stress field, hence, it is sufficient to check the stresses in the corners to ensure a lower bound solution. Lower bound elements require traction continuity along every element boundary, however, this may lead to linear dependencies which are undesirable as they may cause numerical instability for the solver. Makrodimopoulos and Martin (2006) discuss this issue in details for lower bound plane strain elements and provide guidelines for avoiding linear dependencies for both internal and boundary nodes. Nielsen (2014) suggests a subdivision of the triangular element to avoid linear dependencies and to increase the accuracy: A centre node is added to the triangular element which is divided into three subelements, each with a linear stress variation. Several of the additional stress variables and equations can be eliminated, hence, the number of equations and variables only increase marginally.

In this section, the plane stress element by Poulsen and Damkilde (2000) is presented. The method for element enhancement by subdivision (Nielsen, 2014) will be presented as well. Next, the formulation of a generalised lower bound plane stress element for 3D analysis of structures will be given, and a yield criterion for reinforced concrete based on the Mohr-Coulomb criterion

is presented. Finally, four examples are analysed and the convergence rates and computational times will be discussed.

A plane stress state is described by three stress variables, namely σ_x, σ_y, and τ_{xy}. As mentioned, the lower bound element uses a linear stress field, thus, a total of 9 stress variables are required. The stress variables are shown in Figure 4.1 together with the tractions given in local coordinates of the element boundary, which must be in equilibrium with adjacent elements. The stress variables of an element is given as:

$$\boldsymbol{\sigma}_{el} = \begin{bmatrix} \boldsymbol{\sigma}_1 \\ \boldsymbol{\sigma}_2 \\ \boldsymbol{\sigma}_3 \end{bmatrix}, \quad \text{and} \quad \boldsymbol{\sigma}_i = \begin{bmatrix} \sigma_{xi} \\ \sigma_{yi} \\ \tau_{xyi} \end{bmatrix} \tag{4.1}$$

where $\boldsymbol{\sigma}_i$ is the stress state in the ith corner node.

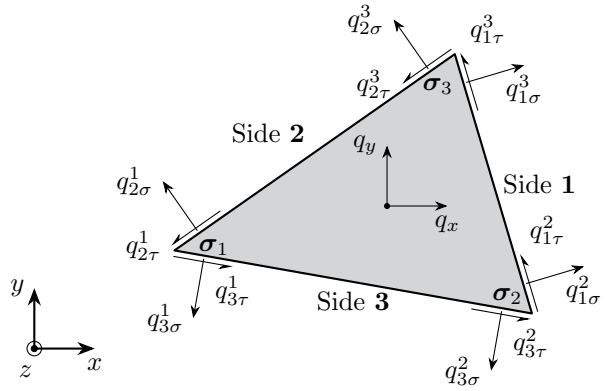

***Figure 4.1**: Stress vectors and tractions in local coordinate systems of the plane stress element (Poulsen and Damkilde, 2000).*

The stresses are given in global coordinates and for the traction equilibrium along the element boundaries transformations are needed. Due to the linear stress field of the element, traction continuity is enforced at both ends of a boundary. We define the following geometric quantities:

$$a_i = x_k - x_j, \quad b_i = y_k - y_j, \quad l_i = \sqrt{a_i^2 + b_i^2}$$

where i, j, and k are permutations of 1, 2, and 3. We also define the stress-to-traction array

$$\mathbf{P}^T = \frac{1}{l_i} \begin{bmatrix} b_i & 0 & -a_i \\ 0 & -a_i & b_i \end{bmatrix} \tag{4.2}$$

In global coordinates, the tractions of side i near node j can now be stated as $\boldsymbol{t}_i^j = \mathbf{P}_i^T \boldsymbol{\sigma}_j$. Introducing a transformation matrix $\mathbf{E}_i$ for side i,

$$\mathbf{E}_i = \frac{1}{l_i} \begin{bmatrix} b_i & a_i \\ -a_i & b_i \end{bmatrix},$$

the tractions in local coordinates at side i is given as

$$\hat{\boldsymbol{t}}_i^j = \mathbf{E}_i^T \mathbf{P}_i^T \boldsymbol{\sigma}_j = \hat{\mathbf{P}}_i^T \boldsymbol{\sigma}_j$$

with

$$\hat{\mathbf{P}}_i^T = \mathbf{E}_i^T \mathbf{P}_i^T = \frac{1}{l_i^2} \begin{bmatrix} b_i^2 & a_i^2 & -2a_i b_i \\ a_i b_i & -a_i b_i & b_i^2 - a_i^2 \end{bmatrix} \tag{4.3}$$

Using (4.3), the tractions in local coordinates related to node i can now be stated as

$$\boldsymbol{q}_i = \begin{bmatrix} q_{j\sigma}^i \\ q_{j\tau}^i \\ q_{k\sigma}^i \\ q_{k\tau}^i \end{bmatrix} = \begin{bmatrix} \hat{\mathbf{P}}_j^T \\ \hat{\mathbf{P}}_k^T \end{bmatrix} \boldsymbol{\sigma}_i \tag{4.4}$$

where j and k are the two sides which meet in node i.

The nodal forces q_x and q_y, shown in the centre of the element in Figure 4.1, ensure internal equilibrium within the element. The element is subjected to surface loads, γ_x and γ_y, acting on the entire surface area of the element. This gives rise to two partial differential equations:

$$\begin{aligned} \frac{\partial \sigma_x}{\partial x} + \frac{\partial \tau_{xy}}{\partial y} + \gamma_x = 0 \\ \frac{\partial \sigma_y}{\partial y} + \frac{\partial \tau_{xy}}{\partial x} + \gamma_y = 0 \end{aligned} \tag{4.5}$$

Introducing linear shape functions, the stress in a point (x, y) can be stated as

$$\boldsymbol{\sigma}(x, y) = \sum_{i=1}^{3} N_i(x, y) \boldsymbol{\sigma}_i \tag{4.6}$$

with

$$N_i(x, y) = \frac{b_i x - a_i y + d_i}{2A}, \tag{4.7}$$

where $d_i = -x_j y_k + x_k y_j$ and A is the surface area of the element. Using the shape functions (4.7), the differential equations (4.5) can be restated as

$$\begin{bmatrix} q_x \\ q_y \end{bmatrix} = A \begin{bmatrix} \gamma_x \\ \gamma_y \end{bmatrix} = \frac{1}{2} \begin{bmatrix} \tilde{\mathbf{P}}_1^T & \tilde{\mathbf{P}}_2^T & \tilde{\mathbf{P}}_3^T \end{bmatrix} \boldsymbol{\sigma}_{el} \tag{4.8}$$

where $\boldsymbol{\sigma}_{el}$ is the element stress vector, see (4.1), and $\tilde{\mathbf{P}}_i^T$ is defined as

$$\tilde{\mathbf{P}}_i^T = l_i \mathbf{P}_i^T = \begin{bmatrix} b_i & 0 & -a_i \\ 0 & -a_i & b_i \end{bmatrix}$$

The element equilibrium matrix $\mathbf{B}_{el}^T$ comprise the contributions from the traction continuity (4.4) as well as internal equilibrium (4.8):

$$\boldsymbol{q}_{el} = \begin{bmatrix} \hat{\mathbf{P}}_2^T & & \\ \hat{\mathbf{P}}_3^T & & \\ & \hat{\mathbf{P}}_3^T & \\ & \hat{\mathbf{P}}_1^T & \\ & & \hat{\mathbf{P}}_1^T \\ & & \hat{\mathbf{P}}_2^T \\ \frac{1}{2}\tilde{\mathbf{P}}_1^T & \frac{1}{2}\tilde{\mathbf{P}}_2^T & \frac{1}{2}\tilde{\mathbf{P}}_3^T \end{bmatrix} \begin{bmatrix} \boldsymbol{\sigma}_1 \\ \boldsymbol{\sigma}_2 \\ \boldsymbol{\sigma}_3 \end{bmatrix} = \mathbf{B}_{el}^T \boldsymbol{\sigma}_{el} \tag{4.9}$$

The basic plane stress element by Poulsen and Damkilde (2000) contributes to a total of 14 equilibrium equations on the global level and requires 9 stress variables.

4.1.2 Element enhancement by subdivision

The formulation presented here is based on the work of Nielsen (2014) and also presented in Paper I (Herfelt et al., 2016). The basic plane stress triangle is divided into three subelements, each with a linear stress variation. This subdivision will of course increase the accuracy of the element, however, it will also ensure that no linear dependencies are present. Utilising local coordinate systems for the stress variables, several of variables and equations can be eliminated, hence, the subdivision only increases the problem size marginally.

A centre node divides the element into three subelements as seen in Figure 4.2. The enhanced element requires four stress nodes, three located at the corners as well as one located in the centre. Two subelements meet in each corner and in the global coordinate system, two times three variables are needed to describe the two plane stress states near the corner. Utilising a local coordinate system, however, the number of stress variables can be reduced to four, and the traction continuity in the particular corner will always be fulfilled, while the normal stress in the local t-direction can be discontinuous, see Figure 4.2. The stress vector of the ith corner, $\boldsymbol{\sigma}_i^C$, therefore contains four stress variables

$$\boldsymbol{\sigma}_i^C = \begin{bmatrix} \sigma_{ni} & \tau_{nti} & \sigma_{ti}^- & \sigma_{ti}^+ \end{bmatrix}^T,$$

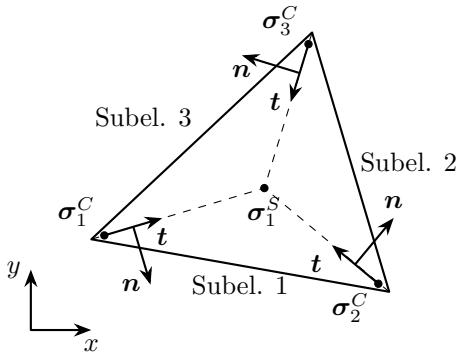

***Figure 4.2**: The three subelements of the plane stress element as well as local coordinate systems for the corner stresses.*

where superscripts $-$ and $+$ indicate that the normal stress is associated with the subelement clockwise and counter-clockwise from the corner, respectively. For the centre node we have

$$\boldsymbol{\sigma}_1^S = \begin{bmatrix} \sigma_x & \sigma_y & \tau_{xy} \end{bmatrix},$$

which is defined in global coordinates. The enhanced element requires a total of 15 stress variables. The element equilibrium matrix (4.9) is given in global coordinates, hence, transformations are necessary for the enhanced element:

$$\boldsymbol{\sigma}_{el} = \begin{bmatrix} \mathbf{T}_C & \\ & \mathbf{T}_S \end{bmatrix} \begin{bmatrix} \boldsymbol{\sigma}^C \\ \boldsymbol{\sigma}_1^S \end{bmatrix} \tag{4.10}$$

where

$$\boldsymbol{\sigma}^C = \begin{bmatrix} \boldsymbol{\sigma}_1^C \\ \boldsymbol{\sigma}_2^C \\ \boldsymbol{\sigma}_3^C \end{bmatrix}$$

$\boldsymbol{\sigma}_{el}$ contains 27 stress variables in global coordinates, which are used to establish the equilibrium equations on the global level according to the equations presented in Section 4.1.1 and Poulsen and Damkilde (2000). The matrix $\mathbf{T}_C \in \mathbb{R}^{18\times 12}$ transforms the stresses from the local coordinates of the corner to the global coordinates, while $\mathbf{T}_S \in \mathbb{R}^{9\times 3}$ defines the other sets of stresses in the centre. Given the unit normal vector $\boldsymbol{n} = [n_x \; n_y]^T$ to the boundary connecting the ith corner node and the centre node, the transformation of the corner stresses can be stated as:

$$\begin{bmatrix} \sigma_x \\ \sigma_y \\ \tau_{xy} \end{bmatrix} = \begin{bmatrix} n_x^2 & n_y^2 & -2n_xn_y \\ n_y^2 & n_x^2 & 2n_xn_y \\ n_xn_y & -n_xn_y & n_x^2 - n_y^2 \end{bmatrix} \begin{bmatrix} \sigma_n \\ \sigma_t^{\pm} \\ \tau_{nt} \end{bmatrix} \tag{4.11}$$

Equation (4.11) defines the contributions to $\mathbf{T}_C$. At the centre node S, equilibrium across the subelement boundaries gives the following equations:

$$\begin{aligned} \mathbf{T}_1^{xy}\left(\boldsymbol{\sigma}_3^S - \boldsymbol{\sigma}_1^S\right) &= 0, \\ \mathbf{T}_2^{xy}\left(\boldsymbol{\sigma}_1^S - \boldsymbol{\sigma}_2^S\right) &= 0, \\ \mathbf{T}_3^{xy}\left(\boldsymbol{\sigma}_2^S - \boldsymbol{\sigma}_3^S\right) &= 0, \end{aligned} \tag{4.12}$$

where $\mathbf{T}_i^{xy}$ is given as

$$\mathbf{T}_i^{xy} = \begin{bmatrix} n_x & 0 & n_y \\ 0 & n_y & n_x \end{bmatrix}$$

where i is the corner associated with the particular subelement boundary and $\boldsymbol{n} = \begin{bmatrix} n_x & n_y \end{bmatrix}^T$ is the aforementioned unit normal to the boundary. The relation (4.12) can be rewritten as a linear system:

$$\begin{bmatrix} -\mathbf{T}_1^{xy} & 0 & \mathbf{T}_1^{xy} \\ \mathbf{T}_2^{xy} & -\mathbf{T}_2^{xy} & 0 \\ 0 & \mathbf{T}_3^{xy} & -\mathbf{T}_3^{xy} \end{bmatrix} \begin{bmatrix} \boldsymbol{\sigma}_1^S \\ \boldsymbol{\sigma}_2^S \\ \boldsymbol{\sigma}_3^S \end{bmatrix} = 0 \tag{4.13}$$

Rearranging the terms gives

$$\begin{bmatrix} 0 & \mathbf{T}_1^{xy} \\ -\mathbf{T}_2^{xy} & 0 \\ \mathbf{T}_3^{xy} & -\mathbf{T}_3^{xy} \end{bmatrix} \begin{bmatrix} \boldsymbol{\sigma}_2^S \\ \boldsymbol{\sigma}_3^S \end{bmatrix} = - \begin{bmatrix} -\mathbf{T}_1^{xy} \\ \mathbf{T}_2^{xy} \\ \mathbf{0} \end{bmatrix} \boldsymbol{\sigma}_1^S \tag{4.14}$$

The two matrices, $\mathbf{T}_1$ and $\mathbf{T}_{23}$, are now defined as

$$\mathbf{T}_1 = \begin{bmatrix} -\mathbf{T}_1^{xy} \\ \mathbf{T}_2^{xy} \\ \mathbf{0} \end{bmatrix}, \quad \mathbf{T}_{23} = \begin{bmatrix} \mathbf{0} & \mathbf{T}_1^{xy} \\ -\mathbf{T}_2^{xy} & \mathbf{0} \\ \mathbf{T}_3^{xy} & -\mathbf{T}_3^{xy} \end{bmatrix},$$

and the stresses near the centre node can now be obtained from the following equation:

$$\begin{bmatrix} \boldsymbol{\sigma}_1^S \\ \boldsymbol{\sigma}_2^S \\ \boldsymbol{\sigma}_3^S \end{bmatrix} = \begin{bmatrix} \mathbf{I} \\ -\mathbf{T}_{23}^{-1}\mathbf{T}_1 \end{bmatrix} \boldsymbol{\sigma}_1^S = \mathbf{T}_S \boldsymbol{\sigma}_1^S \tag{4.15}$$

Equation (4.15) also defines $\mathbf{T}_S$, one of the matrices needed for the transformation from local to global coordinates, see (4.10).

4.1.3 Generalised lower bound element

For three-dimensional concrete structures, carrying external loading as in-plane forces rather than moments is more efficient. Modern buildings are usually designed with this in mind using shear walls as the main load carrying component for lateral loading. Moreover, most walls and slabs are simply supported with respect to bending action, hence, no plastic redistribution of forces can occur. The moment capacity of shear walls is therefore to some degree irrelevant for the overall distribution of forces in the building, and sufficient capacity for combined bending and in-plane action can be ensured by a detailed analysis at a later point in the design process.

In this section, the formulation of a generalisation of the plane stress lower bound element presented in Section 4.1.1 is given. The element is enhanced by subdivision, see Section 4.1.2, which increases accuracy of the element and removes linear dependencies for a marginally larger computational effort.

For the three-dimensional element, a local coordinate system is needed. The element itself is defined by three corner nodes, and associated with each node i is a stress vector $\boldsymbol{\sigma}_i = \begin{bmatrix}\sigma_x & \sigma_y & \tau_{xy}\end{bmatrix}^T$ given in the local coordinates of the element.

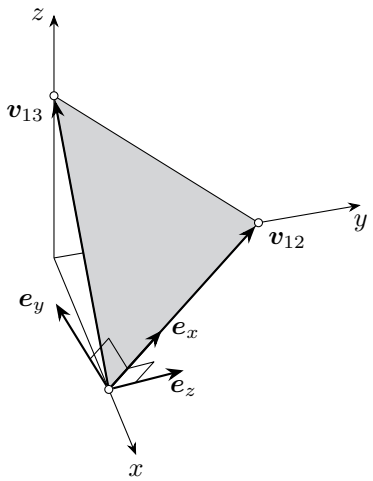

***Figure 4.3**: Geometry and local coordinate system of the generalised plane stress element.*

The local coordinate system of a given element is defined by the three basis vectors seen in Figure 4.3:

$$\boldsymbol{e}_x = \frac{\boldsymbol{v}_{12}}{\|\boldsymbol{v}_{12}\|}, \quad \boldsymbol{e}_z = \frac{\boldsymbol{v}_{12} \times \boldsymbol{v}_{13}}{\|\boldsymbol{v}_{12} \times \boldsymbol{v}_{13}\|}, \quad \boldsymbol{e}_y = \boldsymbol{e}_z \times \boldsymbol{e}_x \tag{4.16}$$

where $\boldsymbol{v}_{ij}$ is a vector going from node i to node j given in the global coordinates. The local coordinates of the three nodes $\boldsymbol{x}_i$ of the element can now be calculated as

$$\boldsymbol{x}_i = \mathbf{E}^T \boldsymbol{X}_i,$$

where $\boldsymbol{X}_i$ is the global coordinates of node i, and $\mathbf{E} = \begin{bmatrix} \boldsymbol{e}_x & \boldsymbol{e}_y & \boldsymbol{e}_z \end{bmatrix}$ is the transformation matrix. For each side i, a unit normal vector is defined in the local coordinate system:

$$\boldsymbol{n}_i = \begin{bmatrix} n_x^i \\ n_y^i \end{bmatrix}$$

Similarly to the two-dimensional element, traction continuity is required for the three-dimensional element to ensure a lower bound solution. Figure 4.1 illustrates this for the two-dimensional case where the global coordinate system is used. For the present element, the local coordinate system is used, and the tractions are then afterwards transformed to global coordinates using the transformation matrix $\mathbf{E}$. We define the stress-to-traction array for the three-dimensional element as

$$\mathbf{P}_i^T = \begin{bmatrix} n_x^i & 0 & n_y^i \\ 0 & n_y^i & n_x^i \\ 0 & 0 & 0 \end{bmatrix} \tag{4.17}$$

and

$$\tilde{\mathbf{P}}_i^T = l_i \mathbf{P}_i^T$$

where l_i is the length of side i. The matrix $\mathbf{P}_i^T$ transforms the stresses given in local coordinates to the tractions of element side i, still in local coordinates of the element. Traction equilibrium is enforced in global coordinates, and the generalised nodal forces can be stated as

$$\boldsymbol{q}_i = \begin{bmatrix} q_{kx}^i \\ q_{ky}^i \\ q_{kz}^i \\ q_{jx}^i \\ q_{jy}^i \\ q_{jz}^i \end{bmatrix} = \frac{1}{2} \begin{bmatrix} \mathbf{E}^T & \\ & \mathbf{E}^T \end{bmatrix} \begin{bmatrix} \tilde{\mathbf{P}}_j^T \\ \tilde{\mathbf{P}}_k^T \end{bmatrix} \boldsymbol{\sigma}_i \tag{4.18}$$

where $\mathbf{E}$ is the element transformation matrix, and j and k are the two element boundaries which meet in node i. Equation (4.18) appears almost identical to (4.4) with the exception of the transformation, which is necessary for the three-dimensional element.

The three-dimensional plane stress element is subjected to surface loads given in local coordinates. This leads to the same equations as presented in Section 4.1.1 in Equation (4.8):

$$\boldsymbol{q}_c = A \begin{bmatrix} \gamma_x \\ \gamma_y \end{bmatrix} = \frac{1}{2} \begin{bmatrix} \tilde{\mathbf{P}}_1^T & \tilde{\mathbf{P}}_2^T & \tilde{\mathbf{P}}_3^T \end{bmatrix} \boldsymbol{\sigma}_{el} \tag{4.19}$$

where A is the surface area of the given element and γ_x and γ_y are the surface loads. The element equilibrium matrix in global coordinates can now be stated as follows by combining (4.18) and (4.19):

$$\boldsymbol{q}_{el} = \frac{1}{2} \begin{bmatrix} \mathbf{E}\tilde{\mathbf{P}}_2^T & & \\ \mathbf{E}\tilde{\mathbf{P}}_3^T & & \\ & \mathbf{E}\tilde{\mathbf{P}}_3^T & \\ & \mathbf{E}\tilde{\mathbf{P}}_1^T & \\ & & \mathbf{E}\tilde{\mathbf{P}}_1^T \\ & & \mathbf{E}\tilde{\mathbf{P}}_2^T \\ \tilde{\mathbf{P}}_1^T & \tilde{\mathbf{P}}_2^T & \tilde{\mathbf{P}}_3^T \end{bmatrix} \begin{bmatrix} \boldsymbol{\sigma}_1 \\ \boldsymbol{\sigma}_2 \\ \boldsymbol{\sigma}_3 \end{bmatrix} = \mathbf{B}_{el}^T \boldsymbol{\sigma}_{el} \tag{4.20}$$

which appears similar to the element equilibrium matrix of the two-dimensional element (4.9) with the exception of the transformations. As mentioned previously, the element enhancement by division into three subelements introduced in Section 4.1.2 is also used for the generalised three-dimensional element.

4.1.4 Yield criterion for plane stress

Reinforced concrete yield criterion

The stresses on the element level $\boldsymbol{\sigma}_{el}$ is the so-called total stresses which comprise the stresses carried by the reinforcement and concrete, respectively. The reinforcement is assumed to be constituted by an orthogonal mesh of rebars oriented in an angle ϕ with respect to the local coordinate system (in which the stresses are defined).

Figure 4.4 shows an element with an orthogonal reinforcement mesh including the local coordinate system and the orientation of the reinforcement. The stresses are transformed to the coordinate system of the reinforcement and split into concrete and reinforcement stresses accordingly:

$$\begin{bmatrix} c^2 & s^2 & 2cs \\ s^2 & c^2 & -2cs \\ -cs & cs & c^2 - s^2 \end{bmatrix} \begin{bmatrix} \sigma_x \\ \sigma_y \\ \tau_{xy} \end{bmatrix} = \begin{bmatrix} \sigma_{xm} \\ \sigma_{ym} \\ \tau_{xym} \end{bmatrix} + \begin{bmatrix} \tilde{\sigma}_{xs} \\ \tilde{\sigma}_{ys} \\ 0 \end{bmatrix} \tag{4.21}$$

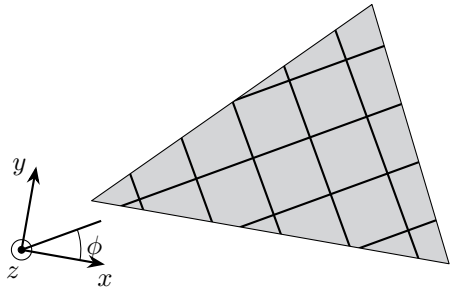

***Figure 4.4**: Orthogonal reinforcement oriented in an angle ϕ to the local coordinate system.*

where $c = \cos\phi$ and $s = \sin\phi$. Subscript m indicates concrete stresses (matrix material) and subscript s indicate reinforcement stresses (steel). Equation (4.21) uses equivalent reinforcement stresses, $\tilde{\sigma}_{is}$, which are defined as

$$\tilde{\sigma}_{is} = \frac{A_{si}}{t}\sigma_{is}$$

where A_{si} is the reinforcement area per unit length in the ith direction and t is the out-of-plane thickness of the concrete. As seen in (4.21), it is assumed that the reinforcement only carries axial forces (Nielsen and Hoang, 2010). A simple, linear yield criterion can then be used:

$$\begin{aligned} 0 \leq \tilde{\sigma}_{xs} \leq \tilde{f}_{yx} = \frac{A_{sx}}{t} f_y \\ 0 \leq \tilde{\sigma}_{ys} \leq \tilde{f}_{yy} = \frac{A_{sy}}{t} f_y \end{aligned} \tag{4.22}$$

where $\tilde{f}_y$ is the equivalent reinforcement strength which is implicitly defined in (4.22). As seen in (4.22), the compressive strength of the reinforcement is neglected and the reinforcement stresses must be non-negative.

The concrete is treated as a Mohr-Coulomb material with a tension cut-off. For plane stress, the criterion is given as follows in principal stresses:

$$\begin{aligned} \sigma_1 &\leq f_t \\ k\sigma_1 - \sigma_2 &\leq f_c \\ -\sigma_2 &\leq f_c \end{aligned} \tag{4.23}$$

where f_t is the uniaxial tensile strength of the concrete, f_c is the uniaxial compressive strength, and k is a friction parameter. The criterion is linear in principal stresses, but non-linear in terms of σ_{xm}, σ_{ym}, and τ_{xym}. The criterion (4.23) can be cast as a single conic constraint and a couple of linear

constraints, hence, the criterion fits the format of second-order cone programming. The exact formulation for second-order cone programming of the Mohr-Coulomb criterion for plane stress has been given in Section 3.3 and will not be repeated here.

Von Mises yield criterion

The von Mises yield criterion is commonly used for metals and is based on the second stress invariant, J_2. The criterion can be stated as:

$$\sqrt{3\,J_2} \leq f_y \tag{4.24}$$

where f_y is the uniaxial yield strength of the material. For plane stress, J_2 is given as

$$J_2 = \frac{(\sigma_x - \sigma_y)^2}{6} + \frac{\sigma_y^2}{6} + \frac{\sigma_x}{6} + \tau_{xy}^2,$$

and by introducing three auxiliary variables, (4.24) can be formulated as a single conic constraint. The details are given in Section 3.3.

4.1.5 Examples

In this section, four examples using the two-dimensional and the three-dimensional plane stress elements are presented. The convergence rate and computational time will be analysed for the different examples. The meshes for examples 3 and 4 are generated using GiD v12 (Ribó et al., 1998).

Example 1: Deep beam with shear supports

The first examples is a deep reinforced concrete beam subjected to a uniformly distributed load acting on the top boundary. The deep beam is supported at the left and right boundaries by shear supports as seen in Figure 4.5.

The analytical solution to the deep beam problem is well-known (Nielsen and Hoang, 2010) and can be obtained using homogeneous stress triangles (Nielsen, 1971) and the mesh on the left side in Figure 4.5. The exact limit load is given as

$$p^* = \frac{4\,\Phi\,h^2\,f_c}{(1+\Phi)\,L^2} \leq f_c. \tag{4.25}$$

The mechanical reinforcement ratio Φ is defined as

$$\Phi = \frac{A_s\,f_y}{t f_c}$$

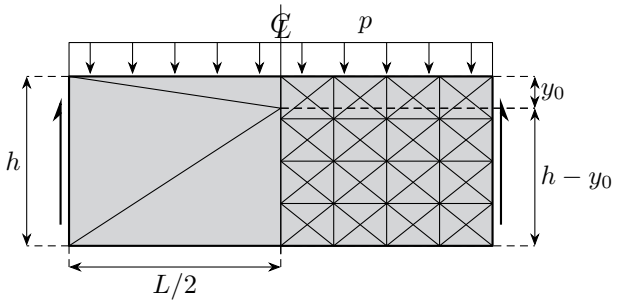

***Figure 4.5**: Deep beam with shear supports including mesh for the analytical solution (left) and for the convergence analysis (right).*

where A_s was the cross sectional area of the reinforcement per unit length. Using $h = 2$ m, $L = 6$ m, $f_c = 20$ MPa, and $\Phi = 0.075$, the exact limit load is $p^* = 0.6202$ MPa. The symmetry is exploited for the model, and a lower bound to the exact limit load is calculated using the structured mesh shown on the right-hand side of Figure 4.5.

***Table 4.1**: Limit load, error, and computational time for the deep beam problem.*

nel	p [MPa]	Error [%]	Time [s]
64	0.5555	10.42	0.15
256	0.6053	2.40	0.68
1,024	0.6177	0.39	3.57
4,096	0.6191	0.17	16.18
16,384	0.6193	0.13	67.36

Table 4.1 shows that the structured mesh approaches the exact limit load p^* from below as the number of elements *nel* increases. The computational time appears to be roughly proportional to the problem size (or at least a low order polynomial complexity), which will be discussed later in this section.

Example 2: Circular disk with hole

The second example is a circular concrete disk with a concentric hole loaded by radial pressure. The geometry, mesh, and loading are shown in Figure 4.6. The geometry of the disk is defined by the radius of the hole, a, and the radius of the disk, R.

A structured mesh is used for the modelling, and only one quarter of the disk is modelled as seen in Figure 4.6 utilising the symmetry. The only

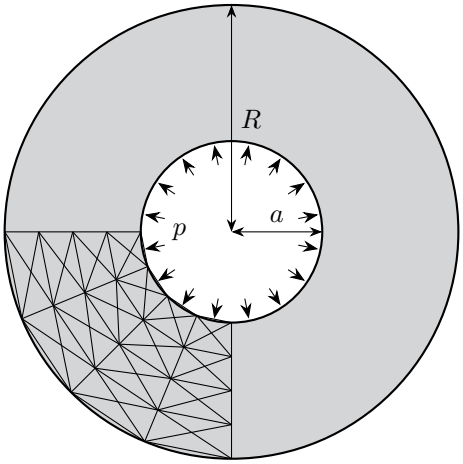

***Figure 4.6**: Circular disk with a concentric hole loaded by radical pressure p. Mesh discretisation is shown in the lower right quarter.*

supports used for the model is symmetry supports. Due to the curved edges of the disk, the mesh approximates the actual geometry of the disk, and the accuracy of the approximation will increase with the mesh density. The exact analytical solution to the circular disk problem is given as

$$p^* = \Phi f_c \left(\frac{R}{a} - 1 \right) \leq f_c$$

according to Nielsen and Hoang (2010). R is chosen as 3 m, a as 1 m, f_c as 30 MPa, and Φ as 0.100, hence, the exact limit load is $p^* = 6$ MPa.

***Table 4.2**: Limit load, error, and computational time for the circular disk problem.*

nel	p [MPa]	Error [%]	Time [s]
64	5.6086	6.62	0.15
256	5.8842	1.93	0.67
1,024	5.9675	0.54	2.07
4,096	5.9901	0.17	9.26
16,384	5.9924	0.13	46.44

Table 4.2 shows that the model approaches the exact limit load from below, which is to be expected using a lower bound element. The computational time is slightly lower than for the deep beam example, but the overall tendency is the same: The computational time is proportional to the problem size to a lower order of power.

Example 3: Cantilever I-beam

A cantilever steel I-beam is subjected to a uniformly distributed load acting in the centreline on the top of the web. The beam is modelled using the generalised, three-dimensional plane stress element introduced in Section 4.1.3. The material is modelled using the von Mises criterion with a yield strength of $f_y = 250$ MPa. The beam has a length of 3 metres. The web has a height of 300 mm and a thickness of 10 mm, while the flanges have a width of 300 mm and a thickness of 10 mm. The plastic moment capacity of the I-beam is calculated to be 281 kNm, which corresponds to a limit load of $p^* = 62.5$ kN/m.

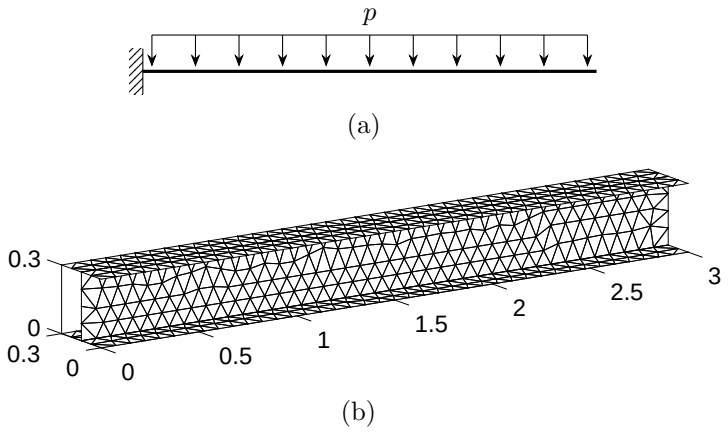

Figure 4.7*: a) Support condition and loading, b) medium mesh density of the I-beam using 948 elements.*

Four different meshes are analysed whereas the medium density mesh is shown in Figure 4.7(b). The beam is supported in all three directions at the left end as shown in Figure 4.7(a). With a thickness of just 10 mm, the effect of local bending in the web and flanges will be negligible, and the external load will be carried almost exclusively via in-plane forces. Using a plane stress element will therefore provide a decent estimate of the load carrying capacity despite omitting the local bending in the web and flanges.

The von Mises criterion requires fewer constraints and variables than the reinforced concrete criterion, hence, the computational time is lower for the same number of element as seen in Table 4.3. The load capacity is also shown in Table 4.3 and it is seen that it exceeds the analytical capacity slightly. This is due to the nature of the von Mises criterion where the stresses can exceed the yield strength f_y provided either compression or tension in two directions. Figure 4.8 shows the largest and smallest principal stresses near the supported end of the cantilever, and it can be seen that the stresses exceeds

***Table 4.3**: Limit load and computational time for the cantilever I-beam example.*

mesh	*nel*	p [kN/m]	Time [s]
Coarse	238	63.24	0.28
Medium	948	64.18	0.95
Fine	3,616	64.90	4.47
Very fine	14,646	65.24	21.38

f_y in areas where both principal stresses are either positive or negative.

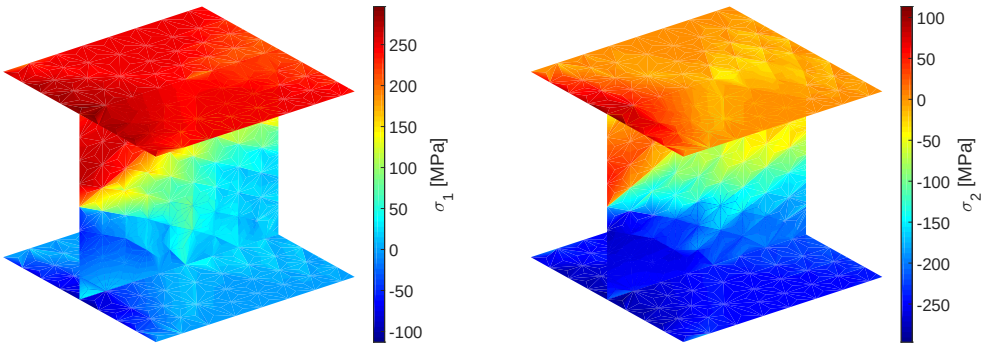

(a) σ_1 (b) σ_2

***Figure 4.8**: Largest and smallest principal stresses, σ_1 and σ_2 respectively, near the support of the I-beam using the fine mesh with 3616 elements.*

Example 4: Four-storey stairwell with door openings

The fourth and final example is a four-storey stairwell of reinforced concrete. The stairwell features four door openings and is subjected to a shear force acting on the top the wall with the door openings as illustrated in Figure 4.9.

The shear load cause shear and torsion in the structure. The shear walls have a thickness of 180 mm and are reinforced with two layers of Ø8 rebars per 150 mm in both directions. The shear walls will have a considerable bending strength which is not taken into account when using the presented generalised plane stress element. The model will therefore provide a somewhat conservative lower bound of the capacity of the wall. In order to utilise the local bending of the walls, sufficient connections between the panels are required. This can be ensured for in-situ cast structures, but not necessarily for precast concrete structures.

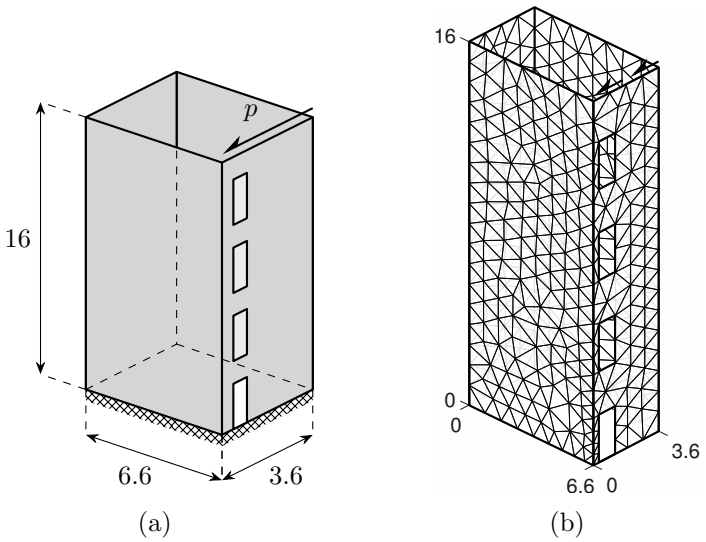

Figure 4.9*: a) Four-storey stairwell subjected to a shear force which induces bending, torsion and shear in the structure. b) Coarse mesh with 864 elements. Dimensions are given in metres.*

The reinforcement has a design yield strength of $f_{yd} = 458$ MPa, and it is assumed that the reinforcement only carries tension. The concrete has a uniaxial compressive design strength of $f_{cd} = 21.43$ MPa and the tensile strength is taken as zero. The wall is analysed for two different effectiveness factors ν, namely $\nu = 1$ and $\nu = 0.7 - f_c/200 = 0.55$ where f_c is the characteristic concrete strength ($f_c = 30$ MPa). The effective design concrete strength is given as $\nu\, f_{cd}$.

Table 4.4*: Limit load and computational time for the stairwell example.*

		p [kN/m]		
mesh	*nel*	$\nu = 1$	$\nu = 0.55$	Time [s]
Coarse	864	85.27	85.06	2.15
Medium	3,564	88.62	87.80	14.78
Fine	11,379	89.25	88.46	56.53

Table 4.4 shows that the coarse mesh gives a reasonable estimate despite only using 864 elements. The fine mesh gives less than 5 % additional capacity even though it uses more than 13 times the number of elements. It is also observed that the effectiveness factor ν hardly affects the capacity in this example, since the reinforcement is governing the behaviour of the stairwell:

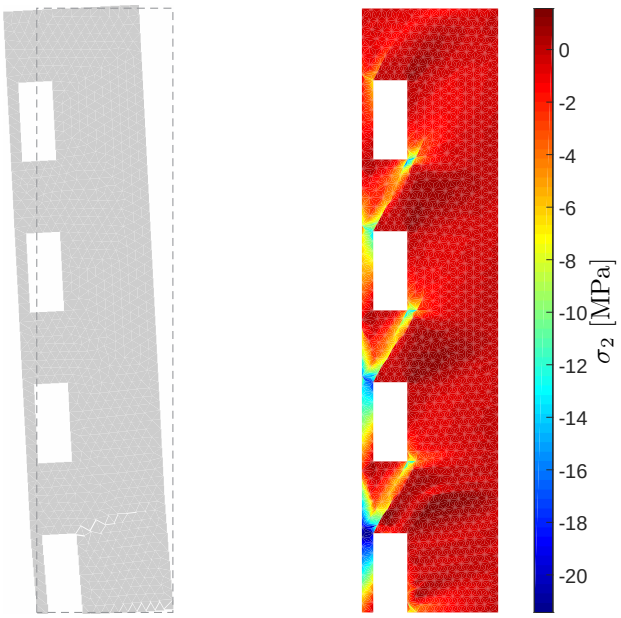

(a) (b)

***Figure 4.10**: Failure mode (a) and smallest principal stresses (b) of the stairwell example using the fine mesh and $\nu = 1$.*

Less than one percent difference is found between using $\nu = 1$ and $\nu = 0.55$.

Figure 4.4 shows the failure mode and smallest principal stress for the shear wall with the door openings. The failure mode is interpreted from the dual solution, i.e. the solution to the corresponding kinematic problem. The stairwell fails in a bending failure as illustrated in Figure 4.4(a). Local failure also occurs near the top of the door openings in the bottom storey. Figure 4.4(b) shows that compression struts are formed between the door openings. The slender columns to the left of the door openings carry considerable stresses, and the largest compressive stresses approach the compressive strength of the concrete.

Computational time

The computational times for the four examples are plotted as a function of the number of elements in Figure 4.11. It is observed that all curves are approximately linear in the double logarithmic coordinate system and are therefore power functions.

It is seen that the computational time is approximately proportional to the number of elements to the power of 1.1, illustrated by the curve denoted $O\left(n^{1.1}\right)$. The third example, the cantilever I-beam, had a lower computa-

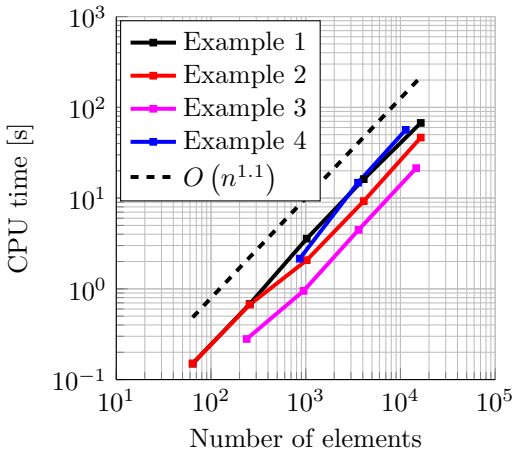

***Figure 4.11**: Computational time for the four examples as a function of the number of elements.*

tional time, however, the slope is still the same as the other examples.

4.2 Modelling in-situ cast joints

Joints cast on the construction site are necessary to connect the precast concrete elements. The boundaries of the precast panels (with the exception of the bottom) are typically reinforced with loop reinforcement, i.e. U-bar loops. The vertical interfaces of the precast panels are often indented, and these types of joints are commonly referred to as keyed joints.

A four-storey precast shear wall is shown in Figure 4.13. The wall is subjected to external loads and the in-situ cast joints are crucial to transfer the loads to the foundations of the shear wall. The strut-and-tie and stringer methods are commonly used in practice to assess the capacity of shear walls and joints. A strut of a given width crossing a joint will subject the joint and interfaces to shear and confinement, which in practice is checked against the design criterion of the standard. If the confinement is insufficient, transverse reinforcement can be added to increase the shear capacity of the joint.

As discussed in Section 1.1.1, the construction techniques for in-situ cast joints lead to several issues and impose rather high requirements on the ductility of the steel used for the U-bar loops. Moreover, the U-bars are straightened through a narrow gap as seen in Figure 4.13, and it cannot be guaranteed that the U-bars are placed closely together in practice.

During the 1970s and 80s, several papers were published on the topic of shear capacity of keyed joints: Fauchart and Cortini (1972), Hansen and

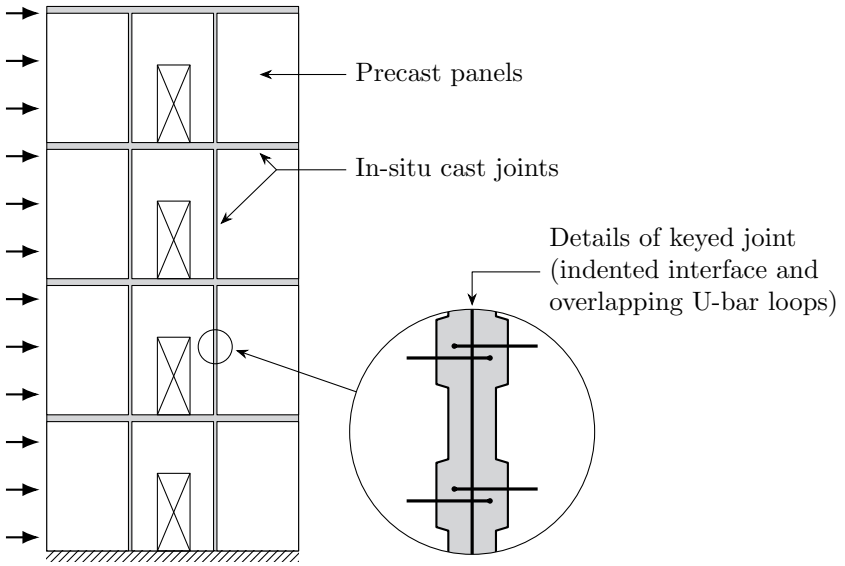

***Figure 4.12**: Four-storey shear wall constructed from precast panels connected by in-situ cast joints.*

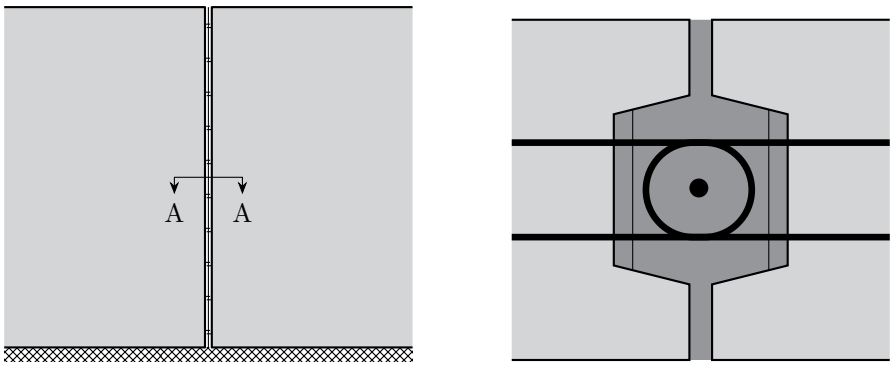

(a) In-situ cast joint connecting two precast panels

(b) Horizontal section A-A

***Figure 4.13**: a) Precast concrete panels connected by in-situ cast joints. b) Horizontal section of a keyed joint reinforced with U-bar loops and a locking bar in the centre.*

Olesen (1976), and Rizkalla et al. (1989) present experimental results for various different geometries and material parameters. Moreover, Hansen and Olesen tested joints with different reinforcement layouts. Cholewicki (1971) also presents experimental results and discuss the deformation capacity of such joints, while Bhatt (1973) and Bljuger (1976) discuss analytical and semi-analytical models for keyed joints.

Attempts to establish simple mechanical models based on limit analysis

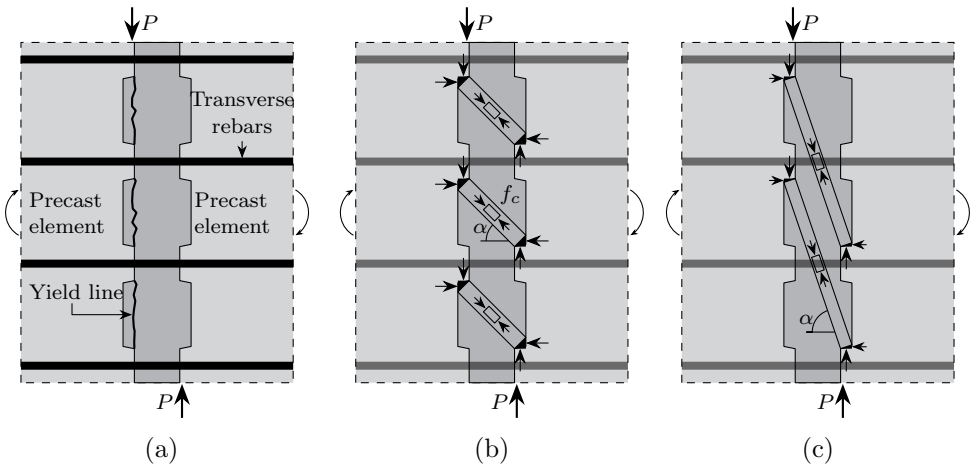

***Figure 4.14**: (a) Simplified failure mechanism (Jensen, 1975; Christoffersen, 1997) and (b, c) strut-and-tie models (Christoffersen, 1997; Nielsen and Hoang, 2010) for analytical modelling of shear capacity of keyed joints.*

for the ultimate limit state design of in-situ cast joints have been published: This includes both upper bound solutions based on the yield line theory (Jensen, 1975; Christoffersen, 1997) and lower bound methods based on strut-and-tie models (Christoffersen, 1997; Nielsen and Hoang, 2010; *fib* bulletin 43, 2008), see Figure 4.14. Jørgensen (2014) presented several analytical upper bound solutions to a similar type of joints, namely wire loop connections.

In spite of the extensive work to establish a rational mechanical model for the behaviour of in-situ cast joints, the standards still use simple design formulas derived from experimental data (see e.g. Eurocode 2, European Committee for Standardization, 2008, discussed in Section 1.1.1). Moreover, neither the models based on limit analysis nor the current standards consider the reinforcement layout or the effects it can have on the capacity and failure mode of the joint. Hansen and Olesen (1976) observed that the reinforcement layout severely altered the failure mode of the specimens and decreased the capacity as well. Depending on the joint and reinforcement layout, the current standards may overestimate the capacity as the complex stress field within the joint is not accounted for.

4.3 Detailed modelling of joints

In order to assess the behaviour of keyed shear joints for different reinforcement layouts, a detailed plane stress model based on finite element limit analysis is developed. The work presented in this section is also presented in

Paper I (Herfelt et al., 2016).

Lower bound limit analysis

The method of finite element limit analysis was deliberately chosen over conventional incremental non-linear finite element analysis for several reasons: First and foremost, the chosen approach allows the results to be placed in the same context as the existing analytical models based on limit analysis. Secondly, finite element limit analysis is extremely efficient from a computational point of view as discussed in Section 1.3 and shown in Section 4.1.5: Large problems with millions of variables can be solved in a matter of minutes on a standard PC. Moreover, interior point methods discussed in Section 2.5 are stable and numerical instability is rare. Finally, this detailed analysis should be seen as the first, small step towards developing a general framework based on finite element limit analysis for precast concrete structures.

The general formulation of lower bound finite element limit analysis was presented in Section 3.2 and is repeated below:

$$\begin{aligned} &\text{maximise} && \lambda \\ &\text{subject to} && \mathbf{B}^T\boldsymbol{\sigma} = \boldsymbol{p}\lambda + \boldsymbol{p}_0 \\ &&& f(\boldsymbol{\sigma}_i) \leq 0, \quad i = 1, 2, \ldots, m \end{aligned} \tag{4.26}$$

where $\boldsymbol{\sigma}$ is the stress vector, and $\mathbf{B}^T$ is the global equilibrium matrix. The load comprises a constant part $\boldsymbol{p}_0$ and a scalable part $\boldsymbol{p}\lambda$ where λ is the load factor sought to be maximised. The inequalities $f(\boldsymbol{\sigma}_i) \leq 0$ ensure that the stress in point i satisfies the yield criterion described by the function f.

4.3.1 Keyed joints

We consider a keyed joint reinforced with U-bar loops in the transverse direction and a locking bar in the longitudinal direction. The U-bar loops are placed with a mutual distance u as indicated in Figure 4.15, thus, it is necessary to mobilise the surrounding concrete in order to activate the reinforcement.

The geometry of the keyed interface is defined by h_1, h_2, and d, while the reinforcement layout is defined by o and u. The width of the joint is given by b and the out-of-plane thickness by t.

The detailed model will use the enhanced plane stress element presented by Poulsen and Damkilde (2000) and Nielsen (2014) as well as in Section 4.1.1 and 4.1.2. The joint mortar and surrounding precast panels will be modelled as unreinforced concrete using the plane stress element. Due to the

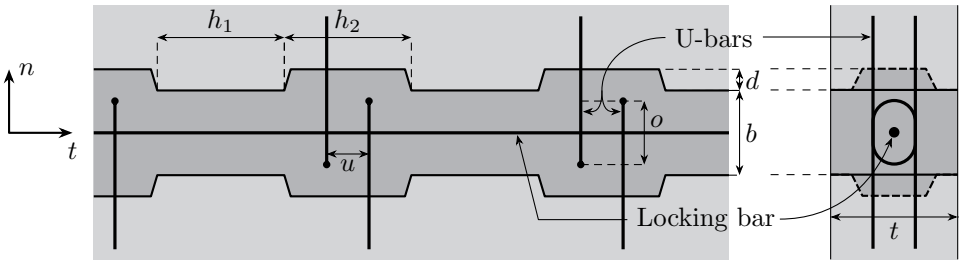

***Figure 4.15**: Elevation and cross section of the basic keyed joint reinforced with U-bar loops.*

size of the model, the reinforcement will be modelled discretely instead of smeared using a one-dimensional bar element (Poulsen and Damkilde, 2000). The bar element only provides dissipation along its axis and dowel action is neglected. All shear forces and confinement has to be transferred via the interface between the joint and the precast panels, hence, a suitable finite element is needed to assess the behaviour and capacity of the interface.

A one-dimensional interface element with a width of zero is introduced. The element has to be compatible with the plane stress element presented in Section 4.1.1, thus, linear variation of stresses is required. Two stress components can be present in the interface, namely a shear stress and a normal stress, and traction continuity between the interface element and adjacent plane stress elements must be satisfied, see Figure 4.16.

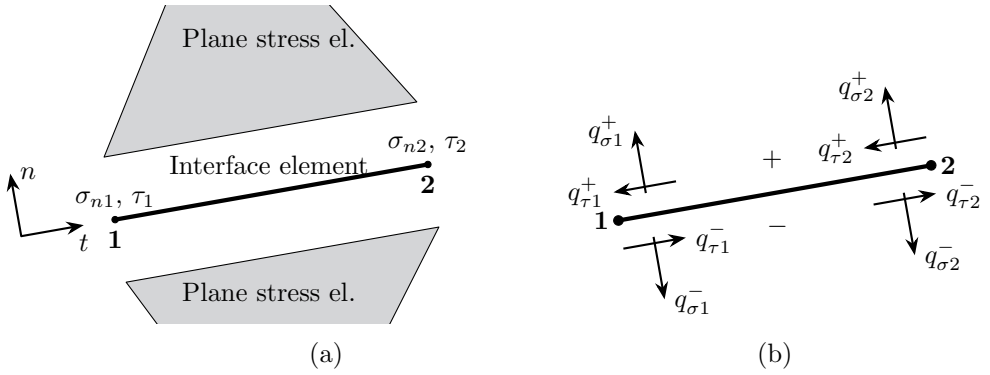

***Figure 4.16**: a) Local coordinate system and stress variables of the interface element, b) generalised nodal forces.*

The four stress variables and eight generalised nodal forces are illustrated in Figure 4.16. The stresses are simply transferred directly through the interface, which simplifies the equations greatly together with the fact that

the stresses are given in the local coordinate system. The local equilibrium can be stated as:

$$\boldsymbol{q} = \begin{bmatrix} q_{\sigma 1}^{+} \\ q_{\tau 1}^{+} \\ q_{\sigma 2}^{+} \\ q_{\tau 2}^{+} \\ q_{\sigma 1}^{-} \\ q_{\tau 1}^{-} \\ q_{\sigma 2}^{-} \\ q_{\tau 2}^{-} \end{bmatrix} = \begin{bmatrix} 1 & 0 & 0 & 0 \\ 0 & -1 & 0 & 0 \\ 0 & 0 & 1 & 0 \\ 0 & 0 & 0 & -1 \\ -1 & 0 & 0 & 0 \\ 0 & 1 & 0 & 0 \\ 0 & 0 & -1 & 0 \\ 0 & 0 & 0 & 1 \end{bmatrix} \begin{bmatrix} \sigma_{n1} \\ \tau_1 \\ \sigma_{n2} \\ \tau_2 \end{bmatrix} = \mathbf{B}_{el}^{T} \boldsymbol{\sigma}_{el} \tag{4.27}$$

where $\mathbf{B}_{el}^{T}$ is the element equilibrium matrix. Nielsen and Hoang (2010) describe a suitable yield criterion for interfaces between joints and precast concrete, which corresponds to the plane stress Mohr-Coulomb criterion with a tension cut-off and one free normal stress, σ_t.

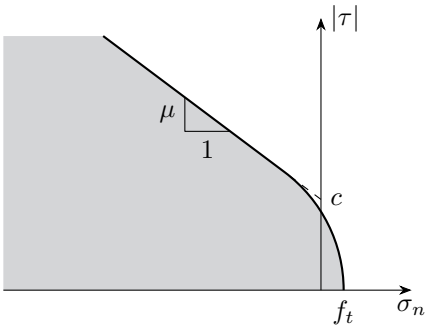

***Figure 4.17**: Yield envelope for the interface element.*

Figure 4.17 shows the yield criterion described by Nielsen and Hoang (2010). The modified Mohr-Coulomb criterion and its formulation for second-order cone programming are presented in Section 3.3 and will not be repeated here. While the criterion described by Nielsen and Hoang (2010) is slightly different, the formulation is identical. In principal stresses, the criterion can be stated as

$$\begin{aligned} \sigma_1 &\leq f_t \\ k\sigma_1 - \sigma_2 &\leq 2c\sqrt{k} \end{aligned} \tag{4.28}$$

where σ_1 and σ_2 are the largest and smallest principal stresses, respectively. The properties of the interface are given by f_t, the uniaxial tensile strength,

c, the cohesion, and k, a friction parameter defined as:

$$k = \left(\sqrt{\mu^2 + 1} + \mu\right)^2 \tag{4.29}$$

where μ is the friction coefficient of the interface. The cohesion c is sensitive to curing conditions. If cracking has not taken place, the cohesion can be taken as $c = 0.55\sqrt{f_c}$ (Nielsen and Hoang, 2010). In practice, cracking due to shrinkage will more or less always occur and the cohesion has to be reduced substantially. For the following analysis, a cohesion in the range of 0 to 0.5 MPa will be used. The friction coefficient depends on the type of interface, and for smooth interfaces, a friction coefficient of $\mu = 0.75$ can be used according to Dahl (1994) and Nielsen and Hoang (2010). Moreover, the separation strength of the interface f_t is chosen as zero for all interface elements.

4.3.2 Model

The detailed numerical model will be compared with experimental data from Hansen and Olesen (1976) and Fauchart and Cortini (1972). Moreover, the model and the experimental data will be compared to the current design formulas of the Eurocode 2. Hansen and Olesen tested 16 specimens in total: Six were reinforced with U-bar loops and the remaining 10 were subjected to external confinement. Fauchart and Cortini tested 10 specimens, all reinforced with U-bar loops.

***Table 4.5**: Geometry for the specimens by Hansen and Olesen (1976) and Fauchart and Cortini (1972). All parameters are given in millimetres.*

	h_1	h_2	d	b	t	o	l
Hansen and Olesen (1976)	40	40	6	50	50	30	1200
Fauchart and Cortini (1972)	167	83	20	145	90	115	1500

The geometric parameters of the two sets of specimens are listed in Table 4.5, see also Figure 4.15. The specimens by Hansen and Olesen (1976) featured short keys with a small key depth with a total of 14 full keys, while the specimens by Fauchart and Cortini (1972) had longer and deeper keys and a total of 5 full keys. Figure 4.18(a) shows the model including loading and support conditions, while the meshes used for the model are displayed in 4.18(b)-(e). The loading ensures that the centre line of the joint is loaded in pure shear, and due to the anti-symmetric loading no forces are actually

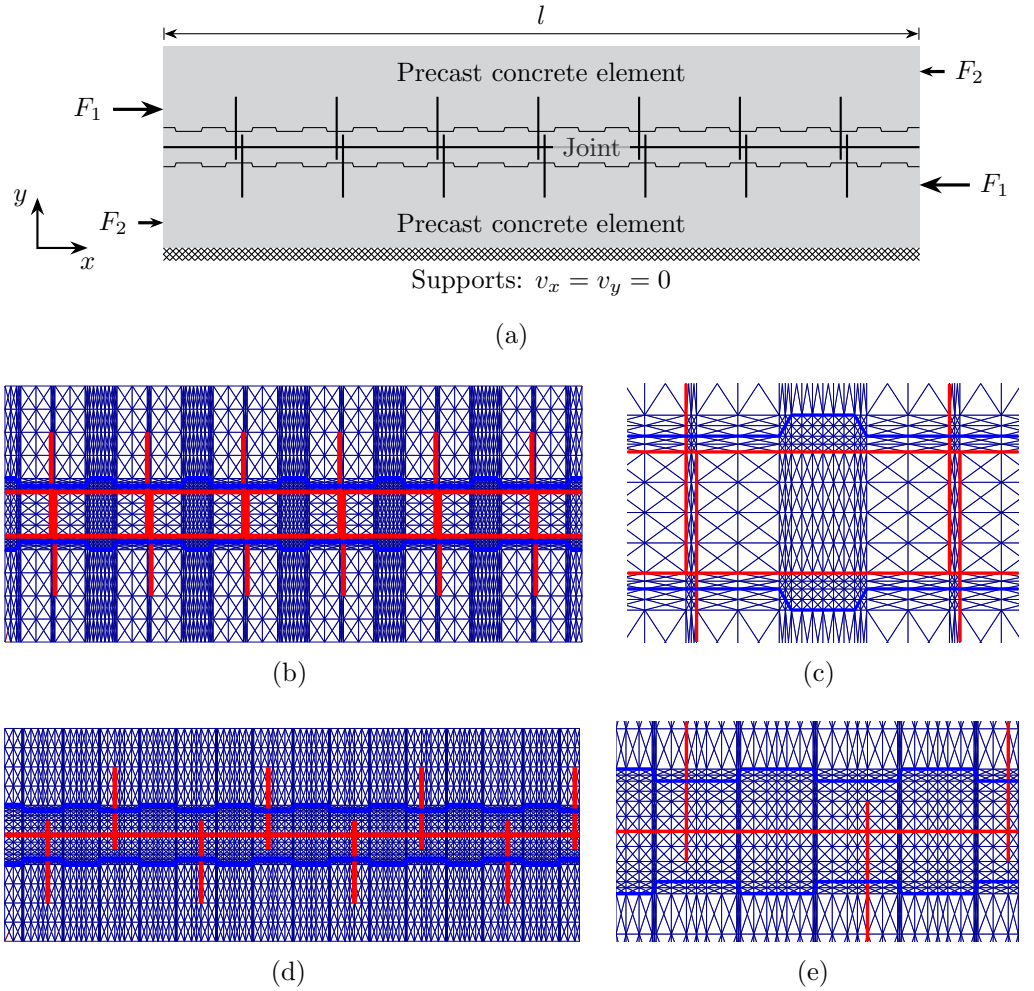

***Figure 4.18**: a) Sketch of the numerical model including boundary conditions and loading; b) mesh for the specimens by Fauchart and Cortini (8,064 elements); c) zoom of the mesh seen in b) showing the keyed interface, two pairs of U-bars (thick vertical lines), and two locking bars (thick, straight horizontal lines), d) half of the mesh for the specimens by Hansen and Olesen (20,024 elements); e) zoom of the mesh seen in d) showing the keyed interface, a locking bar (thick horizontal line), and a pair of U-bars (thick vertical lines).*

transferred to the supports, which are only used to restrict the model against rigid-body movement.

The concrete of the joint is modelled using the Mohr-Coulomb criterion for plane stress, see Section 3.3. Near the U-bar loops, the joint will necessarily experience triaxial stress, hence, the assumption of plane stress is conservative in those regions. Due to the poor behaviour of concrete loaded in tension, a tensile strength of $f_t = 0$ is assumed. The choice of effectiveness factor ν is discussed in Section 1.2: For lower bound models featuring direct strut action an effectiveness factor of $\nu = 1$ has been used by Nielsen and Hoang (2010). Jørgensen (2014) adopted an effectiveness factor smaller than unity, however, the models by Jørgensen are upper bound models.

4.3.3 Comparison and analysis

The experimental results of Hansen and Olesen (1976) and Fauchart and Cortini (1972) are compared to the detailed model based on finite element limit analysis and the Eurocode 2. First and foremost, we define the reinforcement ratio as

$$\Phi = \frac{\sum A_{su} f_y}{A_c f_c}, \tag{4.30}$$

where A_{su} is the cross sectional area of the U-bar loops, f_y is the yield strength, and $A_c = tl$ is the cross sectional area of the concrete. The Eurocode design formulas were presented in Section 1.1 and are repeated below. The shear capacity of keyed joints can be calculated as

$$\tau = \begin{cases} c f_t A_{key}/A_c + \mu \Phi f_c \\ \frac{1}{2} \nu f_c A_{key}/A_c \end{cases} \tag{4.31}$$

where A_{key} is the area of the keys, cf_t is an expression for the cohesion of the joint, and f_t can be taken as $0.21 f_c^{2/3}$ according to the Eurocode 2. For keyed interfaces, an friction coefficient of $\mu = 0.9$ and a cohesion paramter $c = 0.5$ can be used. It is worth noting that $\mu = 0.9$ is higher than the value recommended by Dahl (1994) and Nielsen and Hoang (2010). For the Eurocode 2 design formula, the effectiveness factor

$$\nu_{EC2} = 0.7 - \frac{f_c}{200} \tag{4.32}$$

is used, where f_c should be in MPa. It is important to emphasise that the mean values of the material parameters are used for the comparison.

Figure 4.19 shows that the presented numerical model predicts a satisfactory estimate of the shear capacity for a wide range of experiments. It

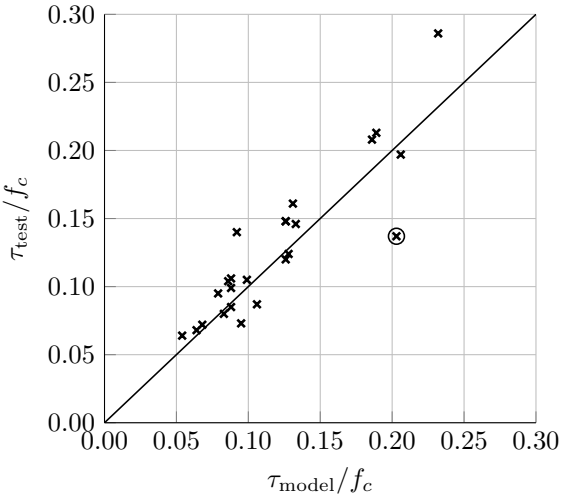

***Figure 4.19**: Comparison of normalised shear capacity of the 24 experiments (Hansen and Olesen, 1976; Fauchart and Cortini, 1972) and the numerical model.*

is observed that the model on average predicts a capacity slightly below the experimental results, however, for a single specimen (no. 29, indicated by a circle in Figure 4.19) the model overestimates the shear capacity considerably. It is worth noting that specimen 29 is the only specimen where the Eurocode 2 overestimates the capacity, see Figure 4.20(a) and Tabel 4.6.

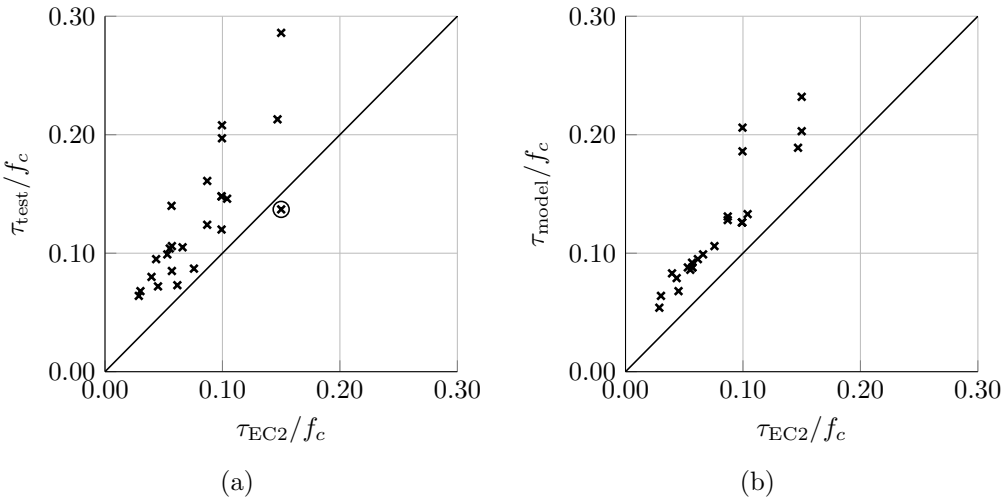

***Figure 4.20**: Comparison of the Eurocode design formulas with (a) experimental results and (b) the presented numerical model.*

Figure 4.20(a) shows that the Eurocode generally underestimates the shear capacity of the joints, in some cases by almost 60 %, see Table 4.6. The errors shown in Tables 4.6 and 4.7 are computed as

$$\epsilon_{\text{model}} = \frac{\tau_{\text{model}}}{\tau_{\text{test}}} - 1, \quad \text{and} \quad \epsilon_{\text{EC2}} = \frac{\tau_{\text{EC2}}}{\tau_{\text{test}}} - 1$$

The average error is -4.3 % for the presented model and -37.9 % for the Eurocode design formulas. Figure 4.20(b) shows that the presented model predicts a shear capacity considerably larger than the Eurocode. It is also observed that only little scatter is seen in Figure 4.20(b) for $\tau/f_c \leq 0.1$. Table 4.6 and 4.7 shows all results in addition to the material data and geometry. Specimens 01, 02, 03, 04, 05, 12, 13, 14, 18, and 29 by Hansen and Olesen (1976) listed in Table 4.6, did not have any transverse reinforcement, and external confinement pressure was added instead. Table 4.6 lists a reinforcement ratio equivalent to the external confinement. It is seen that specimen 29 is the only externally confined specimen with an equivalent reinforcement ratio above 0.10, however, the specimen yielded a shear capacity similar to the capacities of specimens 12 and 13, which have equivalent reinforcement ratios of 0.43 and 0.95, respectively.

The reinforcement layout of specimens 24 and 26 by Hansen and Olesen (1976) makes them particular interesting: They both feature a suboptimal reinforcement layout, i.e. a large value of u, and the presented model seems to capture the behaviour well in comparison to the Eurocode 2. Specimen 25 is identical to specimen 26 with the exception of the reinforcement layout. The determined stress fields and collapse modes of the two specimens are displayed in Figure 4.21 and 4.22.

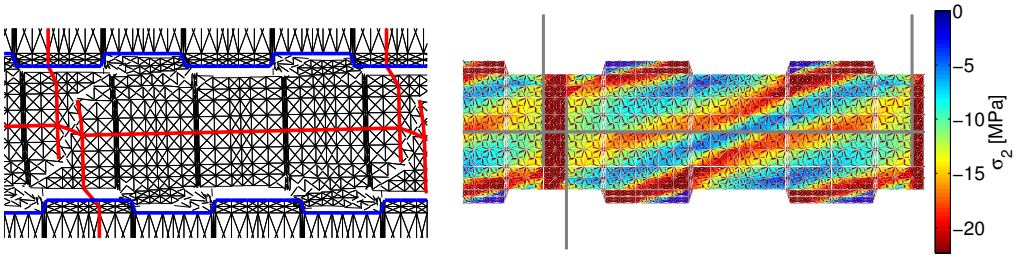

(a) (b)

***Figure 4.21**: a) Collapse mode and b) lowest principal stress for specimen 25 by Hansen and Olesen (1976).*

The thick blue lines in Figure 4.21(a) and 4.22(a) indicates the interface between the precast panels and the joint mortar. The red lines represent the

***Table 4.6**: Data and results of experiments by Hansen and Olesen (1976), the numerical model, and Eurocode 2.*

	f_c	Φ	u	**Test**	**Numerical**		**Eurocode 2**	
No.	[MPa]	[-]	mm	τ/f_c	τ/f_c	Error [%]	τ/f_c	Error [%]
01	29	0.013	-	0.064	0.053	-17.2	0.029	-55.0
02	32	0.030	-	0.095	0.079	-16.8	0.044	-54.2
03	32	0.055	-	0.105	0.102	-2.9	0.066	-37.1
04	16	0.061	-	0.087	0.107	23.0	0.076	-13.0
05	53	0.018	-	0.068	0.064	-5.9	0.030	-55.6
12	25	0.043	-	0.140	0.092	-34.3	0.057	-59.9
13	23	0.095	-	0.146	0.133	-8.9	0.104	-28.8
14	25	0.039	-	0.099	0.088	-11.1	0.053	-46.4
18	27	0.049	-	0.073	0.097	32.9	0.062	-15.6
29	17	0.188	-	0.137	0.203	48.2	0.150	9.5
23	31	0.025	10	0.080	0.083	3.8	0.040	-50.5
24	26	0.030	150	0.072	0.068	5.6	0.045	-37.3
25	24	0.076	10	0.161	0.131	-18.6	0.087	-45.9
26	24	0.076	70	0.124	0.128	3.2	0.087	-29.8
27	15	0.139	10	0.213	0.189	-11.3	0.147	-31.0
28	13	0.235	10	0.286	0.230	-19.6	0.150	-47.6

***Table 4.7**: Data and results of experiments by Fauchart and Cortini (1972), the numerical model, and Eurocode 2.*

	f_c	Φ	u	**Test**	**Numerical**		**Eurocode 2**	
No.	[MPa]	[-]	mm	τ/f_c	τ/f_c	Error [%]	τ/f_c	Error [%]
5	20	0.049	10	0.106	0.088	-17.0	0.057	-46.3
6	20	0.049	10	0.085	0.088	3.5	0.057	-33.0
7	20	0.096	10	0.120	0.126	5.0	0.099	-17.3
8	20	0.246	10	0.197	0.206	4.6	0.100	-49.4
9	20	0.047	10	0.104	0.086	-17.3	0.055	-47.0
10	20	0.096	10	0.148	0.126	-14.9	0.099	-32.9
11	20	0.096	10	0.148	0.126	-14.9	0.099	-32.9
12	20	0.191	10	0.208	0.186	-10.6	0.100	-52.2

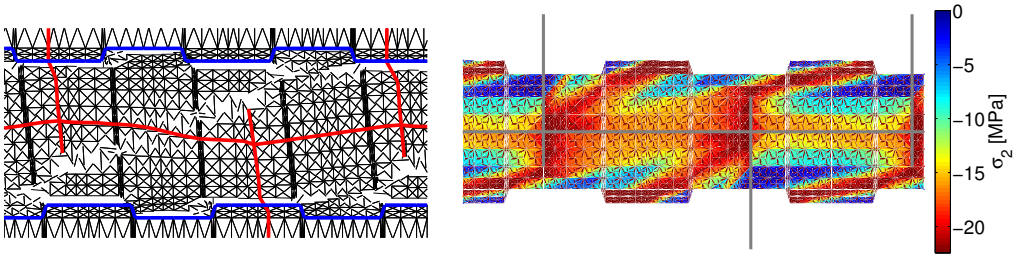

(a) (b)

Figure 4.22*: a) Collapse mode and b) lowest principal stress for specimen 26 by Hansen and Olesen (1976).*

reinforcement, i.e. the loop reinforcement and locking bar. The deformed shape of the reinforcement is determined by interpolating the location of the nodes in the deformed mesh. The gray lines in Figure 4.21(b) and 4.22(b) represents the reinforcement.

Figure 4.21(a) shows failure of the interface of specimen 25, whereas Figure 4.22(a) shows that the primary failure mechanism is a diagonal yield zone through the core of the joint. This correlates well with what Hansen and Olesen (1976) reported, namely that specimen 23, 25, and 27 failed by shearing off the keys, while for specimens 24 and 26 the core of the joint was almost completely destroyed. From Figure 4.21(b) and 4.22(b) it is clear that the reinforcement layout heavily affects the stress field within the joint. Figure 4.21(b) displays clear, distinct struts, whereas Figure 4.22(b) shows that the compression struts are disrupted by reinforcement layout. For specimen 26, localised strut action are necessary to mobilise the loop reinforcement, which of course affects the entire stress field. It is worth noting that the collapse mode seen in Figure 4.21(a) as well as the stress field seen in Figure 4.21(b) are similar to the simplified analytical models shown in Figure 4.14.

Figure 4.23 shows the shear capacity for the different specimens as a function of the reinforcement ratio (or equivalent reinforcement ratio for Figure 4.23(b)). The curves are computed by varying the yield strength of the reinforcement. All specimens by Fauchart and Cortini (1972) have the same geometry and concrete strength, see Table 4.7, hence, they are all plotted together, and it is seen Figure 4.23(a) that the presented numerical model provides an excellent estimate of the shear capacity of these specimens.

The results of the specimens with external confinement by Hansen and Olesen (1976) are somewhat scattered as seen in Figure 4.23(b), but the numerical model provides a decent estimate nevertheless (with the exception of specimen 29 as discussed earlier). Figure 4.23(c) and (d) show that the

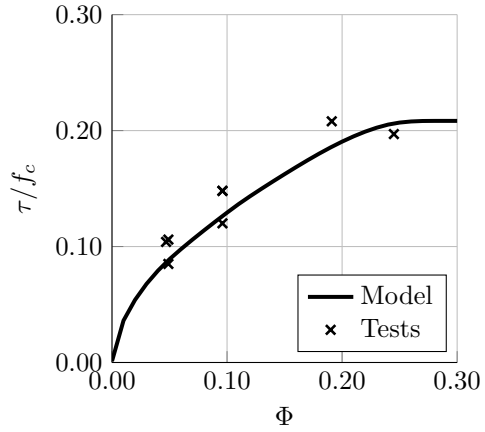

(a) Tests by Fauchart and Cortini (1972).

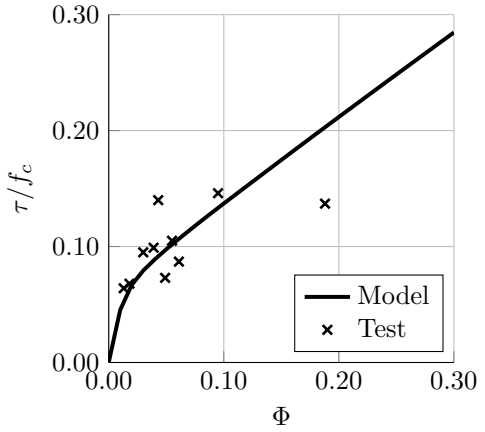

(b) Specimens 01, 02, 03, 04, 05, 12, 13, 14, 18, and 29 (Hansen and Olesen, 1976).

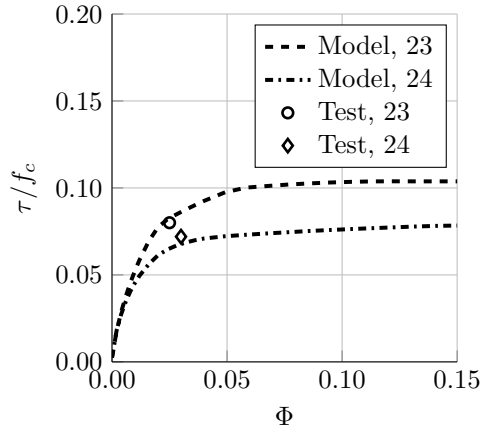

(c) Specimens 23 and 24 (Hansen and Olesen, 1976).

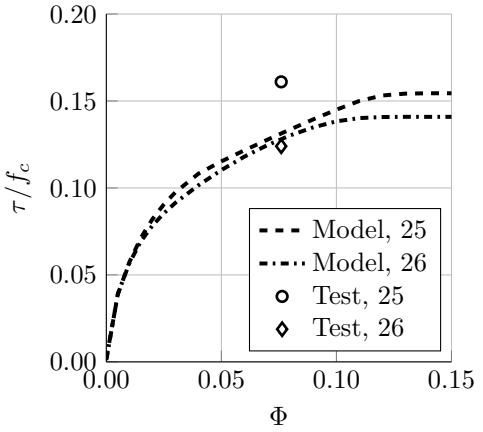

(d) Specimens 25 and 26 (Hansen and Olesen, 1976).

***Figure 4.23**: Experimental for the specimens by Fauchart and Cortini (1972) and Hansen and Olesen (1976) and capacity curves computed using the presented numerical model.*

experimental results fall close to the computed capacity curves for the specimens. A substantial difference is observed between the curves of specimens 23 and 24, as well as specimens 25 and 26, respectively, and the effect of the reinforcement layout can be seen clearly.

Despite the fact that little to no cohesion was assumed for the interface of the numerical model, a *pseudo cohesion* seems to be present in Figure 4.23(a) and (b), if the linear part of the curves is extended to intersect the (τ/f_c)-axis. This is similar to the cohesion shown in Figure 4.17. The pseudo

cohesion seems to take a value of approximately 5 % of the compressive strength, however, this value will most likely depend on the reinforcement layout amongst other parameters. This pseudo cohesion seems to be a result of the keyed interface, where local failure at the corners of the keys occur.

Computational effort

The presented model requires several thousand plane stress elements in addition to the interface elements and bar elements. Solving the resulting mathematical optimisation problem (4.26) requires a considerable computational effort. The detailed model for the specimens by Fauchart and Cortini (1972) uses more than 8,000 finite elements, while the model for the specimens by Hansen and Olesen (1976) uses 20,000 finite elements. The sparsity of the problem (4.26) will increase with the number of elements, and for larger problems the system matrix will be extremely sparse. The sparsity is exploited in the solver (MOSEK ApS, 2015).

***Table 4.8**: Number of elements, problem size, and computational time for the numerical model.*

	Hansen and Olesen (1976)	Fauchart and Cortini (1972)
Plane stress el.	19,040	7,520
Interface el.	596	236
Bar elements.	388	308
Variables	1,364,509	539,709
Linear constraints	1,305,890	516,428
Conic constraints	134,472	53,112
Computational time	94.14 s	37.10 s

Table 4.8 shows the problem sizes and computational time for the two meshes seen in Figure 4.18. The model for the specimens by Hansen and Olesen (1976) uses more elements due to the number of keys, and the resulting optimisation problem has more than 1.3 million variables and linear constraints. Moreover, 134,472 conic constraints are required to model the yield functions of the plane stress elements and interface elements. Table 4.8 shows that the computational time is approximately proportional to the problem size, similar to the analysis in Section 4.1.5, and even large problem can be solved in a matter of minutes.

4.3.4 Summary

The presented model was validated by comparison to the experimental data and satisfactory correlation was found: The numerical model predicted a decent estimate of the shear capacity approximately 4 % below the experimental result on average. The design formulas of the Eurocode 2, on the other hand, underestimate the shear capacity by 38 % on average despite the use of mean strength values for the materials.

The numerical model accounts for the effect of the reinforcement layout, which was shown to be quite substantial for some of the experiments by Hansen and Olesen. Moreover, the model computes the optimal, statically admissible stress field from the lower bound model and corresponding failure mechanism can be interpreted from the solution to the corresponding dual problem. All in all, the model provides unique insights into the ultimate limit state behaviour of keyed joints.

The findings can be used to optimise the joint geometry, i.e. computing the optimal depth of the keys. Such optimisation is relevant for precast concrete manufactures which will benefit from the optimisation through the mass production of the optimised panels. For consulting engineers designing entire buildings, however, the level of detail of the presented model is far to high. Moreover, modelling larger structures using the presented model would result in enormous computational problems which would require computational resources not available to consulting engineering companies.

4.4 Joints in two dimensions

The scope of the present work is to develop a framework for finite element limit analysis of precast concrete structures. The detailed model presented in Section 4.3 and Paper I (Herfelt et al., 2016) is able to assess the complex stress field within the joint and capture the local failure mechanisms, however, for practical design of precast concrete structures it is simply not feasible to use that level of detail. The four-storey wall seen in Figure 4.12 comprises a total of 12 panels and more than 50 metres of in-situ cast joints in total, hence, it would require millions of elements to obtain the same level of detail as the model presented in Section 4.3.

In this section, a multiscale finite element for modelling of in-situ cast joints is presented (see also Paper II, Herfelt et al., 2017a). The multiscale element comprises a macro joint element, which interacts on the element level, and a so-called submodel criterion which is used to assess the behaviour of the joint on the sub-element level. Like the plane stress elements, the joint

element will be a lower bound element, and it will be compatible with the aforementioned plane stress elements presented by Poulsen and Damkilde (2000) and in Section 4.1. The scope is to be able to model entire wall systems, e.g. the four-storey wall seen in Figure 4.12, using a limited number of the joint elements. The element of course also requires an adequate yield function which can capture the mechanisms identified by the detailed model in Section 4.3. For this purpose a submodel yield criterion is developed, i.e. a simple mechanical submodel is used on the sub-element level to obtain the relevant stress field within the joint and enforce the material yield criterion on the submodel level.

Plane stress is still assumed, and the presented joint element and submodel yield criterion will fit the format of second-order cone programming. The developed macro element and submodel will be compared to the detailed numerical model as well as the experimental results by Hansen and Olesen (1976) and Fauchart and Cortini (1972).

4.4.1 Macro joint element

A lower bound element is developed, and the general problem formulation will be identical to the one presented in Section 3.2:

$$\begin{array}{ll} \text{maximise} & \lambda \\ \text{subject to} & \mathbf{B}^T\boldsymbol{\sigma} = \boldsymbol{p}\lambda + \boldsymbol{p}_0 \\ & f(\boldsymbol{\sigma}_i) \leq 0, \quad i = 1, 2, \ldots, m \end{array} \tag{4.33}$$

In this case, however, the yield function $f(\boldsymbol{\sigma}_i)$ is the so-called submodel yield criterion, i.e. the notation $f(\boldsymbol{\sigma}_i)$ represents both several additional equilibrium equations which are enforced on the submodel level, and the material yield criterion which take the submodel stress fields as input. Expanding the yield function in (4.33) gives

$$\begin{array}{ll} \text{maximise} & \lambda \\ \text{subject to} & \mathbf{B}^T\,\boldsymbol{\sigma} = \boldsymbol{p}\,\lambda + \boldsymbol{p}_0 \\ & \mathbf{C}_\beta\boldsymbol{\beta} + \mathbf{C}_\alpha\boldsymbol{\alpha} + \mathbf{C}_\gamma\boldsymbol{\gamma} = \boldsymbol{C}_0 \\ & \mathbf{E}_\sigma\boldsymbol{\beta} + \mathbf{E}_\alpha\boldsymbol{\alpha} + \mathbf{E}_\gamma\boldsymbol{\gamma} \leq \boldsymbol{E}_0 \\ & \boldsymbol{\gamma}_i \in \mathcal{Q}_{k_i}, \quad i = 1, 2, \ldots, m \end{array} \tag{4.34}$$

where $\mathbf{C}_\sigma$, $\mathbf{C}_\alpha$, and $\mathbf{C}_\gamma$ are the matrices associated with the equality constraints for the yield function, and $\mathbf{E}_\sigma$, $\mathbf{E}_\alpha$, and $\mathbf{E}_\gamma$ are the matrices associated with the inequality constraints. The vectors, $\boldsymbol{C}_0$ and $\boldsymbol{E}_0$, typically contain material strength parameters or similar.

Two different vectors are used for the auxiliary variables for the yield function, namely $\boldsymbol{\alpha}$ and $\boldsymbol{\gamma}$, where $\boldsymbol{\gamma}$ is used to establish the second-order constraints, $\boldsymbol{\gamma}_i \in \mathcal{Q}_{k_i}$. $\boldsymbol{\gamma}_i$ is a subset of $\boldsymbol{\gamma}$ associated with the ith check point and $\mathcal{Q}_{k_i}$ represents a conic set of size k_i, see Section 2.3.

On the element level, the equilibrium equations and yield functions can be stated as

$$\begin{aligned}
&\mathbf{B}_{el}^T \boldsymbol{\sigma}_{el} = \boldsymbol{q}_{el} \\
&\mathbf{C}_{\sigma}^{el,i} \boldsymbol{\sigma}_{el} + \mathbf{C}_{\alpha}^{el,i} \boldsymbol{\alpha}_i + \mathbf{C}_{\gamma}^{el,i} \boldsymbol{\gamma}_i = \boldsymbol{C}_0^{el,i}, \qquad && i = 1, 2, \ldots, m_{el} \\
&\mathbf{E}_{\sigma}^{el,i} \boldsymbol{\sigma}_{el} + \mathbf{E}_{\alpha}^{el,i} \boldsymbol{\alpha}_i + \mathbf{E}_{\gamma}^{el,i} \boldsymbol{\gamma}_i \leq \boldsymbol{E}_0^{el,i}, \qquad && i = 1, 2, \ldots, m_{el} \\
&\boldsymbol{\gamma}_i \in \mathcal{Q}_{k_i}, && i = 1, 2, \ldots, m_{el}
\end{aligned} \tag{4.35}$$

The vector $\boldsymbol{q}_{el}$ contains the contributions to the equilibrium equations on the global level, $\boldsymbol{\sigma}_{el}$ contains the stress variables of the given element, and $\mathbf{B}_{el}^T$ is the element equilibrium matrix. The matrices $\mathbf{C}^{el,i}$ and $\mathbf{E}^{el,i}$ define the yield function for the m_{el} check points of the element.

We now consider a unit section of a joint. The unit section has exactly one pair of U-bar loops and is defined by the length s, see Figure 4.24. The unit joint section will comprise more than one key if the loop reinforcement pairs are placed with a considerably distance, i.e. if s is large, see Figure 4.24(b).

The horizontal black line in the centre of the joint represents the locking bar, while the vertical lines represent the transverse reinforcement, i.e. U-bar loops. The unit joint sections seen in Figure 4.24 are defined by the aforementioned length s, the width b, and the out-of-plane thickness t. The loop reinforcement of the unit section is assumed to be placed with a mutual distance u, see Figure 4.24. It has already been shown in Section 4.3 that this value, u, affects the capacity as well as the failure mode of the joint, and it is therefore crucial to establish a model capable of modelling this behaviour.

The joint element only models the behaviour of the core of the concrete, i.e. the localised effects that take place inside the joint. The behaviour of the interfaces will be modelled using the interface element presented in Section 4.3, and the values adopted for the cohesion and friction for the comparison to the detailed numerical model and experimental results will be discussed later.

The macro finite element is formulated in the following. The length and orientation of the macro joint element is defined by the two end nodes seen in Figure 4.25(a). The joint element will dictate the distribution and transfer of stresses through the joint. The element will be formulated for interaction with the plane stress element which has a linear stress field. Due to the requirement of traction continuity, the joint element will necessarily also have a linear variation of stresses.

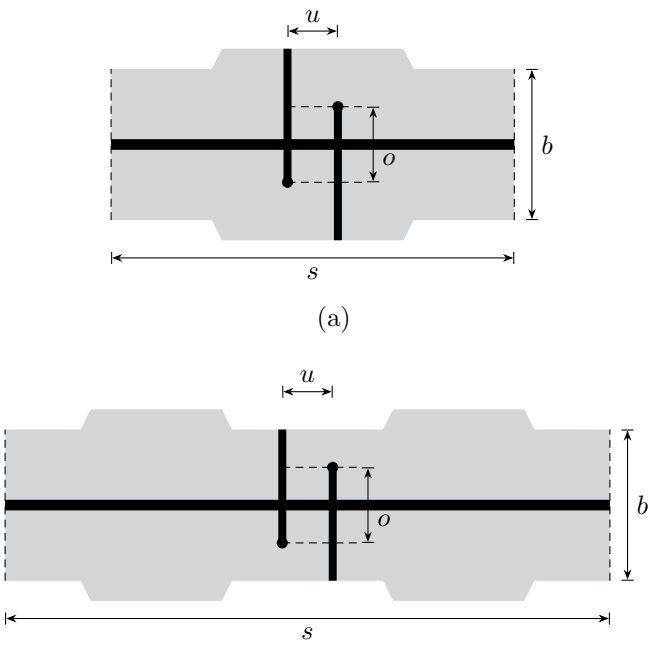

***Figure 4.24**: Unit section forming the basis of the joint model.*

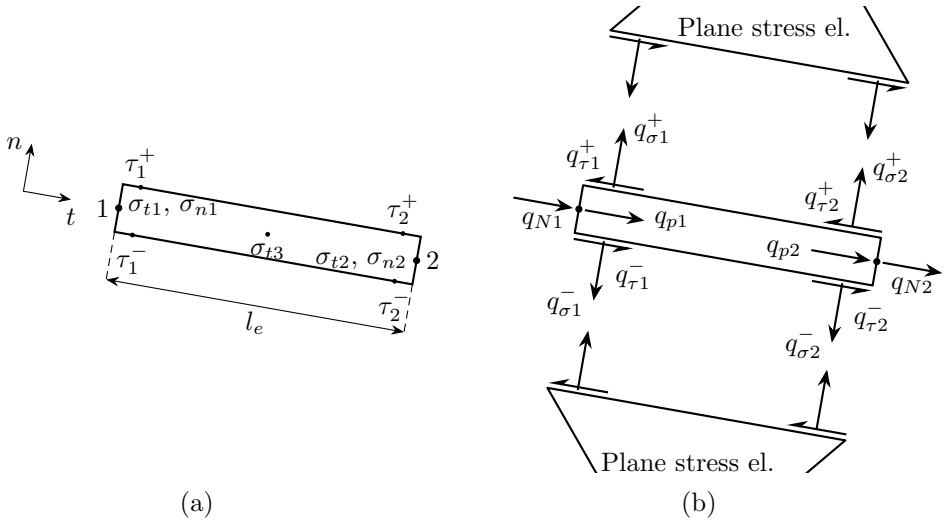

***Figure 4.25**: a) Geometry of the macro joint element including local coordinate system and stress variables. b) Nodal forces of the joint element and compatibility with the plane stress element.*

One key feature of the joint element is the ability to establish compression in the longitudinal direction via shear from adjacent panels. This means that the shear stress can vary in the top and bottom halves of the element and a four shear stress variables are necessary to describe two linear variations. The transverse normal stress is assumed to be transferred directly through the joint, hence, two variables are sufficient. The linear variation of shear stresses leads to a quadratic variation in the normal stress in the longitudinal direction (t-direction), thus, three variables are needed. In total, nine stress variables are used for the joint element:

$$\boldsymbol{\sigma}_{el} = \begin{bmatrix} \sigma_{n1} & \sigma_{n2} & \tau_1^+ & \tau_2^+ & \tau_1^- & \tau_2^- & \sigma_{t1} & \sigma_{t2} & \sigma_{t3} \end{bmatrix}^T \tag{4.36}$$

The macro element contributes to 12 equilibrium equations, four for each of the two adjacent plane stress elements ensures traction continuity, and four equations to ensure equilibrium in the longitudinal direction. The equilibrium equation on the element level can be stated as

$$\boldsymbol{q}_{el} = \mathbf{B}_{el}^T \boldsymbol{\sigma}_{el},$$

where $\boldsymbol{q}_{el}$ contains the 12 nodal forces, and $\mathbf{B}_{el}^T$ is the local equilibrium matrix. Due to the fact that the stress variables are given in local coordinates, no transformations are needed. The quantities $\boldsymbol{q}_{el}$ and $\mathbf{B}_{el}^T$ are explicitly given in (4.37):

$$\begin{bmatrix} \boldsymbol{q}^+ \\ \boldsymbol{q}^- \\ \boldsymbol{q}_N \end{bmatrix} = \begin{bmatrix} q_{\sigma 1}^+ \\ q_{\tau 1}^+ \\ q_{\sigma 2}^+ \\ q_{\tau 2}^+ \\ \hline q_{\sigma 1}^- \\ q_{\tau 1}^- \\ q_{\sigma 2}^- \\ q_{\tau 2}^- \\ \hline q_{N1} \\ q_{N2} \\ q_{p1} \\ q_{p2} \end{bmatrix} = \left[\begin{array}{ccccccccc} t & 0 & 0 & 0 & 0 & 0 & 0 & 0 & 0 \\ 0 & 0 & -t & 0 & 0 & 0 & 0 & 0 & 0 \\ 0 & t & 0 & 0 & 0 & 0 & 0 & 0 & 0 \\ 0 & 0 & 0 & -t & 0 & 0 & 0 & 0 & 0 \\ \hline -t & 0 & 0 & 0 & 0 & 0 & 0 & 0 & 0 \\ 0 & 0 & 0 & 0 & t & 0 & 0 & 0 & 0 \\ 0 & -t & 0 & 0 & 0 & 0 & 0 & 0 & 0 \\ 0 & 0 & 0 & 0 & 0 & t & 0 & 0 & 0 \\ \hline 0 & 0 & 0 & 0 & 0 & 0 & bt & 0 & 0 \\ 0 & 0 & 0 & 0 & 0 & 0 & 0 & -bt & 0 \\ 0 & 0 & t & 0 & -t & 0 & 3\frac{bt}{l_e} & \frac{bt}{l_e} & -4\frac{bt}{l_e} \\ 0 & 0 & 0 & t & 0 & -t & -\frac{bt}{l_e} & -3\frac{bt}{l_e} & 4\frac{bt}{l_e} \end{array}\right] \begin{bmatrix} \sigma_{n1} \\ \sigma_{n2} \\ \tau_1^+ \\ \tau_2^+ \\ \tau_1^- \\ \tau_2^- \\ \sigma_{t1} \\ \sigma_{t2} \\ \sigma_{t3} \end{bmatrix} = \mathbf{B}_{el}^T \boldsymbol{\sigma}_{el} \tag{4.37}$$

and

$$\boldsymbol{q}_{el} = \begin{bmatrix} \boldsymbol{q}^+ \\ \boldsymbol{q}^- \\ \boldsymbol{q}_N \end{bmatrix}$$

where $\boldsymbol{q}^+$ denotes the four nodal forces associated with the positive side of the joint, $\boldsymbol{q}^-$ denotes the four nodal forces associated with the negative side,

see Figure 4.25(b), and $\boldsymbol{q}_N$ denotes the four equations that ensure equilibrium in the longitudinal direction. Each point along the joint element has a stress state defined by four stress variables, namely σ_n, σ_t, τ^+, and τ^-, which is passed on to the submodel yield criterion and checked using the submodel yield criteiron.

4.4.2 Submodel for two-dimensional behaviour

The scope of the submodel yield criterion is to capture the behaviour and the critical mechanisms within the joint identified by the detailed model in Section 4.3. The submodel is based on the aforementioned unit joint section illustrated in Figure 4.24, which is subjected to shear as well as axial forces in two directions.

The general idea of the submodel yield criterion is to divide the seemingly complex problem into smaller parts. This is illustrated in Figure 4.26 where three rather simple stringer models are introduced. A modified version of the stringer models is used where confinement stresses acting on the rectangular panels replace the function of the smeared reinforcement, which is not available in the zones considered. For a general description of the stringer method, the reader is referred to Kærn (1979) and Damkilde et al. (1994). Each of the three models imposes constraints on the stress field in the joint and represents a basic state of stresses. The three basic stress states are then added together to obtain the actual stress state of the combined problem, which is then checked against the appropriate material yield criteria for the joint mortar and reinforcement, respectively.

Plane stress is assumed for the submodel yield criterion similarly to the detailed model presented in Section 4.3. The geometry of the loop reinforcement will necessarily lead to a triaxial stress state within the joint, however, the out-of-plane mechanisms are neglected and plane stress is assumed to obtain a safe lower bound solution. Due to this assumption, the model may underestimate the capacity in some cases.

The first stringer model, see Figure 4.26(b), activates the reinforcement, which is required in order to transfer tension across the joint or to establish confinement pressure on the joint. From the stringer model, it can be seen that tension in the loop reinforcement necessarily will induce shear in the centre row of panels. From the moment equilibrium of the model, the following relations can be derived:

$$\tau_{21} = \frac{V}{o\,t} = \frac{u}{s}\frac{T}{o\,t}, \qquad \tau_{22} = \left(\frac{u}{s} - 1\right)\frac{T}{o\,t} \tag{4.38}$$

where T is the tension force in the U-bar loops. From the antisymmetry of

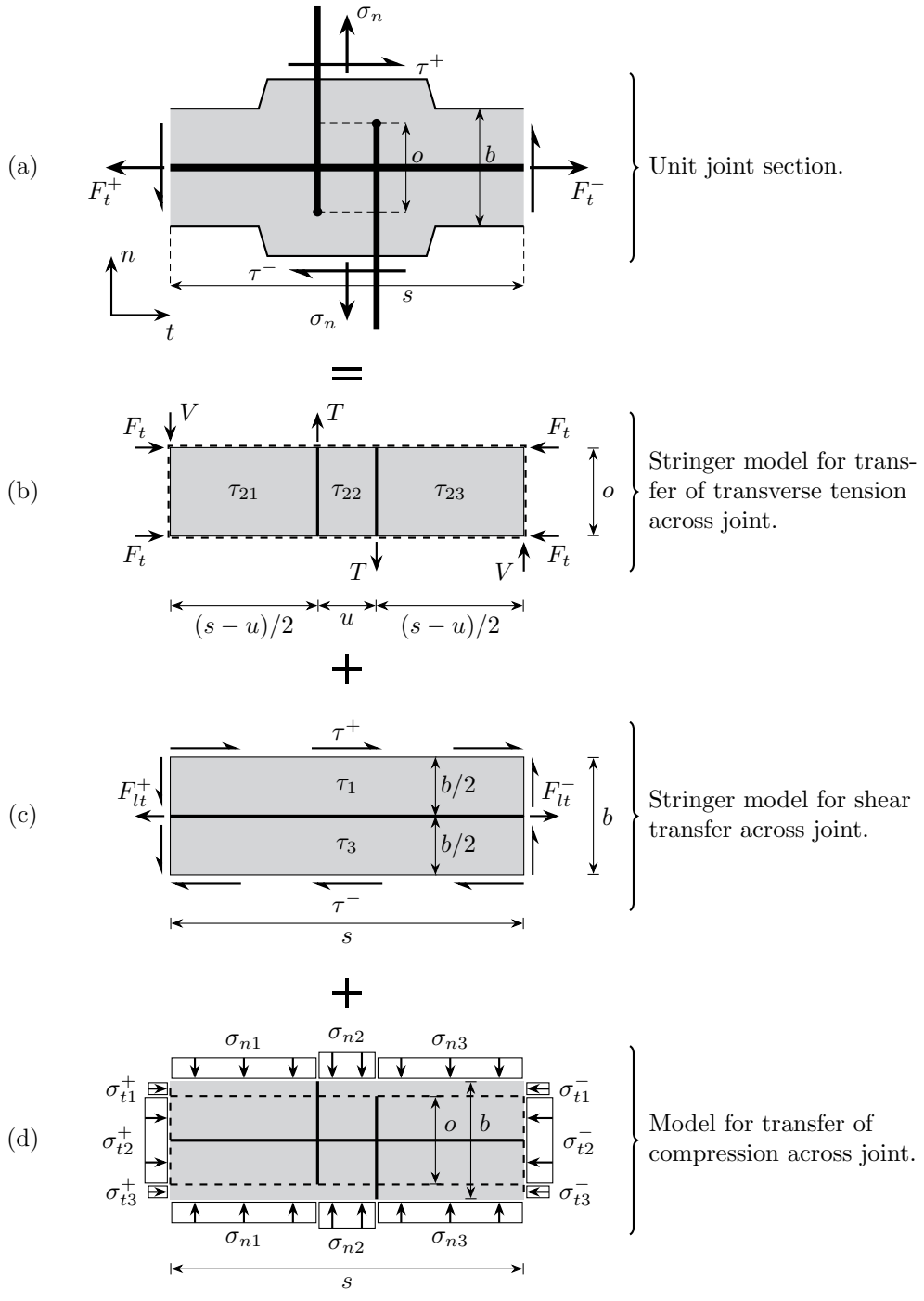

***Figure 4.26**: Unit joint section and the three stringer models: The behaviour of the unit joint section is governed by three stringer models, each describing a key mechanism, namely transverse tension, shear, and compression, respectively.*

the stringer model, it can be concluded that $\tau_{21} = \tau_{23}$. The stringer force V seen in Figure 4.26(b) will be balanced out by an adjacent joint element.

The stringer model for transfer of shear stresses is shown in Figure 4.26(c). The horizontal boundaries of the model may be subjected to shear of different magnitudes, which leads to a linear varying normal force in the central stringer, i.e. the locking bar. The shear in the two panels of the stringer model will be equal to the applied shear stresses, τ^+ and τ^-:

$$\tau_1 = \tau^+, \qquad \tau_3 = \tau^-, \tag{4.39}$$

Horizontal equilibrium for the central stringer gives the following equation:

$$F_{lt}^+ - F_{lt}^- = s\,t\,(\tau_1 - \tau_3) \tag{4.40}$$

The shear panels 1 and 3 seen in Figure 4.26(c) overlap the three shear panels of the first stringer model, Figure 4.26(b). The resulting shear stresses can simply be computed by adding the appropriate stresses.

Contrary to the ordinary stringer method, the panels are not reinforced and all reinforcement is modelled discretely as stringers. Instead, confinement pressure is added, which may originate from externally applied loads or from stresses developed to create internal equilibrium with the tensile forces of the reinforcement. The stringer model shown in Figure 4.26(d) describes the transfer of compression through the joint. Equilibrium is required for the horizontal boundaries of the unit joint section: The transverse normal stress σ_n is balanced by the stringer forces of the two previous stringer models, T and V, as well as the confinement pressure σ_{ni}:

$$s\,t\,\sigma_n = T - V - \frac{s-u}{2} t\,(\sigma_{n1} + \sigma_{n3}) - u\,t\,\sigma_{n2} \tag{4.41}$$

Equilibrium is likewise required for the horizontal boundaries of the unit joint section:

$$\begin{aligned} F_t^+ &= F_{lt}^+ - 2F_t - \frac{b-o}{2} t\left(\sigma_{t1}^+ + \sigma_{t3}^+\right) - o\,t\,\sigma_{t2}^+ \\ F_t^- &= F_{lt}^- - 2F_t - \frac{b-o}{2} t\left(\sigma_{t1}^- + \sigma_{t3}^-\right) - o\,t\,\sigma_{t2}^- \end{aligned} \tag{4.42}$$

The shear stress in the panels will be symmetric about the vertical centre line of the unit join section, hence, the confinement pressure in the n-direction will be symmetric as well, i.e. $\sigma_{n1} = \sigma_{n3}$. For simplicity, the same is assumed for the confinement in the longitudinal direction, i.e. $\sigma_{t1} = \sigma_{t3}$, which may lead to a lower shear capacity when $\tau^+ \neq \tau^-$.

Yield criteria on the submodel level

The normal stress in the t-direction will vary linearly when $\tau^+ \neq \tau^-$, hence, to ensure a statically admissible and safe stress field on the submodel level, the stresses have to be checked in several locations. Given a position in the joint, the resulting stress state can be established from the shear stresses of the two first stringer models and the normal stresses of the last stringer model, see Figure 4.26. The number of stress states to be checked can be reduced by exploiting the symmetry of the model, and a total of eight stress states is sufficient for the panels to ensure a safe stress field. The submodel comprises two different types of stringers, namely reinforcement stringers and compression stringers. The reinforcement stringers are, as the name indicates, stringers where reinforcement is present, hence, they can carry tension. Compression stringers, on the other hand, cannot carry tension since no reinforcement is present and confinement is required to keep the stringer in compression.

We assume that the reinforcement stringers only carry tension, and the tensile force is limited by the yield strength of the reinforcement. The yield condition can be stated as

$$\begin{aligned} 0 \leq\ & T\ \leq A_{su} f_{yu} \\ 0 \leq & F_{lt}^{+} \leq A_{sl} f_{yl} \\ 0 \leq & F_{lt}^{-} \leq A_{sl} f_{yl} \end{aligned} \tag{4.43}$$

where A_{su} and A_{sl} seen in (4.43) are the cross sectional areas of the U-bar loops and locking bar, respectively, while f_{yu} and f_{yl} are the yield strengths.

The horizontal stringers shown in the stringer model for transverse tension, Figure 4.26(b), are the aforementioned compression stringers. The confinement force F_t shown in 4.26(b) and 4.27 ensures that the stringer is loaded in compression.

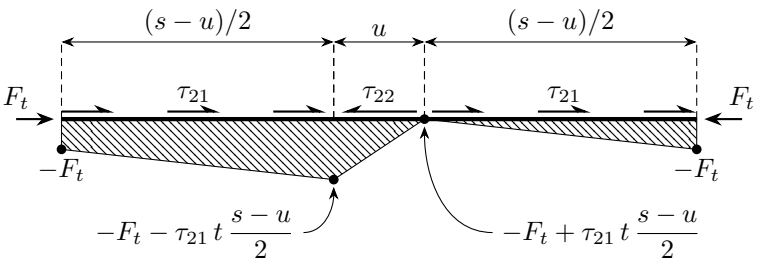

***Figure 4.27**: Stringer force distribution of the unreinforced compression stringers subjected to shear stress from adjacent panels as well as confining forces at the ends.*

Figure 4.27 shows the stringer force distribution, and the criterion for the compression stringers can be stated as a linear inequality:

$$-F_t + \tau_{21}\, t\, \frac{s-u}{2} \leq 0 \tag{4.44}$$

Finally, the Mohr-Coulomb criterion for plane stress is used for the shear panels of the submodel. The exact formulation of the criterion using second-order cone programming is given in Section 3.3, where it was shown that the criterion can be formulated for second-order cone programming using a single conic constraint. In principal stresses, the criterion can be stated as:

$$\begin{aligned} \sigma_1 &\leq f_t \\ k\sigma_1 - \sigma_2 &\leq f_c \\ -\sigma_2 &\leq f_c \end{aligned} \tag{4.45}$$

where σ_1 and σ_2 are the largest and smallest principal stresses, respectively. f_t and f_c are the uniaxial tensile and compression strengths of the joint mortar, and k is a friction parameter usually taken as 4 for normal strength concrete corresponding to an internal angle of friction of approximately 37°.

4.4.3 Validation and comparison

In the following section, the developed multiscale joint element is analysed. The results are compared to the detailed model presented in Section 4.3 as well as the experimental results by Hansen and Olesen (1976) and Fauchart and Cortini (1972). The scope of this analysis is to maximise the applied shear load for a given joint configuration. The shear load is applied on both sides of the joint, see $q^+_{\tau 1}$, $q^-_{\tau 1}$, $q^+_{\tau 2}$, and $q^-_{\tau 2}$ in Figure 4.25(b). No normal forces are introduced via the external loading, see Figure 4.28.

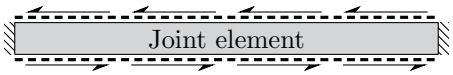

Figure 4.28*: Model for the analysis including supports and loading: The dashed lines indicates the interface elements representing the interface between the precast panels and the in-situ cast joint.*

In practice, the keys near the ends of the joint is used to establish a compressive force in the longitudinal direction, which increase the shear capacity considerably. To simulate this behaviour using just a single joint element, both ends are modelled as supported, i.e. equilibrium is not required for the generalised nodal forces q_{N1} and q_{N2}, see Figure 4.25(b). The specimens

tested by Hansen and Olesen (1976) and Fauchart and Cortini (1972) and the detailed model are of course subject to such boundary effects, and the analysis using the presented joint element may therefore overestimate the capacity slightly due to this choice of supports.

Two interfaces are indicated in Figure 4.28 (dashed lines), which are used to represent the interface between the precast panels and the in-situ cast joints. The yield envelope of the interface element is defined by two parameters, namely the cohesion and the friction coefficient. For the analysis, these parameters will be fitted to the curve of the detailed model. It was observed in Section 4.3.3 that the keys add *pseudo cohesion* to the interface in the order of approximately 5 % of the compressive strength, however, the magnitude of this pseudo cohesion depends on the geometry of the keys as well as the reinforcement layout. A friction coefficient of $\mu = 0.6$ is used for all specimens by Hansen and Olesen (1976), while $\mu = 0.75$ is used for the specimens by Fauchart and Cortini (1972). The cohesion for the interface elements varies between 5 % and 11 % of the concrete strength of the given specimen and is listed in Table 4.9.

***Table 4.9**: Fitted values of the cohesion and friction coefficient for the interface elements used for the analysis.*

Hansen and Olesen Specimens	c [f_c]	μ [-]
23	7 %	0.6
24	6 %	0.6
25, 26	8 %	0.6
27, 28	11 %	0.6
01, 02, 03, 04, 05, 12, 13, 14, 18, 29	6 %	0.6

Fauchart and Cortini Specimens	c [f_c]	μ [-]
All	5 %	0.75

Similarly to the detailed model, an efficiency factor of $\nu = 1$ has been used, i.e. the compressive strength is not reduced. This is due to the fact that the detailed model showed that the primary load carrying mechanisms is direct strut action with a deep strut inclination. A brief discussion on the efficiency factor was given in Section 1.2.

The normalised shear capacity of the joints will be plotted as a function of the mechanical reinforcement ratio which was defined as:

$$\Phi = \frac{\sum A_{su} f_{yu}}{A_c f_c}$$

where $A_c = t\,l$ is the cross sectional area of the concrete with t being the thickness of the joint and l is the the total length of the considered joint.

Hansen and Olesen (1976) investigated the behaviour of keyed joints with different reinforcement layouts, and some of the specimens features a considerable distance between the U-bar loops, i.e. a large value of u, see Figure 4.24 and 4.26. Hansen and Olesen reported that the specimens with a large value of u gave a lower shear capacity and that the joints were completely destroyed upon failure. As shown in Section 4.3.3, the detailed model in captured this behaviour to a satisfactory degree.

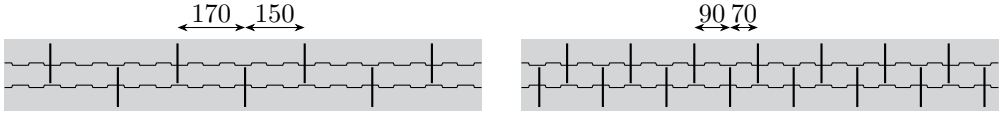

(a) Specimen 24 (b) Specimen 26

Figure 4.29*: The two specimens with a considerable distance between the U-bars tested by Hansen and Olesen (Hansen and Olesen, 1976), measurements in millimetres.*

The geometry of the specimens are given in Table 4.5. Figure 4.29 shows the two specimens which featured large values of u, while the U-bar loops were placed with a distance of 10 mm for the remaining specimens by Hansen and Olesen. For specimen 24 and 26, the shear capacity is illustrated as a function of the reinforcement degree in Figure 4.30 together with experimental results and the results of the detailed model. Figure 4.31 and Table 4.10 and 4.11 shows the results for all specimens.

Figure 4.30 shows that a single joint element using the submodel yield criterion can capture the same behaviour as the detailed model. The first, non-linear part of the curve is governed by the interface elements, which can represent the behaviour of the keyed interface with a reasonably accuracy by fitting the cohesion and friction coefficient of the interface element to the detailed model.

The submodel criterion governs the horizontal limit for the capacity. It is observed that the submodel provides an excellent estimate of the plateau, i.e. the upper limit for the shear capacity. The submodel criterion overestimates the capacity of specimen 24 slightly for lower reinforcement ratios, however,

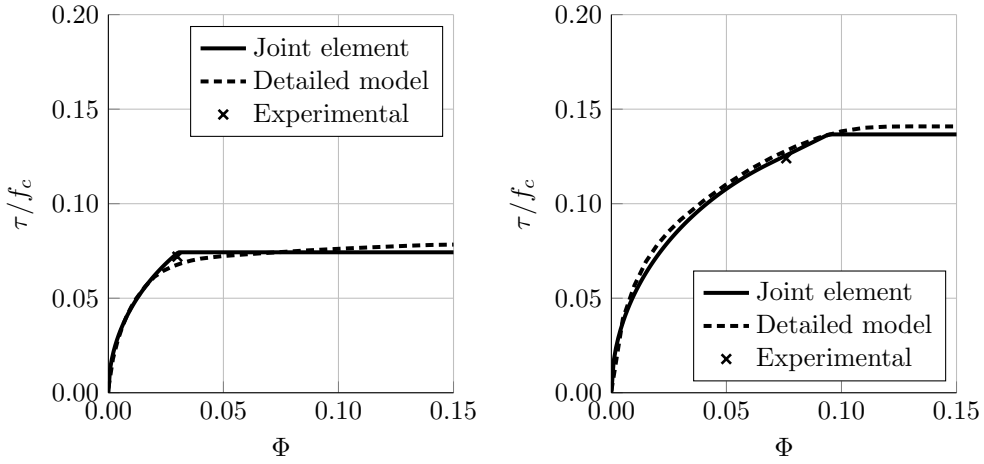

(a) Specimen 24 (b) Specimen 26

***Figure 4.30**: Results obtained by a single joint element with the submodel yield criterion compared to the results of the detailed model using several thousand elements. Experimental results for specimens 24 (a) and 26 (b) by Hansen and Olesen (1976).*

the capacity of the detailed model increase as with the reinforcement ratio and surpass the capacity of the submodel criterion.

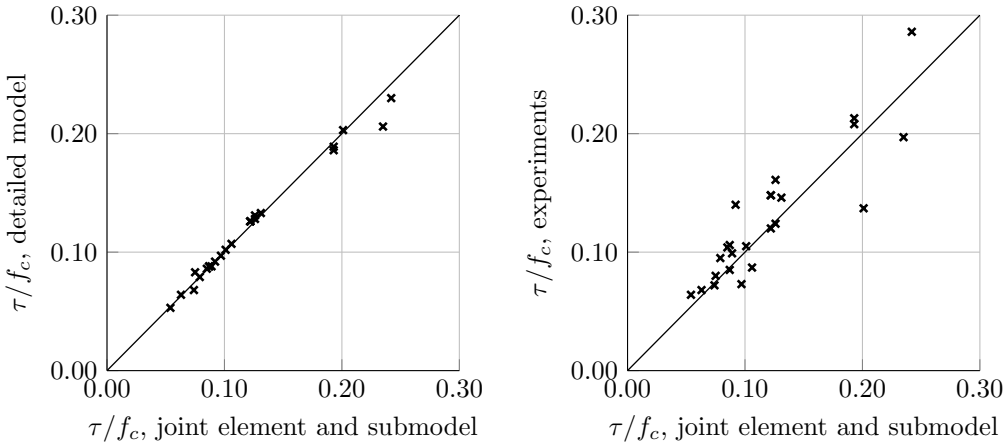

(a) (b)

***Figure 4.31**: Comparison of the results obtained using a single joint element with the submodel yield criterion with (a) the detailed numerical model and (b) experimental results (Hansen and Olesen, 1976; Fauchart and Cortini, 1972).*

***Table 4.10**: Data and results of experiments by Hansen and Olesen (1976), the detailed numerical model, and the presented joint element with the submodel yield criterion.*

Specimen	f_c [MPa]	Φ [-]	u mm	**Experimental** τ/f_c	**Detailed** τ/f_c	**Joint element** τ/f_c
01	29	0.013	-	0.064	0.053	0.054
02	32	0.030	-	0.095	0.079	0.079
03	32	0.055	-	0.105	0.102	0.101
04	16	0.061	-	0.087	0.107	0.106
05	53	0.018	-	0.068	0.064	0.063
12	25	0.043	-	0.140	0.092	0.092
13	23	0.095	-	0.146	0.133	0.131
14	25	0.039	-	0.099	0.088	0.089
18	27	0.049	-	0.073	0.097	0.097
29	17	0.188	-	0.137	0.203	0.201
23	31	0.025	10	0.080	0.083	0.075
24	26	0.030	150	0.072	0.068	0.074
25	24	0.076	10	0.161	0.131	0.126
26	24	0.076	70	0.124	0.128	0.126
27	15	0.139	10	0.213	0.189	0.193
28	13	0.235	10	0.286	0.230	0.242

***Table 4.11**: Data and results of experiments by Fauchart and Cortini (1972), the detailed numerical model, and presented joint element with the submodel yield criterion.*

Specimen	f_c [MPa]	Φ [-]	$2\,u$ mm	**Experimental** τ/f_c	**Detailed** τ/f_c	**Joint element** τ/f_c
5	20	0.049	10	0.106	0.088	0.087
6	20	0.049	10	0.085	0.088	0.087
7	20	0.096	10	0.120	0.126	0.112
8	20	0.246	10	0.197	0.206	0.235
9	20	0.047	10	0.104	0.086	0.085
10	20	0.096	10	0.148	0.126	0.122
11	20	0.096	10	0.148	0.126	0.122
12	20	0.191	10	0.208	0.186	0.193

Figure 4.31(a) shows an excellent agreement between the results of the joint element and the detailed model. The joint element overestimates the capacity for a few cases compared to the detailed model, namely for specimens with high reinforcement ratios, see Table 4.10 and 4.11. The choice of

supports for the joint element might be the reason for this. Figure 4.31(b) shows that the single joint element with the submodel yield criterion predicts a satisfactory estimate of the shear capacity compared to the experimental results.

Computational effort

The multiscale joint element comprising the macro finite element and submodel criterion has shown to be able to capture the behaviour of keyed joints with various reinforcement layouts to a satisfactory degree, and compared to the detailed model it provides excellent results. The multiscale joint element leads to a considerably smaller optimisation problem which can be solved in a fraction of a second compared to the detailed model, which required either 37.10 seconds or 94.14 seconds on average depending on the specimen analysed by detailed model, see Table 4.8.

***Table 4.12**: Number of equilibrium elements, problem size, and computational time for a single joint element and the detailed model.*

	Joint element	Detailed model
Equilibrium elements	3	20,024
Variables	302	1,364,509
Linear constraints	388	1,305,890
Conic constraints	44	134,472
Computational time	0.022 s	94.14 s

The computational times shown for the joint element in Table 4.12 is the average of 10 runs. From Table 4.12, it is evident that the proposed joint element is superior for practical modelling and analysis of entire precast concrete structures.

4.4.4 Summary

For practical design and analysis of precast concrete structures within the framework of limit analysis, an adequate equilibrium element representing the in-situ cast joints is needed. The formulation of a multiscale joint element is given. The multiscale element comprises a macro finite element and a submodel yield criterion, which functions on the stress level and makes it possible to account for various local effects within the joint itself. The submodel criterion represents a simple mechanical model based on the stringer method, and the material yield criteria are then applied on the resulting

stress state of this mechanical model. The submodel yield criterion was formulated using second-order conic constraints, hence, the multiscale element fits the format of second-order cone programming, see Section 2.3.

The multiscale joint element is validated by comparison to the detailed numerical model presented in Section 4.3 and experimental results by Hansen and Olesen (1976) and Fauchart and Cortini (1972). Satisfactory agreement was found between the multiscale joint element and the experimental results, and excellent agreement was found between the joint element and the detailed model. The fact that the joint element only poses a rather small mathematical optimisation problem compared to the detailed model makes it more relevant for practical applications. It can be concluded that the developed multiscale joint element makes it possible to assess the capacity of real size precast concrete structures while accounting for the local behaviour of the in-situ cast joints. This will be demonstrated in Chapter 5.

4.5 Joints in three dimensions

Many types of in-situ cast joints typically used in precast concrete structures transfer shear stress from one plane to another, see Figure 4.32. As discussed in Section 4.2, several papers on the behaviour of shear joints were published in the 1970s and 80s (see e.g. Fauchart and Cortini, 1972; Hansen and Olesen, 1976), however, no experimental studies on the behaviour of joints in three-dimensions have been published. The simplified, empirical expression of the Eurocode 2 (European Committee for Standardization, 2008) only considers the capacity of the interface. The actual stress field within the joint is not considered.

Both joints shown in Figure 4.32 are commonly used in precast concrete structures, and they both experience triaxial stress since they transfer shear from one plane to another. Many types of joints feature loop reinforcement and for design and analysis, it is assumed that the U-bar loops are placed closely together, however, this is not always the case as discussed, and the capacity of the joint is reduced as a consequence. The joint model presented in this section and in Paper IV (Herfelt et al., 2017b) will account for this behaviour similar to the two-dimensional joint model, namely by use of a mechanical submodel.

The multiscale joint element comprises a macro joint element and a submodel yield criterion, see Figure 4.33. The macro joint element is a lower bound element, hence, traction continuity is required between the joint element and adjacent 3D plane stress elements. The stresses on the element level are transferred to the submodel level, where a mechanical model is used

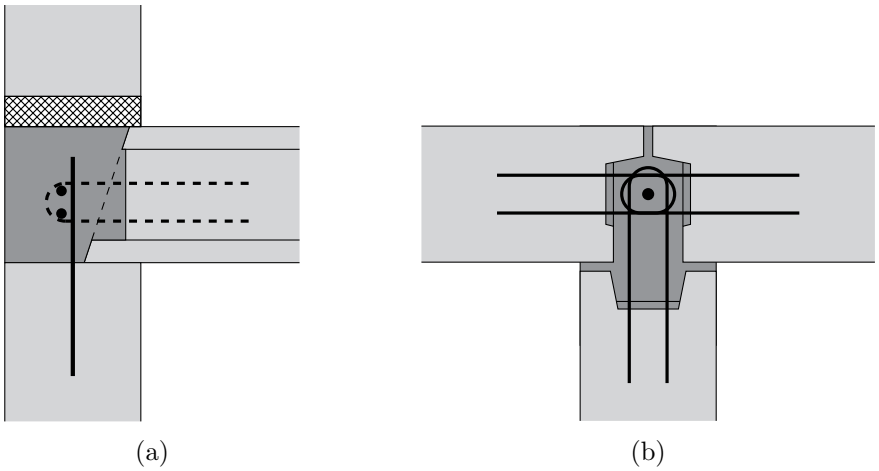

***Figure 4.32**: a) Vertical section of slab-to-panel joint reinforced with U-bar loops and embedded rebars. b) Horizontal section of panel-to-panel T-joint reinforced with U-bar loops extruding from all three panels.*

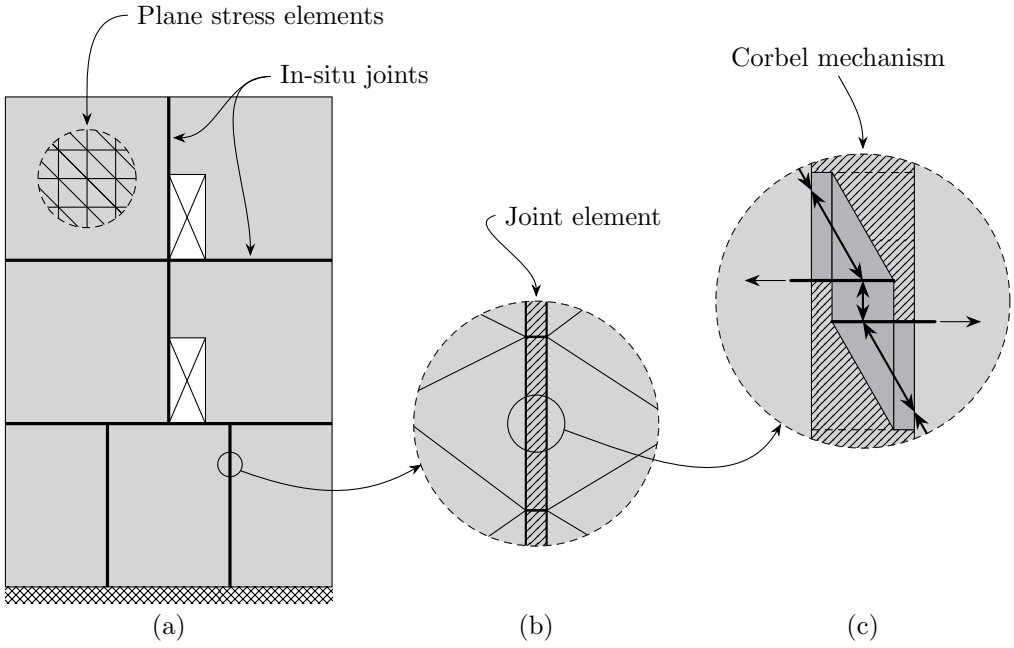

***Figure 4.33**: The general concept of the 3D joint model shown visualised two dimensions: a) Precast concrete structure on the structural level, b) Joint element and plane stress elements on the element level, c) corbel mechanisms and load path on the submodel level.*

to determine the local stress field within the joint.

4.5.1 Lower bound macro element

First, a lower bound macro joint element is introduced. The mathematical optimisation problem on the structural level can be stated as the general lower bound formulation (3.11). The yield criterion of the element is in this case a submodel criterion, which is formulated for semidefinite programming due to the triaxial stress state in the core of the joint. On the element level, the equilibrium equations and yield criterion can be stated as follows:

$$\begin{aligned}
&\mathbf{B}_{el}^T \boldsymbol{\sigma}_{el} = \boldsymbol{q}_{el} \\
&\mathbf{C}_{\sigma}^{el,i} \boldsymbol{\sigma}_{el} + \mathbf{C}_{\alpha}^{el,i} \boldsymbol{\alpha}_i + \mathbf{C}_{\gamma}^{el,i} \boldsymbol{\gamma}_i = \boldsymbol{C}_0^{el,i}, \quad i = 1,2 \\
&\mathbf{E}_{\sigma}^{el,i} \boldsymbol{\sigma}_{el} + \mathbf{E}_{\alpha}^{el,i} \boldsymbol{\alpha}_i + \mathbf{E}_{\gamma}^{el,i} \boldsymbol{\gamma}_i \leq \boldsymbol{E}_0^{el,i}, \quad i = 1,2 \\
&\mathbf{F}_{\alpha}^{el,j} \boldsymbol{\alpha}_j + \mathbf{F}_0^{el,j} \succeq 0, \quad j = 1,2,\ldots,m_{el} \\
&\boldsymbol{\gamma}_l \in \mathcal{Q}_{k_l}, \quad l = 1,2,\ldots,q_{el}
\end{aligned} \tag{4.46}$$

The element equilibrium matrix $\mathbf{B}_{el}^T$ ensures equilibrium of the element. The element is designed to be compatible with the generalised plane stress element presented in Section 4.1.3 and a linear varying stress field is therefore assumed. Moreover, the normal stresses in the longitudinal direction of the joint is not considered, hence, to ensure a lower bound, it is sufficient to enforce the submodel yield criterion in the two ends of the macro element.

The matrices $\mathbf{C}_{\sigma}^{el,i}$, $\mathbf{C}_{\alpha}^{el,i}$, and $\mathbf{C}_{\gamma}^{el,i}$ define the equality constraints of the two submodels, while $\mathbf{E}_{\sigma}^{el,i}$, $\mathbf{E}_{\alpha}^{el,i}$, and $\mathbf{E}_{\gamma}^{el,i}$ define the inequality constraints. The variables $\boldsymbol{\alpha}$ and $\boldsymbol{\gamma}$ are associated with the yield function, whereas $\boldsymbol{\gamma}$ is used to define the second-order constraints, and $\boldsymbol{\alpha}$ is used to define the linear matrix inequalities together with the symmetric matrices $\mathbf{F}_{\alpha}^{el,j}$ and $\mathbf{F}_0^{el,j}$. The scalar m_{el} is the number of linear matrix inequalities for the submodels while q_{el} is the number of second-order constraints. The matrices will only be given implicitly in the following.

The submodel criterion assumes that the adjacent plane stress elements are oriented in right angles. Despite this assumption, the present model will cover the vast majority of joints in precast structures, e.g. the two joints shown in Figure 4.32. The formulation of the macro finite element, however, is general and does not assume any specific orientation and is applicable to any configuration and any number of adjacent plane stress elements.

The macro element comprises a number of strips, one for each adjacent plane stress element, see Figure 4.34. As mentioned, for the macro element to be compatible with the 3D plane stress element, linear stress field are required

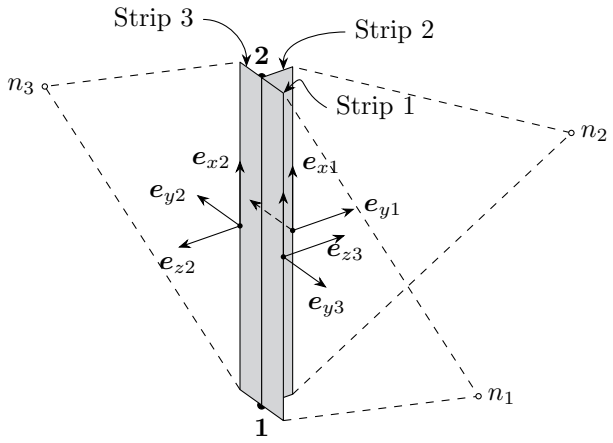

***Figure 4.34**: Sketch of a joint element with three adjacent plane stress elements: Local coordinate systems for the three joint strips are shown.*

for the strips, which are assumed to be in plane stress. The stress field in a strip is given in local coordinates and comprise two unique components, namely σ_y and τ_{xy}. The element stress vector is given as

$$\boldsymbol{\sigma}_{el} = \begin{bmatrix} \boldsymbol{\sigma}_1 \\ \vdots \\ \boldsymbol{\sigma}_N \end{bmatrix} \tag{4.47}$$

where N is the number of strips and $\boldsymbol{\sigma}_i$ denotes the stress vector of the ith strip,

$$\boldsymbol{\sigma}_i = \begin{bmatrix} \boldsymbol{\sigma}_{i1} \\ \boldsymbol{\sigma}_{i2} \end{bmatrix} = \begin{bmatrix} \sigma_{y1} \\ \tau_{xy1} \\ \sigma_{y2} \\ \tau_{xy2} \end{bmatrix} \tag{4.48}$$

The strips balance the tractions of the adjacent elements as well as internally within the element. Figure 4.34 shows local coordinate systems for each strip, which is defined based on the plane of the adjacent triangular element. The local x-axis is in the longitudinal direction of the joint going from node 1 to node 2, while the local y-axis lies in the plane of the adjacent triangular element. The basis of the local coordinate system of strip i can be defined based on the vectors $\boldsymbol{v}_{12}$, going from node 1 to 2, and $\boldsymbol{v}_{1n_i}$, going from node 1 to the third node of the adjacent element, see Figure 4.34:

$$\boldsymbol{e}_{xi} = \frac{\boldsymbol{v}_{12}}{\|\boldsymbol{v}_{12}\|_2}, \quad \boldsymbol{e}_{zi} = \frac{\boldsymbol{v}_{12} \times \boldsymbol{v}_{1n_i}}{\|\boldsymbol{v}_{12} \times \boldsymbol{v}_{1n_i}\|_2}, \quad \boldsymbol{e}_{yi} = \boldsymbol{e}_{zi} \times \boldsymbol{e}_{xi} \tag{4.49}$$

The transformation matrix for strip i can then be stated as $\mathbf{E}_i = \begin{bmatrix} \boldsymbol{e}_{xi} & \boldsymbol{e}_{yi} & \boldsymbol{e}_{zi} \end{bmatrix}$. The traction continuity is enforced in global coordinates, and the contributions for strip i at node j can be stated as:

$$\boldsymbol{q}_{ij} = \mathbf{E}_i \begin{bmatrix} 0 & t_i l \\ t_i l & 0 \\ 0 & 0 \end{bmatrix} \begin{bmatrix} \sigma_{yj} \\ \tau_{xyj} \end{bmatrix} = \tilde{\mathbf{P}}_i^T \boldsymbol{\sigma}_{ij}, \quad j = 1, 2 \tag{4.50}$$

where $\boldsymbol{q}_{ij}$ is the generalised nodal forces, l is the length of the macro element, and t_i is the thickness of strip i. Equation (4.50) also defines $\tilde{\mathbf{P}}_i^T$ implicitly. Traction continuity is enforced in both ends of the element due to the linear stress field.

Traction continuity between the N strips of the macro element is also required. This is likewise enforced in both ends of the element:

$$-\tilde{\mathbf{P}}_1^T \boldsymbol{\sigma}_{1j} - \cdots - \tilde{\mathbf{P}}_N^T \boldsymbol{\sigma}_{Nj} = 0, \quad j = 1, 2 \tag{4.51}$$

where j is the node number. Equilibrium on the element level for a macro joint element with N adjacent plane stress element can be stated as:

$$\boldsymbol{q}_{el} = \begin{bmatrix} \tilde{\mathbf{P}}_1^T & & & & & \\ & \tilde{\mathbf{P}}_1^T & & & & \\ & & \ddots & & & \\ & & & \ddots & & \\ & & & & \tilde{\mathbf{P}}_N^T & \\ & & & & & \tilde{\mathbf{P}}_N^T \\ -\tilde{\mathbf{P}}_1^T & & \cdots & \cdots & -\tilde{\mathbf{P}}_N^T & \\ & -\tilde{\mathbf{P}}_1^T & \cdots & \cdots & & -\tilde{\mathbf{P}}_N^T \end{bmatrix} \begin{bmatrix} \boldsymbol{\sigma}_1 \\ \vdots \\ \boldsymbol{\sigma}_N \end{bmatrix} = \mathbf{B}_{el}^T \boldsymbol{\sigma}_{el} \tag{4.52}$$

where $\mathbf{B}_{el}^T$ is the element equilibrium matrix, see also (4.46). The size of the element equilibrium matrix depends on the number of adjacent plane stress elements, N.

4.5.2 Submodel for 3D behaviour

Identically to the two-dimensional case, a unit section of the joint is considered. The unit section has the shape of a rectangular box and is reinforced with U-bar loops from up to four faces. The placement of the U-bars are defined by u, u_{y1}, and u_{z1} according to Figure 4.35. The geometry of the unit joint section is given by the length, s, the widths, t_y and t_z. The overlap of the U-bars is given by o_y and o_z.

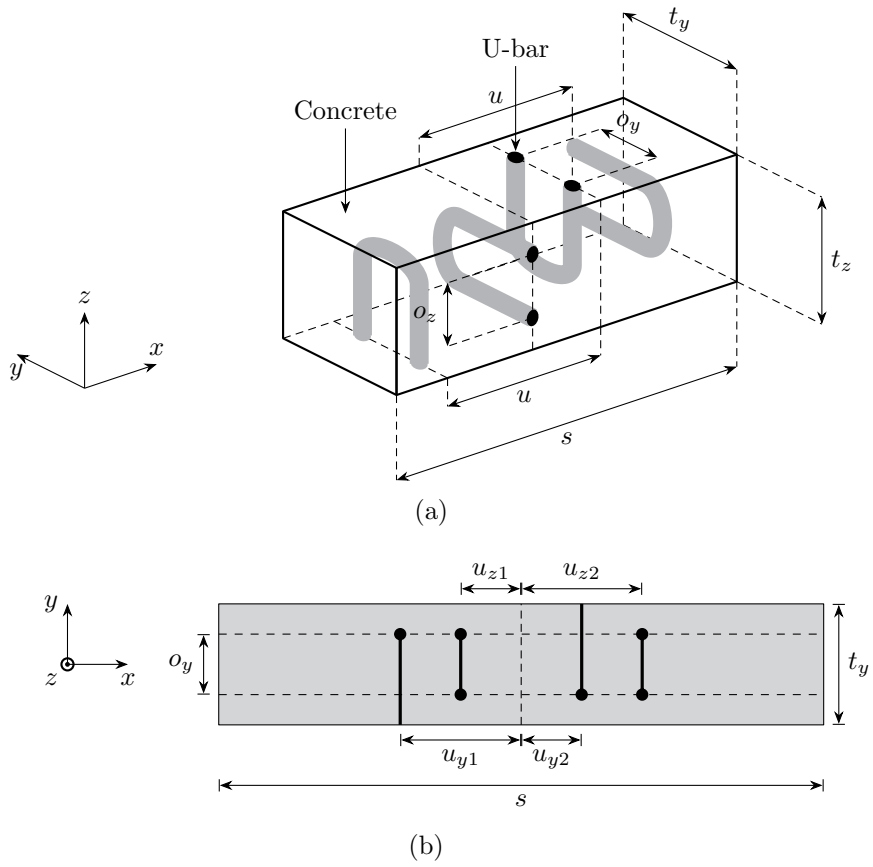

***Figure 4.35**: Unit joint section forming the basis of the submodel yield criterion: a) three-dimensional representation of the geometry including U-bar loops, b) two-dimensional sketch of the U-bar placement.*

As indicated in Figure 4.35, the distances between the U-bars in the y and the z-directions, respectively, are assumed to be identical, i.e. $u = u_{y1} + u_{y2}$ and $u = u_{z1} + u_{z2}$. This greatly reduce the number of possible combinations of stress fields for the submodel.

In practice, joints are always reinforced in the longitudinal direction with a so-called locking bar. The present model, however, does not consider the behaviour in the longitudinal direction and the locking bar will therefore not affect the model. The stresses of the strips are given in local coordinates, thus, a common coordinate system is needed. The coordinate system of strip number 1 is chosen, and the stresses of the remaining strips are transformed accordingly:

$$\hat{\mathbf{S}}_{ij} = \mathbf{E}_1^T \mathbf{E}_i \mathbf{S}_{ij} \mathbf{E}_i^T \mathbf{E}_1 \tag{4.53}$$

where $\mathbf{E}_i$ is the transformation matrix of strip i, and $\mathbf{S}_{ij}$ is the stress tensor

of strip i at node j. For example, for strip 1 at node 2 - which is always chosen for the common coordinate system - we have

$$\mathbf{S}_{12} = \begin{bmatrix} 0 & \tau_{xy12} & 0 \\ \tau_{xy12} & \sigma_{y12} & 0 \\ 0 & 0 & 0 \end{bmatrix}$$

Most of the components in $\mathbf{S}_{ij}$ will only contain two stress components, σ_y and τ_{xy} or σ_z and τ_{zx} depending on the orientation of the considered strip. The shear stress component of $\hat{\boldsymbol{S}}$ will be used for the corbel presented in the following, while the normal stress component of $\hat{\boldsymbol{S}}$ is assumed to be transferred directly through the joint and is simply added to the final stress filed of the submodel.

Corbel mechanisms for local shear transfer

The purpose of the submodel is to transfer shear from one plane to another, e.g. from τ_{xy} to τ_{zx}. A model based on concrete corbels is proposed. The corbels utilises the U-bar loops to transform a shear stress (from $\hat{\boldsymbol{S}}$, see Equation 4.53) acting on the face of the unit section to a normal stress in the core of the joint.

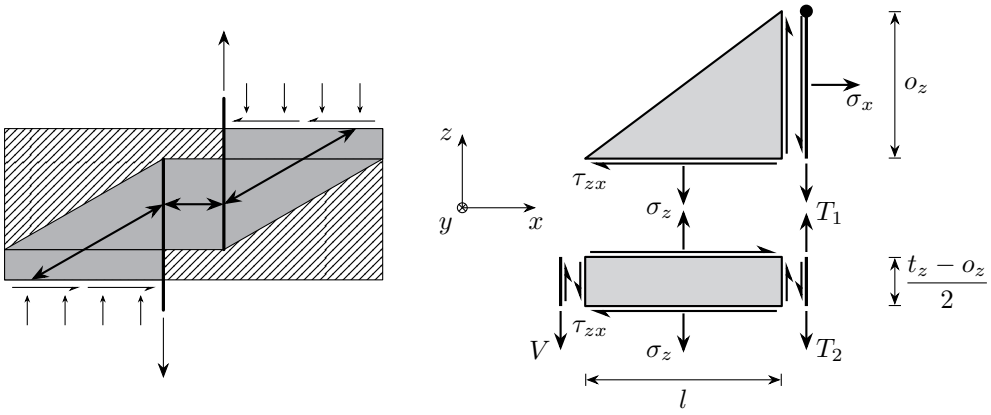

***Figure 4.36**: a) Sketch of two corbel mechanisms working in two-dimensions. b) Two-dimensional visualisation of a corbel model in the xz-plane transforming a shear stress τ_{zx} to a normal stress σ_x. Positive directions of forces and stresses are shown. The panels indicated by gray has a out-of-plane thickness of o_y.*

The corbel model illustrated in Figure 4.36 comprises a rectangular shear panel and a triangle in uniaxial stress. Two stringers are shown in the figure,

whereas the rightmost represent the transverse reinforcement, i.e. the U-bar loops, and leftmost is a compression stringer without any reinforcement. The tensile force in the reinforcement T balances the stress σ_z as well as V. For a single corbel, see Fig. 4.36(b), we have the following variables:

$$\boldsymbol{\alpha}_i = \left[\sigma_x^{(i)},\ \ \sigma_z^{(i)},\ \ \tau_{zx}^{(i)},\ \ T_1^{(i)},\ \ T_2^{(i)},\ \ V^{(i)}\right]^T \tag{4.54}$$

or

$$\boldsymbol{\alpha}_i = \left[\sigma_x^{(i)},\ \ \sigma_y^{(i)},\ \ \tau_{xy}^{(i)},\ \ T_1^{(i)},\ \ T_2^{(i)},\ \ V^{(i)}\right]^T \tag{4.55}$$

depending on the orientation of the corbel. From the corbel model, a system of linear equations can be derived which ensures equilibrium for the considered corbel:

$$\begin{bmatrix} o_z o_y & 0 & -lo_y & 0 & 0 & 0 \\ 0 & -lo_y & 0 & 0 & -1 & -1 \\ 0 & -lo_y & o_z o_y & 0 & 0 & 0 \\ 0 & 0 & -\dfrac{t_z - o_z}{2} o_y & 0 & 0 & -1 \\ 0 & 0 & -\dfrac{t_z - o_z}{2} o_y & 1 & -1 & 0 \\ 0 & 0 & -o_z o_y & -1 & 0 & 0 \end{bmatrix} \begin{bmatrix} \sigma_x \\ \sigma_z \\ \tau \\ T_1 \\ T_2 \\ V \end{bmatrix} = \mathbf{0} \tag{4.56}$$

The first three equations of (4.56) ensure vertical, horizontal, and moment equilibrium of the corbel model, while the last three equations ensure equilibrium for the stringers. The stresses σ_x and σ_z will practically always be negative.

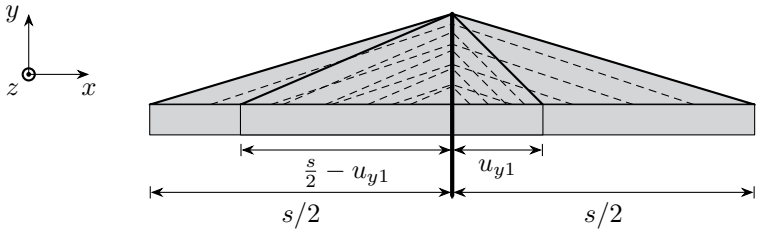

***Figure 4.37**: Four corbel models surrounding a single U-bar: The length is fixed at $s/2$ for the two largest, while the length of the two smallest depends on the position of the U-bar in the unit joint section. Dashed lines indicate the load path through the triangular corbels. Some of the corbels overlap and their stress fields are added to obtain the actual stress state.*

The corbels have a predefined length l, see Figure 4.36. The optimal value of l depends on the reinforcement and loading, and to ensure a reasonable model four corbels are used for each of the four boundaries, hence, the complete submodel may use up to 16 corbels. This is illustrated in Figure 4.37 which shows four corbels and a single U-bar. The corbels shown in the figure overlap to some degree. Moreover, corbels associated with the other U-bars in the submodel overlap these as well, hence, to obtain the actual stress state of the submodel, the stress states of the appropriate corbels are added.

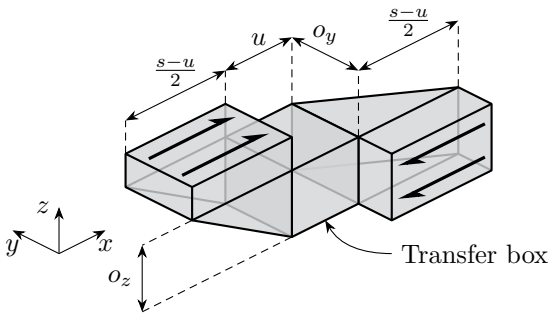

***Figure 4.38**: Shear transfer from one plane to another via two corbels. The central transfer box will experience uniaxial compression in the x-direction.*

Several corbels are needed to transfer shear stress from one plane to another, since each corbel only can transfer a shear stress to a normal stress in the centre of the joint. Combining several corbels enables the desired transfer of shear stresses and the process is illustrated schematically in Figure 4.38.

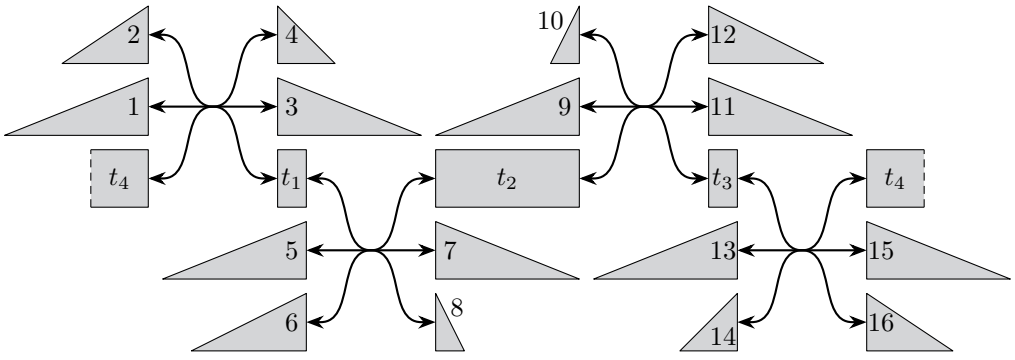

***Figure 4.39**: Interaction of the 16 corbels and four transfer boxes illustrated schematically: The triangles represent a corbel mechanism, while the rectangles represent the transfer boxes. Each set of arrows represent an equilibrium equation. The size and locations of corbels are not to scale.*

Figure 4.39 illustrates the transfer of normal stresses σ_x in the centre

of the joint. Each set of arrows represents an equilibrium equation and is located at the position of an U-bar loop. The four equilibrium equations are given as

$$\begin{aligned}
&\sigma_x^{(1)} + \sigma_x^{(2)} - \sigma_x^{(3)} - \sigma_x^{(4)} + \sigma_x^{t4} - \sigma_x^{t1} = 0,\\
&\sigma_x^{(5)} + \sigma_x^{(6)} - \sigma_x^{(7)} - \sigma_x^{(8)} + \sigma_x^{t1} - \sigma_x^{t2} = 0,\\
&\sigma_x^{(9)} + \sigma_x^{(10)} - \sigma_x^{(11)} - \sigma_x^{(12)} + \sigma_x^{t2} - \sigma_x^{t3} = 0,\\
&\sigma_x^{(13)} + \sigma_x^{(14)} - \sigma_x^{(15)} - \sigma_x^{(16)} + \sigma_x^{t3} - \sigma_x^{t4} = 0,
\end{aligned} \tag{4.57}$$

where $\sigma_x^{(i)}$ is the stress in the x-direction associated with the ith corbel, see Figure 4.36. The first four corbels are associated with the first U-bar loop, the next four with the second U-bar loop and so on, see Figure 4.39 for the numbering, and σ_x^{tj} is the normal stress of the jth transfer box. Two corbels associated with the same U-bar loop, e.g. the two corbels on the left-hand side in Figure 4.37, can work together, each transferring a fraction of the total shear force on the particular face of the submodel.

The stress fields of the up to 16 corbels are combined to obtain the actual stress field in the unit joint section. As mentioned, the corbels overlap to some degree, and - depending on the values of u, u_{y1} and u_{z1} - up to ten triaxial stress states might be present within the core of the joint. The shear stress τ_{yz} will always be zero in the local coordinate system of the particular strip and also in the coordinate system of strip 1. The triaxial stress states inside the joint can therefore be described by three normal stresses and two shear stresses.

The triaxial stress states in the centre of the unit joint section must satisfy the Mohr-Coulomb criterion presented in Section 3.3. As discussed, semidefinite programming is required to represent the general Mohr-Coulomb criterion for triaxial stress. The rectangular panels shown in Figure 4.36 will experience plane stress and must satisfy the Mohr-Coulomb criterion for plane stress, which can be formulated exactly using second-order constraints, see Section 3.3 for the formulation.

The U-bar loops are loaded in tension, and the tensile force must be lower than or equal to the yield strength. Moreover, the compressive strength of the reinforcement is neglected, hence, the yield condition is given as

$$0 \leq T_i \leq f_y A_{su} \tag{4.58}$$

where A_{su} is the cross sectional area of the U-bar and f_y is the yield strength.

The compressive stringer shown in Figure 4.36 must be in compression, i.e. V must be non-negative:

$$V \leq 0$$

The macro element and submodel yield criterion are implemented in Matlab with the commercial solver MOSEK (see MOSEK ApS, 2015).

4.5.3 Analysis and parameter study

Behaviour in two-dimensions

The three-dimensional multiscale joint element is compared to the two-dimensional joint element presented in Section 4.4. The 3D submodel is designed for the shear transfer in three-dimensions, but the corbel models are capable of handling the two-dimensional case as well. It is, however, expected that the three-dimensional submodel underestimates the capacity. The following parameters are used for the comparison:

$$f_c = 30 \text{ MPa}, \ f_t = 0, \ t_y = t_z = 200 \text{ mm}, \ o_y = o_z = 50 \text{ mm}$$

A single element for each of the two joint models is used for the comparison, while no interface elements are used. The value of u, i.e. the distance between the U-bar pairs, and the reinforcement degree Φ are varied. We define the reinforcement degree as

$$\Phi = \frac{A_{su} f_y}{s t f_c}$$

where A_{su} is the cross sectional area of a single U-bar. The normalised capacities are illustrated in Figure 4.40 and 4.41 for two different values of s, namely 200 and 400 mm.

Figure 4.40 shows that the three-dimensional joint element predicts a lower capacity than the two-dimensional element. Moreover, the corbels mean that the capacity varies linearly with the reinforcement degree until the compressive concrete stress reach the compressive strength, f_c. The slope of the first, linear part of the capacity curve increases when s increases from 200 to 400 mm.

For the 2D joint element, it is observed that $u/s = 0.90$ gives a higher capacity than $u/s = 0.5$ for all reinforcement degrees. This makes sense, physically, since the U-bars are closer together for $u/s = 0.90$ than for $u/s = 0.50$. The corbel mechanisms, however, do not capture this, and $u/s = 0.50$ gives a slightly higher capacity than $u/s = 0.90$. It is observed that the curves for $u/s = 0.50$ for the two submodels are nearly identical for $s = 400$, which indicates that the corbel mechanism becomes favourable for $u/s \approx 0.50$ in combination with larger values of s, even for the two-dimensional case.

Figure 4.41 shows the same tendencies as Figure 4.40: The three-dimensional element generally predicts a lower capacity for most values of u. Figure

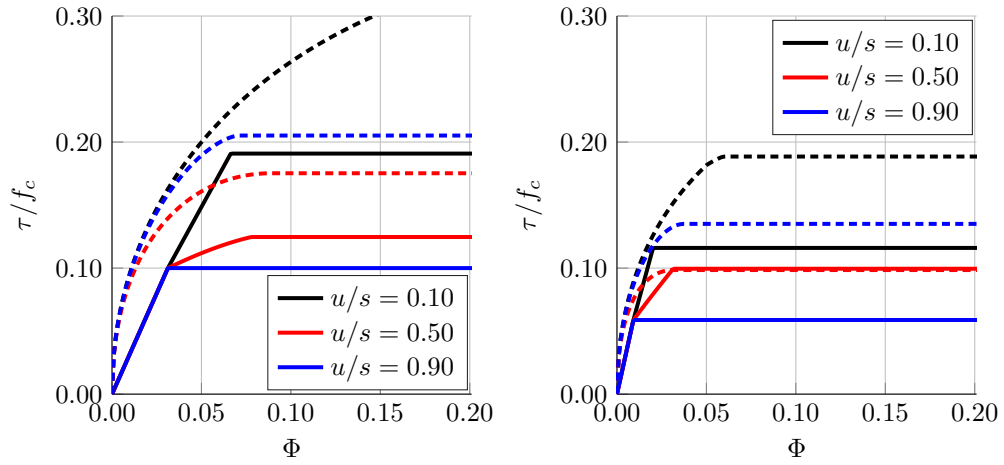

(a) $s = 200$ mm (b) $s = 400$ mm

***Figure 4.40**: Shear capacity for the two submodels as a function of the reinforcement ratio. The solid lines indicate the three-dimensional joint element, while dashed lines indicate the two-dimensional one.*

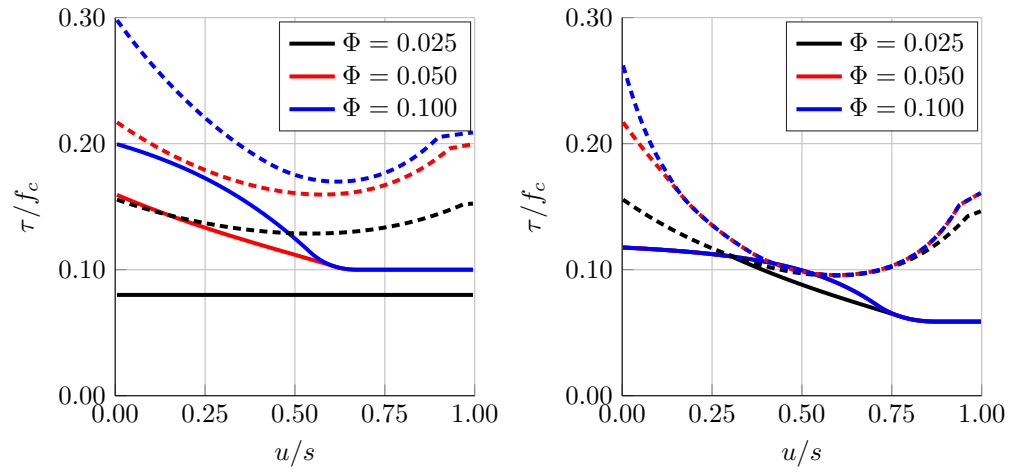

(a) $s = 200$ mm (b) $s = 400$ mm

***Figure 4.41**: Shear capacity for the two submodels as a function of u. The solid lines indicate the three-dimensional joint element, while dashed lines indicate the two-dimensional one.*

4.41(b) clearly visualise that the corbel mechanisms become favoured for larger values of s with $u/s \approx 0.50$.

As shown in Figure 4.41, the three-dimensional element severely underestimates the shear capacity for joins with close to optimal reinforcement layout, i.e. $u/s \approx 0$ and $u/s \approx 1$, especially for larger reinforcement ratios. It can be concluded that the developed three-dimensional multiscale element predicts a safe estimate of the capacity and the model is mostly applicable to joints with severely suboptimal reinforcement layouts.

Corner joint subject to shear

The three-dimensional macro element and submodel are designed to model the transfer of shear stresses from one plane to another. A corner joint subjected to pure shear is analysed using the multiscale element. Unfortunately, no experimental results for three-dimensional U-bar joints have been published to the best knowledge of the author. The results are therefore compared to the design formula of the Eurocode 2, which only considers a criterion for the interface and a simple upper bound on the shear stress, but nevertheless is the basis of practical design of joints in three dimensions currently.

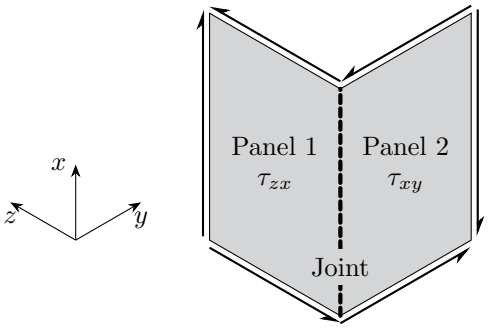

***Figure 4.42**: Corner joint connecting two reinforced concrete panels subject to pure shear analysed using a single joint element.*

Figure 4.42 shows a in-situ cast corner joint connecting two precast panels subjected to pure shear. According to the Eurocode 2, see also Section 1.1.1, the shear capacity can be evaluated as

$$\tau = c f_t \frac{A_{key}}{A_c} + \mu \rho f_y \leq \frac{1}{2} \nu f_c \frac{A_{key}}{A_c} \tag{4.59}$$

where A_{key} and A_c are the area of the keys and the total area, respectively. A keyed interface is assumed, hence, $c = 0.5$ and $\mu = 0.9$ can be used. ρ is

defined as

$$\rho = \frac{\sum A_{su}}{A_c}$$

An effectiveness factor of $\nu = 0.7 - f_c/200$ (f_c in MPa) is used for the comparison as well as the following parameters:

$$f_t = 0 \text{ MPa}, \; t_z = t_y = 50 \text{ mm}, \; o_z = o_y = 40 \text{ mm}$$

For the Eurocode formula (4.59), $f_t = 0.21 f_c^{2/3}$ and $A_{key}/A_c = 0.5$ are used. The multiscale joint element is analysed using varying values of u with $u/2 = u_{y1} = u_{z1}$, see Figure 4.35. Three U-bar loops commonly used in practice is used for the analysis.

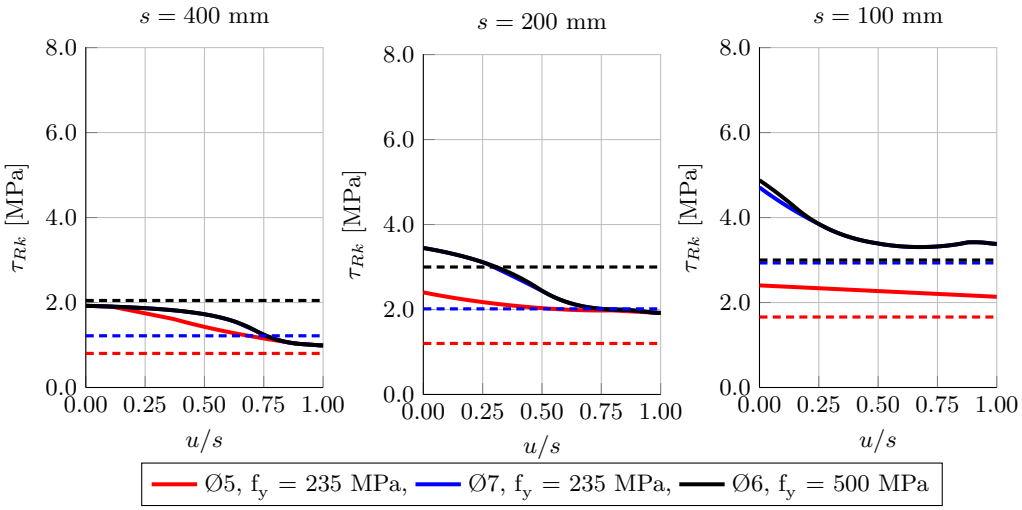

***Figure 4.43**: Characteristic shear capacity of the corner joint with f_c = 20 MPa and different values of s: The results of the multiscale joint element are represented using solid lines, while the capacity predicted using the Eurocode 2 is shown with dashed lines.*

The shear capacity of the corner joint is illustrated in Figure 4.43 and 4.44. Similar to the two-dimensional case, considerable variations in the capacity is seen for varying values of u. The figures also show that the concrete strength affects the heavily reinforced joints, which is to be expected.

The shear capacity estimated with the Eurocode 2 design formula is surprisingly similar to the joint element despite the fact that no consideration to the actual stress state of the joint is given. For low values s, the Eurocode might underestimate the capacity significantly, while it might overestimate it for larger values of s depending on u. Based on the two-dimensional case

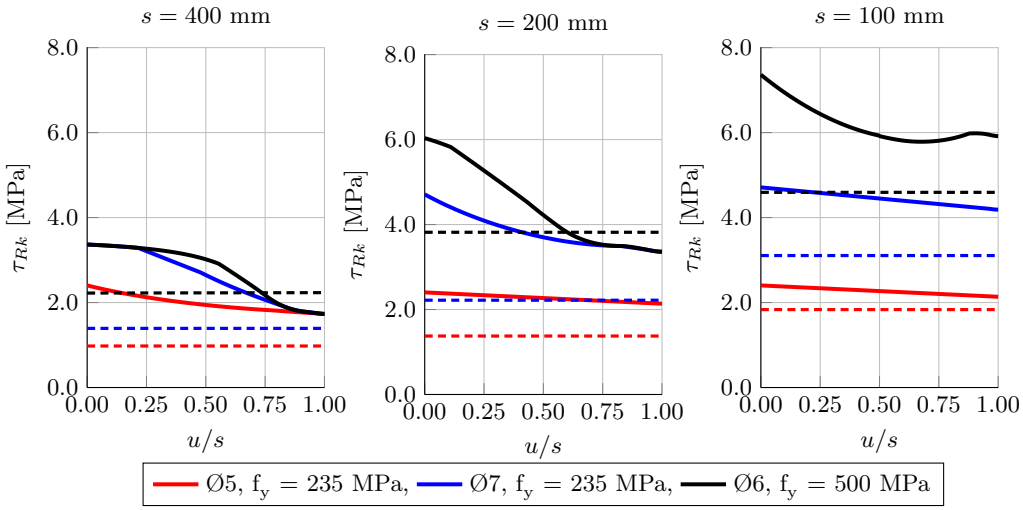

***Figure 4.44**: Characteristic shear capacity of the corner joint with f_c = 35 MPa and different values of s: The results of the multiscale joint element are represented using solid lines, while the capacity predicted using the Eurocode 2 is shown with dashed lines.*

it was concluded that the accuracy of the three-dimensional joint model was highest for large values s, hence, it is somewhat worrisome that the Eurocode overestimates the capacity for larger values of s. In any case, based on the analysis of the corner joint it can be concluded that it is necessary to consider the actual mechanisms and stress field within the joint for design.

Chapter 5

Applications

5.1 Introduction

The structural design of buildings has to meet several different, and sometimes opposing, requirements. The geometry of the structure is often decided by the architects who do not necessarily consider optimal structural performance as a key requirement. For the serviceability limit state, i.e. everyday use of the building, it is necessary to consider e.g. vibrations, deflections, acoustics, and crack widths. The behaviour of the structure in the serviceability limit state can be the critical case, and the aforementioned considerations might govern the final design of the structure. Similarly, accidental loads, e.g. fire loads, have to be considered, which again might govern the design and the final structural layout.

The present study is only concerned with the requirements at ultimate limit state, where the scope is to ensure a sufficiently level of safety against structural collapse, and issues such as crack widths and deflections are not considered.

The scope of this chapter is to demonstrate the strength and efficiency of the presented framework and models when used to analyse real life structures. Precast concrete structures comprise several different components, and the focus of this thesis is on the precast panels and the in-situ cast joints. As discussed in Chapter 1, the behaviour of the in-situ cast joints is crucial to the overall capacity of precast concrete structures. The current practice is to design the joints as the weaker part of the structure, which makes analysis by general purpose software, e.g. finite element analysis, difficult and inaccurate.

Based on the findings presented in Section 4.3, a macro joint element and submodel for two-dimensional modelling of joints were developed (see also Paper II, Herfelt et al., 2017a). The presented joint element makes it possible

to model real life precast concrete structure in a framework based on finite element limit analysis. In this chapter, an example of a four-storey shear wall with door openings will be analysed using the plane stress elements representing the precast panels, and the joint element and submodel representing the in-situ cast joins.

A three-dimensional macro joint element and submodel were developed and presented in Section 4.5 and Paper IV (Herfelt et al., 2017b). The model can be seen as a generalisation of the two-dimensional element, however, the normal forces in the longitudinal direction are not incorporated in the model. In Section 5.3, an example of a four-storey stairwell subjected to shear and torsion is analysed, and the influence of the joints will be discussed.

5.2 Two-dimensional precast shear wall

A four-storey shear wall is considered. The wall comprises 12 precast panels of which three have door openings. The panels are connected on the construction site using in-situ cast joints. The wall is analysed using the presented framework, i.e. the plane stress element and two-dimensional joint element, and the results are compared to the original design of the wall which was done by manual calculations, i.e. strut-and-tie methodology combined with the Eurocode expression for the capacity of the joints.

The vertical joints shown in Figure 5.1 have keyed interfaces and are reinforced with U-bar loops extruding from the adjacent precast panels. The interfaces of the horizontal joints, on the other hand, are considered as rough. The horizontal joints are reinforced with rebar rods extruding from the precast panel below. As shown in Figure 5.1, a reinforcement stringer is placed in the left side of the wall to carry the overturning moment induced by the horizontal forces H_1 to H_4.

The shear wall is designed for multiple load cases including accidental loads, however, for the present analysis only the three critical load cases are considered. All of the three load cases include horizontal wind loads as well as vertical loads from the dead load of the structure and additional imposed loads. Table 5.1 lists the loads, where L1, L2, L3, and L4 refer to the four storeys of the wall, see Figure 5.1. The vertical loads from the stairs are applied on top of the three door openings. The horizontal loads, H_1 to H_4, are treated as scalable, i.e. applied as $\boldsymbol{p}\lambda$ where λ is the load factor sought to be maximised. The vertical loads are treated as constant and applied as the vector $\boldsymbol{p}_0$ in the optimisation problem, see the lower bound formulation, Equation (3.11) in Section 3.2.

All precast panels and joints have a thickness of 240 mm. The panels are

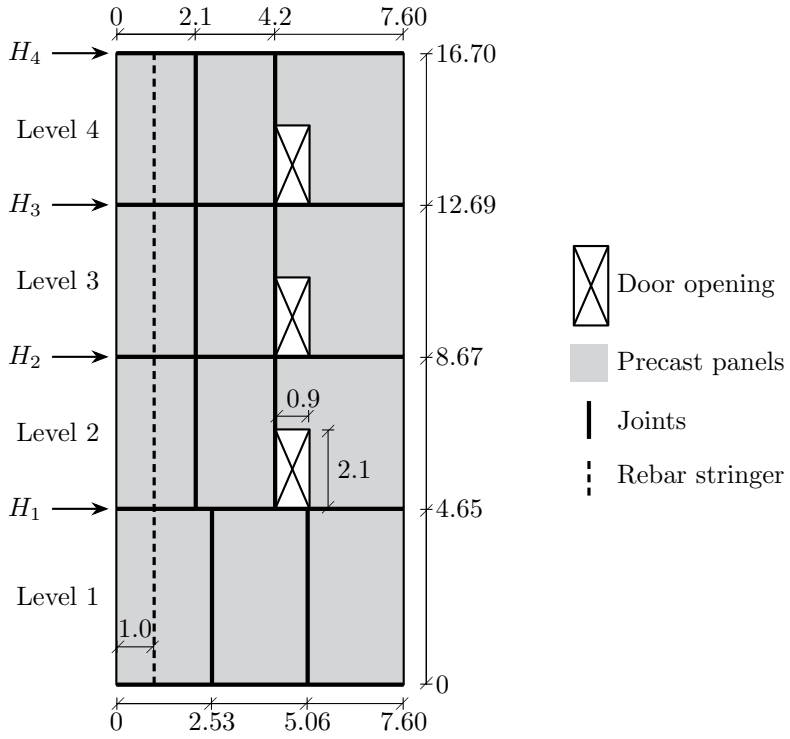

***Figure 5.1**: Geometry of the four-storey shear wall. All measurements are given in metres.*

***Table 5.1**: Design loads acting on the shear wall.*

	Vertical loads [kN/m]			Vertical loads, stairs [kN/m]		Horizontal loads [kN]		
Load case:	L1	L2, L3	L4	L2, L3	L4	L1	L2, L3	L4
1	65.2	61.8	67.6	68.4	70.3	45.0	42.0	73.0
2	33.4	31.0	31.7	24.2	24.2	45.0	42.0	73.0
3	74.2	70.2	74.2	65.9	76.9	46.0	46.0	58.0

reinforced with two layers of Ø8 rebars per 300 mm in both directions (corresponding to 335 mm^2/ m). The reinforcement has a design yield strength of $f_{yd} = 350$ MPa, while the concrete has a design compressive strength of $f_{cd} = 22$ MPa. The tensile strength of the concrete is assumed to be zero, and the reinforcement is assumed only to carry tension.

The vertical joints have a width of 60 mm, and the horizontal joints have a width of 200 mm. The joint mortar has a design compressive strength of 22 MPa and the tensile strength is taken as zero for the joints, identical to the concrete of the precast panels. The reinforcement of the joints is listed

in Table 5.2. For the horizontal joints, L1 indicates that the joint is located above level 1.

***Table 5.2**: Transverse and longitudinal reinforcement of the in-situ cast joints.*

	Horizontal joints		Vertical joints		
	L0, L1	L2, L3, L4	L1	L2	L3, L4
Top side	-	-	Ø10	Ø10	Ø10
Bottom side	Ø10	Ø10	Ø10	Ø10	Ø10
s [mm]	200	200	150	450	600
Locking bar	4 Ø25	2 Ø20	-	-	-

The joint reinforcement listed in Table 5.2 has a design yield strength of 385 MPa. The parameter s in Table 5.2 refers to the distance between the pairs of U-bars (or rebar rods for the horizontal joints). The horizontal joints are reinforced with several rebars in the longitudinal direction, while no locking bar is used for the vertical keyed joints. For the interface elements of the model, the friction coefficient for the keyed interfaces of the vertical joints is taken as $\mu = 0.90$, while $\mu = 0.7$ is used for the rough interfaces of the horizontal joints according to the Eurocode 2. The cohesion is taken as zero.

The submodel yield criterion presented in Section 4.4 makes it possible to account for local failure in the core of the joint caused by suboptimal reinforcement layout. An off-set u is defined and for the present analysis the worst-case scenario is assumed i.e. $u/s = 0.5$, see Figure 4.24. This will affect the shear capacity of the joints in the top storeys substantially due to the larger value of s, however, it will only affect the joints in the lower storeys to a minor degree as the U-bar pairs are placed closely together.

The reinforcement stringer shown in Figure 5.1 balances the overturning moment from the horizontal forces. In the bottom storey, two Ø25 rebars with a design yield strength of 664 MPa are used, and for the remaining storeys a single Ø25 with a design yield strength of 385 MPa is used.

The shear wall is analysed using different meshes to assess the convergence rate and behaviour of the model. The meshes are generated using the Distmesh package for Matlab (Persson and Strang, 2004). Figure 5.2 shows that the capacity generally increases with the number of elements and approach the exact (unknown) limit load from below. An exception to this is load case 2 with a mesh of 2,646 plane stress elements which yield a slightly larger load factor than some of the finer meshes. Figure 5.2 also shows that load case 2 is the critical one: For the finest mesh analysed (16,940 plane

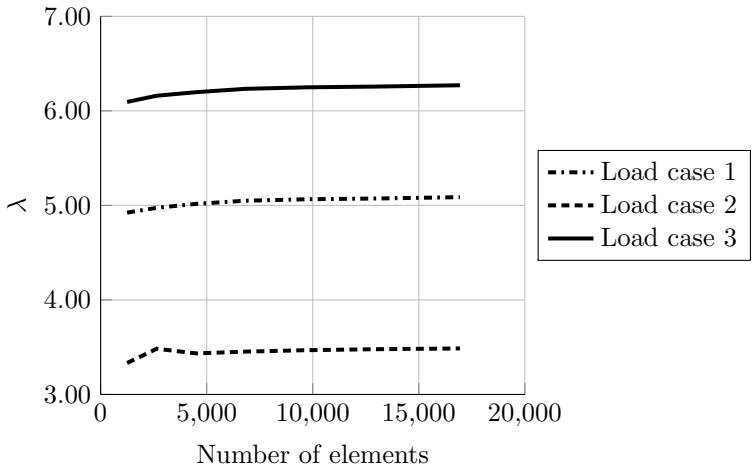

***Figure 5.2**: Load factor λ for the three load cases as a function of the number of plane stress elements.*

stress elements) a load factor of $\lambda = 5.09$ was found for load case 1, $\lambda = 3.48$ for load case 2, and $\lambda = 6.27$ for load case 3.

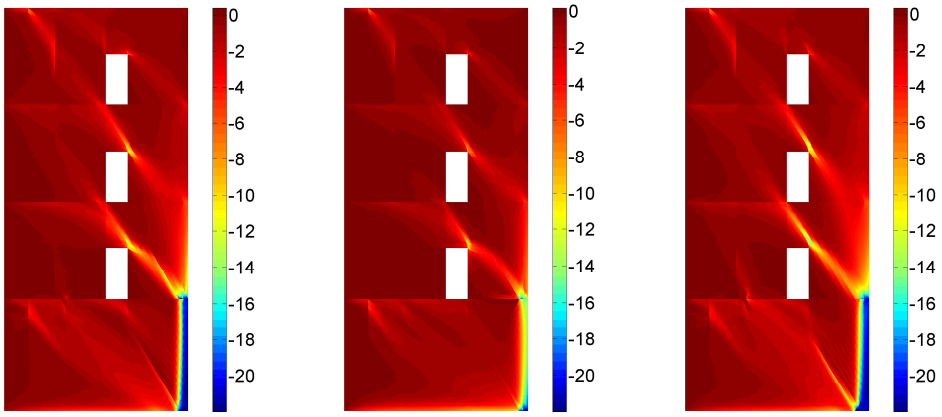

(a) Load case 1 (b) Load case 2 (c) Load case 3

***Figure 5.3**: Smallest principal stress for the three load cases using 6834 plane stress elements. The stresses are given in MPa, and compression is negative.*

Figure 5.3 shows that the horizontal forces are transferred via strut action to the supports for all three load cases. The struts are more pronounced for load cases 1 and 3, which give the largest load factors and, therefore, are subjected to the largest horizontal loads. The joints affect the stress field to some degree: This is visible in the top storey where the strut is obstructed

near the leftmost joint. In the bottom storey, the joints and rebar stringer also affect the stress field and introduce a wide strut with a moderate stress level.

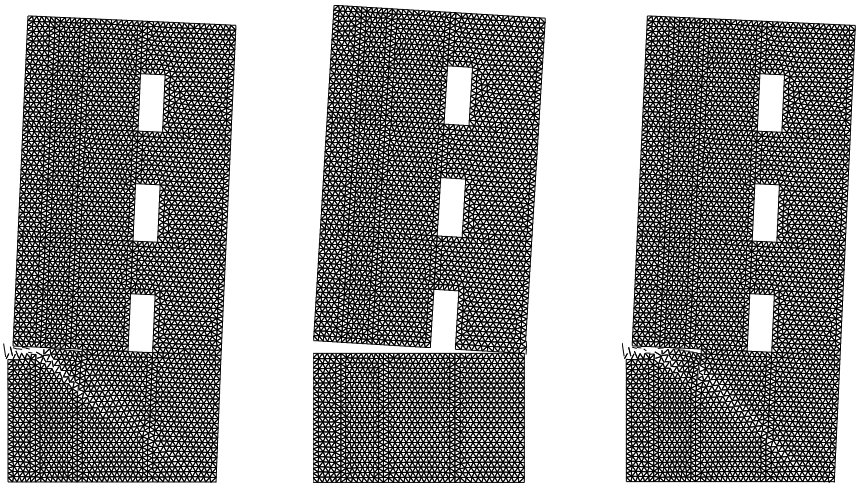

(a) Load case 1 (b) Load case 2 (c) Load case 3

***Figure 5.4**: Collapse mode of the four-storey precast shear wall determined from the dual solution to the lower bound problem using 6834 plane stress elements.*

The primal and dual problems are solved simultaneously and the dual solution can be interpreted as the collapse mode of the structure, however, the collapse mode will not be kinematically admissible. The dual variables, i.e. the displacement field, are associated with the traction equilibrium, hence, the displacements are associated with the element boundaries and not the nodes, which gives a somewhat scattered image in the failure zones.

For load case 1 and 3, it is seen that the failures occur in the bottom level and feature a diagonal failure zone through the three precast panels. The rebar stringer is yielding as well, thus, the wall can start to rotate. Moreover, some sliding and separation are observed near the joints above the bottom storey. For load case 2, Figure 5.4(b), the wall fails in bending failure: The horizontal joints have no tensile capacity as the top boundary is unreinforced, hence, the rebar stringer is responsible for carrying the overturning moment. The vertical loads, see Table 5.1, are beneficial to the structure and load case 2 features the lowest vertical loads, which ultimately leads to the bending failure. A ductile failure is expected due to yielding of the rebar stringer.

The stress field and collapse mode provide excellent tools for validating the calculations. The collapse mode can be used to establish a simple upper bound solution using the yield line method, hence, the numerical calculations

can be checked analytically. This is often a major issue for non-linear finite element models, where the results cannot be checked easily by hand due to the often complex non-linear material models and black-box nature of the software.

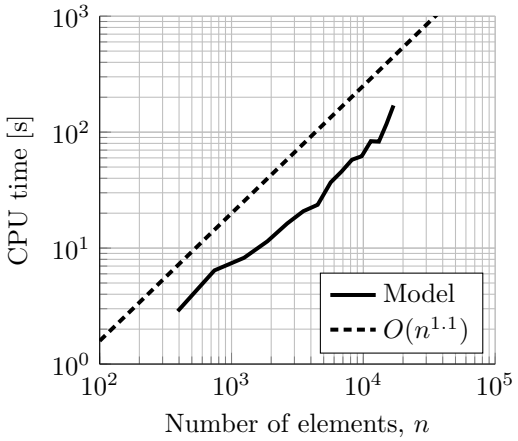

Figure 5.5*: Computational time as a function of the number of plane stress elements for the two-dimensional shear wall problem.*

The shear wall problem is analysed for varying mesh densities and the computational time required for solving the optimisation problem on a desktop PC with an Intel Xeon CPU W3565 with 8 CPUs and 3.2 GHz clock frequency is illustrated in Figure 5.5. For the finest mesh, the resulting optimisation problem has 1,384,026 variables, 1,384,947 linear constraints, and 144,980 second-order constraints, however, it is solved in about three minutes.

As shown in Figure 5.5, the computational time is approximately proportional to the problem size to the power of 1.1, which is identical to the findings in Section 4.1.5. The structure of the optimisation problem and sparsity of the problem matrices make the computational time scale well with the problem size, and large problems can be solved efficiently on a standard PC.

5.3 Three-dimensional precast stairwell

The four-storey stairwell analysed in Section 4.1.5 is now considered as a precast concrete structure. The four walls are assumed to be monolithic and connected by vertical in-situ cast corner joints. The wall panels are modelled using the generalised plane stress element (see Paper III, Herfelt et al., 2017c) and the corner joints are modelled using the three-dimensional

multiscale joint elements presented in Section 4.5 and in Paper IV (Herfelt et al., 2017b). The following analysis is likewise presented in Paper IV.

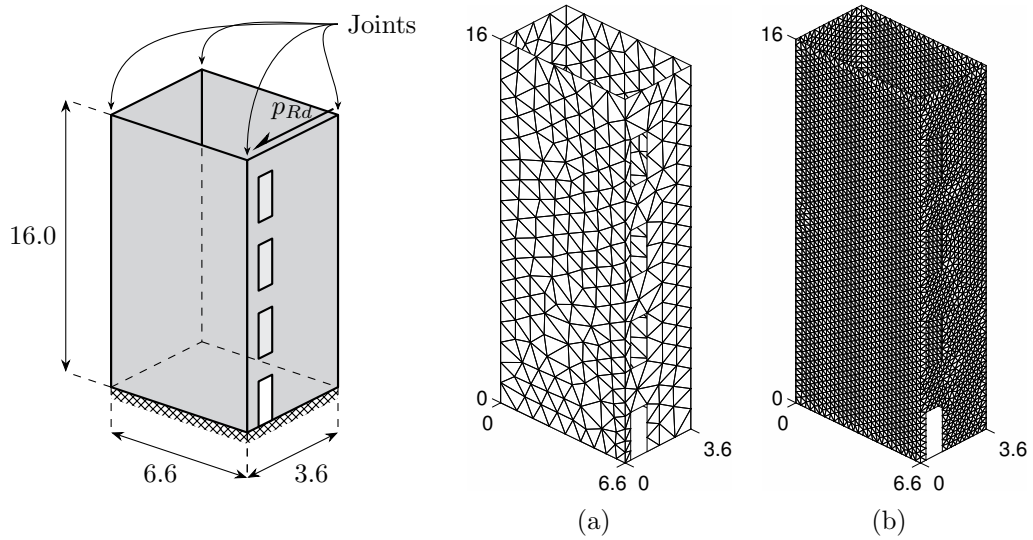

***Figure 5.6**: Precast concrete stairwell subjected to shear and torsion: a) Sketch of the structure with loading and positions of the joints, b) coarse mesh with 864 plane stress elements, c) fine mesh with 11,379 plane stress elements. All dimensions are given in metres.*

The precast concrete stairwell as well as the imposed line load, the positions of the joints, and the dimensions are shown in Figure 5.6 together with the two meshes used for the analysis, which are generated using GiD v12 (Ribó et al., 1998). The door openings have a height of 2.10 metres and a width of 0.90 metres. The precast panels have a thickness of 180 mm and are reinforced with two layers of Ø8 rebars per 150 mm in both directions which has a design yield strength of $f_{yd} = 458$ MPa. The concrete has a design compressive strength of $f_{cd} = 21.4$ MPa and the tensile strength is taken as zero. For the present analysis, two different values of the effectiveness factor are considered, namely $\nu = 1$ and $\nu = 0.7 - f_c/200 = 0.55$ (where the characteristic compressive strength f_c is in MPa). The interfaces in-between the precast panels and the joints are not considered for the present analysis.

The joints have the same width as the precast panels, i.e. $t_z = t_y = 180$ mm. The overlap of the U-bar loops in the core of the joint is assumed to be 50 mm, i.e. $o_z = o_y = 50$ mm. The U-bar pairs are placed every 300 mm, hence, $s = 300$ mm is used. For the joint mortar, $f_{cd} = 21.4$ MPa and $f_t = 0$ are used as well. Considering a single U-bar, the reinforcement ratio

of the joint is given as

$$\Phi = \frac{A_{su} f_y}{s t f_c}$$

where A_{su} is the cross sectional area of a single U-bar. The reinforcement ratio for the joint is varied and the results for $\nu = 1$ are illustrated in Figure 5.7 for the coarse and the fine meshes with 864 and 11,379 plane stress elements, respectively. The precast stairwell is analysed using two different values of u in order to assess the influence of the reinforcement layout on the overall capacity.

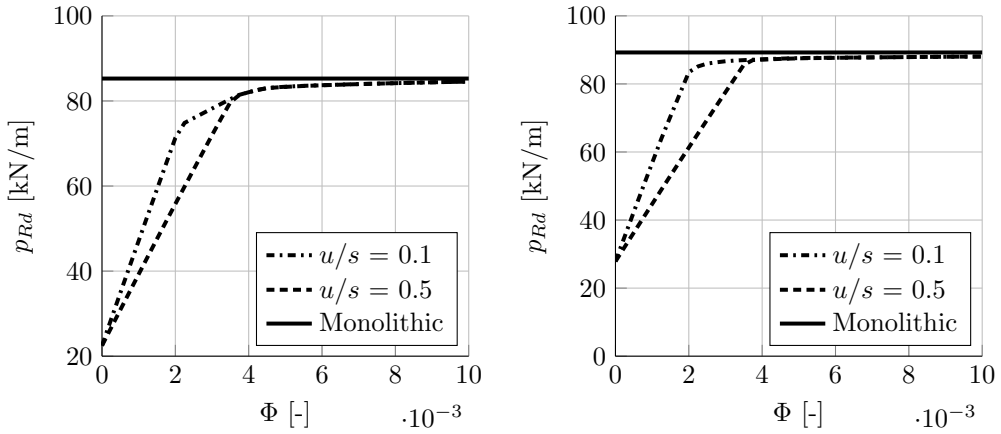

(a) Coarse mesh (b) Fine mesh

***Figure 5.7**: Load carrying capacity of the precast concrete stairwell as a function of the reinforcement ratio of the joints for two different values of u and $\nu = 1$.*

Figure 5.7 shows that the capacity depends heavily on the joint reinforcement for lower reinforcement ratios, however, at $\Phi \approx 0.004$ the curves reach a plateau close to the capacity of the monolithic stairwell. The joints with the lowest value of u/s perform better and reach this plateau at lower levels of reinforcement. Assuming a design strength of 214 MPa, a reinforcement degree of $\Phi = 0.004$ corresponds to Ø5 U-bar loop per 544 mm, which is far below what is typically used in practice.

Figure 5.8 shows the same behaviour as observed in Figure 5.7 despite the reduced concrete strength. For the fine mesh, see Figure 5.8(b), it is seen that the slope of the curve for $u/s = 0.1$ decreases at $\Phi \approx 0.002$. An effectiveness factor of $\nu = 0.55$ reduces the capacity by less than 5 per cent since the reinforcement is the main limiting factor of the structure and the compressive stresses can be redistributed.

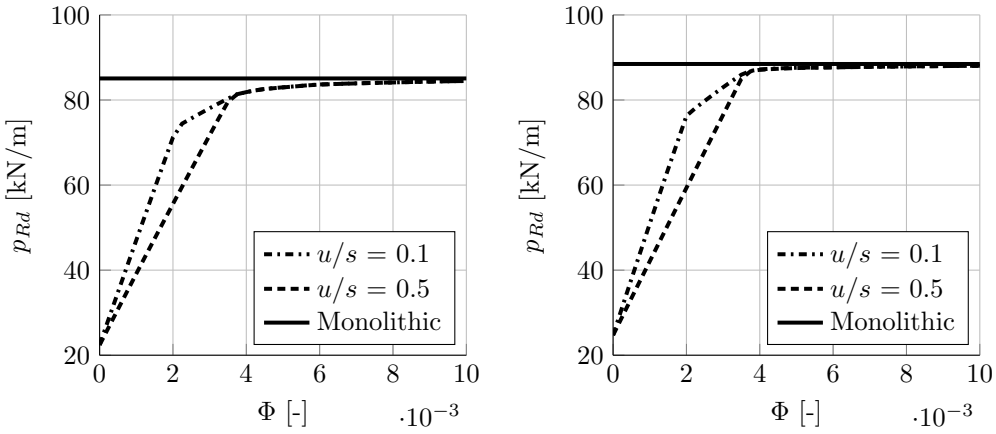

(a) Coarse mesh (b) Fine mesh

***Figure 5.8**: Load carrying capacity of the precast concrete stairwell as a function of the reinforcement ratio of the joints for two different values of u and $\nu = 0.55$.*

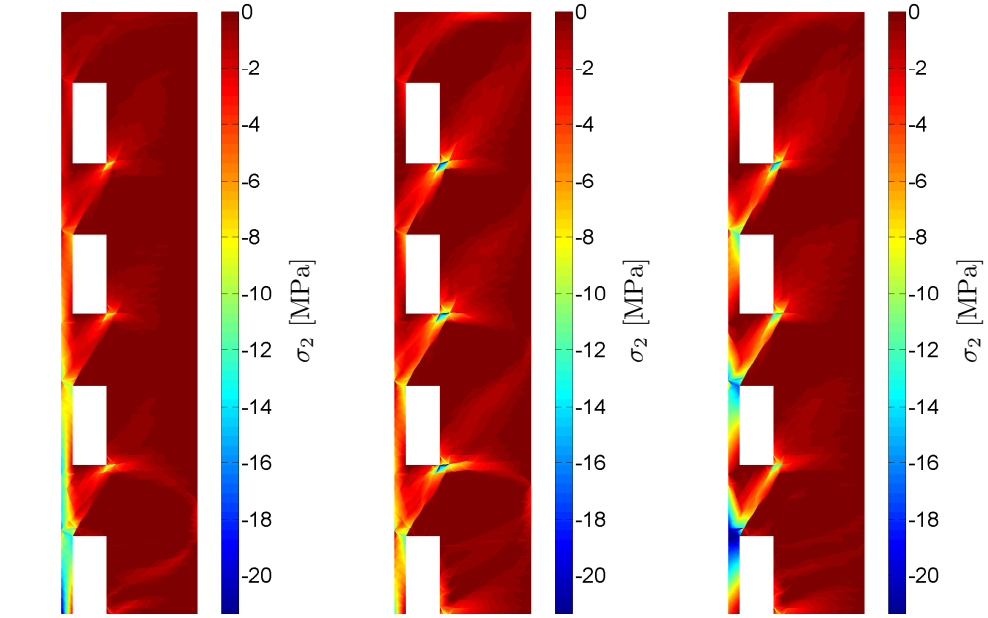

(a) Joints: $\Phi = 0.001$, $p_{Rd} = 47.12$ kN/m (b) Joints: $\Phi = 0.004$, $p_{Rd} = 87.14$ kN/m (c) Monolithic: $p_{Rd} = 89.25$ kN/m

***Figure 5.9**: Comparison of the smallest principal stress for the wall with the door openings using the finest mesh. For the joints, $u/s = 0.5$ is used.*

Figure 5.9 shows that compression struts are formed in-between the door openings to transfer the load from the top to the supports at the bottom. Comparing Figure 5.9(a) and (b) to Figure 5.9(c) shows that the joints push the structure towards a more evenly distribution of stresses. Due to the low capacity of the joints for $\Phi = 0.001$, Figure 5.9(a), bending is observed for the slender panel next to the bottom door opening: The compressive stress from the strut cannot be transferred to the adjacent wall, hence, the slender panel has to transfer the forces to the foundations via bending.

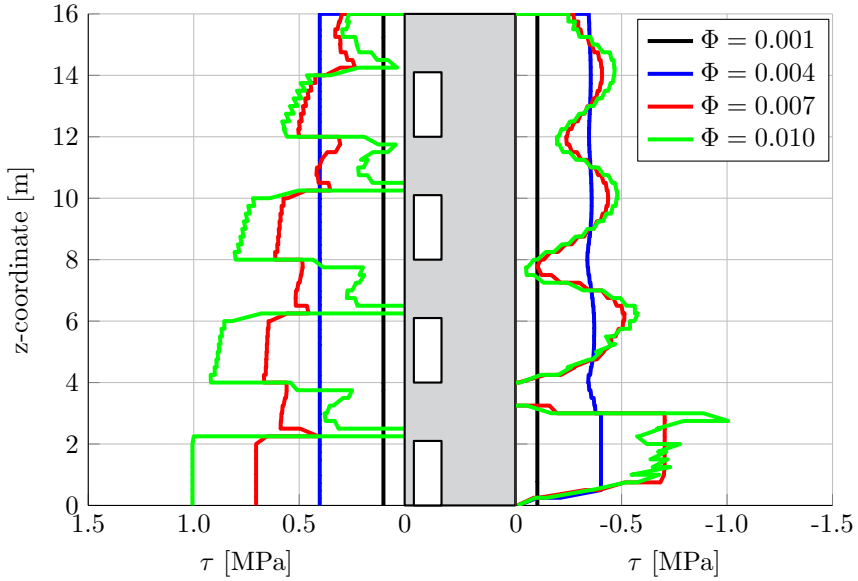

***Figure 5.10**: Shear stress distribution over the height of the structure in the joints at the slender wall with the door openings for different reinforcement degrees Φ using the fine mesh. The ratio $u/s = 0.5$ is used for the joints. The wall structure is shown in the centre.*

Figure 5.10 shows that for $\Phi = 0.001$ the joints on either side of the wall with the door openings are fully utilised. For $\Phi = 0.004$, only the joint near the door openings is fully utilised, but the other joint (right-hand side of the figure) is still loaded quite evenly. In order to activate the U-bar reinforcement over the entire height of the structure simultaneously, significant ductility is needed.

For $\Phi = 0.007$ and 0.010, it is observed that the shear distribution becomes more uneven and a shear reserve is present in the joints. The effect of the door openings and the struts is clearly seen on the curves to the left in Figure 5.10, and to some degree on the curves to the right which display an almost wave-like pattern. The bottom parts of the joints are fully utilised

for $\Phi = 0.007$ and 0.010, hence, the requirement to the ductility of the joints is considerably lower, and the structure is more robust.

The analysis has shown that the generalised plane stress element and the multiscale joint element are capable of modelling real life structures in three-dimensions. For lower levels of reinforcement, joints decrease the capacity of the structure significantly, however, provided sufficient reinforcement, the overall capacity becomes hardly unaffected by the joints. The stress field is, however, affected by the joints for all analysed reinforcement ratios, and the joints push the structure towards more evenly distributed stress fields. The computational time of the precast concrete stairwell with joints using the fine mesh was approximately 65 seconds, which is a marginal increase compared to the monolithic stairwell problem presented in Section 4.1.5.

Chapter 6

Auxiliary work

6.1 Introduction

This section presents several finite elements, which are not considered part of the core of the present thesis, but they are nevertheless important and can be relevant for future work. The primary work of the Ph.D. project presented in Section 4 and 5 is based on the lower bound method: The plane stress triangles and the developed joint elements are all lower bound elements, which will yield a statically admissible and safe stress field.

While lower bound solutions generally are considered the most useful for practical design and applications, upper bound solutions as well as so-called mixed solutions also have merit. In some cases, the lower bound solution may be far from the exact limit load, hence, an upper bound solution provide some intelligence on the level of approximation. A stress field and collapse mode is determined from both the lower bound problem and the upper bound problem.

For the lower bound problem, the stress field will be statically admissible and safe, while the determined collapse mode will (most likely) not be kinematically admissible. Contrarily, the stress field of the upper bound problem will not be statically admissible, but the collapse mode will be kinematically admissible.

Mixed formulations are something in-between the lower and upper bound solutions. Such formulations cannot be used to establish rigorous bounds for the given problem. The solution to the mixed problem, however, will typically be closer to the exact limit load. The mixed formulations presented in this chapter can be considered as *relaxed lower bounds*, where the rigorous traction continuity is relaxed and the tractions are distributed to the nodes according to the displacement field. In the case of the solid elements, the

mixed formulation results in a numerically stable and well-scaled problem compared to the lower bound problem. Moreover, the lower bound plane stress element might have linear dependencies, but this appears not to be an issue with the proposed mixed element (see Makrodimopoulos and Martin (2006) for a description of linear dependencies in two-dimensional problems).

6.2 Mixed plane stress element

The mixed element presented in this section is a relaxed version of the lower bound element presented by Poulsen and Damkilde (2000) and in Section 4.1.1. The element is developed by Krabbenhøft (2016) and will be used for the mixed shell element. The traction continuity along the element boundaries are relaxed by distributing the stresses to the three nodes of the given element side according to the quadratic displacement field of the element.

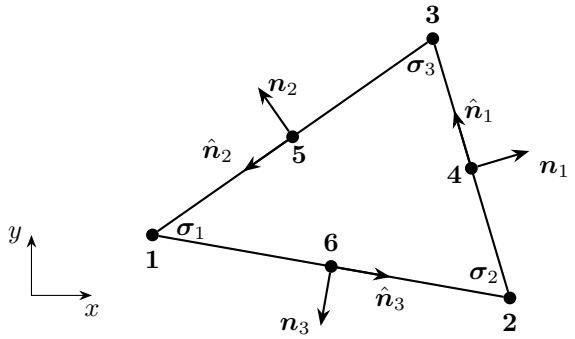

***Figure 6.1**: Geometry of the six-node mixed element: Unit normal vectors to the three sides and stress variables are shown.*

The element stress vector comprise the three stress vectors of the corners, which each describe a plane stress state:

$$\boldsymbol{\sigma}_{el} = \begin{bmatrix} \boldsymbol{\sigma}_1 \\ \boldsymbol{\sigma}_2 \\ \boldsymbol{\sigma}_3 \end{bmatrix}, \quad \text{with} \quad \boldsymbol{\sigma}_i = \begin{bmatrix} \sigma_{xi} \\ \sigma_{yi} \\ \tau_{xyi} \end{bmatrix}$$

As shown in Figure 6.1, we have a unit normal vector for each side:

$$\boldsymbol{n}_i = \begin{bmatrix} n_x^i \\ n_y^i \end{bmatrix}$$

The tractions on side i opposite node i are defined in global coordinates and

are given as

$$\boldsymbol{t}_i(s) = \begin{bmatrix} t_x^i(s) \\ t_y^i(s) \end{bmatrix} = \left(\frac{1}{2} - s\right) \mathbf{P}_i^T \boldsymbol{\sigma}_k + \left(s - \frac{1}{2}\right) \mathbf{P}_i^T \boldsymbol{\sigma}_j \tag{6.1}$$

where i, j, and k are permutations of 1, 2, and 3. The scalar s is a length coordinate ranging from $-1/2$ to $1/2$. The matrices $\mathbf{P}_i^T$ gives the tractions from the stress vector and are defined as for side i:

$$\mathbf{P}_i^T = \begin{bmatrix} n_x^i & 0 & n_y^i \\ 0 & n_y^i & n_x^i \end{bmatrix}$$

The element has a linear stress field, hence, the displacement field is quadratic. The tractions along each element side is distributed to the three nodes of the side by use of the quadratic shape functions, see Figure 6.2.

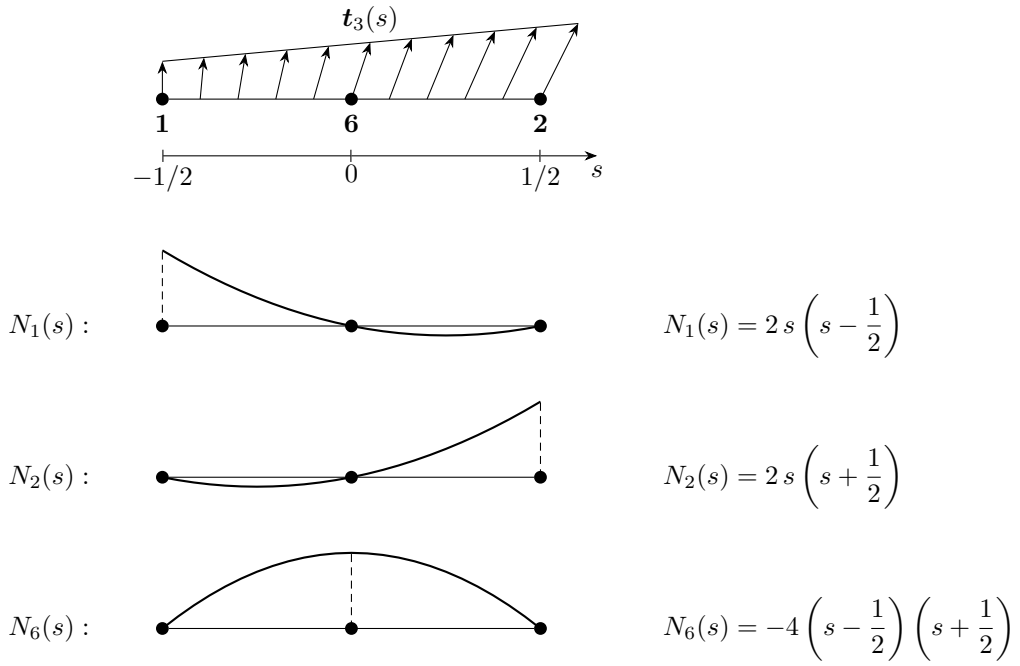

Figure 6.2*: Traction, $\boldsymbol{t}_3(s)$, and shape functions, $N_1(s)$, $N_2(s)$, and $N_6(s)$, for side 3 of an element.*

Figure 6.2 shows an element side with three nodes, 1, 2, and 6. The tractions are linear along the boundary as the figure shows, and the resulting nodal forces in each of the three nodes can be calculated as

$$\boldsymbol{q}_j^i = l_i \int_{-1/2}^{1/2} N_j^i(s) \boldsymbol{t}_i(s) \mathrm{d}s \tag{6.2}$$

where j refers to the node number and i to the side number, and l_i is the length of side i. The middle node of the particular side gets the majority of the tractions according to (6.2). Using the example of side 3 of an element shown in Figure 6.2, we obtain

$$\boldsymbol{q}_1^3 = \frac{\tilde{\mathbf{P}}_3^T}{6}\boldsymbol{\sigma}_1, \quad \boldsymbol{q}_2^3 = \frac{\tilde{\mathbf{P}}_3^T}{6}\boldsymbol{\sigma}_2, \quad \boldsymbol{q}_6^3 = \frac{\tilde{\mathbf{P}}_3^T}{3}\boldsymbol{\sigma}_1 + \frac{\tilde{\mathbf{P}}_3}{3}\boldsymbol{\sigma}_2,$$

where

$$\tilde{\mathbf{P}}_i^T = l_i \mathbf{P}_i^T$$

The corner nodes, i.e. nodes 1, 2, and 3, receive contributions from the two adjacent sides, e.g. sides 2 and 3 both contribute to node 1. Similar to the lower bound plane stress element presented in Section 4.1, internal equilibrium is enforced for the element, which gives the following equilibrium equations:

$$A \begin{bmatrix} \gamma_x \\ \gamma_y \end{bmatrix} = \frac{1}{2} \begin{bmatrix} \tilde{\mathbf{P}}_1^T & \tilde{\mathbf{P}}_2^T & \tilde{\mathbf{P}}_3^T \end{bmatrix} \boldsymbol{\sigma}_{el} \tag{6.3}$$

where γ_x and γ_y are surface loads imposed on the surface area of the element in the x and y-directions, respectively, and A is the surface area of the element. The element equilibrium matrix can be written as follows:

$$\mathbf{B}_{el}^T = \frac{1}{6} \begin{bmatrix} \tilde{\mathbf{P}}_2^T + \tilde{\mathbf{P}}_3^T & \mathbf{0} & \mathbf{0} \\ \mathbf{0} & \tilde{\mathbf{P}}_3^T + \tilde{\mathbf{P}}_1^T & \mathbf{0} \\ \mathbf{0} & \mathbf{0} & \tilde{\mathbf{P}}_1^T + \tilde{\mathbf{P}}_2^T \\ \mathbf{0} & 2\tilde{\mathbf{P}}_1^T & 2\tilde{\mathbf{P}}_1^T \\ 2\tilde{\mathbf{P}}_2^T & \mathbf{0} & 2\tilde{\mathbf{P}}_2^T \\ 2\tilde{\mathbf{P}}_3^T & 2\tilde{\mathbf{P}}_3^T & \mathbf{0} \\ 3\tilde{\mathbf{P}}_1^T & 3\tilde{\mathbf{P}}_2^T & 3\tilde{\mathbf{P}}_3^T \end{bmatrix} \tag{6.4}$$

The element requires a total of 14 equilibrium equations. The element is implemented in a finite element limit analysis framework using the Mohr-Coulomb criterion for plane stress presented in Section 3.3.

Comparison to the lower bound element

The deep beam with shear support presented in Section 4.1.5 is analysed using the plane stress mixed element. We recall the analytical solution from Nielsen and Hoang (2010):

$$p^* = \frac{4\,\Phi\,h^2\,f_c}{(1+\Phi)\,L^2} \leq f_c, \qquad \Phi = \frac{A_s\,f_y}{t f_c} \tag{6.5}$$

Using the same parameters as in Section 4.1.5, namely $h = 2$ m, $L = 6$ m, $f_c = 20$ MPa, and $\Phi = 0.075$, the exact limit load is $p^* = 0.6202$ MPa. An identical structured mesh is used for the mixed element, see Figure 6.3.

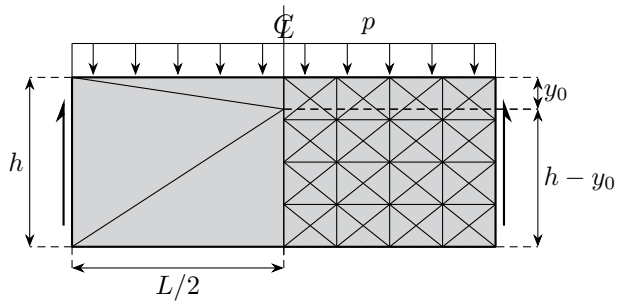

***Figure 6.3**: Deep beam with shear supports including mesh for the analytical solution (left) and for the convergence analysis (right).*

***Table 6.1**: Limit load and error for the deep beam problem using the lower bound and mixed elements.*

	Lower bound		Mixed	
nel	p [MPa]	Error [%]	p [MPa]	Error [%]
64	0.5555	10.42	0.5890	5.02
256	0.6053	2.40	0.6124	1.25
1,024	0.6177	0.39	0.6189	0.20
4,096	0.6191	0.17	0.6196	0.08
16,384	0.6193	0.13	0.6198	0.05

Table 6.1 shows that the mixed element generally gives a limit load closer to the exact limit load. The error is approximately halved compared to the lower bound element, and the fine mesh with 16,384 elements give an error of just 0.05 %. It is observed that the mixed element approaches the exact limit from below, however, this might not always be the case.

6.3 Mixed shell element

The mixed shell element combines the in-plane behaviour of the mixed plane stress element with a plate bending element (Krabbenhøft, 2016). Based on the unit normal vectors $\boldsymbol{n}_i$ seen in Figure 6.1, we define the following

geometric quantities:

$$
\begin{aligned}
\mathbf{P}_i^T &= \begin{bmatrix} n_x^i & 0 & n_y^i \\ 0 & n_y^i & n_x^i \end{bmatrix} \\
\hat{\boldsymbol{n}}_i &= \begin{bmatrix} -n_y^i \\ n_x^i \end{bmatrix} \\
\boldsymbol{a}_{ij} &= \mathbf{P}_i \boldsymbol{n}_j \\
\boldsymbol{b}_i &= \mathbf{P}_i \hat{\boldsymbol{n}}_i \\
\boldsymbol{c}_{ij} &= l_i l_j \boldsymbol{a}_{ij} \\
\hat{\mathbf{P}}_i &= l_i \mathbf{P}
\end{aligned}
\tag{6.6}
$$

where l_i is the length of side i opposite of node i. The vectors $\boldsymbol{a}_{ii}^T$ and $\boldsymbol{b}_i^T$ give the tractions in local coordinates which is used to ensure moment continuity similarly to the lower bound plane stress element presented in Section 4.1.1 which required traction continuity.

6.3.1 Plate bending

We now consider a triangular element with a linear moment field and a quadratic displacement field. The element has six displacement nodes (corners and centre of the element sides) and six rotation nodes (two for each side near the corners). The geometry is illustrated in Figure 6.4.

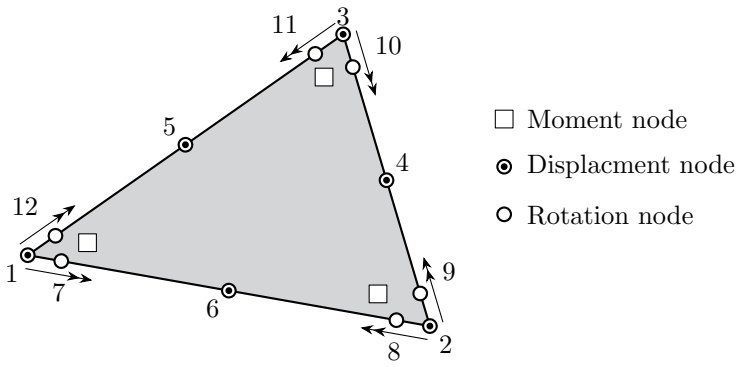

***Figure 6.4**: Plate bending element: Location of the displacement nodes and rotation nodes (Krabbenhøft, 2016).*

The moment nodes indicated in Figure 6.4 describe the linear moment

field. The element moment vector is given as

$$\boldsymbol{m}_{el} = \begin{bmatrix} \boldsymbol{m}_1 \\ \boldsymbol{m}_2 \\ \boldsymbol{m}_3 \end{bmatrix}, \quad \text{with} \quad \boldsymbol{m}_i = \begin{bmatrix} m_x^i \\ m_y^i \\ m_{xy}^i \end{bmatrix}$$

The equilibrium equations for the element can be stated as

$$\begin{bmatrix} \boldsymbol{q}_{\text{ext}} \\ \boldsymbol{m}_{\text{ext}} \end{bmatrix} = \begin{bmatrix} \mathbf{B}_z^T \\ \mathbf{B}_\theta^T \end{bmatrix} \boldsymbol{m}_{el} \tag{6.7}$$

where $\mathbf{B}_z^T$ are the equations associated with the displacement nodes and $\mathbf{B}_\theta^T$ are the equations associated with the rotation nodes, see Figure 6.4. The vectors $\boldsymbol{q}_{\text{ext}}$ and $\boldsymbol{m}_{\text{ext}}$ are the externally applied transverse forces and moments, respectively. The matrix $\mathbf{B}_z^T$ comprise contributions from the concentrated nodal forces in the corners and the Kirchhoff shear forces:

$$\mathbf{B}_z^T = \mathbf{B}_r^T + \mathbf{B}_q^T + \mathbf{B}_t^T$$

where $\mathbf{B}_r^T$ are the contributions from the concentrated nodal forces, $\mathbf{B}_q^T + \mathbf{B}_t^T$ are the contributions from the Kirchhoff shear forces.

Concentrated nodal forces acting in the corners of the element are given as the difference in the twisting moments along the two sides that meet in a given corner. The twisting moment along side i is given as

$$m_t^i = \boldsymbol{b}_i^T \boldsymbol{m}$$

where $\boldsymbol{m}$ is the moment in a given point. The contributions to the displacement nodes from the twisting moment are therefore given as

$$\begin{bmatrix} r_1 \\ r_2 \\ r_3 \\ r_4 \\ r_5 \\ r_6 \end{bmatrix} = \begin{bmatrix} \boldsymbol{b}_2^T - \boldsymbol{b}_3^T & \mathbf{0} & \mathbf{0} \\ \mathbf{0} & \boldsymbol{b}_3^T - \boldsymbol{b}_1^T & \mathbf{0} \\ \mathbf{0} & \mathbf{0} & \boldsymbol{b}_1^T - \boldsymbol{b}_2^T \\ \mathbf{0} & \mathbf{0} & \mathbf{0} \\ \mathbf{0} & \mathbf{0} & \mathbf{0} \\ \mathbf{0} & \mathbf{0} & \mathbf{0} \end{bmatrix} \begin{bmatrix} \boldsymbol{m}_1 \\ \boldsymbol{m}_2 \\ \boldsymbol{m}_3 \end{bmatrix} = \mathbf{B}_r^T \boldsymbol{m} \tag{6.8}$$

where r_i are the forces in the displacement nodes.

The Kirchhoff forces acting along each side of the element are given by the sum of the shear forces and the derivative of the twisting moment:

$$V_i = q_i + \frac{\mathrm{d}m_t^i}{\mathrm{d}s} \tag{6.9}$$

where $s \in [0, l_i]$ is a local coordinate along side i of the element. The shear forces along the element sides are given as

$$q_i = \boldsymbol{n}_i^T \boldsymbol{q} = \boldsymbol{n}_i^T \left(\boldsymbol{\nabla}^T \boldsymbol{m} \right) \tag{6.10}$$

where $\boldsymbol{\nabla}^T$ is a differential operator. The derivative of the linear moment field can be found in a similar manner as for the plane stress element in Section 4.1.1 using linear shape functions:

$$\boldsymbol{q} = \boldsymbol{\nabla}^T \boldsymbol{m} = -\frac{1}{2\,A} \sum_{i=1}^{3} l_i \mathbf{P}_i^T \boldsymbol{m}_i$$

and (6.10) can be rewritten as

$$q_j = \boldsymbol{n}_j^T \boldsymbol{q} = -\boldsymbol{n}_j^T \left(\frac{1}{2A} \sum_{i=1}^{3} l_i \mathbf{P}_i^T \boldsymbol{m}_i \right) = -\frac{1}{2A} \sum_{i=1}^{3} l_i \boldsymbol{a}_{ij}^T \boldsymbol{m}_i \tag{6.11}$$

The shear forces along the element sides q_j are distributed to the six displacement nodes according to the chosen quadratic displacement field, and their contributions to the displacement nodes are given as

$$\begin{bmatrix} q_1 \\ q_2 \\ q_3 \\ q_4 \\ q_5 \\ q_6 \end{bmatrix} = \frac{1}{12A} \begin{bmatrix} -\boldsymbol{c}_{11}^T & -\boldsymbol{c}_{21}^T & -\boldsymbol{c}_{31}^T \\ -\boldsymbol{c}_{12}^T & -\boldsymbol{c}_{22}^T & -\boldsymbol{c}_{32}^T \\ -\boldsymbol{c}_{13}^T & -\boldsymbol{c}_{23}^T & -\boldsymbol{c}_{33}^T \\ 4\boldsymbol{c}_{11}^T & 4\boldsymbol{c}_{21}^T & 4\boldsymbol{c}_{31}^T \\ 4\boldsymbol{c}_{12}^T & 4\boldsymbol{c}_{22}^T & 4\boldsymbol{c}_{32}^T \\ 4\boldsymbol{c}_{13}^T & 4\boldsymbol{c}_{23}^T & 4\boldsymbol{c}_{33}^T \end{bmatrix} \begin{bmatrix} \boldsymbol{m}_1 \\ \boldsymbol{m}_2 \\ \boldsymbol{m}_3 \end{bmatrix} = \mathbf{B}_q^T \boldsymbol{m} \tag{6.12}$$

The gradient of the twisting moments along element side i is given as

$$t_i = \frac{\mathrm{d}m_t^i}{\mathrm{d}s} = \frac{\boldsymbol{b}_i^T \left(\boldsymbol{m}_k - \boldsymbol{m}_j \right)}{l_i}$$

where i, j, and k are permutations of 1, 2, and 3. The contribution from the twisting moment is likewise distributed to the six displacement nodes according to the chosen quadratic displacement field:

$$\begin{bmatrix} t_1 \\ t_2 \\ t_3 \\ t_4 \\ t_5 \\ t_6 \end{bmatrix} = \frac{1}{6} \begin{bmatrix} \boldsymbol{b}_3^T - \boldsymbol{b}_2^T & -\boldsymbol{b}_3^T & \boldsymbol{b}_2^T \\ \boldsymbol{b}_3^T & \boldsymbol{b}_1^T - \boldsymbol{b}_3^T & -\boldsymbol{b}_1^T \\ -\boldsymbol{b}_2^T & \boldsymbol{b}_1^T & \boldsymbol{b}_2^T - \boldsymbol{b}_1^T \\ \mathbf{0} & 4\boldsymbol{b}_1^T & -4\boldsymbol{b}_1^T \\ -4\boldsymbol{b}_2^T & \mathbf{0} & 4\boldsymbol{b}_2^T \\ 4\boldsymbol{b}_3^T & -4\boldsymbol{b}_3^T & \mathbf{0} \end{bmatrix} \begin{bmatrix} \boldsymbol{m}_1 \\ \boldsymbol{m}_2 \\ \boldsymbol{m}_3 \end{bmatrix} = \mathbf{B}_t^T \boldsymbol{m} \tag{6.13}$$

The equations (6.8), (6.12), and (6.13) give the contributions to the displacement nodes.

Finally, the moment along element side i is given as

$$m_n^i = \boldsymbol{a}_{ii}^T \boldsymbol{m} \tag{6.14}$$

where $\boldsymbol{m}$ is the moment in a given point. To ensure bending moment continuity for the linear moment field, this equation is enforced twice for each element side in the rotation nodes illustrated in Figure 6.4. This gives the final matrix for the equilibrium matrix (6.7):

$$\mathbf{B}_\theta^T = \begin{bmatrix} \mathbf{0} & \boldsymbol{a}_{11}^T & \mathbf{0} \\ \mathbf{0} & \mathbf{0} & -\boldsymbol{a}_{11}^T \\ \mathbf{0} & \mathbf{0} & \boldsymbol{a}_{22}^T \\ -\boldsymbol{a}_{22}^T & \mathbf{0} & \mathbf{0} \\ \boldsymbol{a}_{33}^T & \mathbf{0} & \mathbf{0} \\ \mathbf{0} & -\boldsymbol{a}_{33}^T & \mathbf{0} \end{bmatrix} \tag{6.15}$$

6.3.2 Combining in-plane and bending actions

The plane stress and the plate bending elements are combined to obtain a mixed shell element. The plane stress element governs the in-plane behaviour of the element while the plate bending element governs the out-of-plane behaviour. Both elements have six displacement nodes and the generalised nodal forces in a local two-dimensional coordinate system can be computed using the presented equilibrium equations for the two elements.

The equilibrium matrix for the plane stress element is now denoted $\mathbf{B}_{xy}^T$ and the contributions to displacement node j from the stress vector associated with corner i, $\boldsymbol{\sigma}_i$, is denoted $\mathbf{B}_{xyij}^T$, i.e.:

$$\mathbf{B}_{xy}^T = \begin{bmatrix} \mathbf{B}_{xy11}^T & \mathbf{B}_{xy21}^T & \mathbf{B}_{xy31}^T \\ \vdots & \vdots & \vdots \\ \vdots & \vdots & \vdots \\ \mathbf{B}_{xy16}^T & \mathbf{B}_{xy26}^T & \mathbf{B}_{xy36}^T \end{bmatrix}$$

Similarly, the contributions to displacement node j from the moment vector associated with corner i, $\boldsymbol{m}_i$, is denoted $\mathbf{B}_{zij}^T$, i.e.:

$$\mathbf{B}_z^T = \begin{bmatrix} \mathbf{B}_{z11}^T & \mathbf{B}_{z21}^T & \mathbf{B}_{z31}^T \\ \vdots & \vdots & \vdots \\ \vdots & \vdots & \vdots \\ \mathbf{B}_{z16}^T & \mathbf{B}_{z26}^T & \mathbf{B}_{z36}^T \end{bmatrix}$$

The contributions to displacement node j from the stress and moment vectors associated with corner j can now be stated as:

$$\mathbf{B}_{xyzij}^T = \begin{bmatrix} \mathbf{B}_{xyij}^T & \mathbf{0} \\ \mathbf{0} & \mathbf{B}_{zij}^T \end{bmatrix},$$

and the full matrix can be stated as

$$\mathbf{B}_{xyz}^T = \begin{bmatrix} \mathbf{B}_{xyz11}^T & \mathbf{B}_{xyz21}^T & \mathbf{B}_{xyz31}^T \\ \vdots & \vdots & \vdots \\ \vdots & \vdots & \vdots \\ \mathbf{B}_{xyz16}^T & \mathbf{B}_{xyz26}^T & \mathbf{B}_{xyz36}^T \end{bmatrix}$$

The stress and moment variables are collected in a single vector

$$\boldsymbol{\chi} = \begin{bmatrix} \boldsymbol{\sigma}_1 \\ \boldsymbol{m}_1 \\ \boldsymbol{\sigma}_2 \\ \boldsymbol{m}_2 \\ \boldsymbol{\sigma}_3 \\ \boldsymbol{m}_3 \end{bmatrix},$$

and the combined equilibrium equations in local coordinates can now be written as

$$\boldsymbol{p}_{\text{ext}} = \mathbf{B}_{xyz}^T \boldsymbol{\chi} \tag{6.16}$$

The local coordinate system of the shell element is now established in the same manner as for the generalised plane stress element presented in Section 4.1.3.

The vectors $\boldsymbol{v}_{12}$ and $\boldsymbol{v}_{13}$ given in global coordinates, see Figure 6.5, are used to define the basis vectors of the local coordinate system:

$$\boldsymbol{e}_x = \frac{\boldsymbol{v}_{12}}{\|\boldsymbol{v}_{12}\|}, \quad \boldsymbol{e}_z = \frac{\boldsymbol{v}_{12} \times \boldsymbol{v}_{13}}{\|\boldsymbol{v}_{12} \times \boldsymbol{v}_{13}\|}, \quad \boldsymbol{e}_z = \boldsymbol{e}_z \times \boldsymbol{e}_x$$

and the transformation matrix is given as $\mathbf{E} = \begin{bmatrix} \boldsymbol{e}_x & \boldsymbol{e}_y & \boldsymbol{e}_z \end{bmatrix}$. The local nodal coordinates are computed as

$$\boldsymbol{x}_i = \mathbf{E}^T \boldsymbol{X}_i$$

where $\boldsymbol{X}_i$ are the global coordinates for node i. The equilibrium equations can now be transformed to the global coordinates using the block-diagonal

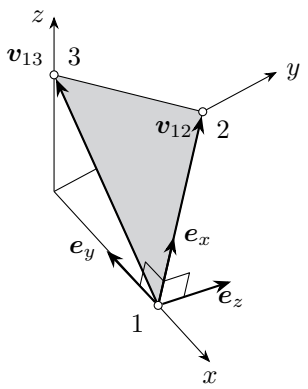

***Figure 6.5**: Definition of the local coordinate system for the shell element.*

transformation matrix $\mathbf{D}$ given as

$$\mathbf{D} = \begin{bmatrix} \mathbf{E} & & \\ & \ddots & \\ & & \mathbf{E} \end{bmatrix}$$

Equilibrium for the shell element in global coordinates can be written as

$$\mathbf{B}_{XYZ}^T = \mathbf{D}\mathbf{B}_{xyz}^T \tag{6.17}$$

The moment continuity is still enforced for the shell element, see (6.15), hence, we obtain the following system of equations:

$$\begin{bmatrix} \boldsymbol{q}_{ext} \\ \boldsymbol{m}_{ext} \end{bmatrix} = \begin{bmatrix} \mathbf{B}_{XYZ}^T \\ \mathbf{B}_\theta \end{bmatrix} \boldsymbol{\chi} \tag{6.18}$$

The internal equilibrium equation for the plane stress element (6.3) is also carried over and enforced in local coordinates for the shell element.

6.3.3 Yield criteria for shells

The subject of yield criteria for shells is rather complicated, especially when considering a complex composite material like reinforced concrete. The stress state in a given point in a shell element is defined by three in-plane stresses and three section moments. Some attempts at establishing an adequate yield criterion for shells within the framework of finite element limit analysis has been done, and Larsen (2010) presented a layer-based yield function which also considered the transverse shear stresses. The criterion was formulated

for semidefinite programming since the inclusion of the transverse shear stress leads to a triaxial stress in the material.

Simplified yield functions can of course be used, however, the section moments give rise to varying levels of stresses throughout the thickness of the shell which complicates matters. A suitable yield function for shells needs to account for this.

Simplified criteria

The section moments and in-plane stresses can either be treated completely separately or combined in a linear manner to ensure a solution which is always safe. Whether or not these criteria provide a good estimate of the exact yield envelope depends on the material. For instance, for steel shells (assuming no instability) the combined criterion will provide a decent approximation.

First, we define two yield functions for in-plane action and slab bending, respectively:

$$\begin{aligned} f_\sigma\left(\boldsymbol{\sigma}, \boldsymbol{S}_\sigma\right) &\leq 0 \\ f_m\left(\boldsymbol{m}, \boldsymbol{S}_m\right) &\leq 0 \end{aligned} \tag{6.19}$$

where f_σ is the yield function for in-plane action, and f_m is the yield function for slab bending. The vectors $\boldsymbol{S}_\sigma$ and $\boldsymbol{S}_m$ denotes the material parameters associated with the two yield functions. The criterion (6.19) can be considered as the simplest yield criterion for shells where the in-plane stresses and section moments are handled completely separately. Introducing an auxiliary variable ζ, the two yield functions are combined linearly:

$$\begin{aligned} &f_\sigma\left(\boldsymbol{\sigma}, \zeta \boldsymbol{S}_\sigma\right) \leq 0 \\ &f_m\left(\boldsymbol{m}, (1-\zeta)\, \boldsymbol{S}_m\right) \leq 0 \\ &\zeta \in [0,\, 1] \end{aligned} \tag{6.20}$$

This formulation means that if e.g. $\zeta = 40$ % of the capacity is used carrying the in-plane stresses (f_σ), $1-\zeta = 60$ % of the capacity remains for the section moments. A set of in-plane stresses and section moments satisfying (6.20) is safe compared to the exact yield envelope.

Using the Mohr-Coulomb criterion for plane stress with a tension cut-off, $\boldsymbol{S}_\sigma$ represents the uniaxial compressive strength f_c as well as the tensile strength f_t, and the criterion can be stated as follows in principal stresses:

$$\begin{aligned} \sigma_1 &\leq \zeta f_t \\ k\sigma_1 - \sigma_2 &\leq \zeta f_c \\ \sigma_2 &\leq \zeta f_c \end{aligned} \tag{6.21}$$

For reinforced concrete slabs, Johansen's criterion is commonly used (see e.g. Johansen, 1962; Nielsen and Hoang, 2010). Reducing the moment capacities by $(1-\zeta)$, the criterion can be stated as:

$$\begin{aligned} -\left((1-\zeta)\, m_{px}^{+} - m_x\right)\, \left((1-\zeta)\, m_{py}^{+} - m_y\right) + m_{xy}^2 \leq 0 \\ -\left((1-\zeta)\, m_{px}^{-} + m_x\right)\, \left((1-\zeta)\, m_{py}^{-} + m_y\right) + m_{xy}^2 \leq 0 \end{aligned} \tag{6.22}$$

where m_x, m_y, and m_{xy} are the moment about the x-axis, the y-axis, and the twisting moment, respectively. The positive moment capacities are denoted m_p^+, while m_p^- denotes the negative moment capacities. All capacities are reduced by a factor of $(1-\zeta)$. Introducing four auxiliary variables,

$$\begin{aligned} \alpha_1 &= \frac{1}{\sqrt{2}}\left((1-\zeta)\, m_{px}^{+} - m_x\right) \geq 0, \quad \alpha_2 = \frac{1}{\sqrt{2}}\left((1-\zeta)\, m_{py}^{+} - m_y\right) \geq 0, \\ \alpha_3 &= \frac{1}{\sqrt{2}}\left((1-\zeta)\, m_{px}^{-} + m_x\right) \geq 0, \quad \alpha_4 = \frac{1}{\sqrt{2}}\left((1-\zeta)\, m_{py}^{-} + m_y\right) \geq 0, \end{aligned}$$

the criterion (6.22) can be rewritten as

$$\begin{aligned} 2\,\alpha_1\alpha_2 \geq m_{xy}^2 \\ 2\,\alpha_3\alpha_4 \geq m_{xy}^2 \end{aligned} \tag{6.23}$$

which has the shape of two rotated quadratic cones, see Section 2.3.

Layer-based criterion

A layer-based approach will make it possible to approximate the actual yield envelope of the shell. The approach is similar to the one presented by Larsen (2010), however, in this case the transverse shear stress is not considered. This means that the problem can be formulated for second-order cone programming rather than semidefinite programming. Moreover, the reinforcement is treated as separate layers which give a more accurate description of the composite material.

We consider a plane shell of reinforced concrete seen in Figure 6.6. The shell is reinforced in the top and bottom in both the x and the y-directions. The location of the reinforcement in the cross section is given by d_t for the top and d_b for the bottom. The shell is divided into n layers, where t_i defines the thickness of the ith layer, and z_i defines the distance from the centre of the ith layer to the centre of the shell. The shell has a total thickness of $t = \sum t_i$ as shown in Figure 6.6.

The shell cross section is subjected to in-plane forces, N_x, N_y and V_{xy} as well as moments m_x, m_y, and m_{xy}, which are all carried by the stresses in

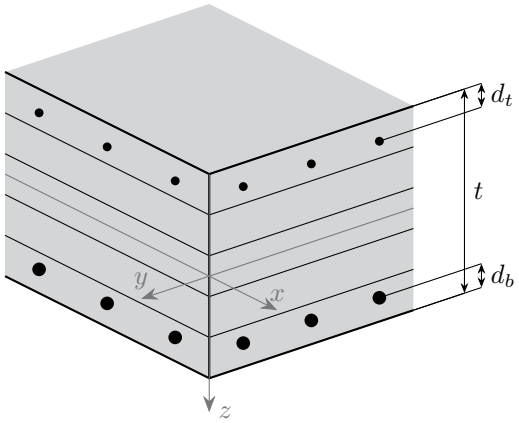

***Figure 6.6**: Reinforced concrete shell split into five layers. Origin of the local coordinate system is located in the centre of the shell.*

the n layers. Each layer is assumed to be in plane stress, i.e. the stress state is defined by σ_x, σ_y, and τ_{xy}. The relation between the section forces and stresses is given as

$$N_x = \sigma_x t = A_{stx}\sigma_{stx} + A_{sbx}\sigma_{sbx} + \sum_{i=1}^{n} \sigma_{xi} t_i \tag{6.24a}$$

$$N_y = \sigma_y t = A_{sty}\sigma_{sty} + A_{sby}\sigma_{sby} + \sum_{i=1}^{n} \sigma_{yi} t_i \tag{6.24b}$$

$$V_{xy} = \tau_{xy} t = \sum_{i=1}^{n} \tau_{xyi} t_i \tag{6.24c}$$

where A_{st} and A_{sb} are the reinforcement areas per unit length in the top and bottom of the shell, respectively. Likewise, σ_{st} and σ_{sb} are the reinforcement stresses in the top and bottom. As seen in (6.24c), it is assumed that the shear is solely carried by the concrete and the reinforcement only carries axial forces. The relation between the section moments and layer stresses are given as follows:

$$m_x = A_{stx}\sigma_{stx}\left(d_t - \frac{t}{2}\right) + A_{sbx}\sigma_{sbx}\left(\frac{t}{2} - d_b\right) + \sum_{i=1}^{n} \sigma_{xi} t_i z_i \tag{6.25a}$$

$$m_y = A_{sty}\sigma_{sty}\left(d_t - \frac{t}{2}\right) + A_{sby}\sigma_{sby}\left(\frac{t}{2} - d_b\right) + \sum_{i=1}^{n} \sigma_{yi} t_i z_i \tag{6.25b}$$

$$m_{xy} = \sum_{i=1}^{n} \tau_{xyi} t_i z_i \tag{6.25c}$$

where z_i and t_i are constants defined based on the layers, thus, (6.25) represents a set of linear equations, which fit the format of the optimisation problem.

Each layer is treated as an unreinforced concrete panel loaded in plane stress. Tension in the discrete reinforcement enables confinement in the concrete layers within the limits of the equations (6.24). The stress state in a given layer must satisfy the Mohr-Coulomb criterion for plane stress, see Section 3.3. The reinforcement is assumed to only carry tension, hence, the criterion for the four reinforcement stresses can be stated as

$$\begin{aligned} 0 \leq \sigma_{stx} \leq f_y \\ 0 \leq \sigma_{sbx} \leq f_y \\ 0 \leq \sigma_{sty} \leq f_y \\ 0 \leq \sigma_{sby} \leq f_y \end{aligned}$$

where f_y is the uniaxial yield strength of the reinforcement.

An external moment λm_x^0 and axial force λN_x^0 is applied and the layer-based criterion for shells used to compute the yield envelope. For the analysis, the layers are distributed evenly and the following parameters are used:

$$\begin{aligned} &f_c = 30 \text{ MPa}, \ f_t = 0, \ k = 4, \ t = 300 \text{ mm}, \ d_b = d_t = 30 \text{ mm} \\ &f_Y = 500 \text{ MPa}, \ A_{stx} = 500 \text{ mm}^2/\text{m}, \ A_{sbx} = 1000 \text{ mm}^2/\text{m}, \\ &A_{sty} = 200 \text{ mm}^2/\text{m}, \ A_{sby} = 1500 \text{ mm}^2/\text{m} \end{aligned}$$

The load factor λ is sought to be maximised to obtain the yield envelope.

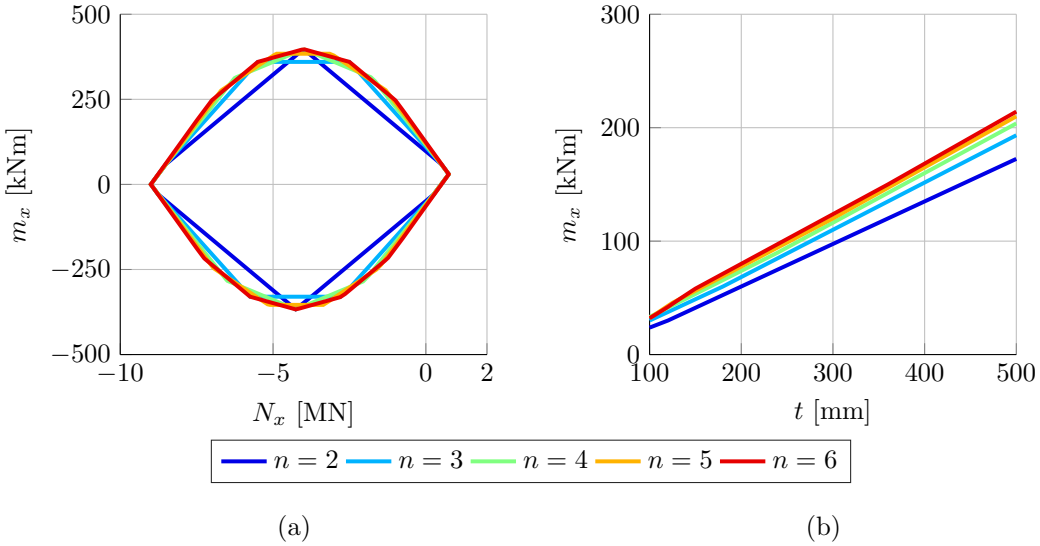

***Figure 6.7**: a) Yield envelope for the shell illustrated for N_x and m_x with $t = 300$ mm. b) Moment capacity for varying t for the shell with $N_x = 0$.*

Figure 6.7(a) shows the yield envelope for the layer-based yield criterion for shells together with the exact criterion for concrete beams. It is observed that the number of layers affects the accuracy of the layer-based criterion to some degree: Using two layers gives a rather crude approximation consisting of four straight line segments, however, the difference between the yield envelope for $n = 5$ and 6 is marginal. Figure 6.7(b) shows the moment capacity as a function of the thickness of the shell, t. The moment capacity generally increase with the number of layers, which is to be expected .

6.3.4 Examples

Two examples will be presented, namely the cantilever steel beam and the four-storey stairwell, both analysed in Section 4.1.5 using the lower bound plane stress element. The different yield criteria will be analysed using the presented shell element and the results will be compared to the results of the generalised plane stress element to assess the contribution of the plate bending component.

The layer-based criterion has also been implemented using the von Mises criterion, however, as discussed in the previous section it is expected that the simplified shell criteria provide decent estimates of the capacity for steel.

Cantilever steel I-beam

The cantilever steel I-beam was presented in Section 4.1.5 using the generalised plane stress element. The model here is identical: The beam is supported at the left end and subjected to a uniformly distributed load acting in the centreline on the top of the web.

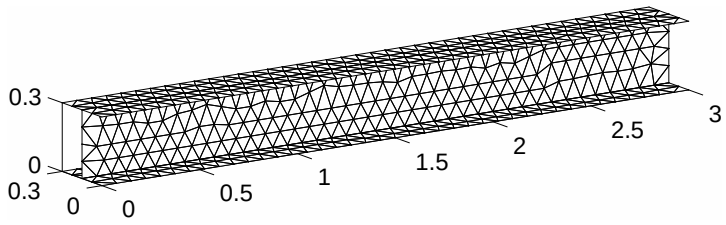

***Figure 6.8**: Medium mesh density of the I-beam using 948 elements.*

The material is modelled using the layer-based criterion with the von Mises criterion for the individual layers, and the yield strength is chosen as $f_y = 250$ MPa. The web has a height of 300 mm while the flanges has a width of 300 mm. The elements have a thickness 10 mm and the beam has length of 3 metres. The beam is analysed using four different mesh densities.

***Table 6.2**: Computed line load p in kN/m for the generalised plane stress element and the shell element using the layer-based yield criterion. Computational time in seconds is listed as well.*

Mesh:	Coarse	Medium	Fine	Very fine
Number of elements:	238	948	3,616	14,646
Plane stress	63.24	64.18	64.90	65.24
t [s]	0.28	0.95	4.47	21.38
Shell: Layer ($n = 2$)	65.07	64.87	65.41	65.54
t [s]	0.80	2.86	14.72	80.82
Shell: Layer ($n = 3$)	65.08	64.87	65.41	65.55
t [s]	0.33	1.71	18.23	104.66

Table 6.2 shows that the shell element gives slightly larger limit loads which is to be expected. Moreover, it is seen that the number of layers used for the yield criterion hardly affects the limit load in this case due to the in-plane behaviour being dominant.

The computational time of the shell element is significantly larger due to the additional equations for the moment continuity and the complex yield function. It is also observed that the number of layers increase the computational time for the fine and very fine mesh, which again is due to the additional constraints.

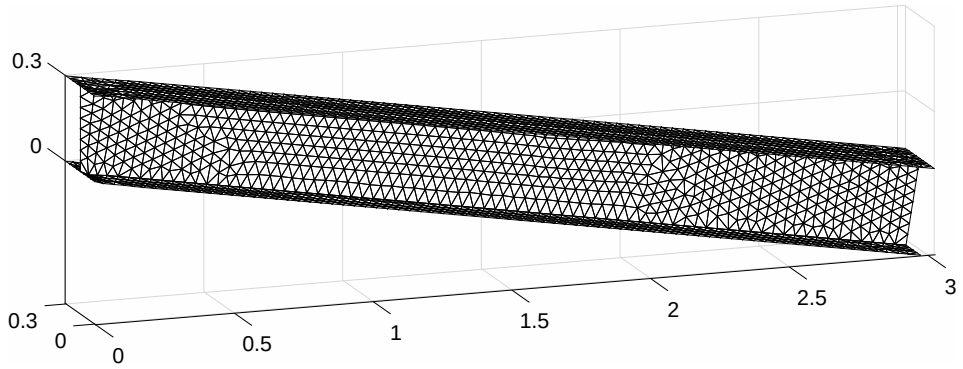

***Figure 6.9**: Collapse mode of the cantilever I-beam using the mixed shell element and the fine mesh (3616 elements).*

Figure 6.9 shows the collapse mode of the I-beam. The beam displays a bending failure near the support which allows the beam to start rotating. The collapse mode is given by the solution to the dual problem. The solution only

gives the direction and relative magnitude of the displacements and strains, and the solution can be scaled for a better visualisation of the failure mode.

The flanges and web of the beam have a 10 mm thickness which cause some numerical problems when using more than three layers. A low thickness leads to badly scaled constraints as the term $z_i t_i$ in (6.25) is proportional to the square of the thickness. The equations for the in-plane behaviour, on the other hand, scale linearly with the thickness, hence, the generalised plane stress element is less prone to badly scaled constraints.

Four-storey stairwell subjected to shear and torsion

This example has been analysed using the generalised plane stress element in Section 4.1.5 and in Section 5.3, where the joint element for triaxial stress was used to represent the in-situ cast corner joints. The stairwell will be analysed using the shell element as well, and the results will be compared to the results of the generalised plane stress element.

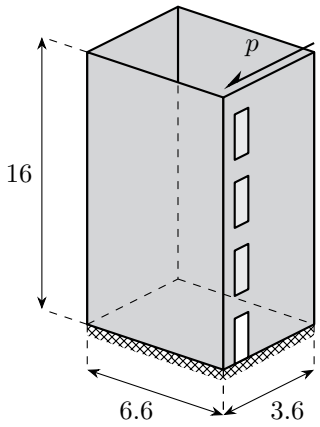

***Figure 6.10**: Four-storey stairwell subjected to a shear force which induces shear and torsion in the structure. Dimensions are given in metres.*

The dimensions of the stairwell are shown in Figure 6.10 and the door openings have a height of 2.10 metres and a width of 0.90 metres. A shear load is applied on the top boundary of the wall with the door openings which induces shear and torsion into the structure. The walls have a thickness of 180 mm and are reinforced with two layers of Ø8 rebars per 150 mm, which both have cover layers of 25 mm concrete.

The reinforcement has a design yield strength of 458 MPa. The concrete has a design compressive strength of 21.43 MPa and the tensile strength is taken as zero. The stairwell is analysed using the simplified yield criteria as well as the layer based criterion, and the results are listed in Table 6.3.

***Table 6.3**: Limit shear load p in kN/m for the stairwell example: Comparison of the generalised plane stress element and the shell element with various yield criteria. Results marked with * indicate that the solver stalled and was unable to reach a solution.*

Mesh:	Coarse	Medium	Fine
Number of elements:	864	3,564	11,379
Plane stress	85.27	88.62	89.25
t [s]	2.15	14.78	56.53
Shell: Combined	99.97	100.36	99.29
t [s]	3.96	26.75	99.31
Shell: Separate	104.08	102.31	99.93
t [s]	2.85	12.03	50.11
Shell: Layer ($n = 4$)	101.87*	100.31*	99.52*
t [s]	7.49	39.65	153.27
Shell: Layer ($n = 5$)	102.34*	98.89*	99.00*
t [s]	7.80	42.32	154.50

In contrary to the cantilever beam example, the shells of the stairwell example have a considerable moment capacity. It is therefore expected that the shell element yields a larger limit load than the plane stress element, which disregards the moment capacity completely. Table 6.3 shows that the shell element gives a capacity of 99 kN/m to 104 kN/m depending on the mesh and yield criterion.

The simplified yield criterion (6.20) combines the in-plane behaviour and plate bending in a linear manner and will give a lower bound to the limit load. The separate criterion (6.19), on the other hand, gives a higher capacity, but the capacity decreases for the finer meshes. Layer-based yield criterion appears to give results in-between the combined and the separate criteria, however, the layer-based yield criterion cause some numerical issues and the solver stalls before reaching optimality. The quality of the solutions marked with * will therefore vary considerably.

The layer-based criterion require the most constraints, hence, it is expected that the computational time will be larger. Compared to the plane stress element, the layer-based criterion requires almost three times the computational time. It is remarkable, however, that the computational time of the separate yield criteria is smaller than the plane stress element for the

medium and fine meshes despite the additional equations for the plate bending behaviour.

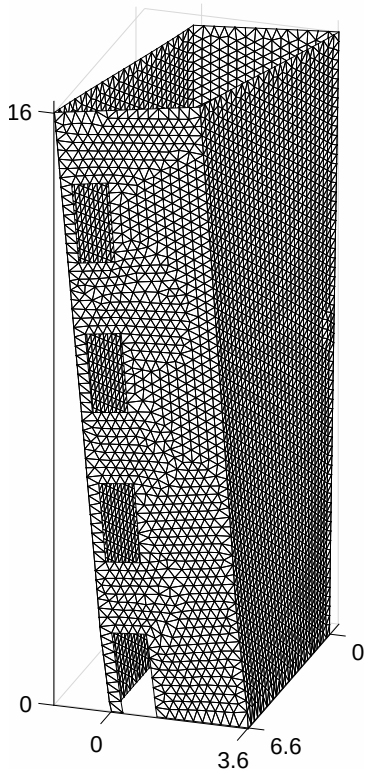

***Figure 6.11**: Collapse mode of the stairwell using the mixed shell element and the fine mesh (11,379 elements).*

From Figure 6.11, it is observed that all walls are activated and contributes to the overall resistance of the stairwell. The stairwell fails in a combination of shear and bending. The wall with the door openings will necessarily experience the largest displacements as the load is acting on the top boundary.

6.4 Mixed solid element

For the overall load distribution and capacity of precast concrete structures, two-dimensional elements, e.g. plane stress elements or shells, are usually preferred, and modelling using solid elements is rarely used. Nevertheless, solid modelling can be used within the present framework for e.g. assessment of the capacity of complicated joints. Solids are, on the other hand, widely

used in the field of geotechnical engineering (see e.g. Krabbenhoft et al., 2005; Krabbenhøft et al., 2008; Makrodimopoulos and Martin, 2008).

Similar to how triangular elements are preferred for two-dimensional problems, tetrahedral elements are generally preferred for three-dimensional. A linear stress field is commonly used and the stresses are checked at the four vertexes of the tetrahedron. Lyamin and Sloan (2002a) presented a lower bound tetrahedron and two approximation of the Mohr-Coulomb criterion, namely a linearisation and a non-linear, smooth version. Upper bound tetrahedral elements were presented by Yu et al. (1994), Lyamin and Sloan (2002b), and Krabbenhoft et al. (2005), again using the Mohr-Coulomb criterion. Larsen (2010) also presented a version of the lower bound tetrahedron as well as the semidefinite formulation of the Mohr-Coulomb criterion for reinforced concrete.

6.4.1 Equilibrium

This section presents a novel mixed tetrahedron, which is based on the same relaxation of the traction continuity as the plane stress element presented in Section 6.2. Two yield criteria will be presented, namely a criterion for reinforced concrete based on the Mohr-Coulomb criterion (see Larsen, 2010) and the Drucker-Prager criterion, which is commonly used for soils.

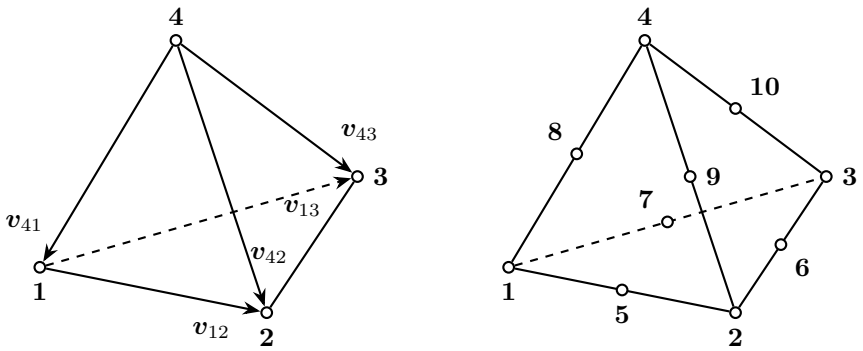

***Figure 6.12**: (a) Geometry of the elements including the geometric nodes. (b) The 10 displacement nodes representing the quadratic displacement field.*

The geometry of the element is defined by the four corner nodes, see Figure 6.12(a). Associated with each corner node is a stress vector which comprises the six unique stress variables,

$$\boldsymbol{\sigma}_j = \begin{bmatrix} \sigma_x & \sigma_y & \sigma_z & \tau_{xy} & \tau_{zx} & \tau_{yz} \end{bmatrix}^T,$$

where j is the node number. The element stress vector is given as

$$\boldsymbol{\sigma}_{el} = \begin{bmatrix} \boldsymbol{\sigma}_1 \\ \boldsymbol{\sigma}_2 \\ \boldsymbol{\sigma}_3 \\ \boldsymbol{\sigma}_4 \end{bmatrix}$$

In the following, face i of an element refers to the face opposite node i. For each face, a normal vector is calculated from the vectors $\boldsymbol{v}$ seen in Figure 6.12(a):

$$\begin{aligned} \hat{\boldsymbol{n}}^1 &= 2A_1\boldsymbol{n}^1 = \boldsymbol{v}_{42} \times \boldsymbol{v}_{43} \\ \hat{\boldsymbol{n}}^2 &= 2A_2\boldsymbol{n}^2 = \boldsymbol{v}_{43} \times \boldsymbol{v}_{41} \\ \hat{\boldsymbol{n}}^3 &= 2A_3\boldsymbol{n}^3 = \boldsymbol{v}_{41} \times \boldsymbol{v}_{42} \\ \hat{\boldsymbol{n}}^4 &= 2A_4\boldsymbol{n}^4 = \boldsymbol{v}_{13} \times \boldsymbol{v}_{12} \end{aligned} \tag{6.26}$$

where A_i is the surface area of face i, and $\boldsymbol{n}_i$ are unit normal vectors implicitly defined in (6.26). The stress-to-traction matrix can be stated as

$$\mathbf{P}_i^T = \begin{bmatrix} n_x^i & 0 & 0 & n_y^i & n_z^i & 0 \\ 0 & n_y^i & 0 & n_x^i & 0 & n_z^i \\ 0 & 0 & n_z^i & 0 & n_x^i & n_y^i \end{bmatrix} \tag{6.27}$$

and

$$\hat{\mathbf{P}}_i^T = 2A_i\mathbf{P}_i^T = \begin{bmatrix} \hat{n}_x^i & 0 & 0 & \hat{n}_y^i & \hat{n}_z^i & 0 \\ 0 & \hat{n}_y^i & 0 & \hat{n}_x^i & 0 & \hat{n}_z^i \\ 0 & 0 & \hat{n}_z^i & 0 & \hat{n}_x^i & \hat{n}_y^i \end{bmatrix}$$

The tractions on face i at node j can be calculated as $\mathbf{P}_i^T\boldsymbol{\sigma}_j$, where $\boldsymbol{\sigma}_j$ is the stress vector associated with node j.

The mixed element has a linear stress field and, therefore, a quadratic displacement field. The element is a relaxed version of the lower bound tetrahedron (see Lyamin and Sloan, 2002a; Larsen, 2010). Similarly to the mixed plane stress element presented in Section 6.2, the strict traction continuity has been relaxed by distributing the tractions to the six nodes of a face according to the quadratic displacement field. The contribution to the nodal force in node j from face i can be calculated using the same approach as in Equation (6.2):

$$\boldsymbol{q}_j^i = \int_{A_i} N_j^i(\xi,\eta)\,\boldsymbol{t}_i(\xi,\eta)\,\partial\eta\partial\xi \tag{6.28}$$

where ξ and η are area coordinates, $N_j^i(\xi,\eta)$ is the quadratic shape function for node j for face i, and $\boldsymbol{t}_i(\xi,\eta)$ are the tractions on face i. The shape functions and integration are similar to the plane case. The tractions on each face contributes to six nodes, and the contributions are summed to obtain the element equilibrium matrix for the mixed element.

The element may be subject to volume loads $V\gamma_i$, where V is the volume of the element. This gives rise to three differential equations,

$$\begin{aligned}
\frac{\partial \sigma_x}{\partial x} + \frac{\partial \tau_{xy}}{\partial y} + \frac{\partial \tau_{zx}}{\partial z} + \gamma_x V = 0,\\
\frac{\partial \tau_{xy}}{\partial x} + \frac{\partial \sigma_y}{\partial y} + \frac{\partial \tau_{yz}}{\partial z} + \gamma_y V = 0,\\
\frac{\partial \tau_{zx}}{\partial x} + \frac{\partial \tau_{yz}}{\partial y} + \frac{\partial \sigma_z}{\partial z} + \gamma_z V = 0,
\end{aligned} \tag{6.29}$$

which can be reduced by use of the linear shape functions, similarly to the internal equilibrium equations in Section 4.1.1, to obtain:

$$\frac{1}{6}\hat{\mathbf{P}}_1^T\sigma_1 + \frac{1}{6}\hat{\mathbf{P}}_2^T\sigma_2 + \frac{1}{6}\hat{\mathbf{P}}_3^T\sigma_3 + \frac{1}{6}\hat{\mathbf{P}}_4^T\sigma_4 = -V\begin{bmatrix}\gamma_x\\ \gamma_y\\ \gamma_z\end{bmatrix}$$

The element equilibrium matrix can be stated as follows:

$$\mathbf{B}_e^T = \frac{1}{120}\begin{bmatrix}
2\hat{\mathbf{P}}_2^T + 2\hat{\mathbf{P}}_3^T + 2\hat{\mathbf{P}}_4^T & -\hat{\mathbf{P}}_3^T - \hat{\mathbf{P}}_4^T & -\hat{\mathbf{P}}_2^T - \hat{\mathbf{P}}_4^T & -\hat{\mathbf{P}}_2^T - \hat{\mathbf{P}}_3^T\\
-\hat{\mathbf{P}}_3^T - \hat{\mathbf{P}}_4^T & 2\hat{\mathbf{P}}_1^T + 2\hat{\mathbf{P}}_3^T + 2\hat{\mathbf{P}}_4^T & -\hat{\mathbf{P}}_1^T - \hat{\mathbf{P}}_4^T & -\hat{\mathbf{P}}_1^T - \hat{\mathbf{P}}_3^T\\
-\hat{\mathbf{P}}_2^T - \hat{\mathbf{P}}_4^T & -\hat{\mathbf{P}}_1^T - \hat{\mathbf{P}}_4^T & 2\hat{\mathbf{P}}_1^T + 2\hat{\mathbf{P}}_2^T + 2\hat{\mathbf{P}}_4^T & -\hat{\mathbf{P}}_1^T - \hat{\mathbf{P}}_2^T\\
-\hat{\mathbf{P}}_2^T - \hat{\mathbf{P}}_3^T & -\hat{\mathbf{P}}_1^T - \hat{\mathbf{P}}_3^T & -\hat{\mathbf{P}}_1^T - \hat{\mathbf{P}}_2^T & 2\hat{\mathbf{P}}_1^T + 2\hat{\mathbf{P}}_2^T + 2\hat{\mathbf{P}}_3^T\\
8\hat{\mathbf{P}}_3^T + 8\hat{\mathbf{P}}_4^T & 8\hat{\mathbf{P}}_3^T + 8\hat{\mathbf{P}}_4^T & 4\hat{\mathbf{P}}_4^T & 4\hat{\mathbf{P}}_3^T\\
4\hat{\mathbf{P}}_4^T & 8\hat{\mathbf{P}}_1^T + 8\hat{\mathbf{P}}_4^T & 8\hat{\mathbf{P}}_1^T + 8\hat{\mathbf{P}}_4^T & 4\hat{\mathbf{P}}_1^T\\
8\hat{\mathbf{P}}_2^T + 8\hat{\mathbf{P}}_4^T & 4\hat{\mathbf{P}}_4^T & 8\hat{\mathbf{P}}_2^T + 8\hat{\mathbf{P}}_4^T & 4\hat{\mathbf{P}}_2^T\\
8\hat{\mathbf{P}}_2^T + 8\hat{\mathbf{P}}_3^T & 4\hat{\mathbf{P}}_3^T & 4\hat{\mathbf{P}}_2^T & 8\hat{\mathbf{P}}_2^T + 8\hat{\mathbf{P}}_3^T\\
4\hat{\mathbf{P}}_3^T & 8\hat{\mathbf{P}}_1^T + 8\hat{\mathbf{P}}_3^T & 4\hat{\mathbf{P}}_1^T & 8\hat{\mathbf{P}}_1^T + 8\hat{\mathbf{P}}_3^T\\
4\hat{\mathbf{P}}_2^T & 4\hat{\mathbf{P}}_1^T & 8\hat{\mathbf{P}}_1^T + 8\hat{\mathbf{P}}_2^T & 8\hat{\mathbf{P}}_1^T + 8\hat{\mathbf{P}}_2^T\\
20\hat{\mathbf{P}}_1^T & 20\hat{\mathbf{P}}_2^T & 20\hat{\mathbf{P}}_3^T & 20\hat{\mathbf{P}}_4^T
\end{bmatrix} \tag{6.30}$$

The majority of the tractions are distributed to the edge nodes (nodes 5 to 10 in Figure 6.12(b)), and in the case of a constant stress field in the given element, no nodal forces will be present for the corner nodes, since rows 1 to 4 in the element equilibrium matrix (6.30) sum to zero. The last row of (6.30) ensures the internal equilibrium of the element.

6.4.2 Yield criteria

For the solid elements, two general yield criteria for triaxial stress are considered, namely a criterion for reinforced concrete using the Mohr-Coulomb criterion, and the Drucker-Prager criterion.

Mohr-Coulomb criterion for reinforced concrete

Similar to the plane stress case in Section 4.1.4, the stresses are divided into concrete stresses and reinforcement stresses:

$$\boldsymbol{\sigma} = \boldsymbol{\sigma}_c + \hat{\boldsymbol{\sigma}}_s \tag{6.31}$$

where $\boldsymbol{\sigma}_c$ is the concrete stresses. It is assumed that the the reinforcement only carries normal stresses, hence, the equivalent reinforcement stresses $\hat{\boldsymbol{\sigma}}_s$ is defined as

$$\hat{\boldsymbol{\sigma}}_s = \begin{bmatrix} \sigma_{sx} A_{sx} \\ \sigma_{sy} A_{sy} \\ \sigma_{sz} A_{sz} \\ 0 \\ 0 \\ 0 \end{bmatrix}$$

where A_{si} is reinforcement area per unit area in the i-direction. The reinforcement is assumed to be smeared, however, if smeared reinforcement is not a reasonable assumption, 3D bar elements can be used to model the reinforcement discretely. The reinforcement stresses are checked against the uniaxial yield strength f_{yi}:

$$-f_{yi} \leq \sigma_{si} \leq f_{yi} \tag{6.32}$$

The concrete stresses must satisfy the Mohr-Coulomb yield criterion with a tension cut-off presented in Section 3.3. The criterion has a rather simple form in principal stresses which is repeated below:

$$\begin{aligned} \sigma_1 &\leq f_t \\ k\sigma_1 - \sigma_3 &\leq f_c \end{aligned} \tag{6.33}$$

where σ_1 and σ_3 are the largest and smallest principal stresses, respectively. The properties of the concrete material are given by the uniaxial tensile strength f_t, the uniaxial compressive strength f_c, and the friction parameter k. Since the criterion is formulated in principal stresses, which are the eigenvalues of the stress tensor, the criterion can be formulated exact using semidefinite programming.

Drucker-Prager criterion

The Drucker-Prager criterion can be considered as a smooth version of the Mohr-Coulomb criterion, and is often used in geotechnical engineering. The criterion is based on the first and second stress invariants, I_1 and J_2, defined as

$$I_1 = 3\sigma_v = \sigma_x + \sigma_y + \sigma_z,$$
$$J_2 = \frac{(\sigma_x - \sigma_y)^2}{6} + \frac{(\sigma_y - \sigma_z)^2}{6} + \frac{(\sigma_z - \sigma_x)^2}{6} + \tau_{xy}^2 + \tau_{zx}^2 + \tau_{yz}^2$$

The criterion can be stated as

$$\sqrt{J_2} \leq A - BI_1 \tag{6.34}$$

where A and B are constants. The criterion (6.34) has the shape of a quadratic cone and can be represented exact using second-order cone programming.

$$\begin{aligned}
&\text{Circumscribe} && A = \frac{6c\cos\theta}{\sqrt{3}\,(3-\sin\theta)}, \quad B = \frac{2c\sin\theta}{\sqrt{3}\,(3-\sin\theta)}, \\
&\text{Middle-circumscribe} && A = \frac{6c\cos\theta}{\sqrt{3}\,(3+\sin\theta)}, \quad B = \frac{2c\sin\theta}{\sqrt{3}\,(3+\sin\theta)}, \\
&\text{Inscribe} && A = \frac{3c\cos\theta}{\sqrt{9-3\sin^2\theta}}, \quad B = \frac{c\sin\theta}{\sqrt{9-3\sin^2\theta}}
\end{aligned} \tag{6.35}$$

where c is the cohesion of the material and θ is the internal angle of friction. The choice of A and B depends on if the Drucker-Prager envelope is going to circumscribe, middle-circumscribe, or inscribe the Mohr-Coulomb yield envelope as listed in (6.35).

The difference between the three sets of constants varies with the internal angle of friction, θ. Figure 6.13(b) shows the yield envelope for some typical values of concrete, and it is observed that the red line which circumscribes the Mohr-Coulomb yield envelope will give significantly larger capacities in compression. The blue and black lines will give lower results in case of uniaxial compression compared to the yield envelope of the Mohr-Coulomb criterion. If the internal angle of friction is zero degrees, the constant B will be zero and (6.34) will be identical to the von Mises criterion.

6.4.3 Example

A rebar with a diameter of 25 mm is embedded in a $200 \times 200 \times 200$ mm concrete cube. The rebar is modelled as a von Mises material using the Drucker-

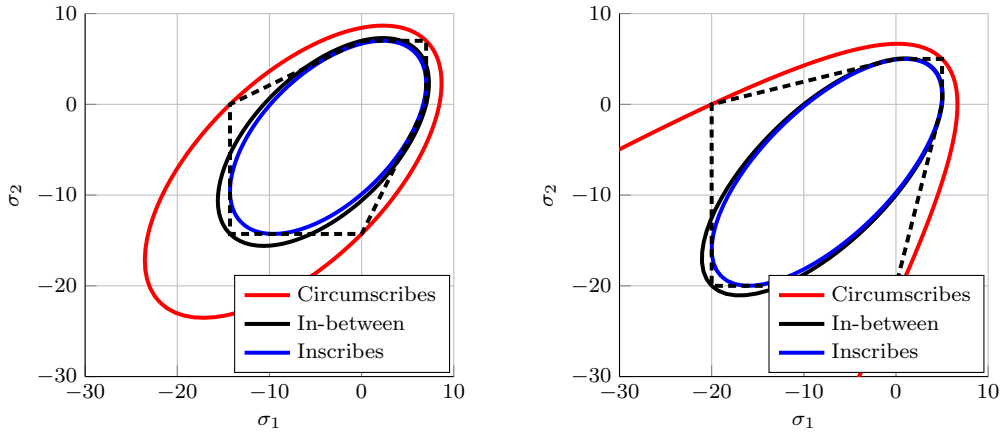

(a) $\theta = 20°$, $c = 5$ MPa. (b) $\theta = 37°$, $c = 5$ MPa.

***Figure 6.13**: Comparison of the Mohr-Coulomb criterion (dashed line) and the Drucker-Prager criterion for plane stress using different values of A and B shown in principal stresses.*

Prager criterion with a friction angle of $\theta = 0$ and $f_y = 2\,c = 500$ MPa, while the concrete cube is modelled using the Mohr-Coulomb criterion with $f_c = 20$ MPa and $k = 4$ corresponding to $\theta \approx 37°$, while no additional limit for the tensile strength is considered. For comparison, the concrete is also modelled using the Drucker-Prager criterion with the three different sets of constants, A and B, see (6.35), with $\theta = \arctan(3/4) \approx 37°$ and $c = 5$ MPa (equivalent to the uniaxial compressive strength of 20 MPa for the Mohr-Coulomb criterion). No special consideration has been given to the interface between the rebar and the concrete, and a perfect bond is assumed.

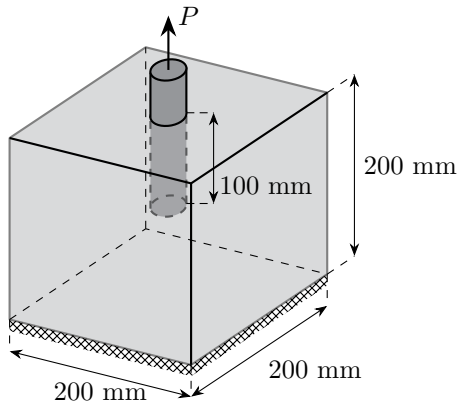

***Figure 6.14**: Pull out of the Ø25 rebar embedded in a concrete cube.*

The rebar is embedded 100 mm into the concrete cube as illustrated in Figure 6.14 which also shows the load and support conditions. The yield strength of the rebar is chosen sufficiently large to ensure failure in the concrete. The separation criterion is not implemented for the Drucker-Prager criterion, hence, to be able to compare the two criteria, no tension cut-off is used for the Mohr-Coulomb criterion. The model is analysed using three different meshes, one structured and two free.

***Table 6.4**: Limit load P for the pull out of a rebar embedded in concrete using different material models and meshes (load given in kN).*

	Structured	Free	
Material	$nel = 2628$	$nel = 1649$	$nel = 6422$
Mohr-Coulomb	140.8	130.6	137.7
Drucker-Prager			
Circumscribes	189.2	183.3	195.9
Middle-circumscribes	104.4	98.0	101.4
Inscribes	101.7	95.3	98.5

Table 6.4 shows that the model approaches the limit load from below as the free mesh with 1649 elements give the lowest capacity. The structured mesh yields the largest capacity for the Mohr-Coulomb material as well as for two versions of the Drucker-Prager criterion. Moreover, a significant difference is seen between the three versions of the Drucker-Prager criterion, where the yield envelope circumscribing the Mohr-Coulomb criterion gives almost double the capacity.

Figure 6.15 shows the failure modes using the Drucker-Prager and Mohr-Coulomb criteria. A clear difference is observed between the two criteria: The displacements occur in close proximity to the rebar for the model using the Drucker-Prager criterion, while a cone shape is seen for the Mohr-Coulomb criterion which corresponds better to the failure modes observed for experiments.

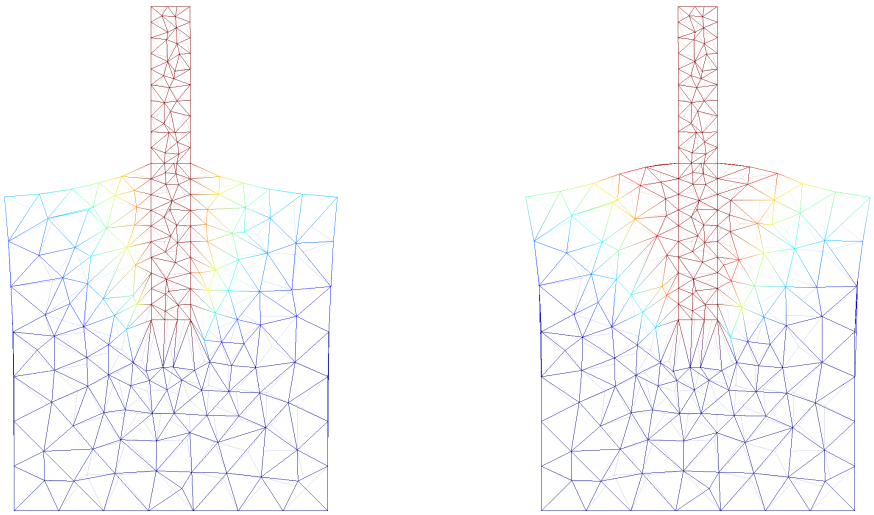

(a) Drucker-Prager (inscribing) (b) Mohr-Coulomb

***Figure 6.15**: Failure modes for the pull out of a rebar embedded in concrete using the fine free mesh with 6422 elements. The colour represents the relative magnitude of the displacements, and red indicates the largest displacements.*

Chapter 7

Conclusions and future work

Despite an increased preference of clients for architecturally complex structures and the extensive use of computer-aided drawing software in practice, concrete structures - and especially precast concrete structures - are often designed by manual methods or simple numerical tools in the ultimate limit state. The current practice is to design the joints as the weakest part of the structure, which makes analysis by general purpose finite element software difficult and inaccurate. Within the framework of finite element limit analysis, several finite elements and mechanical models have been developed to facilitate efficient modelling of precast concrete structures. Summary and conclusions of the research conducted is given in the following section.

7.1 Conclusions

Identification of the critical mechanisms of shear joints in 2D

The behaviour of joints in precast concrete structures is one of the main topics of the present thesis. In order to develop an adequate joint model, identification of the critical mechanisms inside the joint was necessary. For this purpose, a detailed model based on lower bound finite element limit analysis was presented in Section 4.3 and Paper I.

The detailed model was validated by comparison to experimental results, and satisfactory agreement was found with an average error of just -4.3 per cent. The model was able to capture the effect of the discontinuous layout of the U-bars to a reasonable degree. The failure mode was interpreted from the dual solution to the optimisation problem, i.e. the solution to the corresponding kinematic problem.

From the the determined stress fields, it can be concluded that direct strut action is the primary load carrying mechanism of keyed shear joints,

however, the reinforcement layout affects the struts and a discontinuous layout will disrupt the distinct struts. Local failures near the keys as well as diagonal failure zones likewise indicate direct strut action. Moreover, it can be concluded that localised failure zones between the U-bar loops may occur as a consequence of the discontinuous reinforcement layout.

The detailed model provides a satisfactory estimate of the capacity and the determined failure mode corresponds to the observed failures of the experiments. The model, however, is rather heavy, computationally speaking, and a simple mechanical model is needed to facilitate modelling of real size structures.

Development of a simplified model for shear joints in 2D

Section 4.4 and Paper II presented a multiscale lower bound joint element. The element uses a mechanical submodel as an advanced yield function, which makes it possible to account for the local behaviour of the joint - identified by the detailed model - on the structural level.

The mechanical submodel is based on the stringer method. Three independent stringer models formed the basis of the submodel, and by adding the stress fields of the three stringer models, the resulting stress field in the joint is obtained, which is then checked against the appropriate yield criterion.

The multiscale joint element was validated by comparison to the detailed model, and excellent agreement was found. The joint element captures the same behaviour as the detailed model, including the effect of the discontinuous reinforcement layout. The results of the joint element was also compared to experimental results, and satisfactory agreement was found here.

The joint element poses a small mathematical optimisation problem which is solved in a fraction of a second, and it can therefore be concluded that the presented multiscale joint element enables modelling of real size precast structures while accounting for the complex behaviour of the in-situ cast joints.

Extension of the findings to the three-dimensional case

Taking the three-dimensional behaviour of structures into account will necessarily increase the capacity of the considered structure. The findings and lower bound finite elements presented for the two-dimensional case in the present thesis were generalised to three dimensions and an adequate multiscale joint model for the behaviour of the in-situ cast joints was developed, see Section 4.5 and Paper IV.

A lower bound macro joint element was formulated, and the element is compatible with the three-dimensional plane stress element, presented in Section 4.1.3 and Paper III. The element uses a mechanical submodel to account for the local behaviour. The submodel utilises concrete corbels inside the joint in order to activate the loop reinforcement and to transfer shear from one structural plane to another. The resulting triaxial stress field of the joint is checked against the Mohr-Coulomb criterion.

A brief analysis of the three-dimensional and the two-dimensional joint was conducted to assess the behaviour in two-dimensions. For the three-dimensional case a parameter study with commonly used reinforcement lay-outs and concrete strengths was conducted, and the results are compared to the Eurocode design equation. Surprisingly, the results of the joint model and Eurocode were relatively close even though the Eurocode equation only considers a criterion for the interface.

It is concluded that the corbel mechanisms produce rather conservative lower bound for the two-dimensional case, which is to be expected. The corbels appear to be a reasonable choice of mechanism for transfer of shear in three-dimensions, and it can be concluded that it is necessary to consider the three-dimensional stress field of the joint for design and analysis.

Framework for design

Two examples of real size structures were given in Chapter 5. First, a four-storey shear wall with three door openings was analysed using the lower bound plane stress element and the two-dimensional joint element and sub-model. The wall was subjected to design loads prescribed by the Eurocode. The material and reinforcement parameters have been chosen based on a conventional design using manual methods.

The model was analysed for varying mesh densities, and the determined load factors increased slightly with the mesh density which was to be expected for a lower bound model. The critical load case, load case 2, gave a load factor 3.48, i.e. the shear wall can sustain a horizontal load more than three times larger than the design load. The two other load cases gave load factors of 5.09 and 6.27, respectively.

It was seen from the stress plots that the forces were transferred via strut action to the supports of the structure. Moreover, the dual solution was used to visualise the failure mode of the shear wall. The joints affected the stress field to some degree, however, their influence on the failure mode was clear: Separation occurred in some of the horizontal joints of the structure, combined with a diagonal failure zone in the bottom storey for load cases 1 and 3.

The second example was concerned with a four-storey precast concrete stairwell with door openings. The precast panels were modelled using the 3D plane stress element and connected in the corners by in-situ cast joints modelled by the developed 3D joint element. The stairwell was subjected to shear and torsion and analysed for varying joint reinforcement degrees.

For low reinforcement degrees in the joints, the entire joint from the foundations to the top of the structure was fully utilised, which will lead to some extreme requirements to the ductility of the joints and panels. At higher levels of reinforcement, the model yielded a capacity only a few per cent lower than the capacity of the monolithic structure. The robustness of the structure increased at the higher levels of joint reinforcement, as only a small portion of the joint was utilised fully which lowered the requirement to the ductility of the joints and panels.

From the two examples, it can be concluded that the joints play a vital roll in the overall behaviour of precast concrete structures and that the presented models and elements are capable of modelling real size structures in an efficient manner. Finally, it is concluded that the presented framework based on finite element limit analysis has significant potential to enable fast and efficient design of precast concrete structures in the near future.

7.2 Future work

The recommendations for future work can be split into two groups: Experimental work on joints and precast structures, and model development to extend and mature the presented framework. This section will highlight some of the areas where further research is needed and attempt to give recommendations.

Experimental work

The developed joint elements attempt to describe the influence of reinforcement layout. An optimal layout cannot be ensured by the current practice, however, nearly all published experiments uses a reinforcement layout where the U-bar loops are placed closely together:

- Additional experimental work on joints in two-dimensions with suboptimal reinforcement layout is needed. Only few experiments consider this phenomenon, but a clear influence has been reported (see Hansen and Olesen, 1976).
- For the three-dimensional case, basic investigations of the mechanisms of shear transfer in the three-dimensional case are needed. To the best

knowledge of the author, no experiments on corner joints have been published, hence, analytical and numerical models cannot be validated. For practical use of the developed three-dimensional joint model, such validation by comparison to experiments is needed.

- A new design of the classical, two-dimensional U-bar joint is presently being developed at the Technical University of Denmark (Sørensen et al., 2016). The results are promising, and findings can hopefully be extended to the design and behaviour of joints in three-dimensions, where ductility of joints is crucial for the robustness.

- Manual methods based on limit analysis have been used in practice for decades. The numerical framework presented here, however, enables structural optimisation on a completely different level, and the structural design can easily be pushed to the limit. This is shown in the example in Section 5.3, where all joints are fully utilised over the entire height of the building when using a low reinforcement degree. This poses some requirements to the ductility of the entire structure - not just locally - and to the best knowledge of the author, no experimental work on the interaction and ductility of large precast structures have been published.

Model development

The present framework presented a novel concept within the field of finite element limit analysis, namely the multiscale elements. The concept enables modelling of local phenomena for the individual elements to be accounted for on the structural model level.

- An extension of the submodel for the three-dimensional joint element is needed. The presented corbel model handles the two-dimensional case as well, but the obtained results are rather conservative compared to the results of the two-dimensional submodel. The framework of the submodel makes it possible to add additional models, and the resulting stress field should be updated accordingly.

- Adequate submodels for e.g. beams can be developed to account for local behaviour. The Eurocode prescribes several loads and moments based on tolerances that need to be treated locally for the individual structural components. Such effects can be included within the submodel concept and can therefore be accounted for on the global model level.

- Structures are designed for a multitude of load cases. For load optimisation, the load cases can be handled individually, however, for material optimisation, it is not the case. A general purpose optimisation solver has been used for the work presented in this thesis, however, to be able to treat multiple load cases efficiently, specialised solvers should be developed. The mathematical optimisation problem of finite element limit analysis with multiple load cases will have a distinct structure, which likely can be exploited by specialised solvers

- Mixed elements were discussed in Chapter 6. The elements do not provide rigorous bounds to the exact limit load, but they are more accurate compared to lower and upper bound elements and often more stable in a numerical sense. The presented joint elements could be extended to mixed formulations to be able to provide increased accuracy.

- Last but not least, material optimisation has a considerable potential for practical applications. The presented framework is only concerned with load optimisation, however, the framework can be extended to cover material optimisation as well.

Bibliography

Alizadeh, F. and Goldfarb, D. (2003). Second-order cone programming. *Mathematical programming*, 95(1):3–51.

Anderheggen, E. and Knöpfel, H. (1972). Finite element limit analysis using linear programming. *International Journal of Solids and Structures*, 8:1413–1431.

Andersen, K. D. and Christiansen, E. (1995). Limit analysis with the dual affine scaling algorithm. *Journal of computational and Applied Mathematics*, 59(2):233–243.

Andersen, K. D., Christiansen, E., Conn, A. R., and Overton, M. L. (2000). An efficient primal-dual interior-point method for minimizing a sum of euclidean norms. *SIAM Journal on Scientific Computing*, 22(1):243–262.

Antoniou, A. and Lu, W.-S. (2007). *Practical optimization: algorithms and engineering applications*. Springer Science & Business Media.

Belytschko, T. and Hodge, P. (1970). Plane stress limit analysis by finite elements. *Journal of the Engineering Mechanics Division*, 96(6):931–944.

Bhatt, P. (1973). Influence of vertical joints on behaviour of precast shear walls. *Building Science*, 8:221–224.

Bisbos, C. and Pardalos, P. (2007). Second-order cone and semidefinite representations of material failure criteria. *Journal of Optimization Theory and Applications*, 134(2):275–301.

Bljuger, F. (1976). Determination of deformability characteristics of vertical shear joints in precast buildings. *Building and Environment*, 11:277–282.

Borges, L. A., Zouain, N., and Huespe, A. E. (1996). A nonlinear optimization procedure for limit analysis. *European Journal of Mechanics Series A Solids*, 15:487–512.

Boyd, S. P. and Vandenberghe, L. (2004). *Convex Optimization*. Cambridge University Press.

Cholewicki, A. (1971). Loadbearing capacity and deformability of vertical joints in structural walls of large panel buildings. *Building Science*, 6:163–184.

Christiansen, E. (1986). On the collapse solution in limit analysis. *Archive for Rational Mechanics and Analysis*, 91(2):119–135.

Christiansen, E. and Andersen, K. D. (1999). Computation of collapse states with von mises type yield condition. *International Journal for Numerical Methods in Engineering*, 46(8):1185–1202.

Christoffersen, J. (1997). *Ultimate Capacity of Joints in Precast Large Panel Concrete Buildings*. PhD thesis, Technical University of Denmark.

Cook, R. D., Malkus, D. S., Plesha, M. E., and Witt, R. J. (2001). *Concepts and applications of finite element analysis*. John Wiley & Sons, 4th ed. edition.

Dahl, K. K. B. (1994). Construction joints in normal and high strength concrete. Technical Report R-311, Department of structural Engineering, Technical University of Denmark.

Damkilde, L., Olsen, J., and Poulsen, P. N. (1994). A program for limit state analysis of plane, reinforced concrete plates by the stringer method. *Bygningsstatiske Meddelelser*, 65(1).

Dantzig, G. B. (1998). *Linear programming and extensions*. Princeton university press.

Delatte, N. J. (2001). Lessons from roman cement and concrete. *Journal of Professional Issues in Engineering Education and Practice*, 127(3):109–115.

Drucker, D., Prager, W., and Greenberg, H. (1952). Extended limit design theorems for continuous media. *Quarterly of Applied Mathematics*, 9:381–389.

European Committee for Standardization (2008). En 1992-1-1 eurocode 2: Design of concrete structures - part 1-1: General rules and rules for buildings.

Exner, H. (1979). On the effectiveness factor in plastic analysis of concrete. *Plasticity in reinforced concrete*, pages 35–42.

Fauchart, J. and Cortini, P. (1972). Étude expérimentale de joints horizontaux entre panneaux préfabriqués pour murs de batiments. *Annales de LInstitut Technique du Batiment et dês Travaux Publics*, 300:86–103.

fib bulletin 43 (2008). Structural connections for precast concrete buildings.

Gilbert, M., He, L., Smith, C. C., and Le, C. V. (2014). Automatic yield-line analysis of slabs using discontinuity layout optimization. *Proceedings of the Royal Society of London A: Mathematical, Physical and Engineering Sciences*, 470(2168).

Gvozdev, A. A. (1960). The determination of the value of the collapse load for statically indeterminate systems undergoing plastic deformation. *International Journal of Mechanical Sciences*, 1(4):322–335.

Hansen, K. and Olesen, S. O. (1976). *SBI-Report 97: Keyed Shear Joints*. Statens Byggeforskningsinstitut.

Herfelt, M. A., Poulsen, P. N., Hoang, L. C., and Jensen, J. F. (2016). Numerical limit analysis of keyed shear joints in concrete structures. *Structural Concrete*, 17(3):481–490.

Herfelt, M. A., Poulsen, P. N., Hoang, L. C., and Jensen, J. F. (2017a). Lower bound equilibrium element and submodel for shear joints in precast concrete structures. *Engineering Structures*, 135:1 – 9.

Herfelt, M. A., Poulsen, P. N., Hoang, L. C., and Jensen, J. F. (2017b). Lower bound multiscale element for in-situ cast joints in triaxial stress. *Engineering Structures*. Submitted for review.

Herfelt, M. A., Poulsen, P. N., Hoang, L. C., and Jensen, J. F. (2017c). Lower bound plane stress element for modelling 3d structures. *Proceedings of the Institution of Civil Engineers-Engineering and Computational Mechanics*, pages 1–11.

Hillerborg, A. (1960). A plastic theory for the design of reinforced concrete slabs. *Prel. Publications, 6th Congr. mt. Ass. Bri. Struct. Eng., Stockholm.*

Ingerslev, Å. (1921). Om en elementær beregningsmetode for krydsarmerede plader. *Ingeniøren*, 30(69):507–515. Translation: On an elementary calculation method for two-way slabs.

Ingerslev, Å. (1923). The strength of rectangular slabs. *Struct. Eng*, 1(1):3–14.

Jensen, B. C. (1975). On the ultimate load of vertical, keyed shear joints in large panel buildings. In *Symposium on Bearing Walls in Warsaw*, volume 8, page 13th.

Joergensen, H. B. and Hoang, L. C. (2013). Tests and limit analysis of loop connections between precast concrete elements loaded in tension. *Engineering Structures*, 52:558–569.

Johansen, K. W. (1931). Beregning af krydsarmerede jernbetonpladers brudmoment. *Bygningsstat. Medd.*, 3:1–18. Translation: Calculation of the rupture moment of two-way slabs.

Johansen, K. W. (1932). Nogle pladeformler. *Bygningsstat. Medd.*, 1:77–84. Translation: Slab formulas.

Johansen, K. W. (1962). *Yield-line theory*. Cement and Concrete Association.

Jørgensen, H. (2014). *Strength of Loop Connections between Precast Concrete Elements: Part I: U-bar Connections Loaded in Combined Tension and Bending -Part II: Wire Loop Connections Loaded in Shear*. PhD thesis, University of Southern Denmark - Faculty of Engineering.

Kærn, J. C. (1979). The stringer method applied to discs with holes. In *Final Report IABSE Colloquium Plasticity in Reinforced Concrete*, volume 29, pages 87–93.

Karihaloo, B. L. (1995). *Fracture Mechanics & Structural Concrete*. Longman Scientific & Technical.

Karmarkar, N. (1984). A new polynomial-time algorithm for linear programming. *Combinatorica*, 4:373–395.

Klee, V. and Minty, G. J. (1972). How good is the simplex algorithm? *In Inequalities, Vol. III*, pages 159–175.

Krabbenhøft, K. (2016). Shell finite element. Optum Computational Engineering.

Krabbenhoft, K. and Damkilde, L. (2002). Lower bound limit analysis of slabs with nonlinear yield criteria. *Computers & structures*, 80(27):2043–2057.

Krabbenhøft, K. and Lyamin, A. (2014). Optum G2. Optum Computational Engineering.

Krabbenhøft, K., Lyamin, A., and Sloan, S. (2007). Formulation and solution of some plasticity problems as conic programs. *International Journal of Solids and Structures*, 44(5):1533–1549.

Krabbenhøft, K., Lyamin, A., and Sloan, S. (2008). Three-dimensional mohr–coulomb limit analysis using semidefinite programming. *Communications in Numerical Methods in Engineering*, 24(11):1107–1119.

Krabbenhoft, K., Lyamin, A. V., Hjiaj, M., and Sloan, S. W. (2005). A new discontinuous upper bound limit analysis formulation. *International Journal for Numerical Methods in Engineering*.

Krenk, S., Damkilde, L., and Høyer, O. (1994). Limit analysis and optimal design of plates with equilibrium elements. *Journal of Engineering Mechanics*, 120:1237–1254.

Kuo, Y.-J. and Mittelmann, H. D. (2004). Interior point methods for second-order cone programming and or applications. *Computational Optimization and Applications*, 28(3):255–285.

Larsen, K. P. (2010). *Numerical Limit Analysis of Reinforced Concrete Structures*. PhD thesis, Technical University of Denmark.

Lobo, M. S., Vandenberghe, L., Boyd, S., and Lebret, H. (1998). Applications of second-order cone programming. *Linear algebra and its applications*, 284(1):193–228.

Lyamin, A. V. and Sloan, S. W. (2002a). Lower bound limit analysis using non-linear programming. *International Journal for Numerical Methods in Engineering*.

Lyamin, A. V. and Sloan, S. W. (2002b). Upper bound limit analysis using linear finite elements and non-linear programming. *International Journal for Numerical and Analytical Methods in Geomechanics*, 26(2):181–216.

Makrodimopoulos, A. and Martin, C. (2006). Lower bound limit analysis of cohesive-frictional materials using second-order cone programming. *International Journal for Numerical Methods in Engineering*, 66(4):604–634.

Makrodimopoulos, A. and Martin, C. (2007). Upper bound limit analysis using simplex strain elements and second-order cone programming. *International Journal for Numerical and Analytical Methods in Geomechanics*.

Makrodimopoulos, A. and Martin, C. (2008). Finite-element limit analysis of mohr–coulomb materials in 3d using semidefinite programming. *Journal for Engineering Mechanics*.

Mehrotra, S. (1992). On the implementation of a primal-dual interior point method. *SIAM Journal on Optimization*.

Monteiro, R. D. and Tsuchiya, T. (2000). Polynomial convergence of primal-dual algorithms for the second-order cone program based on the mz-family of directions. *Mathematical Programming*, 88(1):61–83.

MOSEK ApS (2015). *The MOSEK optimization toolbox for MATLAB manual. Version 7.1 (Revision 33)*.

Muttoni, A., Ruiz, M. F., and Niketic, F. (2015). Design versus assessment of concrete structures using stress fields and strut-and-tie models. *ACI Structural Journal*, 112(5):605.

Muttoni, A., Schwartz, J., and Thürlimann, B. (1997). *Design of Concrete Structures With Stress Fields*. Springer.

Nesterov, Y. and Nemirovsky, A. (1988). A general approach to polynomial-time algorithms design for convex programming. Report, Central Economical and Mathematical Institute, USSR Academy of Sciences, Moscow.

Nesterov, Y., Todd, M. J., and Ye, Y. (1999). Infeasible-start primal-dual methods and infeasibility detectors for nonlinear programming problems. *Mathematical Programming*, 84(2):227–267.

Nesterov, Y. E. and Todd, M. J. (1997). Self-scaled barriers and interior-point methods for convex programming. *Mathematics of Operations research*, 22(1):1–42.

Nielsen, L. O. (2014). Computational ideal cone plasticity. Part 2: The 2D stress structure. Technical University of Denmark, Department of Civil Engineering, U-093.

Nielsen, M. P. (1971). *On the strength of reinforced concrete discs*. Civil engineering and building construction series no.70. Acta polytechnica scandinavica.

Nielsen, M. P. and Hoang, L. C. (2010). *Limit Analysis and Concrete Plasticity, Third Edition*. Taylor & Francis.

Nissen, H. (1961). *Husbygningsteknik 1961*. Teknisk Forlag. Translation: House construction techniques.

Nocedal, J. and Wright, S. (2006). *Numerical Optimization*. Springer.

Olsen, P. C. (1998). The influence of the linearisation of the yield surface on the load-bearing capacity of reinforced concrete slabs. *Computer Methods in Applied Mechanics and Engineering*.

Olsen, P. C. (1999). Evaluation of triangular plate elements in rigid-plastic finite element analysis of reinforced concrete. *Computer Methods in Applied Mechanics and Engineering*.

Persson, P.-O. and Strang, G. (2004). A simple mesh generator in matlab. *SIAM review*, 46(2):329–345.

Poulsen, P. N. and Damkilde, L. (2000). Limit state analysis of reinforced concrete plates subjected to in-plane forces. *International Journal of Solids and Structures*, 37:6011–6029.

Prager, W. (1952). The general theory of limit design. In *Proceedings of the 8th International Congress on theoretical and Applied Mechanics, Istanbul*, volume 19, pages 65–72.

Ribó, R., Pasenau, M., Escolano, E., Ronda, J., and González, L. (1998). GiD reference manual. *CIMNE, Barcelona*.

Rizkalla, S. H., Serrette, R. L., Heuvel, J. S., and Attiogbe, E. K. (1989). *Multiple shear key connections for precast shear wall panels*. Prestressed Concrete Institute.

Roos, C., Terlaky, T., and Vial, J.-P. (1997). *Theory and algorithms for linear optimization: an interior point approach*. Wiley Chichester.

Sloan, S. W. (1988). Lower bound limit analysis using finite elements and linear programming. *International Journal for Numerical and Analytical Methods in Geomechanics*, 12:61–77.

Sloan, S. W. (1989). Upper bound limit analysis using finite elements and linear programming. *International Journal for Numerical and Analytical Methods in Geomechanics*, 13:263–282.

Smith, C., Gilbert, M., Hawksbee, S., and Babiker, A. (2014). Recent advances in the application of discontinuity layout optimization to geotechnical limit analysis problems. *Numerical Methods in Geotechnical Engineering*, 1:415.

Sørensen, J. H., Hoang, L. C., Olesen, J. F., and Fischer, G. (2016). Test and analysis of a new ductile shear connection design for rc shear walls. *Structural Concrete*.

Sturm, J. F. (1997). *Primal-dual interior point approach to semidefinite programming*. PhD thesis, Thesis Publishers Amsterdam, The Netherlands.

Terlaky, T. (2013). *Interior point methods of mathematical programming*, volume 5. Springer Science & Business Media.

Tsuchiya, T. (1999). A convergence analysis of the scaling-invariant primal-dual path-following algorithms for second-order cone programming. *Optimization Methods and Software*, 11(1-4):141–182.

Vandenberghe, L. and Boyd, S. (1996). Semidefinite programming. *SIAM review*, 38(1):49–95.

Wright, S. J. (1997). *Primal-dual interior-point methods*. Siam.

Yu, H., Sloan, S., and Kleeman, P. (1994). A quadratic element for upper bound limit analysis. *Engineering Computations*, 11(3):195–212.

Zienkiewicz, O. C. and Taylor, R. L. (1977). *The finite element method*, volume 3. McGraw-hill London.

Zouain, N., Herskovits, J., Borges, L. A., and Feijóo, R. A. (1993). An iterative algorithm for limit analysis with nonlinear yield functions. *International Journal of Solids and Structures*, 30(10):1397–1417.

Part II

Appended Papers

Paper I

"Numerical limit analysis of keyed shear joints in concrete structures"

M.A. Herfelt, P.N. Poulsen, L.H. Hoang & J.F. Jensen

Published in: *Structural Concrete, 2016*

DOI: 10.1002/suco.201500161

Morten Herfelt*
Peter Poulsen
Linh Hoang
Jesper Jensen

Numerical limit analysis of keyed shear joints in concrete structures

This paper concerns the shear capacity of keyed joints that are transversely reinforced with overlapping U-bar loops. It is known from experimental studies that the discontinuity of the transverse reinforcement affects the capacity and the failure mode. However, to the best knowledge of the authors, previous theoretical works and current design equations in standards do not account for this important effect. This paper introduces a detailed model based on finite element limit analysis to assess the effect of the discontinuous reinforcement. The model is based on the lower bound theorem and uses the modified Mohr-Coulomb yield criterion, which is formulated for second-order cone programming. The model provides a statically admissible stress field as well as the failure mode. Twenty-four different test specimens were modelled and the calculations compared with the experimental results. The results of the model show satisfactory agreement with the experimental observations. The model produces estimates of the shear capacity that are significantly better than those of the Eurocode 2 design equations.

Keywords: shear walls, precast concrete elements, keyed joints, limit analysis, finite element, numerical modelling, plasticity

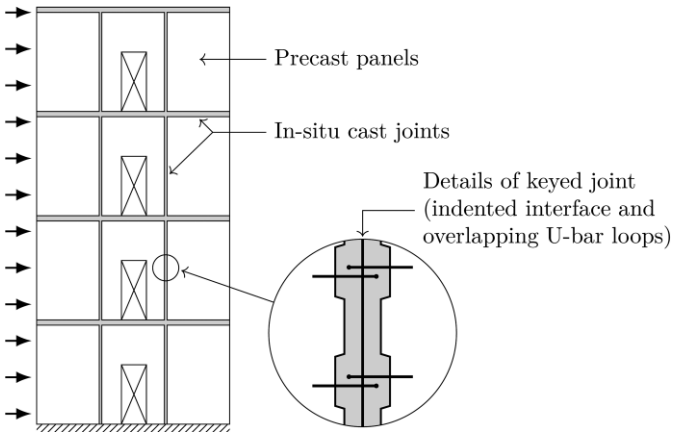

Fig. 1. Four-storey shear wall constructed from precast units connected by in situ joints

1 Introduction

Precast concrete wall units connected by in situ concrete joints are often used to stabilize building structures against horizontal loads. The efficiency of such wall systems (often referred to as shear walls) is highly dependent on the ability of the joints to transfer in-plane shear forces between adjacent precast wall units. The joints are usually designed as so-called keyed joints where U-bar loops protrude from the ends of the precast units and overlap each other in a narrow in situ zone (Fig. 1). A continuous reinforcing bar (locking bar) is typically placed inside the loops to enhance the transfer of tension between pairs of U-bars. Owing to the narrow geometry as well as the discontinuity of the reinforcement layout, the joints are most often the weakest parts of a shear wall system. Hence, in practice, the shear capacity of the keyed joints is often the governing factor for the load capacity of the entire shear wall.

Several papers on the shear capacity of keyed shear joints were published during the 1970s and 1980s (see [1]–[6], for example). The main body of these works concentrates on experimental investigations. As a result, only simple and rather primitive empirical design formulas are available in current design standards, including Eurocode 2 [7]. In attempts to establish simplified mechanical models for the ultimate limit state design of keyed joints, works based on rigid-plastic theory have been presented in the literature. This includes upper bound solutions derived from analyses of failure mechanisms [8], [9] and lower bound solutions based on strut-and-tie models [9]–[11], see Fig. 2. *Jørgensen* et al. [12], [13] also presented several analytical upper bound solutions for similar problems, namely wire loop connections. Common to these plasticity models is that the discontinuity of the transverse reinforcement (i.e. the overlapping U-bars) is not taken into account. This means that depending on the U-bar layout, these models may be oversimplified because they can neither capture the complex stress field nor the complex failure mechanism that develops within the joint. In the end, this will affect the ultimate capacity of the joint.

In this paper we present a detailed study of the effects of the discontinuous transverse reinforcement on the shear capacity of keyed joints. The study was carried out using numerical rigid-plastic limit analysis. This means

* Corresponding author: mahe@alectia.com

Submitted for review: 08 October 2015; revision: 24 November 2015; accepted for publication: 26 November 2015. Discussion on this paper must be submitted within two months of the print publication. The discussion will then be published in print, along with the authors' closure, if any, approximately nine months after the print publication.

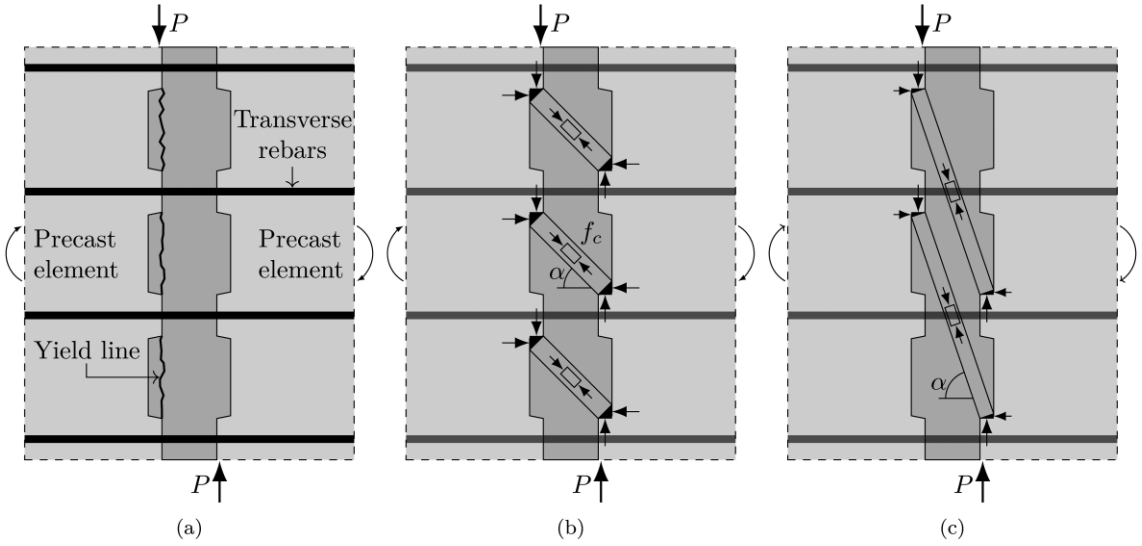

Fig. 2. Simplified failure mechanism (a) [8], [9] and strut-and-tie models (b and c) [9], [10] for the analytical modelling of the shear capacity of keyed joints

that the analysis is based on the same fundamental assumptions as those adopted for the aforementioned upper and lower bound models. However, in numerical limit analysis, the problem is discretized using so-called equilibrium finite elements and subsequently solved as an optimization problem (see section 2); complex stress fields and failure modes can therefore be handled. The results of this study show that the U-bar configuration and, in particular, the mutual distance between adjacent overlapping U-bars play a dominant role in the ultimate shear capacity. It is demonstrated that the effects captured by the detailed numerical limit analysis correlate well with experimental observations.

To emphasize the context in which this study has been undertaken, it is necessary to mention here that the numerical limit analysis approach was deliberately chosen instead of a classical incremental non-linear finite element model. The reason for this is threefold: Firstly, the chosen approach allows the results obtained to be placed in the same context as existing analytical models (i.e. the aforementioned upper and lower bound models) and enables direct comparisons. Secondly, finite element limit analysis is more computationally efficient than incremental non-linear finite element analysis due to the fact that the former approach is only concerned with the load-carrying capacity – the main objective in practical ultimate limit state design. Thirdly, the detailed modelling of keyed joints for finite element limit analysis has to be viewed with a long-term research perspective, where the authors are working on the development of numerical tools for the ultimate limit state design of entire precast buildings (see section 6).

2 Finite element limit analysis

Numerical limit analysis based on the lower bound theorem of plastic theory can be used to determine statically admissible stress fields, which will give a safe estimate of the load-carrying capacity of the structure. The method assumes a rigid-plastic material behaviour where no deformations occur before yielding. The mathematical formulation of the problem consists of a set of equilibrium equations, the yield conditions and an objective function. *Anderheggen* and *Knöpfel* [14] were the first to present the mathematical framework using linear programming to optimize the load-carrying capacity. Since the 1970s, several researchers have contributed to and extended the theory and use of the method [15]–[19]. Numerical limit analysis is a so-called direct method, i.e. the ultimate load capacity is determined in one step, which is a clear advantage over non-linear FEM when it comes to practical applications. The general formulation of lower bound load optimization can be stated as follows [17], [20]:

$$\begin{aligned} &\text{maximize} && \lambda \\ &\text{subject to} && \mathbf{H}\,\boldsymbol{\beta} = \boldsymbol{R}\,\lambda + \boldsymbol{R}_0 \\ & && f(\boldsymbol{\beta}_i) \le 0, \qquad i = 1, 2, \ldots, m \end{aligned} \tag{1}$$

The linear equality constraints ensure equilibrium, while the yield functions ensure that the state of stress does not violate the yield criteria at any point. The load acting on the structure consists of a constant part $\boldsymbol{R_0}$ and a scalable part $\boldsymbol{R}\lambda$. The global equilibrium matrix $\mathbf{H}$ comprises the local contributions from each equilibrium element and $\boldsymbol{\beta}$ is the stress vector. The lower bound problem (Eq. (1)) has a corresponding upper bound problem, which is solved simultaneously, and the solution to the upper bound problem gives the collapse mode of the structure [21].

The yield function f is generally non-linear, but convex; hence, Eq. (1) is a convex optimization problem. We use the modified *Mohr-Coulomb* yield criterion in this paper, which can be formulated exactly using second-order cone programming (SOCP) and solved remarkably efficiently using interior point methods. The problem (Eq. (1)) will be solved using the commercial solver MOSEK [22]. For a detailed description of SOCP and interior point algorithms, the reader is referred to [23]–[25].

3 Keyed joint

Fig. 3 is a schematic drawing of a typical keyed joint; the reinforcement and interfaces are indicated by thick black lines. A local coordinate system (n,t) is also included in Fig. 3. The keys of the interface are defined by the param-

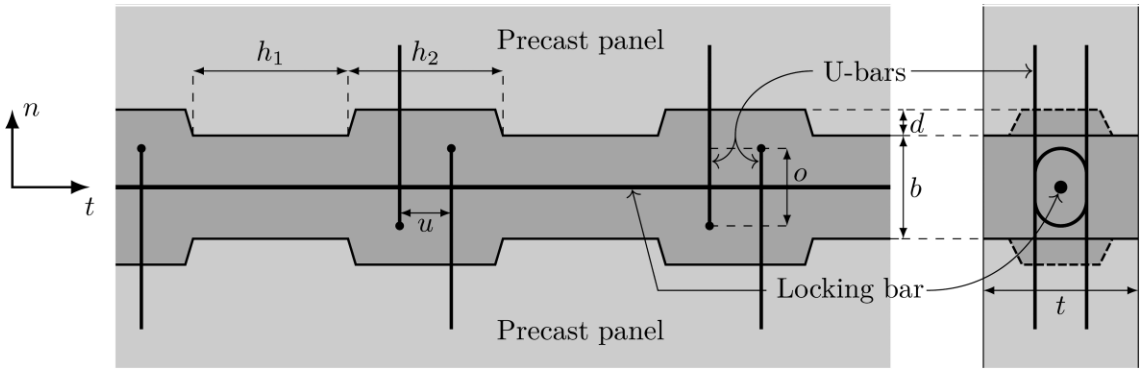

Fig. 3. Elevation on and section through a basic keyed joint design reinforced with U-bars

eters h_1, h_2, and d, while the parameters and define the overlap of the U-bars and the width of the joint respectively. Finally, u is the distance between the two U-bars of a pair.

4 Elements

Three types of equilibrium element are required for the detailed model: Firstly, a triangular element with a linear stress variation (LST element) will represent the precast concrete and joint concrete. In this paper we use an enhanced version of the plate element originally developed by *Sloan* [15] and *Poulsen* and *Damkilde* [17]. The enhanced element was developed by *Nielsen* [26] and a brief description of the element is given in the appendix. The reinforcement can be represented as one-dimensional bars modelled by a bar element developed by *Poulsen* and *Damkilde* [17]. The bar element only provides dissipation along its axis and dowel action is neglected. Finally, a suitable interface element is needed to model the casting interface between the precast panels and the joint concrete.

In this section we present a one-dimensional interface element developed for the detailed model. The interface element has to be compatible with the linear stress variation of the LST element; hence, a linear variation of stresses is also required for the interface element.

The element has four stress variables as seen in Fig. 4a and contributes to eight equilibrium equations on the global level, see Fig. 4b. The stresses are simply transferred directly through the interface as seen in the element equilibrium matrix $\mathbf{h}_{el}$:

$$\boldsymbol{q} = \begin{bmatrix} q^{+}_{\sigma 1} \\ q^{+}_{\tau 1} \\ q^{+}_{\sigma 2} \\ q^{+}_{\tau 2} \\ q^{-}_{\sigma 1} \\ q^{-}_{\tau 1} \\ q^{-}_{\sigma 2} \\ q^{-}_{\tau 2} \end{bmatrix} = \begin{bmatrix} 1 & 0 & 0 & 0 \\ 0 & -1 & 0 & 0 \\ 0 & 0 & 1 & 0 \\ 0 & 0 & 0 & -1 \\ -1 & 0 & 0 & 0 \\ 0 & 1 & 0 & 0 \\ 0 & 0 & -1 & 0 \\ 0 & 0 & 0 & 1 \end{bmatrix} \begin{bmatrix} \sigma_{n1} \\ \tau_1 \\ \sigma_{n2} \\ \tau_2 \end{bmatrix} = \mathbf{h}_{el}\, \boldsymbol{\beta}_{el} \tag{2}$$

Nielsen and *Hoang* [10] suggest a suitable yield criterion for joint interfaces, which corresponds to the modified *Mohr-Coulomb* yield criterion for plane strain with one free normal stress parameter. The yield envelope is illustrated in Fig. 5. In terms of principal stresses, the yield criterion can be written as

$$\begin{aligned} &\sigma_1 \le f_t \\ &k\sigma_1 - \sigma_2 \le 2c\sqrt{k} \end{aligned} \tag{3}$$

where:

σ_1,σ_2	largest and smallest principal stresses respectively
f_t	separation strength of interface
c	cohesion
k	a friction parameter, defined as $k = \left(\sqrt{\mu^2+1}+\mu\right)^2$, where μ is the friction coefficient of the interface

The principal stresses are given as

$$\left.\begin{matrix}\sigma_1 \\ \sigma_2\end{matrix}\right\} = \frac{\sigma_n + \sigma_t}{2} \pm \sqrt{\frac{1}{4}(\sigma_n - \sigma_t)^2 + \tau^2} \tag{4}$$

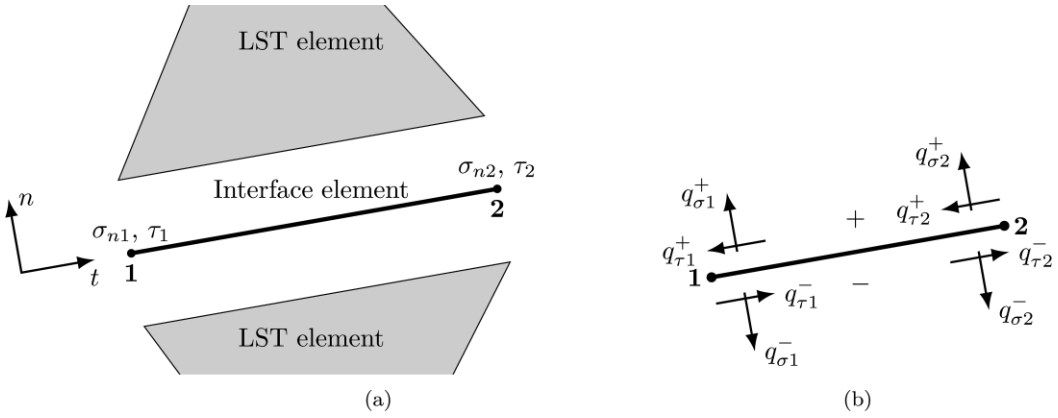

Fig. 4. Interface element: a) geometry, local coordinates system and stress variables and b) generalized nodal forces

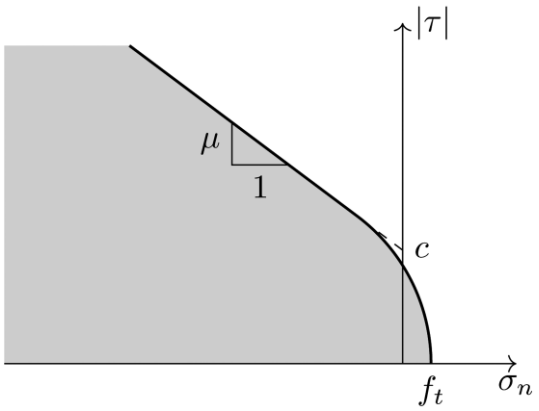

Fig. 5. Yield criterion for the interface – the grey region indicates the interior of the yield envelope

and σ_t is the free normal stress. The yield criterion can be formulated as a single quadratic cone and two linear inequalities by introducing three auxiliary variables [19], [27].

5 Model and analysis

This section will present the numerical model and the results, which will be compared with experimental data from *Hansen* and *Olesen* [5] and *Fauchart* and *Cortini* [2] as well as the design formulas of Eurocode 2 [7]. The geometry of the 16 test specimens of *Hansen* and *Olesen* was: $h_1 = h_2 = 40$ mm, $d = 6$ mm, $b = t = 50$ mm, $o = 30$ mm (see Fig. 3), $l = 1200$ mm, 14 keys. The geometry of the eight test specimens of *Fauchart* and *Cortini* was: $h_1 = 167$ mm, $h_2 = 83$ mm, $d = 20$ mm, $b = 145$ mm, $t = 90$ mm, $o = 115$ mm, $l = 1200$ mm, 4 keys.

Fig. 6 shows the numerical model and the meshes for the models of the specimens. The loads on the model ensure that the moment at the centre of the joint is zero, i.e. pure shear. The joint concrete is modelled using the *Mohr-Coulomb* yield criterion for plane stress conditions. Near the U-bar loops, the concrete will be in a triaxial stress state; hence, the assumption of a plane stress condition is conservative in those regions. The tensile strength of the joint concrete is neglected ($f_t = 0$) and the effectiveness factor is

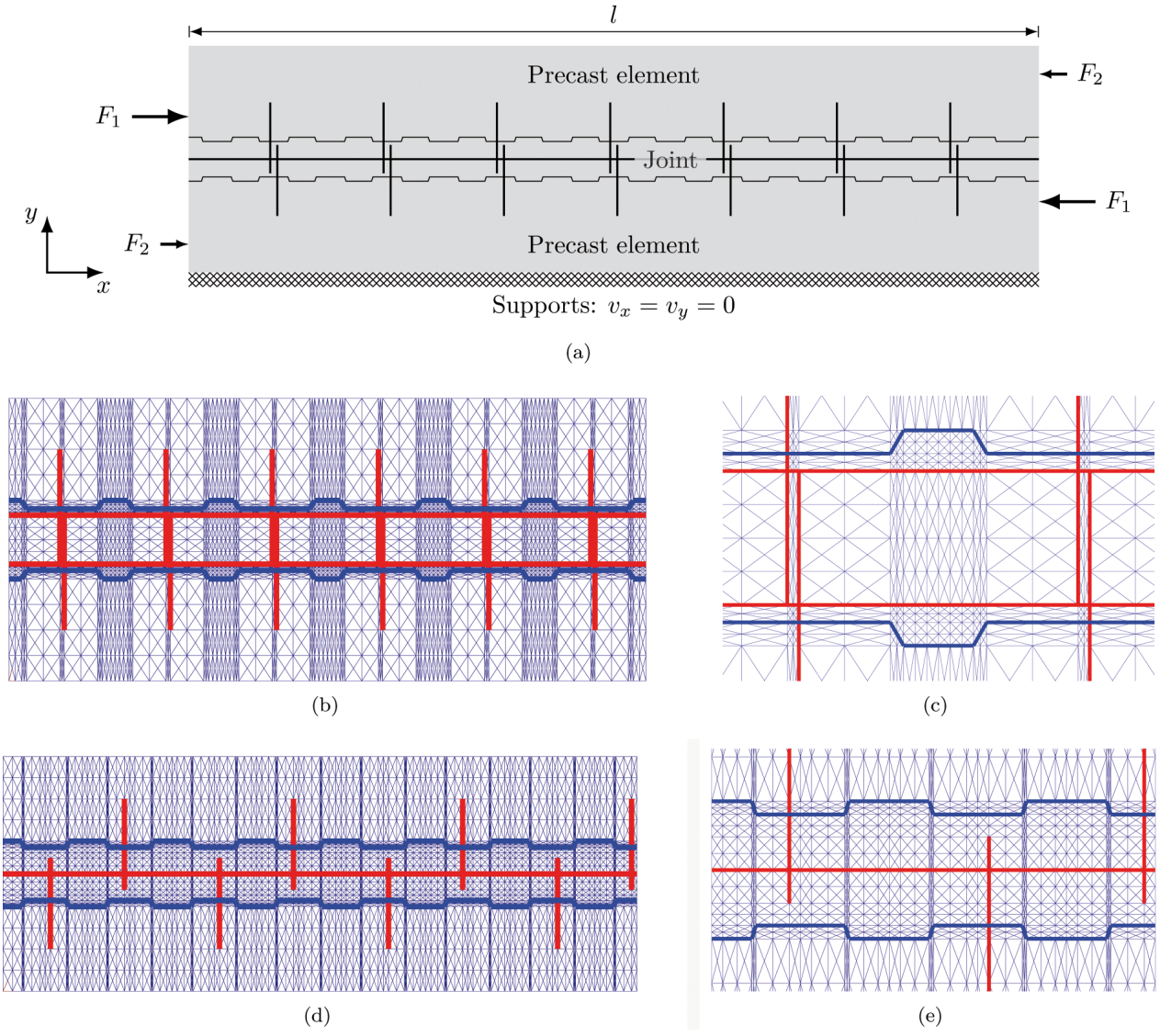

Fig. 6. a) Sketch of the numerical model including boundary conditions and loading; b) mesh for the specimens by *Fauchart* and *Cortini* [2] (8064 elements); c) close-up of the mesh shown in b) showing the keyed interface, two pairs of U-bars (thick vertical lines) and two locking bars (thick, straight horizontal lines); d) half of the mesh for the specimens by *Hansen* and *Olesen* [5] (20 014 elements); e) close-up of the mesh shown in d) showing the keyed interface, a locking bar (thick horizontal line) and a pair of U-bars (thick vertical lines).

chosen as $\nu = 1$, which is the same value adopted for the lower bound strut-and-tie model of *Nielsen* and *Hoang* [10]. It should be mentioned that *Jørgensen* et al. [12], [13] adopted a ν factor smaller than unity for looped joints; however, the models by *Jørgensen* et al. are upper bound models that take into account plane strain conditions as well as the triaxial stress state locally at the loops. Most probably, the best estimate of the ν factor would be somewhere between unity and the value used by *Jørgensen* et al. Determination of such an estimate would require development of a 3D numerical model that can be calibrated with tests heavily reinforced with U-bars. As mentioned in section 4, the capacity of the interface is defined by the cohesion, the friction coefficient and the separation strength. For smooth surfaces, the cohesion is very sensitive to curing and may be taken as $c = 0.55\sqrt{f_c}$, provided that cracking (e.g. due to shrinkage) has not taken place [10]. For the numerical model, a cohesion of 0–0.5 MPa gives the best results, indicating that shrinkage cracking has indeed taken place. The interface is assumed to be smooth and a friction coefficient $\mu = 0.75$ can be used here [10], [28]. Finally, a separation strength $f_t = 0$ was used for the interface elements in all models.

5.1 Comparison and analysis

The experimental results of *Hansen* and *Olesen* [5] and *Fauchart* and *Cortini* [2] were compared with the numerical model and Eurocode 2 [7]. We define the reinforcement ratio as follows:

$$\Phi = \frac{\sum A_{sU} f_y}{t\, l\, f_c}$$

i.e. the total force in the U-bars over the total area times the compressive strength of the joint concrete.

According to Eurocode 2, the shear capacity of a keyed joint can be computed as

$$\tau = \min \begin{cases} c\, f_t A_{key}/(t\, l) + \mu\, \Phi f_c \\ \frac{1}{2}\, \nu\, f_c\, A_{key}/(t\, l) \end{cases} \quad (5)$$

where:

A_{key} total area of keys
f_t tensile strength
c a parameter that relates the tensile strength to the cohesion

The following values were used for keyed joints: $\mu = 0.9$ and $c = 0.5$. The tensile strength was taken as $f_t = 0.21\, f_c^{2/3}$. In Eurocode 2, the effectiveness factor ν used for beam shear problems is also used for shear in joints, i.e. $\nu = 0.7 - f_c/200$ (f_c in MPa).

It is important to emphasize that mean values of the material parameters were used for the comparison. When the numerical model is used for design, however, relevant partial safety coefficients prescribed by codes (e.g. Eurocodes) must be introduced. In this context, it may be useful to mention that the design value for the cohesion of the interfaces should be determined by adopting a partial safety coefficient γ_c that is related to the tensile strength of the concrete (and not the compressive strength).

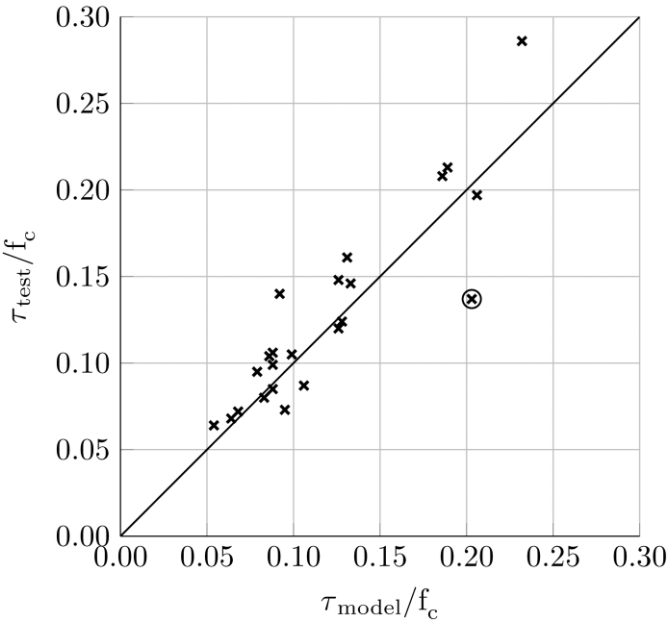

Fig. 7. Numerical results compared with a total of 24 experiments by *Hansen* and *Olesen* [5] and *Fauchart* and *Cortini* [2]

Fig. 7 shows that the numerical model is capable of predicting a satisfactory estimate of the load-carrying capacity for a wide range of experiments. On average, the model predicts shear capacities slightly below the experimental results, but for a single experiment (specimen 29, indicated by a circle in Fig. 7), the model overestimates the capacity by a significant margin. It is worth noting that specimen 29 is the only specimen for which the Eurocode overestimates the shear capacity (see Fig. 8a and Table 1).

Fig. 8a shows that the Eurocode generally underestimates the capacity of the joint – in some cases by almost 60 %. The numerical model predicts a higher shear capacity that the Eurocode formulas, as can be seen in Fig. 8b. All results as well as compressive concrete strength, reinforcement ratio and distance between U-bars are given in Tables 1 and 2. The average error for the numerical model is –4.3 %, whereas for the Eurocode the average error is –37.9 %. The errors shown in the tables were computed using

$$\epsilon_{model} = \frac{\tau_{model} - \tau_{test}}{\tau_{test}} \text{ and } \epsilon_{EC2} = \frac{\tau_{EC2} - \tau_{test}}{\tau_{test}}$$

Specimens 01, 02, 03, 04, 05, 12, 13, 14, 18 and 29, listed in Table 1, did not have any transverse reinforcement (U-bars); instead, external confinement pressure was applied. For these tests, a reinforcement ratio equivalent to the confinement is listed in the table. It is worth noting that specimen 29 is the only specimen in that group with an equivalent reinforcement ratio > 0.10, but the specimen has a rather low capacity similar to the capacities of specimens 12 and 13, which have equivalent reinforcement ratios of 0.43 and 0.95 respectively.

As Table 1 shows, two of the specimens, 24 and 26, both have a large u value. It can be seen that the numerical model produces a very good estimate of the shear capacity for these two specimens in comparison to the Eurocode. Specimen 25 is identical to specimen 26 except

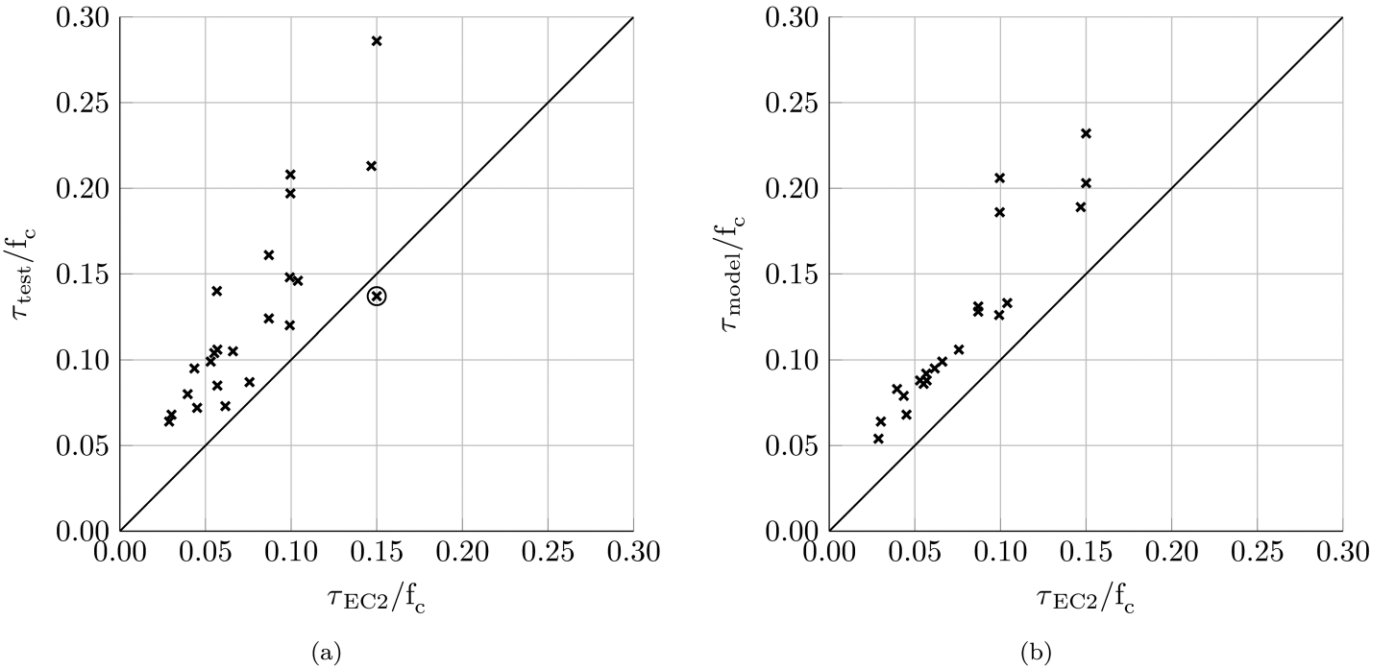

Fig. 8. a) Eurocode design formulas compared with experimental results, b) Eurocode design formulas compared with the results of the numerical model

Table 1. Data and results of experiments by *Hansen* and *Olesen* [5], numerical model and Eurocode 2

Specimen	f_c [MPa]	Φ [–]	u mm	**Experimental** τ/f_c	**Numerical** τ/f_c	Error [%]	**Eurocode 2** τ/f_c	Error [%]
01	29	0.013	–	0.064	0.053	–17.2	0.029	–55.0
02	32	0.030	–	0.095	0.079	–16.8	0.044	–54.2
03	32	0.055	–	0.105	0.102	–2.9	0.066	–37.1
04	16	0.061	–	0.087	0.107	23.0	0.076	–13.0
05	53	0.018	–	0.068	0.064	–5.9	0.030	–55.6
12	25	0.043	–	0.140	0.092	–34.3	0.057	–59.9
13	23	0.095	–	0.146	0.133	–8.9	0.104	–28.8
14	25	0.039	–	0.099	0.088	–11.1	0.053	–46.4
18	27	0.049	–	0.073	0.097	32.9	0.062	–15.6
29	17	0.188	–	0.137	0.203	48.2	0.150	9.5
23	31	0.025	10	0.080	0.083	3.8	0.040	–50.5
24	26	0.030	150	0.072	0.068	5.6	0.045	–37.3
25	24	0.076	10	0.161	0.131	–18.6	0.087	–45.9
26	24	0.076	70	0.124	0.128	3.2	0.087	–29.8
27	15	0.139	10	0.213	0.189	–11.3	0.147	–31.0
28	13	0.235	10	0.286	0.230	–19.6	0.150	–47.6

Table 2. Data and results of experiments by *Fauchart* and *Cortini* [2], numerical model and Eurocode 2

Specimen	f_c [MPa]	Φ [–]	u mm	**Experimental** τ/f_c	**Numerical** τ/f_c	**Error [%]**	**Eurocode 2** τ/f_c	**Error [%]**
5	20	0.049	10	0.106	0.088	–17.0	0.057	–46.3
6	20	0.049	10	0.085	0.088	3.5	0.057	–33.0
7	20	0.096	10	0.120	0.126	5.0	0.099	–17.3
8	20	0.246	10	0.197	0.206	4.6	0.100	–49.4
9	20	0.047	10	0.104	0.086	–17.3	0.055	–47.0
10	20	0.096	10	0.148	0.126	–14.9	0.099	–32.9
11	20	0.096	10	0.148	0.126	–14.9	0.099	–32.9
12	20	0.191	10	0.208	0.168	–10.6	0.100	–52.2

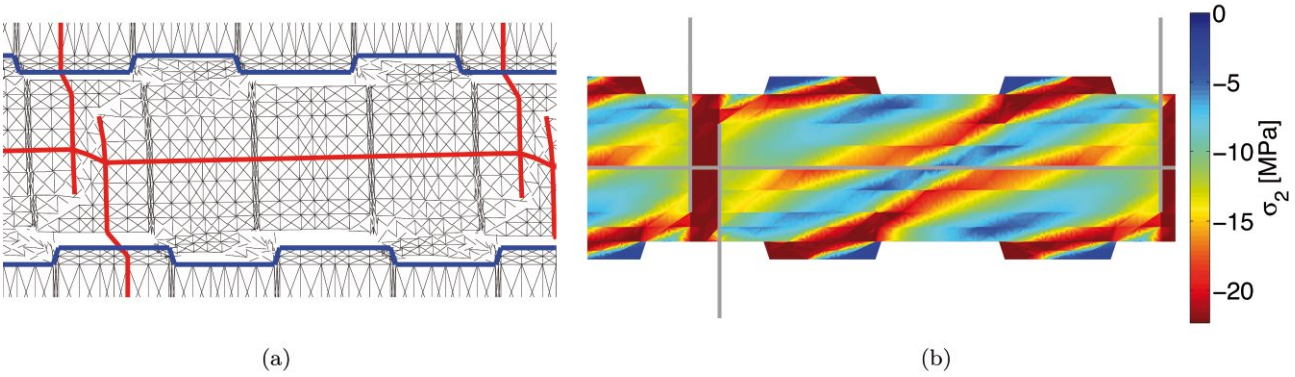

Fig. 9. a) Collapse mode and b) lowest principal stress for specimen 25 from *Hansen* and *Olesen* [5]

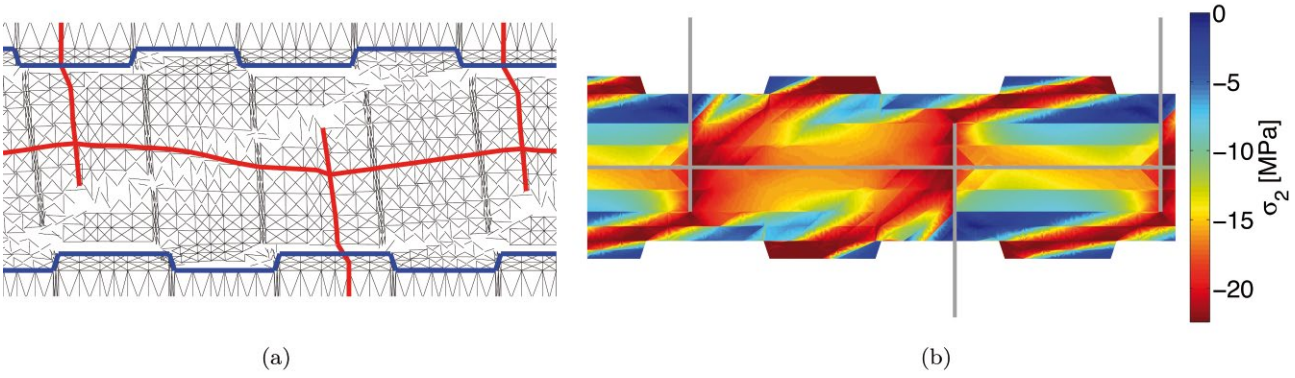

Fig. 10. a) Collapse mode and b) lowest principal stress for specimen 26 from *Hansen* and *Olesen* [5]

for the reinforcement layout; Figs. 9 and 10 show the distribution of the lowest principal stresses and the collapse modes of the two specimens.

The thick blue lines in Figs. 9a and 10a indicate the interface between the precast panels and the joint concrete, and the thick red lines indicate the reinforcement, i.e. U-bars and locking bar. The deformed reinforcement is plotted by interpolating the placement of the nodes in the deformed mesh. The reinforcement is indicated in Figs. 9b and 10b by thick grey lines.

Hansen and *Olesen* [5] reported that specimens 23, 25 and 27 failed by shearing off the keys of the joint concrete, whereas for specimens 24 and 26 the core of the joint was almost completely destroyed. The numerical model captures this as illustrated in Figs. 9a and 10a: The keys are partially sheared off in specimen 25, whereas specimen 26 fails due to a diagonal yield zone through the core of the joint. Figs. 9b and 10b likewise show that the reinforcement layout has a significant influence on the distribution of stresses within the joint: The model of specimen 25 shows distinct diagonal struts throughout the entire core of the joint, but this pattern is disrupted by the reinforcement layout in the model of specimen 26. It should be noted that the collapse mode and stress field observed in Fig. 9 are similar to the simplified failure mechanism and strut-and-tie models shown in Fig. 2. However, this is not the case for specimen 26 (Fig. 10), where the large distance between the overlapping U-bars alters the load path and collapse mode. In both cases the diagonal struts tend to start and end at the corners of the shear keys. This indicates that direct strut action carries the majority of the load and the shear capacity is not that sensitive to the interface friction coefficient.

Fig. 11 shows the shear capacity as a function of the reinforcement for the different specimens. In the calculations, the reinforcement ratio of the transverse reinforcement is simply varied by adjusting the yield strength of the U-bars. The detailed model provides an excellent estimate of the capacity of the experiments by *Fauchart* and *Cortini* [2], as illustrated in Fig. 11a. Likewise, Fig. 11b shows that the model gives a reasonable estimate for the specimens without transverse reinforcement in *Hansen* and *Olesen* [5] despite the somewhat scattered data. Figs. 11c and 11d clearly illustrate the effect of the reinforcement layout, namely, that the shear capacity decreases, even for low reinforcement ratios, when the distance between overlapping U-bars increases.

6 Future work

A detailed model for numerical limit analysis provides unique insights into the ultimate behaviour of keyed joints and may, in practice, be used to optimize the joint layout, i.e. the geometry of shear keys and the positions of overlapping U-bars. Such a task is important and relevant for producers of precast concrete elements, for whom optimization of design details is often motivated by the fact that any benefits gained will accumulate over time because of mass production. On the other hand, for consulting engineers working with the design and calculations of entire building structures, it is not feasible to aim for a level of detail similar to the model presented in this paper. It is simply too time-consuming to work with global models of entire structures (e.g. the four-storey shear wall shown in Fig. 1) where all joints are modelled in details. In global

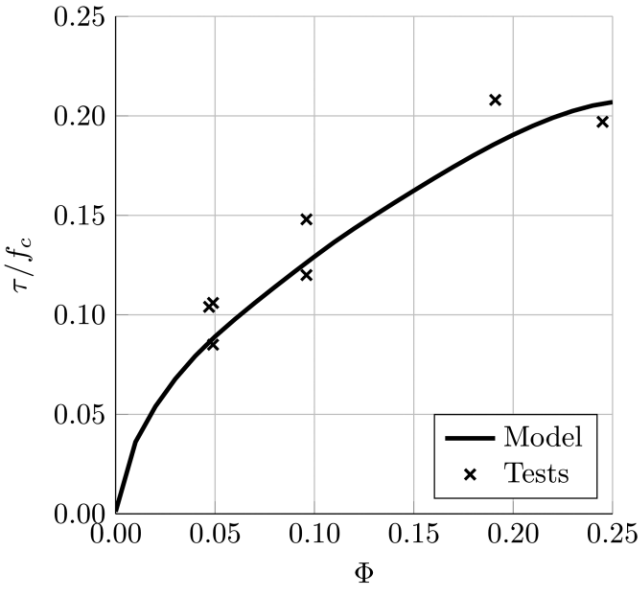

(a) Tests by Fauchart and Cortini [2]

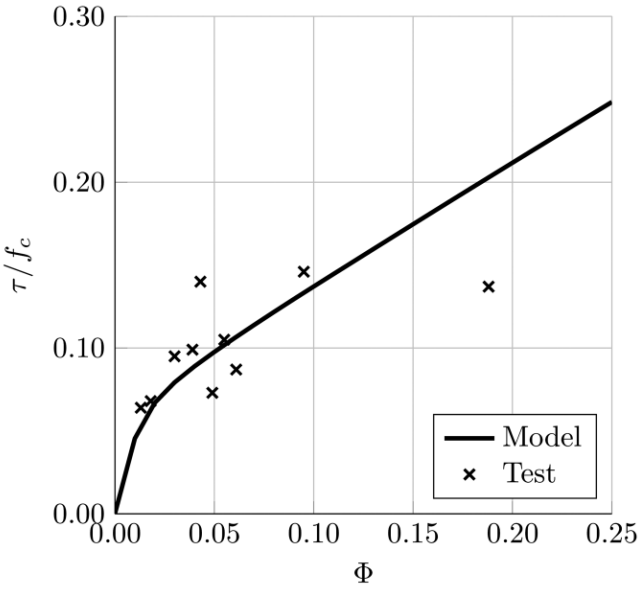

(b) Specimens 01, 02, 03, 04, 05, 12, 13, 14, 18, and 20; Hansen and Olesen [5]

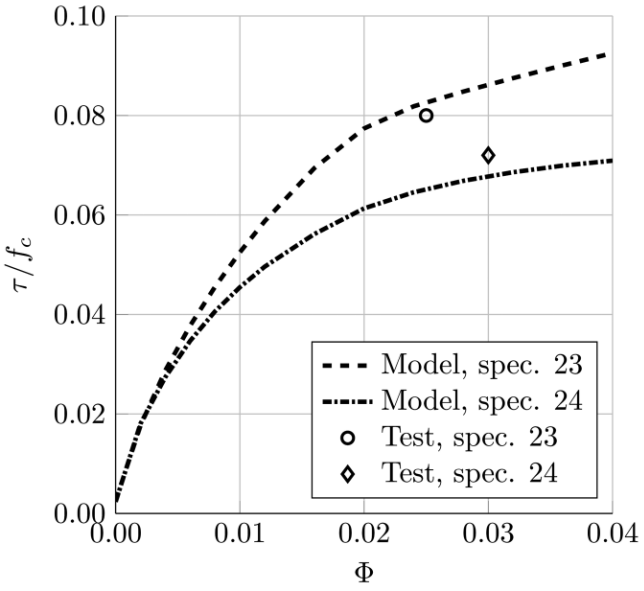

(c) Specimens 23 and 24; Hansen and Olesen [5]

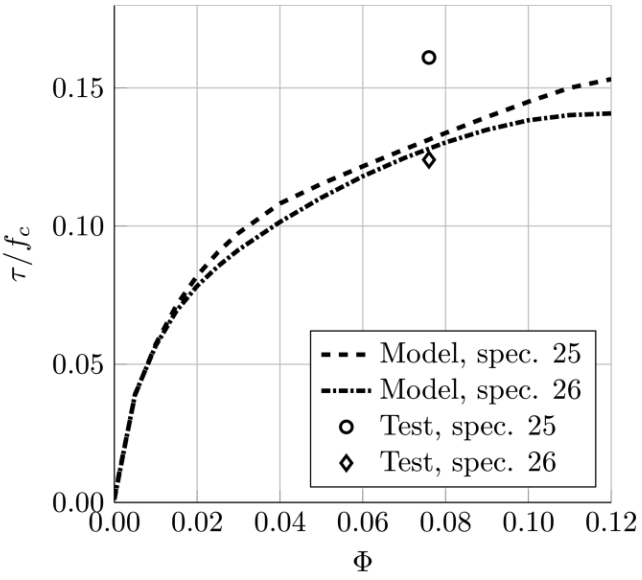

(d) Specimens 25 and 26; Hansen and Olesen [5]

Fig. 11. Capacity curves for various specimens and reinforcement layouts

finite element models, each of the precast wall units should only be modelled by using a limited number of the aforementioned LST elements in order to reduce computational memory requirements and CPU time. The consequence of this is that the keyed joints have to be modelled by one-dimensional equilibrium elements that are compatible with the LST element. Hence, to enable numerical limit analyses of entire structures in the future, it will be necessary to develop a one-dimensional element to model the keyed shear joints. This is in fact an ongoing task for the authors and the primary challenge here is to devise a computationally efficient element that is able to reflect some of the important features of a keyed shear joint. Thus, in this context, the detailed model presented in this paper will be used for benchmarking and comparison. Finally, the authors are currently using the detailed numerical model to carry out an extensive parameter study with the aim of developing a set of simple design equations that will make it possible to account for the effect of the discontinuous reinforcement. These design formulas are thought of as an extension of the Eurocode formulas.

7 Conclusions

The mathematical framework for the limit analysis of keyed shear joints based on a rigid-plastic material model has been presented. A new equilibrium element representing concrete-concrete interfaces was proposed and a detailed finite element limit analysis model for keyed joints between precast concrete panels has been introduced. The model is formulated for second-order cone programming – a class of convex optimization problems that can be solved efficiently using interior point methods. The numerical model has been compared with experimental re-

sults and the design formulas of the Eurocode. A satisfactory correlation between the numerical model and experiments was found, with an average error of -4.3%. The model provides a much better estimate of the load-carrying capacity than the design formulas of the Eurocode, which had an average error of -37.9%. Most importantly, the model also captures the effects of the discontinuous layout of the transverse reinforcement. The results show that the critical mechanisms and the stress fields within the joint are highly dependent on the mutual distance between overlapping U-bars. The approach presented in this paper may be beneficial in optimizing the shear key layout at the boundaries of mass-produced precast wall units and the positioning of the U-bars in the units.

Acknowledgements

The authors would like to thank the ALECTIA Foundation and Innovation Fund Denmark for financial support for the research presented in this paper.

Appendix: Enhanced linear stress triangle

The formulation presented here is based on the work of *Nielsen* [26]. The enhanced linear stress triangle incorporates three subelements, each with a linear stress variation. Several of the variables can be eliminated, which reduces the problem size significantly.

A centre node divides the element into three subelements, as can be seen in Fig. 12, and $\boldsymbol{\beta}_1^S$ is the stress vector associated with this centre node. Stress vector β_i contains the stress variables associated with corner i and β_c collects all stress variables at the corners:

$$\boldsymbol{\beta}_c = \left[\begin{array}{ccc} \boldsymbol{\beta}_1^T & \boldsymbol{\beta}_2^T & \boldsymbol{\beta}_3^T \end{array}\right]^{\mathrm{T}}$$
$$\boldsymbol{\beta}_i = \left[\begin{array}{cccc} \sigma_{ni} & \tau_{nti} & \sigma_{ti}^- & \sigma_{ti}^+ \end{array}\right]^T$$
$$\boldsymbol{\beta}_i^S = \left[\begin{array}{ccc} \sigma_x^S & \sigma_y^S & \tau_{xy}^S \end{array}\right]^{\mathrm{T}}$$

The tractions on two opposing boundaries must be in equilibrium; thus, only four stress variables are necessary to describe the stress state at a corner since they are expressed in the local coordinates of the subelement boundary. Only the normal stress in the t direction is discontinuous. Equilibrium on the local level can be stated as

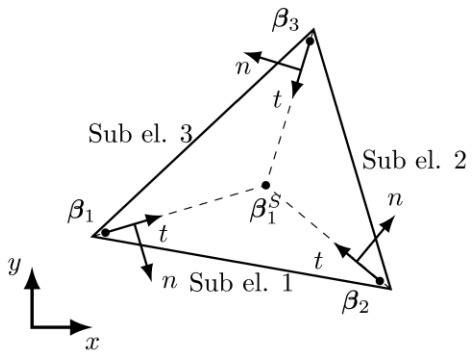

Fig. 12. Subelements, stress variables and local coordinates systems for enhanced plate element (dashed lines indicate subelement boundaries)

$$\boldsymbol{q}_{el} = \mathbf{h}_{el}\boldsymbol{\sigma}_{el} = \mathbf{h}_{el}\,\mathbf{T}_{el}\,\boldsymbol{\beta}_{el}$$

where:

$$\mathbf{T}_{el} = \left[\begin{array}{cc} \mathbf{T}_C & \\ & \mathbf{T}_S \end{array}\right] \text{and } \boldsymbol{\beta}_{el} = \left[\begin{array}{c} \boldsymbol{\beta}_C \\ \boldsymbol{\beta}_S \end{array}\right] \tag{6}$$

$\mathbf{h}_{el}$ is the local equilibrium for the basic linear stress triangle (see [13], [15]),
$\boldsymbol{q}_{el}$ is the generalized nodal forces, i.e. the contribution to the global equilibrium equations,
$\boldsymbol{\sigma}_{el}$ contains 27 stress variables in global coordinates, nine for each subelement, and
$\mathbf{T}_C$ transforms the local stress variables at the corners to global coordinates, which can be written as

$$\begin{aligned} \sigma_x &= \sigma_n n_x^2 + \sigma_t^{\pm}\, n_y^2 - 2\,\tau_{nt}\, n_x\, n_y \\ \sigma_y &= \sigma_n n_y^2 + \sigma_t^{\pm}\, n_x^2 + 2\,\tau_{nt}\, n_x\, n_y \\ \tau_{xy} &= \sigma_n n_x n_y - \sigma_t^{\pm}\, n_x n_y + \tau_{nt}(n_x^2 - n_y^2) \end{aligned} \tag{7}$$

where $n = [n_x\ n_y]^{\mathrm{T}}$ is the normal to the subelement boundary through the given corner. Eq. (7) gives the contributions to $\mathbf{T}_C$. At the central node S, equilibrium across the boundaries between the subelements gives the following equations:

$$\mathbf{T}_1^{xy}(\boldsymbol{\beta}_3^S - \boldsymbol{\beta}_1^S) = 0,\ \mathbf{T}_2^{xy}(\boldsymbol{\beta}_1^S - \boldsymbol{\beta}_2^S) = 0,\ \mathbf{T}_3^{xy}(\boldsymbol{\beta}_2^S - \boldsymbol{\beta}_3^S) = 0,$$

where $\mathbf{T}_1^{xy}$ is the **stress to traction transformation matrix**, defined as:

$$\mathbf{T}_i^{xy} = \left[\begin{array}{ccc} n_x & 0 & n_y \\ 0 & n_y & n_x \end{array}\right]$$

These equations can be organized as a linear system:

$$\left[\begin{array}{ccc} -\mathbf{T}_1^{xy} & 0 & \mathbf{T}_1^{xy} \\ \mathbf{T}_2^{xy} & -\mathbf{T}_2^{xy} & 0 \\ 0 & \mathbf{T}_3^{xy} & -\mathbf{T}_3^{xy} \end{array}\right] \left[\begin{array}{c} \boldsymbol{\beta}_1^S \\ \boldsymbol{\beta}_2^S \\ \boldsymbol{\beta}_3^S \end{array}\right] = \left[\begin{array}{cc} \mathbf{T}_1 & \mathbf{T}_{23} \end{array}\right] \left[\begin{array}{c} \boldsymbol{\beta}_1^S \\ \boldsymbol{\beta}_2^S \\ \boldsymbol{\beta}_3^S \end{array}\right] = 0 \tag{8}$$

Eq. (8) also implicitly defines **T**1 and **T**23 as

$$\mathbf{T}_1 = \left[\begin{array}{c} -\mathbf{T}_1^{xy} \\ \mathbf{T}_2^{xy} \\ 0 \end{array}\right],\ \mathbf{T}_{23} = \left[\begin{array}{cc} 0 & \mathbf{T}_1^{xy} \\ -\mathbf{T}_2^{xy} & 0 \\ \mathbf{T}_3^{xy} & -\mathbf{T}_3^{xy} \end{array}\right]$$

So $\boldsymbol{\beta}_2^S$ and $\boldsymbol{\beta}_3^S$ can now be written as

$$\left[\begin{array}{c} \boldsymbol{\beta}_2^S \\ \boldsymbol{\beta}_3^S \end{array}\right] = -\mathbf{T}_{23}^{-1}\,\mathbf{T}_1\,\boldsymbol{\beta}_1^S$$

and $\mathbf{T}_S$ (see Eq. (6)), can be defined as follows:

$$\left[\begin{array}{c} \boldsymbol{\beta}_1^S \\ \boldsymbol{\beta}_2^S \\ \boldsymbol{\beta}_3^S \end{array}\right] = \left[\begin{array}{c} \mathbf{I} \\ -\mathbf{T}_{23}^{-1}\,\mathbf{T}_1 \end{array}\right] \boldsymbol{\beta}_1^S = \mathbf{T}_S\,\boldsymbol{\beta}_1^S$$

References

1. *Cholewicki, A.*: Loadbearing Capacity and Deformability of Vertical Joints in Structural Walls of Large Panel Buildings. Building Science, 1971, 6, pp. 163–184.
2. *Fauchart, J., Cortini, P.*: Étude expérimentale de joints horizontaux entre panneaux préfabriqués pour murs de batiments. Annales de L'Institut Technique du Batiment et dês Travaux Publics, 1972, 300, pp. 86–103.
3. *Bhatt, P.*: Influence of Vertical Joints on Behaviour of Precast Shear Walls. Building Science, 1973, 8, pp. 221–224.
4. *Bljuger, F.*: Determination of Deformability Characteristics of Vertical Shear Joints in Precast Buildings. Building and Environment, 1976, 11, pp. 277–282.
5. *Hansen, K., Olesen, S. O.*: SBI-Report 97: Keyed Shear Joints. Statens Byggeforskningsinstitut, 1976.
6. *Rizkalla, S. H., Serrette, R. L., Heuvel, J. S., Attiogbe, E. K.*: Multiple shear key connections for precast shear wall panels. Prestressed Concrete Institute, 1989.
7. European Committee for Standardization: EN 1992-1-1 Eurocode 2: Design of concrete structures – Part 1-1: General rules and rules for buildings. CEN, 2005.
8. *Jensen, B. C.*: On the ultimate load of vertical, keyed shear joints in large panel buildings. Symp. on Bearing Walls in Warsaw, vol. 8, 1975, p. 13th.
9. *Christoffersen, J.*: Ultimate Capacity of Joints in Precast Large Panel Concrete Buildings. Technical University of Denmark, 1997.
10. *Nielsen, M. P., Hoang, L. C.*: Limit Analysis and Concrete Plasticity, 3rd ed.. Taylor & Francis, 2010.
11. *fib* Bulletin 43: Structural connections for precast concrete buildings, Fédération Internationale du Béton (*fib*), 2008.
12. *Jørgensen, H.*: Strength of Loop Connections between Precast Concrete Elements; Part I: U-bar Connections Loaded in Combined Tension and Bending; Part II: Wire Loop Connections Loaded in Shear. University of Southern Denmark, Faculty of Engineering, 2014.
13. *Jørgensen, H. B., Hoang, L. C.*: Load carrying capacity of keyed joints reinforced with high strength wire rope loops. Proc. of *fib* Symposium, Copenhagen, 2015.
14. *Anderheggen, E., Knöpfel, H.*: Finite element limit analysis using linear programming. International Journal of Solids and Structures, 1972, 8, pp. 1413–1431.
15. *Sloan, S. W.*: Lower Bound Limit Analysis Using Finite Elements and Linear Programming. International Journal for Numerical and Analytical Methods in Geomechanics, 1988, 12, pp. 61–77.
16. *Sloan, S. W.*: Upper Bound Limit Analysis Using Finite Elements and Linear Programming. International Journal for Numerical and Analytical Methods in Geomechanics, 1989, 13, pp. 263–282.
17. *Poulsen, P. N., Damkilde, L.*: Limit State Analysis of Reinforced Concrete Plates Subjected to In-plane Forces. International Journal of Solids and Structures, 2000, 37, pp. 6011–6029.
18. *Makrodimopoulos, A., Martin, C.*: Lower bound limit analysis of cohesive-frictional materials using second-order cone programming. International Journal for Numerical Methods in Engineering, 2006, 66(4), pp. 604–634.
19. *Krabbenhøft, K., Lyamin, A., Sloan, S.*: Formulation and solution of some plasticity problems as conic programs. International Journal of Solids and Structures, 2007, 44(5), pp. 1533–1549.
20. *Krabbenhoft, K., Damkilde, L.*: A general non-linear optimization algorithm for lower bound limit analysis. International Journal for Numerical Methods in Engineering, 2003.
21. *Krenk, S., Damkilde, L., Høyer, O.*: Limit analysis and optimal design of plates with equilibrium elements. Journal of Engineering Mechanics, 1994, 120, pp. 1237–1254.
22. MOSEK ApS: The MOSEK optimization toolbox for MATLAB manual, version 7.1 (rev. 33), 2015, available from https://www.mosek.com/.
23. *Boyd, S. P., Vandenberghe, L.*: Convex Optimization, Cambridge University Press, 2004.
24. *Andersen, E. D., Roos, C., Terlaky, T.*: On implementing a primal-dual interior-point method for conic quadratic optimization. Mathematical Programming, 2003, 95(2), pp. 249–277.
25. *Alizadeh, F., Goldfarb, D.*: Second-order cone programming. Mathematical programming, 2003, 95(1), pp. 3–51.
26. *Nielsen, L. O.*: Computational ideal cone plasticity; Part 2: The 2D stress structure. Technical University of Denmark, Department of Civil Engineering, U-093, 2014.
27. *Bisbos, C., Pardalos, P.*: Second-order cone and semidefinite representations of material failure criteria. Journal of Optimization Theory and Applications, 2007, 134(2), pp. 275–301.
28. *Dahl, K. K. B.*: Construction joints in normal and high strength concrete, Department of structural Engineering, Technical University of Denmark, R-311, 1994.

Morten A. Herfelt
ALECTIA A/S, Teknikerbyen 34
2830 Virum, Denmark
Department of Civil Engineering
Technical University of Denmark
Brovej, Building 118, 2800 Kgs., Denmark
mahe@alectia.com

Peter N. Poulsen
Department of Civil Engineering
Technical University of Denmark
Brovej, Building 118, 2800 Kgs., Denmark

Linh C. Hoang
Department of Civil Engineering
Technical University of Denmark
Brovej, Building 118, 2800 Kgs., Denmark

Jesper F. Jensen
ALECTIA A/S, Teknikerbyen 34
2830 Virum, Denmark

Paper II

"Lower bound equilibrium element and submodel for shear joints in precast concrete structures"

M.A. Herfelt, P.N. Poulsen, L.H. Hoang & J.F. Jensen

Published in: *Engineering Structures, 2017*

Engineering Structures 135 (2017) 1–9

Contents lists available at ScienceDirect

Engineering Structures

journal homepage: www.elsevier.com/locate/engstruct

Lower bound equilibrium element and submodel for shear joints in precast concrete structures

Morten A. Herfelt [a,*], Peter N. Poulsen [b], Linh C. Hoang [b], Jesper F. Jensen [a]

[a] ALECTIA A/S, Teknikerbyen 34, 2830 Virum, Denmark
[b] Department of Civil Engineering, Technical University of Denmark, Brovej, Building 118, 2800 Kgs. Lyngby, Denmark

ARTICLE INFO

Article history:
Received 5 February 2016
Revised 8 December 2016
Accepted 28 December 2016

Keywords:
In-situ cast joints
Limit analysis
Precast concrete
Finite element
Rigid plasticity
Yield criterion
Multiscale

ABSTRACT

This paper is concerned with the shear capacity of keyed joints reinforced with overlapping U-bar loops in the transverse direction. The layout of the loop reinforcement affects the capacity and failure mode, and currently it is not accounted for by standards or previous theoretical work. A multiscale approach to the issue is proposed: An equilibrium element for finite element limit analysis representing keyed joints is coupled with a suitable submodel, which handles the complex stress states within the joint. The submodel is based on several modified stringer models, which makes it possible to account for local mechanisms in the core of the joint. The element and submodel are validated by comparison to a detailed model based on finite element limit analysis and experimental data. The joint element and submodel lead to a small optimisation problem compared to the detailed model and the computational time is reduced by several magnitudes.

1. Introduction

The lateral stability of modern precast concrete buildings is often ensured by shear walls, i.e. precast wall panels connected by in-situ cast joints. Horizontal forces, e.g. from wind load or seismic action, are transferred as in-plane forces and the shear capacity of the panels and joints are of the utmost importance. In practice, the shear capacity of such walls is usually assessed by analytical lower bound models, e.g. strut-and-tie models or stress field methods [1,2]. The stress fields are also frequently determined by use of linear elastic finite element analysis. Naturally, this practice often leads to suboptimal structures compared to what can be obtained if the stress fields instead are determined from a non-linear elastic-plastic analysis. Use of numerical elastic-plastic analysis to determine stress fields has e.g. been demonstrated in Refs. [3,4].

The joints between the precast panels are of particular interest as they are often a critical part of the structure. In-situ cast joints consist of a concrete core and two interfaces, where the core typically is reinforced in two directions, and the interfaces typically are keyed. The shear capacity of the joints and interfaces is in practice assessed by simple empirical formulas [5] which often gives a conservative estimate of the capacity. Several authors have investigated the behaviour of in-situ cast joints. The investigations cover both experimental testing [see e.g. 6–9] and simplified mechanical models based on the theory of rigid-plasticity, namely upper bound solutions based on yield line theory [10,11] and lower bound solutions based on strut-and-tie models [1,11,12]. The experiments showed that the geometry of the joint and the reinforcement layout affect the shear capacity as well as the collapse mode, but the analytical methods have only been able to capture the observed behaviour to a certain extent. Local failure mechanisms caused by the reinforcement layout, however, have not been investigated using analytical methods. Investigations using numerical tools, e.g. finite element method or similar, have focused on single key joints often used in precast concrete segmental bridges [13,14]. These investigations have primarily been carried out by use of non-linear finite element analysis. This approach is computationally heavy, especially when considering the fact that the ultimate load carrying capacity is the result of main interest.

Herfelt et al. [15] presented a detailed model for keyed joints based on finite element limit analysis. The model was based on a lower bound formulation and the analysis yielded a statically admissible stress field. Moreover, the solution to the dual problem, i.e. the corresponding kinematic problem, was interpreted as the failure mode. The detailed model used triangular plane stress elements [16] representing the concrete, bar elements [16] representing the reinforcement, and an interface elements representing the

* Corresponding author.
E-mail address: mahe@alectia.com (M.A. Herfelt).

http://dx.doi.org/10.1016/j.engstruct.2016.12.054
0141-0296/

concrete-to-concrete interfaces. It was shown that the model could represent the complex stress states within the joint and captured the local failure mechanisms to a satisfactory degree; however, for practical design it is not feasible to use that level of detail. Fig. 1 shows a four storey wall comprising several precast panels connected by in-situ cast joints. As indicated in the figure, plane stress elements may be used to model the precast panels, while a special joint element is needed for the joints.

This paper presents a lower bound equilibrium element representing the in-situ cast joints. The element is designed for interaction with the triangular plane stress element [16] and interface elements [15]. The scope is to be able to model entire wall systems, e.g. the four storey wall seen in Fig. 1. The joint element requires a suitable yield criterion which can capture the critical mechanisms identified by the detailed model [15], and for this purpose, a semi-analytical submodel yield criterion based on the stringer method is developed. The joint element and submodel fit the format of second-order cone programming, and the developed model is compared to the detailed model [15] as well as experimental data [6,7]. The proposed multiscale model captures the behaviour of the detailed model as well as the specimens.

2. Problem formulation

Finite element limit analysis can be considered as a special case of the general finite element method: It is based on the extremum principles for rigid-plastic materials [see e.g. 1,17,18] and deploys a mesh discretisation known from the finite element method. Anderheggen and Knöpfel [19] presented a general formulation as well as equilibrium elements for solids and plates. Since the 1970s several authors have contributed to the method see e.g. [16,20,21]. Finite element limit analysis is a direct method, where the ultimate load is determined in a single step, which is a significant advantage over non-linear finite element methods for practical applications. Moreover, when modelling concrete structures, there is no need to consider any tensile strength to avoid problems related to numerical stability. From the lower bound formulation, the stress field is determined. Associated with the lower bound problem is a so-called dual problem, and the solution to this dual problem can be interpreted as the displacement field and plastic strain. Since we are dealing with a rigid plastic material model, no information on the magnitude of the strains and displacements are determined; only the directions. When the method is applied to structural concrete, it is necessary to operate with effective strength parameters (via the so-called effectiveness factors) to account for the limited ductility of concrete as well as the reduction of the compressive strength as a result of cracking and tension strains transverse to compressive stress fields. In practice, the effective strength parameters have to be found by calibration of calculations with results of tests on structural components.

Numerical lower bound limit analysis is formulated as an optimisation problem where the scope is to maximise a load factor λ. The analysis determines a statically admissible stress, i.e. a stress field which satisfies equilibrium and does not violate the yield criteria in any points. The general problem can be stated as [16,22]:

$$\begin{aligned} &\text{maximise} && \lambda \\ &\text{subject to} && \mathbf{H}\boldsymbol{\beta} = \boldsymbol{R}\lambda + \boldsymbol{R}_0 \\ & && f(\boldsymbol{\beta}_i) \leqslant 0, \quad i = 1,2,\ldots,m \end{aligned} \tag{1}$$

The load acting on the model consists of a constant part $\boldsymbol{R}_0$ and a scalable part $\boldsymbol{R}\lambda$. The linear equality constraints ensure equilibrium while the functions $f(\boldsymbol{\beta}_i) \leqslant 0$ ensure that the stress filed does not violate the yield criteria. $\mathbf{H}$ is the global equilibrium matrix, and $\boldsymbol{\beta}$ is the stress vector. m is the number of check points for the yield function, f, which is generally convex, but non-linear; thus, (1) represents a convex optimisation problem.

In this work, the optimisation problem (1) will be a second-order cone program (SOCP). Second-order cone programming as well as semidefinite programming have been used in the field of finite element limit analysis for more than a decade, see e.g. Refs. [23–25]. Expanding the yield functions f, (1) can be restated as:

$$\begin{aligned} &\text{maximise} && \lambda \\ &\text{subject to} && \mathbf{H}\boldsymbol{\beta} = \boldsymbol{R}\lambda + \boldsymbol{R}_0 \\ & && \mathbf{C}_\beta\boldsymbol{\beta} + \mathbf{C}_\alpha\boldsymbol{\alpha} + \mathbf{C}_\gamma\boldsymbol{\gamma} = \boldsymbol{C}_0 \\ & && \mathbf{E}_\beta\boldsymbol{\beta} + \mathbf{E}_\alpha\boldsymbol{\alpha} + \mathbf{E}_\gamma\boldsymbol{\gamma} \leqslant \boldsymbol{E}_0 \\ & && \boldsymbol{\gamma}_i \in \mathcal{Q}_{k_i}, \quad i = 1,2,\ldots,m \end{aligned} \tag{2}$$

where $\boldsymbol{\alpha}$ and $\boldsymbol{\gamma}$ are problem variables associated with the yield functions, and the $\mathbf{C}$ and $\mathbf{E}$ matrices define the necessary linear equalities and inequalities for the chosen yield criterion. The variables $\boldsymbol{\gamma}_i$, associated with the ith check point for the stresses, are in a quadratic cone $\mathcal{Q}_{k_i}$ of size k_i, defined as:

$$\mathcal{Q}_k = \left\{ \boldsymbol{x} | \boldsymbol{x} \in \mathbb{R}^k,\ x_1 \geqslant \sqrt{x_2^2 + \cdots + x_k^2} \right\} \tag{3}$$

The problem (2) can be solved efficiently using interior point algorithm, and in this work the commercial solver MOSEK [26] is used. The reader is referred to Refs. [27–30] for a detailed description of SOCP and interior point solvers.

On the element level, the equilibrium equations and yield functions can be stated as:

$$\begin{aligned} &\mathbf{h}_{el}\boldsymbol{\beta}_{el} = \boldsymbol{q}_{el} \\ &\mathbf{C}_\beta^{el,i}\boldsymbol{\beta}_{el} + \mathbf{C}_\alpha^{el,i}\boldsymbol{\alpha}_i + \mathbf{C}_\gamma^{el,i}\boldsymbol{\gamma}_i = \mathbf{C}_0^{el,i}, \quad i = 1,2,\ldots,m_{el} \\ &\mathbf{E}_\beta^{el,i}\boldsymbol{\beta}_{el} + \mathbf{E}_\alpha^{el,i}\boldsymbol{\alpha}_i + \mathbf{E}_\gamma^{el,i}\boldsymbol{\gamma}_i \leqslant \mathbf{E}_0^{el,i}, \quad i = 1,2,\ldots,m_{el} \\ &\boldsymbol{\gamma}_i \in \mathcal{Q}_{k_i}, \quad i = 1,2,\ldots,m_{el} \end{aligned} \tag{4}$$

$\boldsymbol{q}_{el}$ is the contributions to the equilibrium equations on the global level, $\boldsymbol{\beta}_{el}$ is the stress variables of the given element, and $\mathbf{h}_{el}$ is the element equilibrium matrix. The matrices $\mathbf{C}^{el,i}$ and $\mathbf{E}^{el,i}$ define the yield function for the m_{el} check points of the element. Similarly to (2), the variables denoted $\boldsymbol{\gamma}_i$ are required to be in a quadratic cone Q_{k_i} of size k_i.

3. Keyed joints and detailed numerical model

A keyed joint reinforced with loop reinforcement (U-bars) and a locking bar is considered. Fig. 2 shows the basic geometry and a unit section (dashed rectangle) which will form the foundation of the submodel yield criterion. The thick vertical lines seen in Fig. 2 represent the loop reinforcement, while the horizontal solid line represents the locking bar. The length of keyed joints in practice usually ranges from a single storey height to the height of the entire building, while the width b and thickness t usually are below 200 mm.

For the detailed numerical model presented by Herfelt et al. [15], several thousand plane stress elements were necessary to capture the local mechanisms and stress fields developed in the core of the joint. The model was loaded such that the centre line of the joint would be subjected to pure shear, i.e. no bending. The concrete is modelled as a Mohr-Coulomb material, while a simple linear criterion is used for the rebars. For the interface, a Coulomb friction model is assumed. The model assumed plane stress state, thus, the confinement provided by the reinforcement loops and general triaxial stress states were disregarded.

Fig. 3(a) shows an example of the collapse mode determined by the aforementioned detailed model [15] using the solution to the dual problem, i.e. the corresponding kinematic problem. The inter-

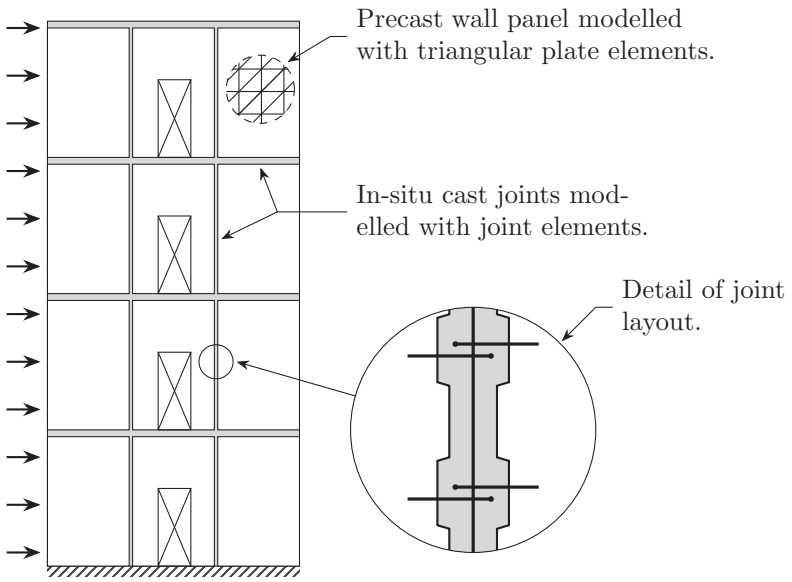

Fig. 1. Four storey wall subjected to horizontal forces: The wall consists of 12 precast panels connected by joints. An example of a mesh (discretisation) for numerical analysis is seen for the top right panel.

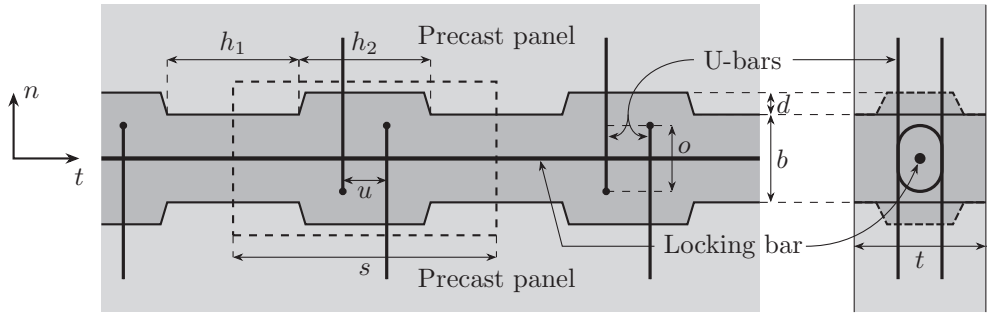

Fig. 2. Elevation and cross section of a basic design of a keyed joint reinforced with U-bars.

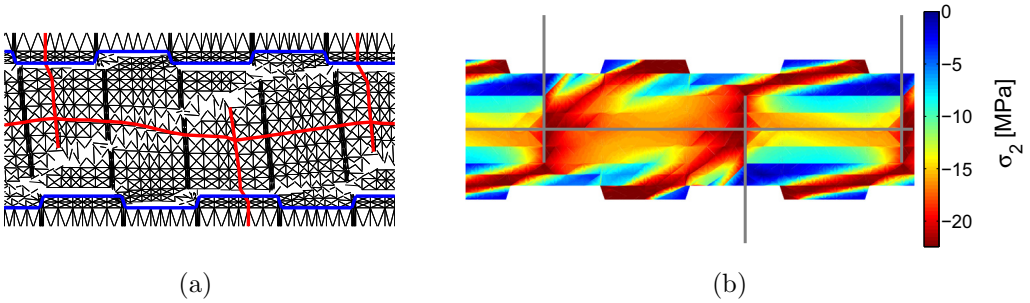

Fig. 3. Detailed numerical model [15] for specimen 26 by Hansen and Olesen [6]: Collapse mode (a) and lowest principal stress (b).

preted velocities are associated with the equilibrium equations, hence, each element edge moves independently. The blue lines indicate the interface between the joint and the precast panels, while the red[1] lines indicate the reinforcement. The critical mechanism features a diagonal yield line through the core of the joint. Fig. 3(b) shows the lowest principal stress. The reinforcement is indicated by gray lines and it is observed that large compressive stresses are present in the area between the vertical U-bars. This also shows that the reinforcement layout has a significant effect on the capacity and failure mode of the joint [15]. The detailed model [15] will be used for comparison in the following analysis.

4. Joint equilibrium element

An equilibrium element representing in-situ cast joints is needed for practical modelling of precast concrete structures. The joint element will dictate the distribution and transfer of stresses through the joint. The element is formulated to be compatible with the plane stress element [16], see in Fig. 4.

The plane stress triangle has a linear stress field defined by the three stress vectors in the corners. Equilibrium of tractions along

[1] For interpretation of color in Fig. 3, the reader is referred to the web version of this article.

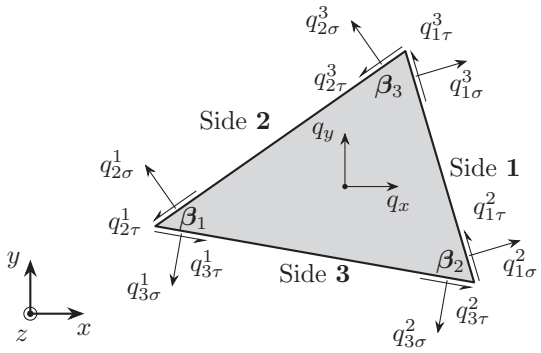

Fig. 4. Generalised nodal forces and stress variables of the plane stress triangle (adapted from [16]).

the element boundaries means that the joint element requires a linear variation of the shear stress and transverse normal stress, which again leads to a quadratic variation of the longitudinal normal stress, see Fig. 5(b).

Fig. 5 shows the joint element. Length and orientation of the element are defined by the two end nodes seen in the figure. The element has 9 stress parameters and contributes to 12 equilibrium equation on the global level. Equilibrium for the element can be stated as:

$$\boldsymbol{q}_{el} = \mathbf{h}_{el}\,\boldsymbol{\beta}_{el} \tag{5}$$

where $\boldsymbol{\beta}_{el}$ is the element stress vector, $\boldsymbol{q}_{el}$ contains the 12 nodal forces seen in Fig. 5(b), and $\mathbf{h}_{el}$ is the local equilibrium matrix. The stress variables are given in local coordinates; thus, no transformations are necessary when establishing $\mathbf{h}_{el}$. $\boldsymbol{\beta}_{el}, \boldsymbol{q}_{el}$, and $\mathbf{h}_{el}$ are explicitly given in (6):

$$\boldsymbol{q}_{el} = \begin{bmatrix} \boldsymbol{q}^+ \\ \boldsymbol{q}^- \\ \boldsymbol{q}_N \end{bmatrix} = \begin{bmatrix} q^+_{\sigma 1} \\ q^+_{\tau 1} \\ q^+_{\sigma 2} \\ q^+_{\tau 2} \\ \hdashline q^-_{\sigma 1} \\ q^-_{\tau 1} \\ q^-_{\sigma 2} \\ q^-_{\tau 2} \\ \hdashline q_{N1} \\ q_{N2} \\ q_{p1} \\ q_{p2} \end{bmatrix} = \left[\begin{array}{ccccccccc} t & 0 & 0 & 0 & 0 & 0 & 0 & 0 & 0 \\ 0 & 0 & -t & 0 & 0 & 0 & 0 & 0 & 0 \\ 0 & t & 0 & 0 & 0 & 0 & 0 & 0 & 0 \\ 0 & 0 & 0 & -t & 0 & 0 & 0 & 0 & 0 \\ \hdashline -t & 0 & 0 & 0 & 0 & 0 & 0 & 0 & 0 \\ 0 & 0 & 0 & 0 & t & 0 & 0 & 0 & 0 \\ 0 & -t & 0 & 0 & 0 & 0 & 0 & 0 & 0 \\ 0 & 0 & 0 & 0 & 0 & t & 0 & 0 & 0 \\ \hdashline 0 & 0 & 0 & 0 & 0 & 0 & b\,t & 0 & 0 \\ 0 & 0 & 0 & 0 & 0 & 0 & 0 & -b\,t & 0 \\ 0 & 0 & t & 0 & -t & 0 & 3\frac{bt}{l_e} & \frac{bt}{l_e} & -4\frac{bt}{l_e} \\ 0 & 0 & 0 & t & 0 & -t & -\frac{bt}{l_e} & -3\frac{bt}{l_e} & 4\frac{bt}{l_e} \end{array}\right] \begin{bmatrix} \sigma_{n1} \\ \sigma_{n2} \\ \tau^+_1 \\ \tau^+_2 \\ \tau^-_1 \\ \tau^-_2 \\ \sigma_{t1} \\ \sigma_{t2} \\ \sigma_{t3} \end{bmatrix} = \mathbf{h}_{el}\,\boldsymbol{\beta}_{el} \tag{6}$$

The equilibrium matrix and generalised nodal force vector can be split into three parts; one for the positive side of the joint (denoted $\boldsymbol{q}^+$), one for the negative side of the joint (denoted $\boldsymbol{q}^-$), and one for the nodal forces in the longitudinal direction (denoted $\boldsymbol{q}_N$). It is assumed that the transverse normal stress (n-direction) is transferred directly through the joint, while the shear stress can be used to build up an axial force in the longitudinal direction.

Each point along the joint element has a stress state defined by four stress parameters, namely $\sigma_n, \sigma_t, \tau^+$, and τ^-, which passed on and checked against the appropriate model on the submodel level.

5. Submodel yield criterion

The stresses on the element level need to satisfy the submodel yield criterion on the joint section scale. The submodel yield criterion is in itself a small optimisation problem, and equilibrium of the submodel is ensured by stress fields that are determined by using a variation of the stringer method [see e.g. 1,31].

The scope of the submodel yield criterion is to capture the critical mechanisms within the joint, and three modified stringer models are introduced for this purpose. The submodel is based on a unit joint section (see the dashed rectangle in Fig. 2) which is subjected to shear as well as axial forces in two directions. Fig. 6 shows the unit joint section and the three modified stringer models which compose the submodel yield criterion. Each of the three modified stringer models imposes certain constraints on the stress distribution in the joint and represents a basic state of stresses. These stress states are then added together to obtain the actual stress state of the combined model, which is checked against the chosen yield criteria to ensure a safe solution.

The geometry of the loop reinforcement will necessarily lead to a local, triaxial stress state in the joint; however, we have chosen to neglect this effect and assume plane stress. This assumption will – for the typical combinations of loop diameters, rebar diameters, and rebar strengths – lead to a lower shear capacity, and the joint element and submodel may underestimate the capacity in some cases.

5.1. Equilibrium of the submodel

In order to transfer tension or to establish confinement pressure on the joint, it is necessary to mobilise the loop reinforcement. Tension in the loop reinforcement will introduce shear in the centre row of panels, see Fig. 6(b). Based on moment equilibrium, the following relations must hold true:

$$\tau_{21} = \frac{V}{o\,t} = \frac{u}{s}\frac{T}{o\,t}, \quad \tau_{22} = \left(\frac{u}{s} - 1\right)\frac{T}{o\,t} \tag{7}$$

Moreover, from the antisymmetric model it can be concluded that $\tau_{21} = \tau_{23}$. The stringer force V seen in Fig. 6(b) will be balanced out by an adjacent joint element.

The horizontal boundaries may be subjected to shear stresses of different magnitudes, which leads to a linear varying normal force in the central stringer seen in Fig. 6(c). A rather simple stringer model is used to describe this behaviour, and the shear stresses in panels 1 and 3, Fig. 6(c), can be stated as:

$$\tau_1 = \tau^+, \quad \tau_3 = \tau^- \tag{8}$$

The locking bar (see Fig. 2) functions as the central stringer. Horizontal equilibrium for the stringer forces of the central stringer and two shear forces gives the following relation:

$$F^+_{lt} - F^-_{lt} = s\,t\,(\tau_1 - \tau_3) \tag{9}$$

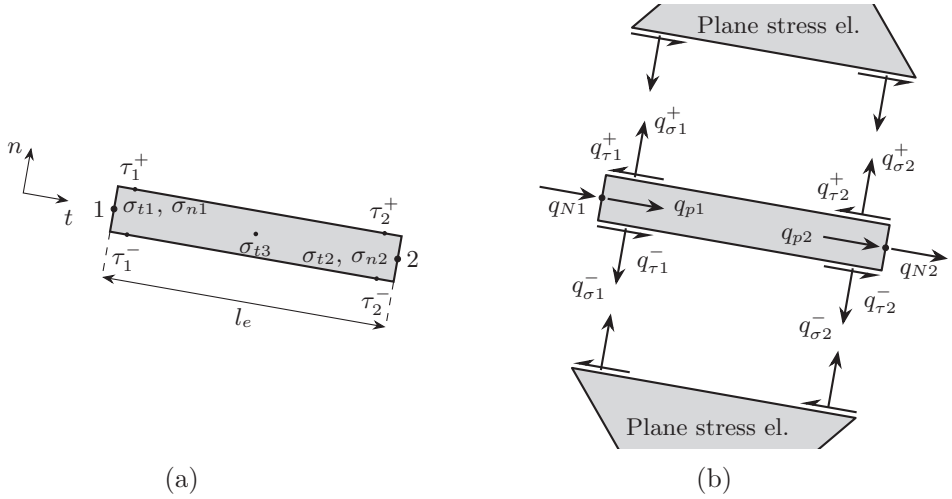

Fig. 5. (a) Geometry, local coordinate system, and stress variables of the joint element. (b) Nodal forces of the joint element and interaction with the plane stress elements.

Shear panels 1 and 3, Fig. 6(c), overlap the three panels from the first stringer model, Fig. 6(b), and the resulting stresses can be determined by simply adding the stress states.

The shear panels need confinement pressure in order to carry shear stresses. The confinement pressure may originate from externally applied loads on the unit joint section, or from stresses developed to create internal equilibrium with the tensile forces in the loop reinforcement or locking bar. The stringer model for transfer of compression, see Fig. 6(d), dictates how compressive loads are transferred through the joint. Equilibrium is required for the horizontal boundaries of the unit joint section; the transverse normal stress σ_n is balanced by the stringer forces T and V as well as the confinement pressure:

$$s\,t\,\sigma_n = T - V - \frac{s-u}{2}\,t\,(\sigma_{n1}+\sigma_{n3}) - u\,t\,\sigma_{n2} \tag{10}$$

and similarly for the horizontal forces:

$$\begin{aligned} F_t^+ &= F_{lt}^+ - 2F_t - \frac{b-o}{2}\,t\,(\sigma_{t1}^+ + \sigma_{t3}^+) - o\,t\,\sigma_{t2}^+ \\ F_t^- &= F_{lt}^- - 2F_t - \frac{b-o}{2}\,t\,(\sigma_{t1}^- + \sigma_{t3}^-) - o\,t\,\sigma_{t2}^- \end{aligned} \tag{11}$$

The shear stress will be symmetric about the vertical center line of the unit joint section; hence, the confinement pressure in the n-direction will be symmetric as well, i.e. $\sigma_{n1} = \sigma_{n3}$. Moreover, for simplicity we assume the same for the confinement in the t-direction, why may lower the shear capacity in cases where $\tau^+ \neq \tau^-$.

5.2. Yield conditions for the submodel components

The actual stress states in the panels and stringers are obtained by adding the stress states of the three stringer models, see Fig. 6 (b)-(d). The actual shear stress in-between the two U-bars will e.g. be given as the sum of τ_1 and τ_{22}. The obtained stress states are required to satisfy the appropriate yield criteria as discussed in this section.

The loop reinforcement and locking bar carry tensile stringer forces, which are limited by the yield strength of the reinforcement. Moreover, we assume that the reinforcement only carries tension, thus, the yield criteria can be stated as:

$$\begin{aligned} 0 &\leqslant T \leqslant A_{su} f_{Yu} \\ 0 &\leqslant F_{lt}^+ \leqslant A_{sl} f_{Yl} \\ 0 &\leqslant F_{lt}^- \leqslant A_{sl} f_{Yl} \end{aligned} \tag{12}$$

where A_{su} and A_{sl} are the cross sectional areas of the loop reinforcement and locking bar, respectively, and f_{Yu} and f_{Yl} are the yield strengths.

The horizontal stringers seen in the stringer model for transverse tension, Fig. 6(b), are so-called compression stringers without any reinforcement to carry tensile forces. The force F_t in Fig. 7 ensures that the stringer force is non-positive. The criterion can be written as a linear inequality:

$$-F_t + \tau_{21}\,\frac{s-u}{2}\,t \leqslant 0 \tag{13}$$

Finally, the shear panels need an adequate yield criterion. The stress state in each panel is described by two normal stresses and a shear stress. We use the Mohr-Coulomb yield criterion for plane stress with a tension cut-off which is given as follows in principal stresses:

$$\begin{aligned} &\sigma_1 \leqslant f_t \\ &k\sigma_1 - \sigma_2 \leqslant f_c \\ &-\sigma_2 \leqslant f_c \end{aligned} \tag{14}$$

where f_t is the uniaxial tensile strength of the joint concrete, and f_c is the effective uniaxial compressive strength. k is a friction parameter defined as

$$k = \left(\sqrt{\mu^2+1} + \mu\right)^2$$

with $\mu = \tan\theta$, where θ is the angle of internal friction. For monolithic concrete, θ is usually taken as 37°, which corresponds to $k = 4$. σ_1 and σ_2 are the largest and smallest principal stresses, respectively, given as:

$$\left.\begin{matrix}\sigma_1 \\ \sigma_2\end{matrix}\right\} = \frac{\sigma_n + \sigma_t}{2} \pm \sqrt{\left(\frac{\sigma_n - \sigma_t}{2}\right)^2 + \tau_{nt}^2} \tag{15}$$

Introducing

$$p_m = -\frac{\sigma_n + \sigma_t}{2}, \quad \sigma_d = \frac{\sigma_n - \sigma_t}{2}, \quad \varphi \geqslant \sqrt{\sigma_d^2 + \tau_{nt}^2}, \tag{16}$$

the principal stresses can now be written as:

$$\begin{aligned} &\sigma_1 \leqslant -p_m + \varphi \\ &-\sigma_2 \leqslant p_m + \varphi \end{aligned}$$

and the Mohr-Coulomb criterion (14) can be stated as:

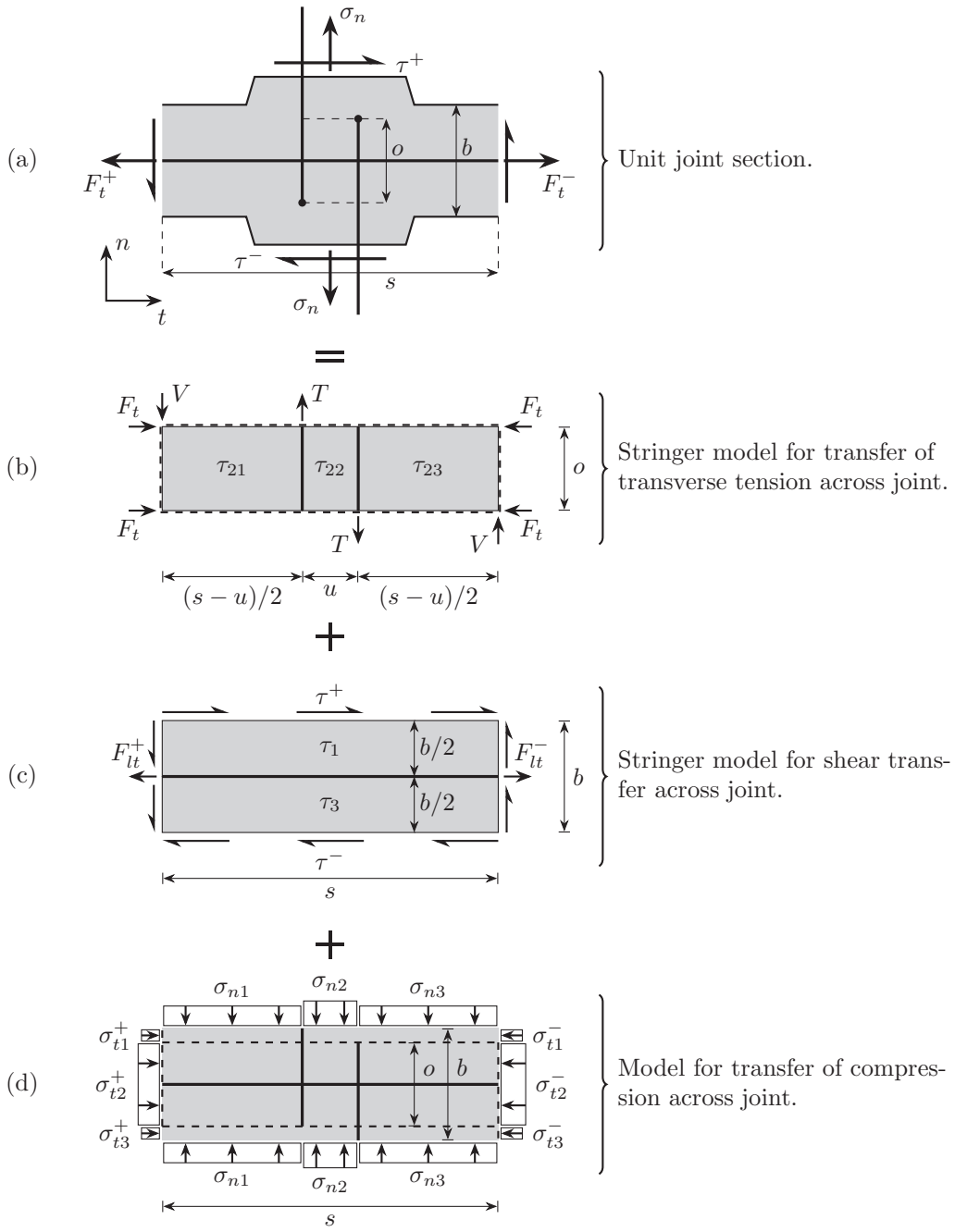

Fig. 6. Unit joint section and the three stringer models: The behaviour of the unit joint section is divided into three main mechanisms, namely transverse tension, shear, and compression.

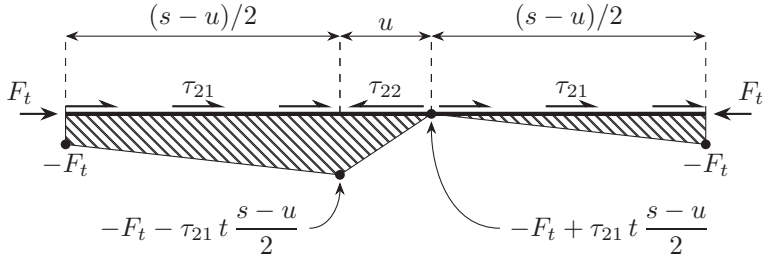

Fig. 7. Compression stringer, confinement pressure F_t, and stringer force distribution.

Fig. 8. Model for the analysis including supports and loading. The dashed lines indicates the interface elements representing the keyed interface.

$$\begin{aligned} &-p_m + \varphi \leqslant f_t \\ &(1-k)p_m + (k+1)\varphi \leqslant f_c \\ &p_m + \varphi \leqslant f_c \end{aligned} \tag{17}$$

The yield criterion fits the format of second-order cone programming since the definition of φ (16) is a quadratic cone, see Eq. (3), while the three constrains in (17) as well as the definitions of p_m and σ_d (16) are linear.

6. Analysis and discussion

6.1. Model

In the following, the results obtained using a single joint element with the submodel yield criterion will be compared to the results of detailed model [15]. The shear load sought to be maximised is applied as on both sides of the joint element, see $q_{\tau 1}^{+}, q_{\tau 1}^{-}, q_{\tau 2}^{+}$, and $q_{\tau 2}^{-}$ in Fig. 5(b), and no normal forces are introduced via the external loading, see Fig. 8.

In practice, the keys near the ends of the joint are used to establish a compressive force in the longitudinal direction, which increase the shear capacity. In order to simulate this behaviour using a single joint element both ends are supported, i.e. equilibrium is not required for the generalised nodal forces q_{N1} and q_{N2}, see Fig. 5. The detailed model [15] and the experiments are subjected to these boundary conditions at the ends, and the single joint element may overestimate the capacity slightly due to this choice of supports.

Two interface elements [15] on either side of the joint element is used to simulate the keyed interface. The interfaces require two material parameters, namely cohesion and friction coefficients, which are fitted to the curve of the detailed model. The magnitude of the cohesion depends on the geometry of the keys as well as the reinforcement layout.

For the analysis, an efficiency factor of $v = 1$ has been used, i.e. no reduction in the compressive strength. This is due to the fact that the primary load carrying mechanisms is direct strut action (as found in the detailed numerical mode [15]) with very deep strut inclination. $v = 1$ was also adopted by Nielsen and Hoang [1] and Herfelt et al. [15].

6.2. Analysis

The calculations have been carried out using the geometry and layout of the tests by Hansen and Olesen [6] and Fauchart and Cortini [7]. The normalised shear capacity is plotted as a function of the mechanical reinforcement ratio, which we define as:

$$\Phi = \frac{\sum A_{su} f_{Yu}}{t\, l f_c} \tag{18}$$

where A_{su} is the cross sectional area of the U-bars, t is the thickness of the joint (see Fig. 2), and l is the total length of the considered joint.

Hansen and Olesen [6] investigated the behaviour of keyed joints with different reinforcement layouts. Some of the specimens featured a significant distance between the U-bars (see Fig. 9) and yielded a lower shear capacity compared to other experiments with similar reinforcement ratios. Moreover, Hansen and Olesen [6] reported that the concrete core of the specimens was completely destroyed at failure. A friction coefficient of $\mu = 0.6$ is used for all specimens by Hansen and Olesen [6], while $\mu = 0.75$ is used for the experiments by Fauchart and Cortini [7]. The cohesion coefficient varies between 1 and 2 MPa.

The specimens seen in Fig. 9 have a length of $l = 1200$ mm, a width of $b = 50$ mm, an overlap of $o = 30$ mm, and 14 keys total. The keys have a depth of 6 mm, a length of $h_2 = 40$ mm, and a spacing of $h_1 = 40$ mm (see Fig. 2). As seen in Fig. 9, the two specimens featured a significant distance between the loop reinforcement, while the U-bars were placed with a mutual distance of 10 mm for the remaining specimens by Hansen and Olesen [6]. For specimens 24 and 26, the results are illustrated as a function of the reinforcement degree in Fig. 10, and the results for all specimens [6,7] are shown in Fig. 11 and listed in Tables 1 and 2.

The cohesion is taken as $c = 1.60$ MPa for specimen 24 and $c = 1.90$ MPa for specimen 26. Fig. 10 shows that the joint element can capture the same behaviour as the detailed model. The plane interface elements can represent the same behaviour as keyed interfaces of the detailed model and the experiments, while the submodel yield criterion predicts an excellent estimate of the *plateau*, i.e. the upper limit for shear capacity. The joint element overestimates the capacity of specimen 24 slightly compared to the detailed model, which may be due to the choice of supports.

Fig. 11 shows the results of the joint element with the submodel yield criterion plotted against the results of the detailed model and the experimental results. Again, the single joint element predicts a satisfactory estimate of the load carrying capacity; only a negligible difference is observed in Fig. 11(a). The joint element predicts a slightly larger shear capacity than the detailed model for some of the experiments, which may be due to the assumptions regarding the supports. Fig. 11(b) shows that the joint element gives satisfactory results compared to experimental data.

It has been shown that the multiscale joint model captures the same behaviour as the detailed model and predicts an excellent estimate of the shear capacity. In this context, it should be mentioned that the multiscale formulation leads to a small optimisation problem which can be solved in a fraction of a second. For the detailed model, on the other hand, CPU time and problem size are several magnitudes larger as seen in Table 3. The computational time shown in Table 3 is the average of 10 runs. The performance is tested on a desktop computer with 12 GB RAM memory and an Intel Xeon CPU W3565 with 8 CPUs and 3.2 GHz clock frequency. The optimisation is performed in MatLab using the commercial solver MOSEK [26]. Based on the required computational time, it is evident that in practice, the joint element model has to be used if entire precast concrete structures should be modelled and analysed within the limited time frame that usually is available in real design projects.

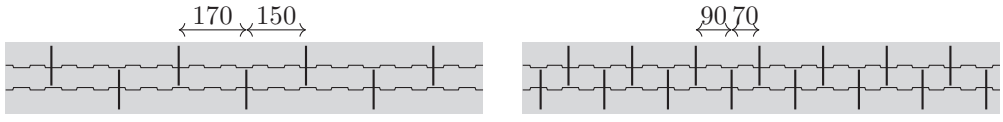

(a) Wall Joint: Specimen 24 (b) Wall Joint: Specimen 26

Fig. 9. The two specimens with a significant distance between the U-bars tested by Hansen and Olesen [6], measurements in millimetres.

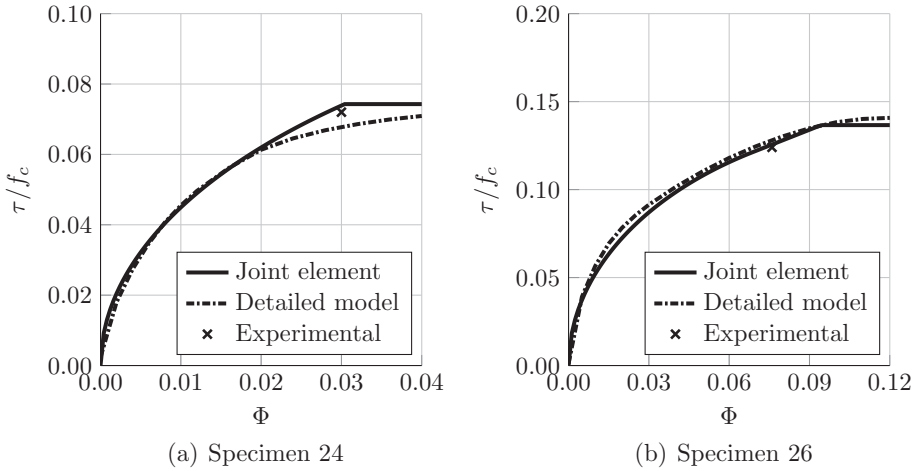

Fig. 10. Comparison of results obtained by the joint element and the detailed model using several thousand elements. Experimental results for specimens 24 (a) and 26 (b) by [6].

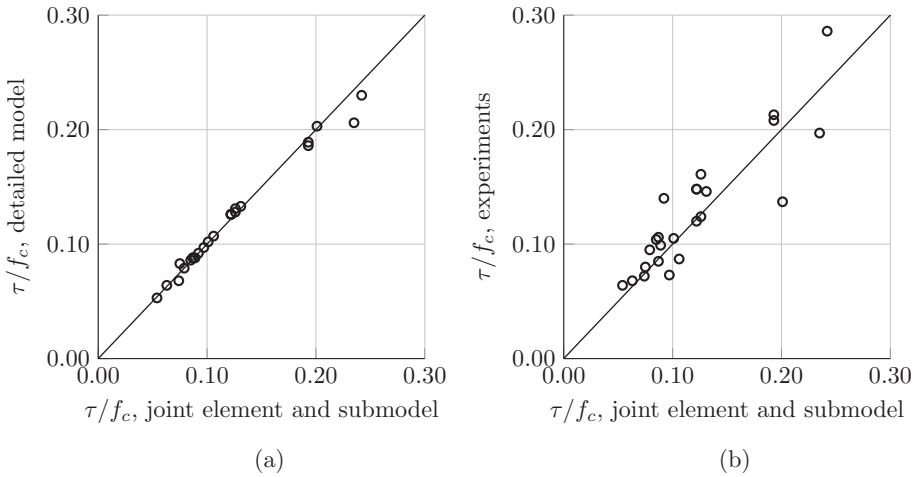

Fig. 11. Analysis using the proposed joint element: (a) Comparison with the detailed model [15], (b) comparison with experimental results [6,7].

Table 1
Data and results of experiments by Hansen and Olesen [6], the numerical model [15], and the proposed joint element.

Specimen	f_c [MPa]	Φ [–]	u [mm]	Experimental τ/f_c	Detailed τ/f_c	Joint element τ/f_c
01	29	0.013	–	0.064	0.053	0.054
02	32	0.030	–	0.095	0.079	0.079
03	32	0.055	–	0.105	0.102	0.101
04	16	0.061	–	0.087	0.107	0.106
05	53	0.018	–	0.068	0.064	0.063
12	25	0.043	–	0.140	0.092	0.092
13	23	0.095	–	0.146	0.133	0.131
14	25	0.039	–	0.099	0.088	0.089
18	27	0.049	–	0.073	0.097	0.097
29	17	0.188	–	0.137	0.203	0.201
23	31	0.025	10	0.080	0.083	0.075
24	26	0.030	150	0.072	0.068	0.074
25	24	0.076	10	0.161	0.131	0.126
26	24	0.076	70	0.124	0.128	0.126
27	15	0.139	10	0.213	0.189	0.193
28	13	0.235	10	0.286	0.230	0.242

Table 2
Data and results of experiments by Fauchart and Cortini [7], the numerical model [15], and the proposed joint element.

Specimen	f_c [MPa]	Φ [–]	u [mm]	Experimental τ/f_c	Detailed τ/f_c	Joint element τ/f_c
5	20	0.049	10	0.106	0.088	0.087
6	20	0.049	10	0.085	0.088	0.087
7	20	0.096	10	0.120	0.126	0.112
8	20	0.246	10	0.197	0.206	0.235
9	20	0.047	10	0.104	0.086	0.085
10	20	0.096	10	0.148	0.126	0.122
11	20	0.096	10	0.148	0.126	0.122
12	20	0.191	10	0.208	0.186	0.193

Table 3
Comparison of problem data for the joint element and detailed model.

	Joint element	Detailed model [15]
Number of equilibrium elements	3	20,024
Number of variables	302	1,364,509
Number of linear constraints	388	1,305,890
Number of conic constraints	44	134,472
Optimisation time	0.022 s	97.89 s

7. Conclusion

An equilibrium joint element for modelling of keyed shear joints has been presented. The scope of the joint element is to be able to assess the strength of shear walls in precast concrete buildings, which is highly dependent on the shear capacity of in-situ cast joints. The main purpose of these joints is to transfer shear, which is done by mobilising the reinforcement, i.e. loop reinforcement and locking bar. The reinforcement layout, however, may introduce local mechanisms inside the concrete core of the joint. A multiscale approach to this problem is taken, and a equilibrium joint element as well as submodel yield criterion have been proposed.

Three modified stringer models form the basis of the submodel. The resulting stress states are obtained by adding the stress states of the three stringer models, which are checked against a suitable yield condition. The submodel is formulated for second-order cone programming, which can be solved efficiently using interior point methods.

The joint element and submodel are validated by comparison to a detailed numerical model based on finite element limit analysis. Excellent agreement between the two models is found, and the joint element captures the same behaviour as the detailed model. The joint element also predicts a satisfactory estimate of the shear capacity when compared to experimental data. The results obtained from the joint element are generally satisfactory, and the fact that the joint element only poses a small mathematical problem, which can be solved in a fraction of a second, makes it more relevant for practical applications than the detailed model presented in [15]. It can be concluded that the proposed multiscale model makes it possible to model real size precast structures while accounting for the complex behaviour of the in-situ cast joints.

Acknowledgement

The authors would like to thank the ALECTIA Foundation and Innovation Fund Denmark for financial support of the research presented in this paper.

References

[1] Nielsen MP, Hoang LC. Limit analysis and concrete plasticity. 3rd ed. Taylor & Francis; 2010.
[2] Muttoni A, Schwartz J, Thürlimann B. Design of concrete structures with stress fields. Springer; 1997.
[3] Muttoni A, Ruiz MF, Niketic F. Design versus assessment of concrete structures using stress fields and strut-and-tie models. ACI Struct J 2015;112(5):605.
[4] Ruiz MF, Muttoni A. On development of suitable stress fields for structural concrete. ACI Struct J 2007;104(4):495.
[5] European Committee for Standardization. En 1992-1-1 eurocode 2: design of concrete structures - part 1-1: general rules and rules for buildings; 2005.
[6] Hansen K, Olesen SO. SBI-Report 97: keyed shear joints. Statens Byggeforskningsinstitut; 1976.
[7] Fauchart J, Cortini P. Étude expérimentale de joints horizontaux entre panneaux préfabriqués pour murs de batiments. Ann LInst Tech Bat Travaux Publics 1972;300:86–103.
[8] Rizkalla SH, Serrette RL, Heuvel JS, Attiogbe EK. Multiple shear key connections for precast shear wall panels. Prestressed Concrete Institute; 1989.
[9] Joergensen HB, Hoang LC. Tests and limit analysis of loop connections between precast concrete elements loaded in tension. Eng Struct 2013;52:558–69.
[10] Jensen BC. On the ultimate load of vertical, keyed shear joints in large panel buildings. Symposium on bearing walls in Warsaw, vol. 8. p. 13th.
[11] Christoffersen J. Ultimate capacity of joints in precast large panel concrete buildings [Ph.D. thesis]. Technical University of Denmark; 1997.
[12] fib bulletin 43. Structural connections for precast concrete buildings; 2008.
[13] Kaneko Y, Mihashi H. Analytical study on the cracking transition of concrete shear key. Mater Struct 1999;32(3):196–202.
[14] Issa MA, Abdalla HA. Structural behavior of single key joints in precast concrete segmental bridges. J Bridge Eng 2007;12:315–24.
[15] Herfelt MA, Poulsen PN, Hoang LC, Jensen JF. Numerical limit analysis of keyed shear joints in concrete structures. Struct Concr 2016;17(3):481–90.
[16] Poulsen PN, Damkilde L. Limit state analysis of reinforced concrete plates subjected to in-plane forces. Int J Solids Struct 2000;37:6011–29.
[17] Hill R. On the state of stress in a plastic-rigid body at the yield point. London, Edinburgh, Dublin Philos Mag J Sci 1951;42(331):868–75.
[18] Drucker D, Prager W, Greenberg H. Extended limit design theorems for continuous media. Quart Appl Math 1952;9:381–9.
[19] Anderheggen E, Knöpfel H. Finite element limit analysis using linear programming. Int J Solids Struct 1972;8:1413–31.
[20] Sloan SW. Lower bound limit analysis using finite elements and linear programming. Int J Numer Anal Methods Geomech 1988;12:61–77.
[21] Krenk S, Damkilde L, Høyer O. Limit analysis and optimal design of plates with equilibrium elements. J Eng Mech 1994;120:1237–54.
[22] Krabbenhoft K, Damkilde L. Lower bound limit analysis of slabs with nonlinear yield criteria. Comput Struct 2002;80(27):2043–57.
[23] Makrodimopoulos A, Martin C. Lower bound limit analysis of cohesive-frictional materials using second-order cone programming. Int J Numer Methods Eng 2006;66(4):604–34.
[24] Bisbos C, Pardalos P. Second-order cone and semidefinite representations of material failure criteria. J Optim Theory Appl 2007;134(2):275–301.
[25] Krabbenhøft K, Lyamin A, Sloan S. Formulation and solution of some plasticity problems as conic programs. Int J Solids Struct 2007;44(5):1533–49.
[26] MOSEK ApS. The MOSEK optimization toolbox for MATLAB manual. Version 7.1 (Revision 33); 2015. <https://www.mosek.com/>.
[27] Andersen ED, Roos C, Terlaky T. On implementing a primal-dual interior-point method for conic quadratic optimization. Math Program 2003;95(2):249–77.
[28] Boyd SP, Vandenberghe L. Convex optimization. Cambridge University Press; 2004.
[29] Alizadeh F, Goldfarb D. Second-order cone programming. Math Program 2003;95(1):3–51.
[30] Lobo MS, Vandenberghe L, Boyd S, Lebret H. Applications of second-order cone programming. Linear Algebra Appl 1998;284(1):193–228.
[31] Damkilde L, Olsen J, Poulsen PN. A program for limit state analysis of plane, reinforced concrete plates by the stringer method. Bygningssta Med 1994;65(1).

Paper III

"Lower bound plane stress element for modelling of 3D structures"

M.A. Herfelt, P.N. Poulsen, L.H. Hoang & J.F. Jensen

Published in: *Proceedings of the ICE: Engineering and Computational Mechanics, 2017*

Lower bound plane stress element for modelling of 3D structures
Herfelt et al.

Proceedings of the Institution of Civil Engineers
Pages 1–11

Keywords: Limit analysis/finite elements/optimisation/reinforced concrete/shear walls

ice | proceedings

Lower bound plane stress element for modelling of 3D structures

M. A. Herfelt, MSc
NIRAS A/S, Teknikerbyen 34, 2830 Virum, Denmark
Department of Civil Engineering, Technical University of Denmark, Brovej, Building 118, 2800 Kgs. Lyngby, Denmark

P. N. Poulsen, Phd
Department of Civil Engineering, Technical University of Denmark, Brovej, Building 118, 2800 Kgs. Lyngby, Denmark

L. C. Hoang, Phd
Department of Civil Engineering, Technical University of Denmark, Brovej, Building 118, 2800 Kgs. Lyngby, Denmark

J. F. Jensen, lic.techn.
NIRAS A/S, Teknikerbyen 34, 2830 Virum, Denmark

In-plane action is often the primary load carrying mechanism of reinforced concrete structures. The plate bending action will be secondary, and the behaviour of the structure can be modelled with a reasonable accuracy using a generalised plane stress element for three-dimensions. In this paper, the formulation of such element is given and the Mohr-Coulomb and von Mises criteria are presented for second-order cone programming. Three examples of increasing complexity are used to analyse the performance of the element and the convergence rate and demonstrate the potential of the proposed element.

1. Introduction

The lateral stability of reinforced concrete structures is often ensured by shear walls. The horizontal loads, e.g. wind or seismic loads, are transferred as in-plane forces via the concrete slabs and the shear walls to the foundations of the structure. The in-plane forces are transferred as shear between the slabs and shear walls as well as in-between shear walls. The transverse forces acting on the slabs and facades are in this regard secondary to the in-plane forces. It is crucial to the overall capacity of the structure that the analysis considers the structural system as a single unit: If the shear walls are analysed individually, a significant portion of the strength is neglected, see Fig. 1.

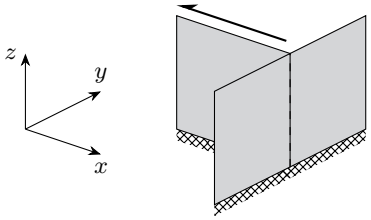

Figure 1. Shear wall subjected to a shear force: The transverse wall increases the capacity of the structure.

Practical design and analysis of reinforced concrete structures in the ultimate limit state often requires consideration of plastic material behaviour. This material behaviour can be incorporated in the analysis by use of either simplified models, e.g. rigid-plasticity (see e.g. Drucker *et al.*, 1952; Prager, 1952), or more advanced model which may include hardening, softening, etc. The latter can be implemented in numerical frameworks, e.g. finite element analysis, and provides the most accurate results compared to the simplified material models. While the advanced models can model the observed material behaviour to a reasonable degree, it is often difficult to obtain the required material parameters for the models.

Models based on the theory of rigid-plasticity have been used for almost a century to assess the capacity of concrete structures (Ingerslev, 1921; Nielsen and Hoang, 2010). The rather crude material model leads to an elegant framework known as limit analysis in which several methods have been developed e.g. homogeneous stress triangles (Nielsen, 1971), the yield line method (Johansen, 1962), and stress field methods (Muttoni *et al.*, 1997).

The methods can be classified as either upper bound methods, where a kinematically admissible displacement field is determined, or as lower bound methods, where a statically admissible stress field is determined. In practice, manual upper bound and lower bound methods are still widely used to assess the capacity in the ultimate limit state. The accuracy of the calculations, however, is very dependent on the skill and intuition of the individual structural engineer. For complex structures, the results may be far from the actual capacity.

Finite element limit analysis is the numerical counterpart of manual limit analysis. The method is a special case of the general finite element method and assumes a rigid-plastic material behaviour. Like manual limit analysis, finite element limit analysis can be formulated either as lower bound, upper bound problems, or mixed problems (which are often more accurate than the strict upper and lower bound problems). Anderheggen and Knöpfel (1972) presented the general framework as well as finite elements for both solids and plate bending. The mathematical problem of finite element limit analysis is formulated as a convex optimisation problem which can be solved remarkably efficiently using state-of-the-art solvers.

Several authors have treated plane stress and plane strain elements (see e.g. Sloan, 1988; Poulsen and Damkilde, 2000; Makrodimopoulos and Martin, 2006, 2007). Plane strain elements, however, have received most of the attention as they are used in geotechnical engineering. More recently, meshless methods have been presented as an alternative to the classical finite element version of limit analysis (Smith *et al.*, 2014). Adaptive meshing has a major potential for finite element limit analysis as displayed by Lyamin *et al.* (2005) amongst others. Numerical limit analysis of concrete structures have not received the same amount of attention, but there have nevertheless been some attempts at treating three-dimensional concrete structures within the framework of finite element limit analysis (Larsen, 2010).

This paper will present the basic mathematical formulation of finite element limit analysis, namely lower bound load optimisation. A brief introduction to second-order cone programming (SOCP) is given and solution strategies will be presented.

The basic lower bound plane stress element is generalised to three-dimensions, which will make it possible to model the load carrying systems of modern concrete buildings in a simple manner while disregarding the plate bending behaviour. For reinforced concrete, the proposed element will use the Mohr-Coulomb yield criterion, which can be cast as second-order cones, hence, the final optimisation problem will be a second-order cone program. Three examples will be presented: The first example will be used to validate the implementation and analyse the convergence rate of the element, while the second and third examples will demonstrate the use and strength of the proposed element.

2. Convex optimisation and limit analysis

2.1. Convex optimisation

Convex optimisation problems, also known as convex programs, can be found within several engineering applications, e.g. antenna ray weight design and truss optimisation (Lobo *et al.*, 1998). The main advantage of convex optimisation is that any optimum will be the global optimum, hence, the class of problems can be solved efficiently using gradient based methods. For general non-linear optimisation problems, several local extrema may exist making it practically impossible to ensure that the found solution is the global extremum. For plane problems in finite element limit analysis, second-order cone programming is often used as the commonly used yield functions can be represented exact using second-order constraints (Bisbos and Pardalos, 2007).

Second-order cone programs are non-linear convex optimisation problems, where a linear objective function is minimised over the intersection of an affine set and the Cartesian product of second-order cones (Andersen *et al.*, 2003). The standard form of SOCP can be stated as:

$$\begin{aligned} &\text{minimise} && \boldsymbol{g}^T\boldsymbol{x} \\ &\text{subject to} && \mathbf{A}\boldsymbol{x} = \boldsymbol{b}, \\ & && \boldsymbol{x} \in \mathcal{Q} \end{aligned} \tag{1}$$

where $\boldsymbol{x}$ is the problem variables. The matrix, $\mathbf{A}$, and two vectors, $\boldsymbol{b}$ and $\boldsymbol{g}$, define the linear constraints and objective function of the optimisation problem. The notation, $\boldsymbol{x} \in \mathcal{Q}$, indicates that the vector $\boldsymbol{x}$ should be in the Cartesian product of second-order cones, i.e.:

$$\boldsymbol{x} \in \mathcal{Q} \quad \Leftrightarrow \quad \boldsymbol{x}_1 \in \mathcal{Q}_{m_1},\, \boldsymbol{x}x_2 \in \mathcal{Q}_{m_2},\, \ldots,\, \boldsymbol{x}_q \in \mathcal{Q}_{m_q} \tag{2}$$

where $\boldsymbol{x}_i$ are subvectors of $\boldsymbol{x}$ and $\mathcal{Q}_{m_i}$ is a quadratic cone of size m_i. All second-order cone programs can be recast to fit the standard form (1) by e.g. adding slack variables. The simplest quadratic cone is the second-order cone also known as the Lorentz cone, which can

be stated as the following set:

$$\mathcal{Q} := \left\{ \boldsymbol{x} \in \mathbb{R}^n \ : \ x_1^2 \geq \sum_{i=2}^{n} x_i^2, \ x_1 \geq 0 \right\} \tag{3}$$

All quadratic cones can be transformed to the second-order cone (3).

SOCP can be solved efficiently by interior point methods, a class of algorithms developed from the polynomial time algorithm proposed by Karmarkar (1984). Interior point methods are based on a steepest descend approach, and in state-of-the-art solvers the Karush-Kuhn-Tucker (KKT) conditions of the original optimisation problem is embedded in a slightly larger model, a so-called homogeneous model (see e.g. Nesterov *et al.*, 1999; Sturm, 1997), which makes it possible to easily detect primal and dual infeasibility as well as ill-posed problems. The homogeneous model is solved using Newton's method, however, the step size is restricted to very small steps. Nesterov-Todd scaling (see Nesterov and Todd, 1997) is used to facilitate longer steps, and the search direction is computed in a scale space where it is uniquely defined.

Modern solvers are capable of solving large scale optimisation problems with hundreds of thousands variables and constraints in a matter of minutes on a standard laptop due to the polynomial time complexity of the algorithm. Large scale finite element limit analysis problems will be extremely sparse, which can be exploited by solvers to reduce the time complexity to near linear. This a major advantage over non-linear finite element analysis, which often requires much longer computational times. For an in-depth description of convex optimisation and state-of-the-art solvers, the reader is referred to Boyd and Vandenberghe (2004), Andersen *et al.* (2003), and Terlaky (2013).

2.2. Lower bound limit analysis

The scope of lower bound limit analysis is to maximise the variable load acting on the structure while ensuring a statically admissible stress field, i.e. a stress field which satisfy equilibrium and does not violate the yield criterion in any point. The objective function of the optimisation problem is the load factor, λ, which is sought to be maximised.

Every optimisation problem has a so-called dual problem, which is linked to the original (primal) problem via the Lagrange function and KKT conditions. The dual problem of lower bound limit analysis is the corresponding kinematic problem. The primal and dual problems are solved simultaneously, and while the solution to the lower bound problem yields a statically admissible stress field, the solution to the corresponding kinematic problem can be interpreted as the collapse mode.

The mathematical problem of lower bound load optimisation can be derived from the virtual work equation and can be stated as follows:

$$\begin{aligned} &\text{maximise} && \lambda \\ &\text{subject to} && \mathbf{B}^T \boldsymbol{\sigma} = \boldsymbol{p}\,\lambda + \boldsymbol{p}_0 \\ & && f(\boldsymbol{\sigma}_i) \leq 0, \ i = 1, 2, \ldots, m \end{aligned} \tag{4}$$

The linear equilibrium equations and yield criteria ensure a statically admissible stress field while the load factor λ is maximised. The structure is subject to a load composed by a fixed part, $\boldsymbol{p}_0$, and a scalable part, $\boldsymbol{p}\lambda$. $\mathbf{B}^T$ is the global equilibrium matrix and $\boldsymbol{\sigma}$ is the stress vector. The yield function f is generally non-linear, but convex, hence, the problem (4) is a convex optimisation problem. For plane problems, the Mohr-Coulomb criterion with a tension cut-off can be cast as second-order cones. Second-order cone programming have been used for more than a decade in the field of finite element limit analysis (Bisbos and Pardalos, 2007; Krabbenhøft *et al.*, 2007; Makrodimopoulos and Martin, 2007) and can be considered as an established technology at this point.

Assuming that the yield function f can be represented by linear and second-order constraints, the problem (4) can be expanded to obtain the following form:

$$\begin{aligned} &\text{maximise} && \lambda \\ &\text{subject to} && \mathbf{B}^T \boldsymbol{\sigma} = \boldsymbol{p}\,\lambda + \boldsymbol{p}_0 \\ & && \mathbf{C}_\beta \boldsymbol{\beta} + \mathbf{C}_\alpha \boldsymbol{\alpha} + \mathbf{C}_\gamma \boldsymbol{\gamma} = \boldsymbol{C}_0 \\ & && \mathbf{E}_\sigma \boldsymbol{\beta} + \mathbf{E}_\alpha \boldsymbol{\alpha} + \mathbf{E}_\gamma \boldsymbol{\gamma} \leq \boldsymbol{E}_0 \\ & && \boldsymbol{\gamma}_i \in \mathcal{Q}_{k_i}, \quad i = 1, 2, \ldots, m, \end{aligned} \tag{5}$$

where $\mathbf{C}_\sigma$, $\mathbf{C}_\alpha$, and $\mathbf{C}_\gamma$ are matrices associated with the linear equality constraints for the yield function, while the matrices, $\mathbf{E}_\sigma$, $\mathbf{E}_\alpha$, and $\mathbf{E}_\gamma$, define the linear inequality constraints. The two vectors $\boldsymbol{C}_0$ and $\boldsymbol{E}_0$ typically contain material parameters. The variable vectors, $\boldsymbol{\alpha}$ and $\boldsymbol{\gamma}$, contain the auxiliary variables used for the yield function, whereas $\boldsymbol{\gamma}$ is used for the second-order constrains: The vector $\boldsymbol{\gamma}_i$ is a subset of $\boldsymbol{\gamma}$ associated with the ith checkpoint which is required to be in a quadratic cone $\mathcal{Q}_{k_i}$ of size k_i. The scalar m is the number of checkpoints.

3. Finite element formulation

3.1. Lower bound plane stress element

The geometry of the element is defined by three corner nodes. A linear stress field is chosen for the element, and a set of stress variables which describe a plane stress state is associated with each of the three nodes. The stresses of the element are given in the local coordinate system of the element. The element stress vector is given as

$$\boldsymbol{\sigma}_{el} = \begin{bmatrix} \boldsymbol{\sigma}_1 \\ \boldsymbol{\sigma}_2 \\ \boldsymbol{\sigma}_3 \end{bmatrix}, \tag{6}$$

where $\boldsymbol{\sigma}_i$ is the set of stress variables associated with the ith node,

$$\boldsymbol{\sigma}_i = \begin{bmatrix} \sigma_x^i \\ \sigma_y^i \\ \tau_{xy}^i \end{bmatrix} \tag{7}$$

The element requires a total of nine variables to describe the linear stress field.

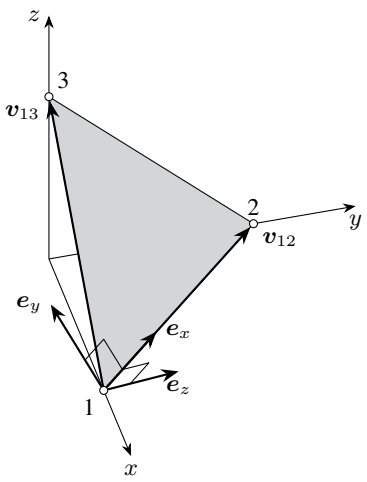

Figure 2. Geometry and local coordinate system of the three-dimensional element.

The local coordinate system of the given element is defined by the following basis vectors:

$$\boldsymbol{e}_z = \frac{\boldsymbol{v}_{12} \times \boldsymbol{v}_{13}}{\|\boldsymbol{v}_{12} \times \boldsymbol{v}_{13}\|}, \quad \boldsymbol{e}_x = \frac{\boldsymbol{v}_{12}}{\|\boldsymbol{v}_{12}\|}, \quad \boldsymbol{e}_y = \boldsymbol{e}_z \times \boldsymbol{e}_x, \tag{8}$$

where $\boldsymbol{v}_{ij}$ is a vector going from node i to node j in the global coordinates. The local coordinates of node i, $\boldsymbol{x}_i$, can now be determined by the transformation,

$$\boldsymbol{x}_i = \mathbf{E}^T \boldsymbol{X}_i, \quad \text{with} \quad \mathbf{E} = \begin{bmatrix} \boldsymbol{e}_x & \boldsymbol{e}_y & \boldsymbol{e}_z \end{bmatrix} \tag{9}$$

where $\boldsymbol{X}_i$ is the global coordinates of node i, and $\mathbf{E}$ is the transformation matrix. For each element boundary, we define a normal vector in the local coordinate system,

$$\boldsymbol{n}_i = \begin{bmatrix} n_x^i \\ n_y^i \end{bmatrix}, \tag{10}$$

where i is the element side number. In order to obtain a lower bound solution, traction continuity is required. Due to the linear stress field, equilibrium of tractions have to be enforced twice for each element side. Based on the normal vectors (10), we define the stress-to-traction array $\mathbf{P}_i^T$ for side i,

$$\mathbf{P}_i^T = \begin{bmatrix} n_x^i & 0 & -n_y^i \\ 0 & -n_y^i & n_x^i \\ 0 & 0 & 0 \end{bmatrix} \tag{11}$$

and

$$\tilde{\mathbf{P}}_i^T = l_i \mathbf{P}_i^T, \tag{12}$$

where l_i is the length of side i. The last row of $\mathbf{P}_i^T$ represent the local z-direction, in which no tractions are present. The global equilibrium of the system is done in global coordinates, hence, it is necessary to transform the tractions. The tractions in global coordinates for node i of the element can therefore be stated as

$$\boldsymbol{q}_i = \begin{bmatrix} q_{jx}^i \\ q_{jy}^i \\ q_{jz}^i \\ q_{kx}^i \\ q_{ky}^i \\ q_{kz}^i \end{bmatrix} = \frac{1}{2} \begin{bmatrix} \mathbf{E}^T & \\ & \mathbf{E}^T \end{bmatrix} \begin{bmatrix} \tilde{\mathbf{P}}_j^T \\ \tilde{\mathbf{P}}_k^T \end{bmatrix} \boldsymbol{\sigma}_i \tag{13}$$

where j and k are the two sides which meet in node i, and q_{jx}^i is the traction in the x-direction on side j at node i of the element.

The element can be subjected to surface loads, γ_x and γ_y in the local x and y-directions, acting on the entire area. The derivatives of the linear stress field must balance these surface loads, which

leads to two additional equilibrium equations:

$$\begin{aligned} \frac{\partial \sigma_x}{\partial x} + \frac{\partial \tau_{xy}}{\partial y} + \gamma_x = 0 \\ \frac{\partial \sigma_y}{\partial y} + \frac{\partial \tau_{xy}}{\partial x} + \gamma_y = 0 \end{aligned} \tag{14}$$

Utilising the shape functions of the linear stress field, the so-called internal equilibrium equations (14) can now be stated as

$$\boldsymbol{q}_c = A \begin{bmatrix} \gamma_x \\ \gamma_y \end{bmatrix} = \frac{1}{2} \begin{bmatrix} \tilde{\mathbf{P}}_1^T & \tilde{\mathbf{P}}_2^T & \tilde{\mathbf{P}}_3^T \end{bmatrix} \sigma, \tag{15}$$

The element equilibrium matrix can be written as follows by combining (13) and (15):

$$\boldsymbol{q} = \frac{1}{2} \begin{bmatrix} \mathbf{E}^T \tilde{\mathbf{P}}_2^T & & \\ \mathbf{E}^T \tilde{\mathbf{P}}_3^T & & \\ & \mathbf{E}^T \tilde{\mathbf{P}}_3^T & \\ & \mathbf{E}^T \tilde{\mathbf{P}}_1^T & \\ & & \mathbf{E}^T \tilde{\mathbf{P}}_1^T \\ & & \mathbf{E}^T \tilde{\mathbf{P}}_2^T \\ \tilde{\mathbf{P}}_1^T & \tilde{\mathbf{P}}_2^T & \tilde{\mathbf{P}}_3^T \end{bmatrix} \begin{bmatrix} \boldsymbol{\sigma}_1 \\ \boldsymbol{\sigma}_2 \\ \boldsymbol{\sigma}_3 \end{bmatrix} = \mathbf{B}_{el}^T \boldsymbol{\sigma}_e \tag{16}$$

Lower bound elements may contain linear dependencies which cause numerical issues (Makrodimopoulos and Martin, 2006). These problems, however, can be avoided by dividing the element into three subelements, each with a linear stress field. This was done by Herfelt *et al.* (2016) for the lower bound plane stress element by Poulsen and Damkilde (2000). The subdivision also increase the accuracy of the element, however, the problem size is likewise increased. Several of the additional variables and equations can be eliminated, hence, the problem size is only increased marginally.

3.2. Reinforced concrete yield criterion

The yield criterion is enforced for all three sets of stresses of the element to ensure a safe stress field. For the equilibrium equations the total stresses are used, which comprise the stresses carried by the concrete and by the reinforcement. The Mohr-Coulomb yield criterion with a tension cut-off is used for the concrete, while a simple, linear criterion is adopted for the reinforcement.

The reinforcement is assumed to consist of an orthogonal mesh of rebars oriented in an angle θ to the local coordinate system of the element, see Fig. 3. Moreover, it is assumed that the reinforcement only carries axial forces (Nielsen and Hoang, 2010). The relation between the total stresses, the concrete stresses, and

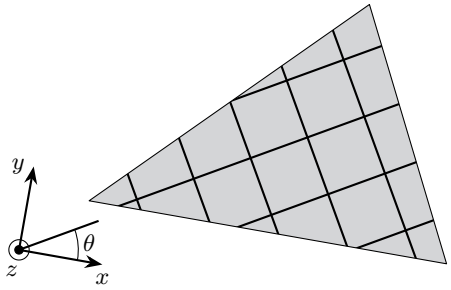

Figure 3. Orthogonal reinforcement in an angle θ to the local coordinate system of the element.

the reinforcement stresses are given as

$$\begin{bmatrix} c^2 & s^2 & 2sc \\ s^2 & c^2 & -2sc \\ -sc & sc & c^2 - s^2 \end{bmatrix} \begin{bmatrix} \sigma_x \\ \sigma_y \\ \tau_{xy} \end{bmatrix} = \begin{bmatrix} \sigma_{xm} \\ \sigma_{ym} \\ \tau_{xym} \end{bmatrix} + \begin{bmatrix} \tilde{\sigma}_{xs} \\ \tilde{\sigma}_{ys} \\ 0 \end{bmatrix}, \tag{17}$$

where $c = \cos\theta$ and $s = \sin\theta$. Subscript m indicates concrete stresses while subscript s indicates reinforcement stresses. Moreover, $\tilde{\sigma}_{si}$ is the equivalent reinforcement stress defined as

$$\tilde{\sigma}_{si} = \frac{A_{si}}{t} \sigma_{si} \tag{18}$$

where A_{si} is the reinforcement area per unit length in the i-direction and t is the out-of-plane thickness of the considered element. The yield criterion for the reinforcement can be written as follows using equivalent stresses:

$$\begin{aligned} 0 \leq \tilde{\sigma}_{xs} \leq \tilde{f}_{yx} = \frac{A_{sx}}{t} f_y \\ 0 \leq \tilde{\sigma}_{ys} \leq \tilde{f}_{yy} = \frac{A_{sy}}{t} f_y \end{aligned} \tag{19}$$

where $\tilde{f}_y$ is the equivalent yield strength. The compressive strength of the reinforcement is neglected as seen in (19), and the reinforcement stresses must be non-negative as a consequence.
The Mohr-Coulomb criterion is given in terms of principal stresses and can be stated as follows for plane stress:

$$\begin{aligned} \sigma_1 &\leq f_t \\ k\sigma_1 - \sigma_2 &\leq f_c \\ -\sigma_2 &\leq f_c \end{aligned} \tag{20}$$

where f_t is the uniaxial tensile strength of the concrete, and f_c is the uniaxial compressive strength. k is a friction parameter, which is usually taken as 4 for normal strength concrete corresponding to

an angle of internal friction of approximately 37°. σ_1 and σ_2 are the largest and smallest principal stresses, respectively, which is given as

$$\left.\begin{matrix}\sigma_1\\ \sigma_2\end{matrix}\right\} = \frac{\sigma_{xm}+\sigma_{ym}}{2} \pm \sqrt{\left(\frac{\sigma_{xm}-\sigma_{ym}}{2}\right)^2 + \tau_{xym}^2} \tag{21}$$

Introducing three auxiliary variables,

$$\begin{aligned} p_m &= -\frac{\sigma_{xm}+\sigma_{ym}}{2},\\ \sigma_d &= \frac{\sigma_{xm}-\sigma_{ym}}{2},\\ \varphi &\geq \sqrt{\sigma_d^2+\tau_{xym}^2}, \end{aligned} \tag{22}$$

bounds to the principal stresses (21) can now be stated:

$$\begin{aligned} \sigma_1 &\leq -p_m + \varphi\\ -\sigma_2 &\leq p_m + \varphi \end{aligned} \tag{23}$$

The yield criterion (20) can be written as three linear inequality constraints in addition to the definitions of the three auxiliary variables (22):

$$\begin{aligned} -p_m + \varphi &\leq f_t\\ (1-k)\,p_m + (k+1)\,\varphi &\leq f_c\\ p_m + \varphi &\leq f_c \end{aligned} \tag{24}$$

The yield criterion fits the form of second-order cone programming since the definition of φ is a second-order cone (3).

3.3. von Mises yield criterion

The von Mises yield criterion is commonly used for metals and is based on the second stress invariant, J_2, which is given as follows:

$$\begin{aligned} J_2 = &\frac{(\sigma_x-\sigma_y)^2}{6} + \frac{(\sigma_y-\sigma_z)^2}{6} + \frac{(\sigma_z-\sigma_x)^2}{6}\\ &+ \tau_{xy}^2 + \tau_{yz}^2 + \tau_{xz}^2 \end{aligned} \tag{25}$$

For plane stress, the second stress invariant is reduced to

$$J_2 = \frac{(\sigma_x-\sigma_y)^2}{6} + \frac{\sigma_y^2}{6} + \frac{\sigma_x^2}{6} + \tau_{xy}^2 \tag{26}$$

The von Mises criterion is given as

$$\sqrt{3J_2} \leq f_y, \tag{27}$$

where f_y is the uniaxial yield strength. Introducing three auxiliary variables,

$$\alpha_1 = \frac{\sqrt{3}}{2}\left(\sigma_x-\sigma_y\right),\quad \alpha_2 = \frac{1}{2}\left(\sigma_x+\sigma_y\right),\quad \alpha_3 = \sqrt{3}\tau_{xy}, \tag{28}$$

the criterion (27) can be restated as a second-order cone:

$$\sqrt{\alpha_1^2+\alpha_2^2+\alpha_3^2} \leq f_y \tag{29}$$

It has been shown that both the reinforced concrete yield criterion and the von Mises yield criterion fit the format of second-order cone programming for plane stress.

4. Examples

The scope of this section is to analyse the performance of the element and illustrate the use. The commercial solver, MOSEK (MOSEK ApS, 2015) is used for the optimisation. For the computational time, please note that all calculations are performed on a laptop with an *Intel core i7-4720HQ* with 8 CPUs and 2.6 GHz clock frequency. The meshes for examples 2 and 3 are generated using GiD v12 (Ribó *et al.*, 1998).

4.1. Deep beam with shear supports

The first example is a deep reinforced concrete beam subject to a uniformly distributed load. The beam is supported in either end by shear supports as seen in Fig 4. The analytical solution to the deep

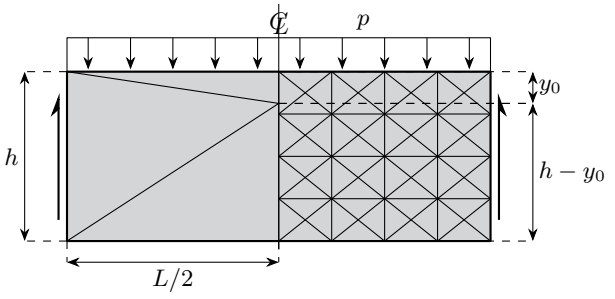

Figure 4. Deep beam with shear supports.

beam example is well-known (Nielsen and Hoang, 2010) and can be obtained by the mesh on the left side in Fig. 4:

$$p^* = \frac{4\Phi h^2 f_c}{(1+\Phi)\,L^2} \tag{30}$$

where Φ is the mechanical reinforcement ratio defined as:

$$\Phi = \frac{A_s f_y}{t f_c} \tag{31}$$

Using $h = 2$ m, $L = 6$ m, $f_c = 20$ MPa, and $\Phi = 0.075$, the exact limit load is $p^* = 0.6202$ MPa. A structured mesh (see the right hand side of Fig. 4) is used to calculate a lower bound of the limit load of the deep beam.

nel	p [MPa]	Error [%]	Time [s]
64	0.5556	10.42	0.31
256	0.6053	2.40	0.88
1024	0.6177	0.39	3.77
4096	0.6191	0.17	9.23
16384	0.6193	0.13	43.40

Table 1. Limit load, error, and computational time for the deep beam example.

Tab. 1 shows that the structured mesh approaches the exact limit load from below as the number of elements (*nel*) increases. The convergence and computational time will be discussed in a following section, but it is observed that the computational time appears to be roughly proportional to the problem size. The stress distribution is illustrated in Fig. 5.

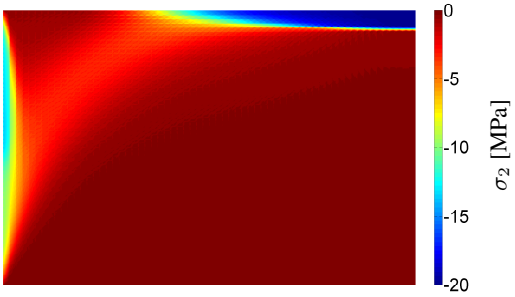

Figure 5. Lowest principal stress σ_2 for the deep beam example using 16384 elements.

4.2. Cantilever I-beam

A cantilever steel I-beam is subjected to a uniformly distributed line load acting on top of the web. The web has a height of 300 mm, and the flanges have a width of 300 mm. The web and flanges have a thickness of 10 mm, and the cantilever beam has a length of 3 metres. The steel has a yield strength of $f_y = 250$ MPa. This gives a plastic moment capacity of 281 kNm and a limit load of $p^* = 62.5$ kN/m assuming a maximum stress of 250 MPa. Four different meshes are analysed. The medium density mesh comprising 948 elements is shown in Fig. 6. With a thickness of just 10 mm, the effect of local bending in the web and flanges is negligible, while

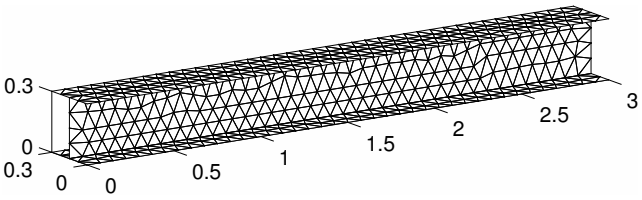

Figure 6. Medium density mesh of the cantilever I-beam using 948 elements. The beam is supported at the left end.

the external load will almost exclusively be carried via in-plane forces, hence, the proposed element will provide a decent estimate of the capacity.

The load capacity of the cantilever I-beam increases with the mesh density as seen in Tab. 2. The von Mises yield criterion requires fewer variables than the reinforced concrete criterion, hence, the computational time is lower for the same number of elements. The model predicts a limit load slightly larger than the analytical moment capacity, however, this is due to the von Mises criterion where the largest stress can exceed f_y for certain stress states. Fig. 7 shows the largest and smallest principal stresses near the supported (left) end of the cantilever.

Mesh	*nel*	p [kN/m]	Time [s]
Coarse	238	63.24	0.44
Medium	948	64.18	1.86
Fine	3616	64.90	3.56
Very fine	14646	65.25	16.06

Table 2. Limit load and computational time for the cantilever I-beam example.

4.3. Four-storey stairwell with door openings

The third example is a four-storey stairwell of reinforced concrete with door openings. The stairwell is subjected to a shear force acting on top of the wall with the door openings (see Fig. 8), which causes both bending and torsion in the stairwell. The shear walls have a thickness of 180 mm, hence, the effect of local bending in each individual wall is not negligible as in the previous example, however, a lower bound value is obtained by neglecting the moment capacity of the walls. In practice, the corners are reinforced with loop reinforcement which ensures the transfer of bending moments between adjacent walls. The dimensions of the shear walls are given in Fig. 8 and the door openings have a height of 2.10 metres and a

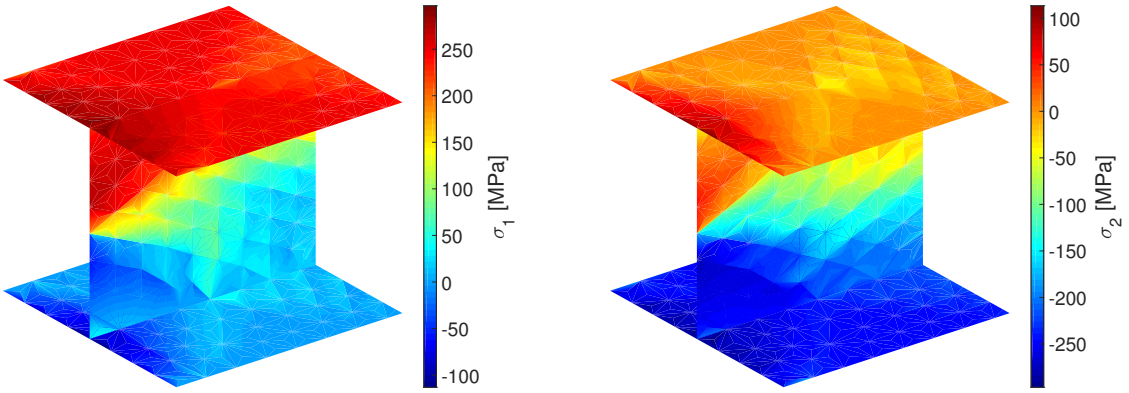

(a) σ_1 (b) σ_2

Figure 7. Largest and smallest principal stresses near the support of the I-beam using the fine mesh.

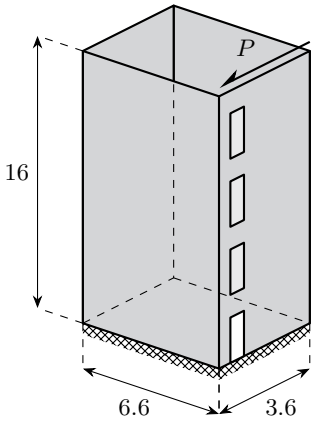

Figure 8. Four-storey shear wall subject to bending and torsion. Dimensions are given metres.

		p [kN/m]		
Mesh	*nel*	$\nu = 1$	$\nu = 0.550$	Time [s]
Coarse	864	85.27	85.06	2.89
Medium	3564	88.62	87.80	10.52
Fine	11379	89.25	88.46	37.38

Table 3. Limit load and computational time for the stairwell example.

width of 0.90 metres. The shear walls are reinforced with two layers of Ø8 bars per 150 mm in both directions. The design yield strength of the reinforcement is chosen as $f_{yd} = 458$ MPa. The concrete has a design compressive strength of $f_{cd} = 21.43$ MPa, while the tensile strength is set to zero. Two different effectiveness factors ν is considered, namely $\nu = 1$ and $\nu = 0.7 - f_c/200 = 0.550$ (where $f_c = 30$ MPa is the characteristic strength), and the design compressive stress is reduced accordingly, $f_{cd} = \nu \cdot 21.43$ MPa.

Tab. 3 shows that the coarse mesh yields a reasonable estimate despite using only 864 elements. The fine mesh yields less than 5 % additional capacity despite having 13 times more elements. It is noted that the model approaches the exact limit load from below which is to be expected from a lower bound element. Tab. 3 also shows that the two effectiveness factors yields approximately the same capacity: Using $\nu = 0.550$ reduces the capacity by less than one percent since the reinforcement is the limiting factor.

Fig. 9(a) shows the collapse mode for the shear wall with door openings: The bending failure occurs near the supports, which allows the wall to start rotating. Moreover, local failures are observed near the door openings and the top. Fig. 9(b) to (e) shows the stress distribution for the four walls of the stairwell. It is seen that all walls mobilised and carry stresses. Struts are formed between the door openings as shown in Figure 9(c), and the slender columns to the left of the door openings carry considerably stresses. The largest compressive stresses occur near the bottom door opening and approach the compressive strength of the concrete, see Figure 9(b) and (c).

4.4. Computational time and convergence

The three examples have demonstrated the strength of the element. For all three examples, the capacity increased with the number of elements, i.e. the models approached the exact limit load from

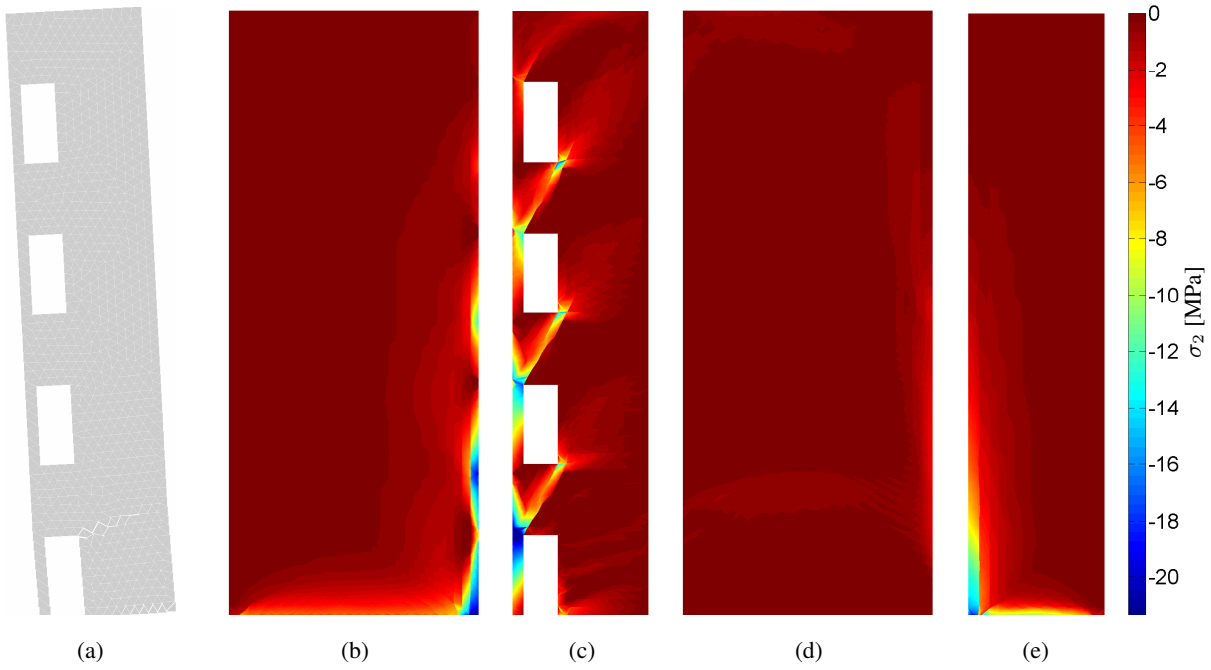

Figure 9. a) Collapse mode of the wall with the door openings. b) - e) Smallest principal stresses of the four walls of the stairwell example with $\nu = 1$ using the fine mesh.

below, which is to be expected. For the first example, the deep beam, the analytical solution is well-known. It is observed from Tab. 1 that the error is approximately inversely proportional to the number of element, i.e. increasing the number of elements by a factor of four decrease the error by a factor of four.

For the cantilever I-beam and stairwell examples, the computed limit loads only increase marginally for the fine meshes compared to the coarse mesh. This indicate that coarse meshes provide reasonable approximations to the actual stress field.

The computational time required for the three examples is illustrated in Figure 10. It is observed that the computational time is approximately proportional to the number of elements to the power of 1.1, indicated by $O(n^{1.1})$ in the figure. Moreover, the cantilever I-beam example required a lower computational time due to the use of the von Mises criterion, but the slope of the curve seems to be approximately the same as the other two examples.

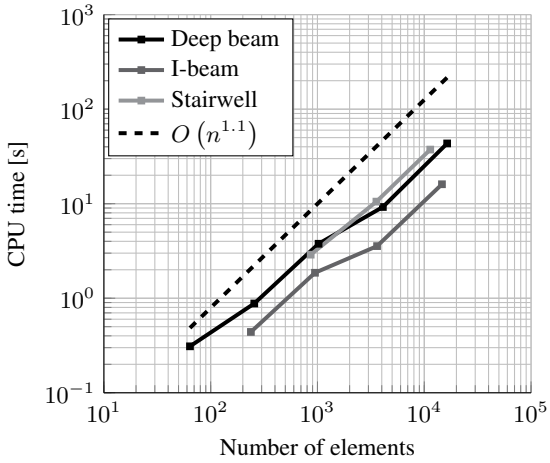

Figure 10. Computational time as a function of the number of elements.

5. Conclusion

A generalised plane stress element subject to in-plane forces has been presented. The element is a lower bound element with a linear stress distribution. The necessary equilibrium equations of the element are presented together with two different yield criteria, namely the Mohr-Coulomb criterion with a tension cut-off and the von Mises criterion, both for plane stress. Both yield criteria fit the format of second-order cone programming, a class of optimisation problems which can be solved efficiently using interior point methods.

Three examples are presented to display the use of the element. The first example is a plane deep beam with shear supports subject to a uniformly distributed load. The analytical solution is well-known and the model approaches the true limit load from below as the mesh density is increased. The next example is a steel cantilever I-beam which uses the von Mises criterion. Again, the model approaches the limit load from below.

The final example is a four-storey stairwell with door openings subject to a shear force which introduces bending and torsion. The limit load is determined using three different meshes using two different effectiveness factors. Stress concentrations are observed near the door openings, however, they are not critical. The collapse mode is illustrated using the solution of the dual problem.

The presented element is capable of modelling complex structures with a satisfactory accuracy. Moreover, it produces a lower bound value and approaches the limit load from below. The computational time is more or less proportional to the problem size, thus, even large problems can be solved in a matter of minutes on a standard laptop.

Acknowledgement

The authors would like to thank the ALECTIA Foundation and Innovation Fund Denmark for financial support of the research presented in this paper.

REFERENCES

Anderheggen E and Knöpfel H (1972) Finite element limit analysis using linear programming. *International Journal of Solids and Structures* **8**: 1413–1431.

Andersen ED, Roos C and Terlaky T (2003) On implementing a primal-dual interior-point method for conic quadratic optimization. *Mathematical Programming* **95(2)**: 249–277.

Bisbos C and Pardalos P (2007) Second-order cone and semidefinite representations of material failure criteria. *Journal of Optimization Theory and Applications* **134(2)**: 275–301.

Boyd SP and Vandenberghe L (2004) *Convex Optimization*. Cambridge University Press.

Drucker D, Prager W and Greenberg H (1952) Extended limit design theorems for continuous media. *Quarterly of Applied Mathematics* **9**: 381–389.

Herfelt MA, Poulsen PN, Hoang LC and Jensen JF (2016) Numerical limit analysis of keyed shear joints in concrete structures. *Structural Concrete* **17(3)**: 481–490.

Ingerslev Å (1921) Om en elementær beregningsmetode for krydsarmerede plader. *Ingeniøren* **30(69)**: 507–515, translation: On an elementary calculation method for two-way slabs.

Johansen KW (1962) *Yield-line theory*. Cement and Concrete Association.

Karmarkar N (1984) A new polynomial-time algorithm for linear programming. *Combinatorica* **4**: 373–395.

Krabbenhøft K, Lyamin A and Sloan S (2007) Formulation and solution of some plasticity problems as conic programs. *International Journal of Solids and Structures* **44(5)**: 1533–1549.

Larsen KP (2010) *Numerical Limit Analysis of Reinforced Concrete Structures*. PhD thesis, Technical University of Denmark.

Lobo MS, Vandenberghe L, Boyd S and Lebret H (1998) Applications of second-order cone programming. *Linear algebra and its applications* **284(1)**: 193–228.

Lyamin AV, Sloan SW, Krabbenhoft K and Hjiaj M (2005) Lower bound limit analysis with adaptive remeshing. *International Journal for Numerical Methods in Engineering* **63(14)**: 1961–1974.

Makrodimopoulos A and Martin C (2006) Lower bound limit analysis of cohesive-frictional materials using second-order cone programming. *International Journal for Numerical Methods in Engineering* **66(4)**: 604–634.

Makrodimopoulos A and Martin C (2007) Upper bound limit analysis using simplex strain elements and second-order cone programming. *International Journal for Numerical and Analytical Methods in Geomechanics* .

MOSEK ApS (2015) *The MOSEK optimization toolbox for MATLAB manual. Version 7.1 (Revision 33)*. https://www.mosek.com/.

Muttoni A, Schwartz J and Thürlimann B (1997) *Design of Concrete Structures With Stress Fields*. Springer.

Nesterov Y, Todd MJ and Ye Y (1999) Infeasible-start primal-dual methods and infeasibility detectors for nonlinear programming problems. *Mathematical Programming* **84(2)**: 227–267.

Nesterov YE and Todd MJ (1997) Self-scaled barriers and interior-point methods for convex programming. *Mathematics of Operations research* **22(1)**: 1–42.

Nielsen MP (1971) *On the strength of reinforced concrete discs*. Civil engineering and building construction series no.70, Acta

polytechnica scandinavica.

Nielsen MP and Hoang LC (2010) *Limit Analysis and Concrete Plasticity, Third Edition*. Taylor & Francis.

Poulsen PN and Damkilde L (2000) Limit state analysis of reinforced concrete plates subjected to in-plane forces. *International Journal of Solids and Structures* **37**: 6011–6029.

Prager W (1952) The general theory of limit design. In *Proceedings of the 8th International Congress on theoretical and Applied Mechanics, Istanbul*, vol. 19, pp. 65–72.

Ribó R, Pasenau M, Escolano E, Ronda J and González L (1998) Gid reference manual. *CIMNE, Barcelona* .

Sloan SW (1988) Lower bound limit analysis using finite elements and linear programming. *International Journal for Numerical and Analytical Methods in Geomechanics* **12**: 61–77.

Smith C, Gilbert M, Hawksbee S and Babiker A (2014) Recent advances in the application of discontinuity layout optimization to geotechnical limit analysis problems. *Numerical Methods in Geotechnical Engineering* **1**: 415.

Sturm JF (1997) *Primal-dual interior point approach to semidefinite programming*. PhD thesis, Thesis Publishers Amsterdam, The Netherlands.

Terlaky T (2013) *Interior point methods of mathematical programming*, vol. 5. Springer Science & Business Media.

Paper IV

"Lower bound multiscale element for in-situ cast joints in triaxial stress"

M.A. Herfelt, P.N. Poulsen, L.H. Hoang & J.F. Jensen

Submitted to: *Engineering Structures, 2017*

Lower bound multiscale element for in-situ cast joints in triaxial stress

Morten A. Herfelt[a,b], Peter N. Poulsen[b], Linh C. Hoang[b], Jesper F. Jensen[a]

[a] *ALECTIA A/S, Teknikerbyen 34, 2830 Virum, Denmark*
[b] *Department of Civil Engineering, Technical University of Denmark, Brovej, Building 118, 2800 Kgs. Lyngby, Denmark*

Abstract

In practice, precast concrete structures are often being designed by manual methods and linear finite element analysis in the ultimate limit state. This practice leads to suboptimal structures, and the behaviour of the in-situ cast joints are unaccounted for. More accurate and efficient means of design are therefore needed, and a framework based on finite element limit analysis is being developed. In this paper, a multiscale joint element is presented, and a mechanical model is proposed as the yield function of the macro element. The scope of the model is to capture the behaviour of joints in three dimensions subjected to triaxial stress, and the resulting mathematical optimisation problem fits the format of semidefinite programming. The presented joint element is analysed and a real size example of a four-storey stairwell subjected to shear and torsion of precast concrete is presented. The influence of the joints on the behaviour of the stairwell is assessed.

Keywords: In-situ cast joints, Precast concrete, Finite element limit analysis, Semidefinite programming, Yield function, Multiscale

1. Introduction

Precast concrete elements are widely used in the construction industry as they provide a number of benefits, however, joints cast on the construction site to connect the precast elements pose several challenges. The current practice is to design the joints as the weakest part of the structure. This

Email address: mahe@alectia.com (Morten A. Herfelt)

makes analysis and design by general purpose finite element software inaccurate as the behaviour of the joints is unaccounted for.

Several types of joints are used in precast concrete structures, e.g. slab-to-beam joints, beam-to-column joints, and panel-to-panel joints, see Fig. 1. The panel-to-panel joints, also called shear joints, are of particular interest as the lateral stability usually is ensured by shear walls composing of precast wall panels. During the 1970s and 80s several papers were published on the topic of shear joints including several experimental studies [1, 2, 3], however, to the best knowledge of the authors, no experimental studies on the behaviour of joints in three-dimensions have been published. The Eurocode 2 [4] uses a simple, empirical design equation, which only considers the interface and not the actual stress state within the joint. Both types of joints shown in Fig. 1 transfer shear from one structural plane to another, and must therefore experience a triaxial stress field which is not accounted for by current design methods.

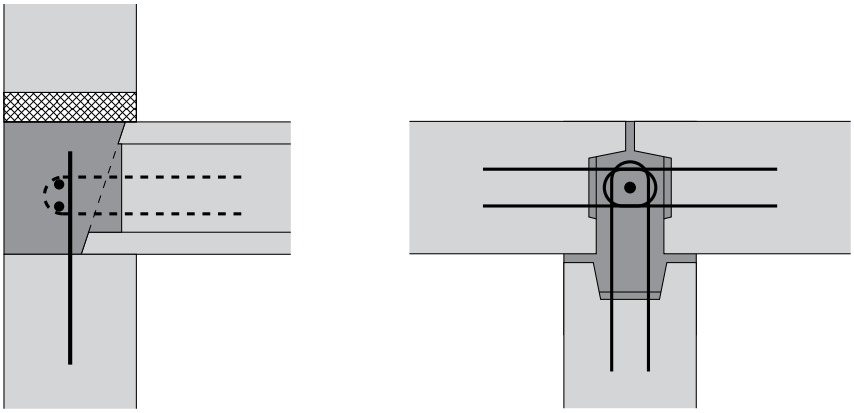

(a) (b)

Figure 1: a) Vertical section of slab-to-panel joint reinforced with U-bar loops and embedded rebars. b) Horizontal section of panel-to-panel T-joint reinforced with U-bar loops extruding from all three panels.

The experiments by Hansen and Olesen [3] featured several specimens, where the U-bar loops were placed with a considerable distance. These experiments displayed a lower capacity and the core of the joint was completely destroyed upon failure. A detailed model based on finite element limit analysis captured this behaviour to a satisfactory degree [5]. The joint model presented in this paper will attempt to account for this behaviour in three

dimensions, as the reinforcement layout necessarily will affect the capacity of joints in triaxial stress as well.

Manual limit analysis is widely used in practice as a tool for assessment of the ultimate limit state behaviour of precast concrete structures. The framework is based on the extremum principles [see e.g. 6, 7, 8], and several methods have been developed within this framework, e.g. the yield line theory [9]. Models for shear joints based on limit analysis have likewise been developed; these models include both upper bound models [10, 11, 12] and lower bound models [11, 13], however, these models are only concerned with the two-dimensional case, i.e. joints between precast elements in the same plane.

Finite element limit analysis is based on the same extremum principles as the manual limit analysis and the element discretisation of the finite element method, and it can be considered as a special case of the general finite element method. The method was developed in the late 1960s and 70s [14, 15] and since then several researchers have contributed to the further development of the field [16, 17, 18, 19, 20]. Herfelt et al. [5] presented a detailed model for two-dimensional shear joints and the findings were used to develop a 2D multiscale joint element with a mechanical submodel as the yield criterion [21].

In this paper a multiscale joint element for three-dimensional analysis is presented. The joint element is compatible with the generalised plane stress element [22] and uses a simplified mechanical model as the yield criterion similar to the two-dimensional joint element [21]. The general concept is visualised for the two-dimensional case in Fig. 2 where three scales are shown, namely the structural level, the element level, and the submodel level.

Due to the triaxial stress state, the yield function submodel will be formulated for semidefinite programming and second-order constraints. A brief introduction to semidefinite programming as well as second-order cone programming will be given in Sec. 2, where the conic representation of the Mohr-Coulomb criterion will be given as well. The behaviour of the multiscale element will be analysed and compared to the equation in the Eurocode 2. Finally, a real size structure is analysed using the proposed joint element and the generalised plane stress element [22], and the influence of the joint elements is discussed.

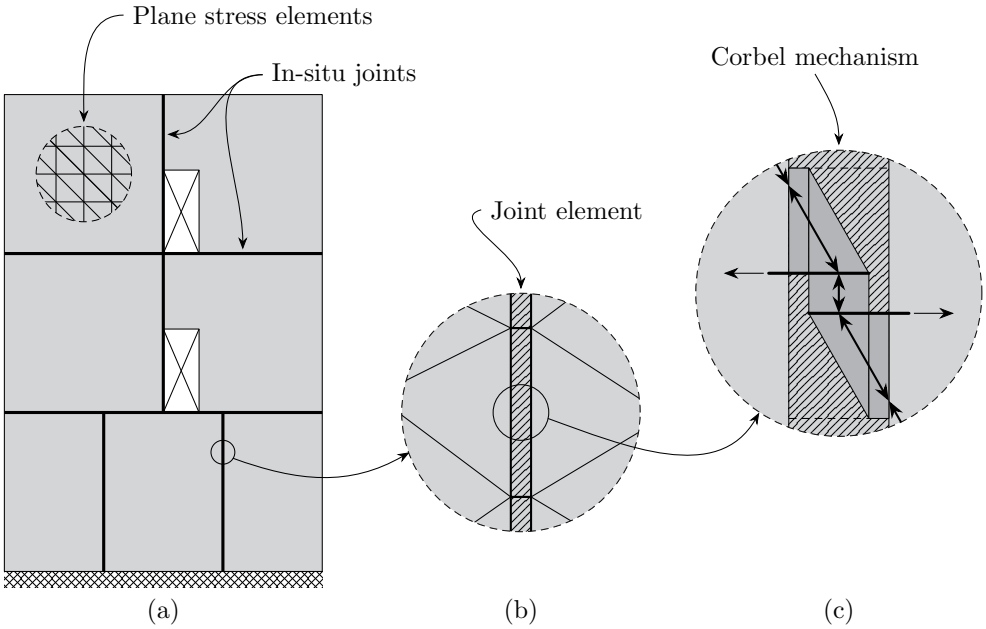

Figure 2: The general concept of the multiscale joint element shown in 2D: a) Precast concrete structure on the structural level, b) Joint element and plane stress elements on the element level, c) corbel mechanisms and load path on the submodel level.

2. Convex optimisation

Convex optimisation is used in many fields of engineering and an extensive research effort has gone into developing efficient algorithms for solving these classes of problems [23, 24, 25]. Second-order cone programming (SOCP) and semidefinite programming (SDP) are subclasses of convex optimisation that have been used in the field of finite element limit analysis for more than a decade [26, 27].

First and foremost, we introduce the k-dimensional second-order cone defined as the set

$$\mathcal{Q}_k = \left\{ \boldsymbol{x} \mid \boldsymbol{x} \in \mathbb{R}^k,\ x_1 \geq \sqrt{x_2^2 + \cdots + x_k^2} \right\} \tag{1}$$

The standard form of a second-order cone program is commonly stated as

$$\begin{aligned} &\text{maximise} && \boldsymbol{c}^T \boldsymbol{x} \\ &\text{subject to} && \mathbf{A}\boldsymbol{x} = \boldsymbol{b} \\ & && \boldsymbol{x}_i \in \mathcal{Q}_{k_i}, \quad i = 1, 2, \ldots, q \end{aligned} \tag{2}$$

where the $\boldsymbol{x}$ is the optimisation variables and q is the number of second-order cones. SOCP is a generalisation of linear programming (LP), and (2) is reminiscent of the well-known standard form of LP.

Semidefinite programing uses so-called matrix variables, symmetric matrices which are required to be positive-semidefinite, i.e. a $n \times n$ matrix $\mathbf{F}$ satisfies

$$\boldsymbol{x}^T \mathbf{F} \boldsymbol{x} \geq 0 \text{ for all } \boldsymbol{x} \in \mathbb{R}^n$$

A curved inequality sign $\succeq$ is often used to denote that a matrix is positive semidefinite, e.g. $\mathbf{F} \succeq 0$. Vandenberghe and Boyd [28] uses the following, very compact form of the semidefinite program:

$$\begin{array}{ll} \text{maximise} & \boldsymbol{c}^T \boldsymbol{x} \\ \text{subject to} & \mathbf{F}(\boldsymbol{x}) \succeq 0 \end{array} \tag{3}$$

with

$$\mathbf{F}(\boldsymbol{x}) = \mathbf{F}_0 + \sum_{i=1}^{m} \mathbf{F}_i x_i$$

where $\mathbf{F}_i$ are symmetric matrices. $\mathbf{F}(\boldsymbol{x}) \succeq 0$ is a so-called linear matrix inequality (LMI), which makes it possible to impose constraints on the eigenvalues of symmetric matrices, e.g. the stress tensor.

2.1. Conic representation of the Mohr-Coulomb criterion

The Mohr-Coulomb criterion is commonly used for concrete and soils. In principal stresses the criterion is given as

$$\sigma_1 \leq f_t \tag{4a}$$

$$k\sigma_1 - \sigma_3 \leq f_c \tag{4b}$$

where $\sigma_1 \geq \sigma_2 \geq \sigma_3$ are the principal stresses, f_t is the uniaxial tensile strength, and f_c is the uniaxial compressive strength. k is a friction parameter defined as

$$k = \left(\sqrt{\mu^2 + 1} + \mu\right)^2 \tag{5}$$

with $\mu = \tan\theta$, where θ is the internal angle of friction. $k = 4$ corresponding to $\mu = 0.75$ and $\theta \approx 37°$ is commonly used for normal strength concrete.

The principal stresses are the eigenvalues of the concrete stress tensor $\boldsymbol{\sigma}_c$, thus, (4) can be represented using linear matrix inequalities [26, 29, 30].

Utilising that $\mathbf{F} \succeq 0$ means that the smallest eigenvalue of $\mathbf{F}$ must be non-negative, and that $-\mathbf{F} \succeq 0$ means that the largest eigenvalue of $\mathbf{F}$ must be non-positive, the separation criterion (4a) can be rewritten as

$$-\boldsymbol{\sigma}_c + f_t \mathbf{I} \succeq 0 \tag{6}$$

where $\mathbf{I}$ is the identity matrix. The sliding criterion (4b) uses two principal stresses and it is therefore necessary to introduce an auxiliary variable α_1, to obtain

$$\begin{aligned} -\sigma_1 + \alpha_1 &\geq 0 \\ \sigma_3 - k\alpha_1 + f_c &\geq 0 \end{aligned}$$

and

$$\begin{aligned} -\boldsymbol{\sigma}_c + \alpha_1 \mathbf{I} &\succeq 0 \\ \boldsymbol{\sigma}_c + (f_c - k\alpha_1)\mathbf{I} &\succeq 0 \end{aligned} \tag{7}$$

using the stress tensor $\boldsymbol{\sigma}_c$. The three LMIs of (6) and (7) can be reduced to two, and the Mohr-Coulomb criterion with a tension cut-off (4) can be stated as

$$\begin{aligned} -\boldsymbol{\sigma}_c + \alpha_2 \mathbf{I} &\succeq 0 \\ \boldsymbol{\sigma}_c + (f_c - k\alpha_1)\mathbf{I} &\succeq 0 \\ \alpha_2 - \alpha_1 &\geq 0 \\ \alpha_2 - f_t &\geq 0 \end{aligned} \tag{8}$$

For plane stress problems (8) can be used, however, it is more efficient in this case to use the second-order cone representation instead. In plane stress, the criterion is given as

$$\begin{aligned} \sigma_1 &\leq f_t \\ k\sigma_1 - \sigma_2 &\leq f_c \\ -\sigma_2 &\leq f_c \end{aligned} \tag{9}$$

where $\sigma_1 \geq \sigma_2$ are the two principal stresses given as

$$\left.\begin{matrix} \sigma_1 \\ \sigma_2 \end{matrix}\right\} = \frac{\sigma_x + \sigma_y}{2} \pm \sqrt{\left(\frac{\sigma_x - \sigma_y}{2}\right)^2 + \tau_{xy}^2}$$

Introducing the auxiliary variables

$$p_m = -\frac{\sigma_x + \sigma_y}{2}, \quad \sigma_d = \frac{\sigma_x - \sigma_y}{2}$$

and the second-order constraint

$$\varphi \geq \sqrt{\sigma_d^2 + \tau_{xy}^2}$$

the Mohr-Coulomb criterion for plane stress can be rewritten as

$$\begin{aligned} -p_m + \varphi &\leq f_t \\ (1-k)p_m + (k+1)\varphi &\leq f_c \\ p_m + \varphi &\leq f_c \end{aligned} \tag{10}$$

and the criterion for plane stress requires a total of five linear constraints and one second-order constraint.

3. Finite element limit analysis

The presented joint element is to be implemented in a framework based on finite element limit analysis for design of precast concrete structures. The mathematical optimisation problem of lower bound limit analysis can be stated as:

$$\begin{aligned} \text{maximise} \quad & \lambda \\ \text{subject to} \quad & \mathbf{B}^T\boldsymbol{\sigma} = \boldsymbol{p}\lambda + \boldsymbol{p}_0 \\ & f(\boldsymbol{\sigma}_i) \leq 0, \quad i = 1, 2, \ldots, m \end{aligned} \tag{11}$$

The scope of the optimisation problem (11) is to find a statically admissible stress field that maximises the load carrying capacity of the given structure. A stress field that satisfies equilibrium is ensured by the linear equations $\mathbf{B}^T\boldsymbol{\sigma} = \boldsymbol{p}\lambda + \boldsymbol{p}_0$, and a stress field that does not violate the yield criterion in any points is ensured by the inequalities $f(\boldsymbol{\sigma}_i) \leq 0$. The load is given by a constant part $\boldsymbol{p}_0$ and a scalable part $\boldsymbol{p}\lambda$, where the load factor λ is sought to be maximised. $\mathbf{B}^T$ is the equilibrium matrix, $\boldsymbol{\sigma}$ is the stress vector, and f is the yield function.

For the joint element presented in Sec. 4, the yield function f will represent a submodel, i.e. an advanced yield function comprising a mechanical

model and sub-element level stress fields. By expanding the yield function f, the lower bound problem(11) can be stated as:

$$\begin{array}{lll} \text{maximise} & \lambda & \\ \text{subject to} & \mathbf{B}^T\boldsymbol{\sigma} = \boldsymbol{p}\lambda + \boldsymbol{p}_0 & \\ & \mathbf{C}_\sigma\boldsymbol{\sigma} + \mathbf{C}_\alpha\boldsymbol{\alpha} + \mathbf{C}_\gamma\boldsymbol{\gamma} = \boldsymbol{C}_0 & \\ & \mathbf{E}_\sigma\boldsymbol{\sigma} + \mathbf{E}_\alpha\boldsymbol{\alpha} + \mathbf{E}_\gamma\boldsymbol{\gamma} \leq \boldsymbol{E}_0 & \\ & \mathbf{F}_\alpha^{(i)}\boldsymbol{\alpha}_i + \mathbf{F}_0^{(i)} \succeq 0, & i = 1, 2, \ldots, m \\ & \boldsymbol{\gamma}_j \in \mathcal{Q}_{k_j}, & j = 1, 2, \ldots, q \end{array} \tag{12}$$

The matrices $\mathbf{C}_\sigma$, $\mathbf{C}_\alpha$, and $\mathbf{C}_\gamma$ defines the equality constraints of the submodels, while $\mathbf{E}_\sigma$, $\mathbf{E}_\alpha$, and $\mathbf{E}_\gamma$ defines the inequality constraints. The variables $\boldsymbol{\alpha}$ and $\boldsymbol{\gamma}$ are associated with the yield function, whereas $\boldsymbol{\gamma}$ is used to define the second-order constraints, and $\boldsymbol{\alpha}$ is used to define the linear matrix inequalities together with the symmetric matrices $\mathbf{F}_\alpha^{(i)}$ and $\mathbf{F}_0^{(i)}$. m is the number of linear matrix inequalities for the submodels while q is the number of second-order constraints. The matrices will only be given implicitly in the following.

The submodel presented in Sec. 5 comprises both triaxial stress states as well as plane stress states, hence, both formulations of the Mohr-Coulomb criterion given in Sec. 2 will be utilised at the stress level of the submodel. The problem (12) comprises therefore both semidefinite constraints as well as second-order constraints.

4. Macro finite element

This section introduces a lower bound macro finite element for analysis and design of 3D structures. The general modelling concept of the element was illustrated in two dimensions in Fig. 2, where a precast concrete wall is modelled using plane stress elements and multiscale elements. On the element level, the proposed macro element is compatible with the plane stress element, and the stress states in the macro joint element are treated using a so-called submodel which incorporates corbel mechanisms to transfer shear.

The lower bound plane stress element has a linear stress field, hence, a safe stress field can be ensured by checking the yield function in the vertexes of the element. Moreover, to ensure a lower bound solution traction continuity has to be satisfied, and for the plane stress element the tractions are given in global coordinates, see Fig. 3.

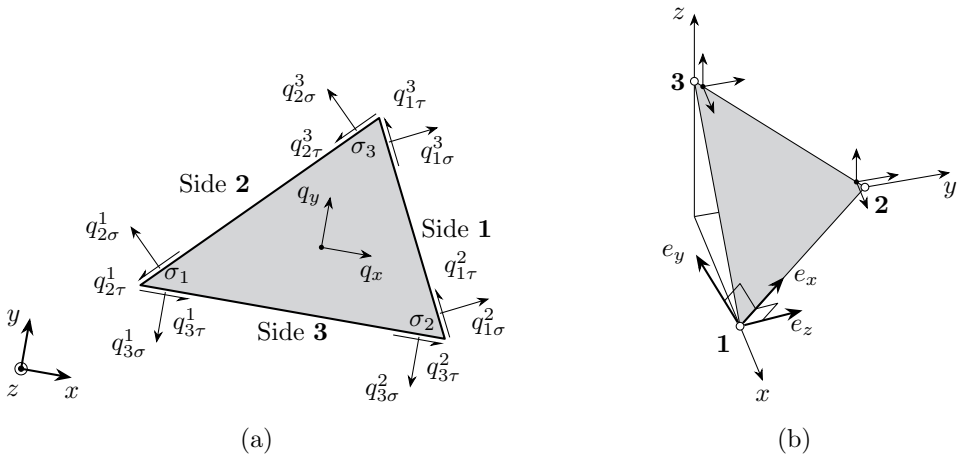

Figure 3: a) The element and tractions illustrated in the local coordinate system (adapted from [19]). b) The generalised plane stress element including local coordinate system and tractions in global coordinates for one of the element boundaries.

The joint is concerned with the transfer of shear forces, and the axial forces in the longitudinal direction are omitted in the present paper for simplicity. The 2D joint element [21] treated this as well, and a two-dimensional model can be added to the submodel criterion for the 3D joint element presented in the following section. Similarly, the necessary equilibrium equations to facilitate longitudinal forces can be added as well.

The submodel criterion to be presented in Sec. 5 assumes that the adjacent elements are oriented in right angles, which covers the vast majority of joints in practice, see e.g. the joints in Fig. 1. The formulation of the macro element, however, is general and applicable to any configuration of adjacent plane stress panels.

The joint element consists of a number of strips, one for each adjacent plane stress element, see Fig. 4. The strips are assumed to be in plane stress and balance the tractions of the adjacent plane stress triangles as well as internally within the joint. For the stress fields of the strips to be compatible with the plane stress elements, a linear variation is prescribed along the joint element.

Each strip has two stress components given in local coordinates, namely σ_y and τ_{xy}, hence, four stress variables are needed to describe the linear stress

field. The element stress vector $\boldsymbol{\sigma}_{el}$ is given as:

$$\boldsymbol{\sigma}_{el} = \begin{bmatrix} \boldsymbol{\sigma}_1 \\ \vdots \\ \boldsymbol{\sigma}_N \end{bmatrix}$$

where N is the number of strips and $\boldsymbol{\sigma}_i$ denotes the stress vector of strip i given as:

$$\boldsymbol{\sigma}_i = \begin{bmatrix} \boldsymbol{\sigma}_{i1} \\ \boldsymbol{\sigma}_{i2} \end{bmatrix} = \begin{bmatrix} \sigma_{yi1} \\ \tau_{xyi1} \\ \sigma_{yi2} \\ \tau_{xyi2} \end{bmatrix} \tag{13}$$

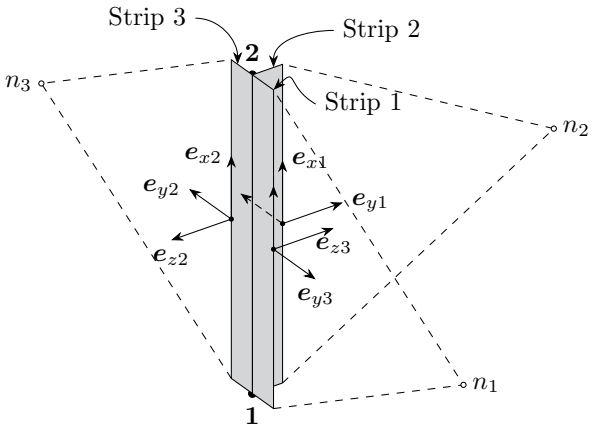

Figure 4: Sketch of a joint element with three adjacent plane stress elements: Local coordinate systems for the three joint strips are shown.

For consistent orientation, a local coordinate system for each strip is defined. The local x-axis is in the longitudinal direction of the joint element, while the y-axis is in the plane of the adjacent plane stress element. Given the vectors $\boldsymbol{v}_{12}$ going from node 1 to node 2 in Fig. 4 and $\boldsymbol{v}_{1n_i}$ going from node 1 to n_i, where n_i is the third node of the adjacent triangular element, the basis of the local coordinate system can be defined as:

$$\boldsymbol{e}_{xi} = \frac{\boldsymbol{v}_{12}}{\|\boldsymbol{v}_{12}\|_2}, \quad \boldsymbol{e}_{zi} = \frac{\boldsymbol{v}_{12} \times \boldsymbol{v}_{1n_i}}{\|\boldsymbol{v}_{12} \times \boldsymbol{v}_{1n_i}\|_2}, \quad \boldsymbol{e}_{yi} = \boldsymbol{e}_{zi} \times \boldsymbol{e}_{xi} \tag{14}$$

where $\|\boldsymbol{v}\|_2$ is the Euclidean norm of the vector $\boldsymbol{v}$. The transformation matrix for the ith strip can be stated as $\mathbf{E}_i = \begin{bmatrix}\boldsymbol{e}_{xi} & \boldsymbol{e}_{yi} & \boldsymbol{e}_{zi}\end{bmatrix}$.

The contributions to traction continuity in global coordinates for strip i at node j can be stated as:

$$\boldsymbol{q}_{ij} = \mathbf{E}_i \begin{bmatrix} 0 & t_i l \\ t_i l & 0 \\ 0 & 0 \end{bmatrix} \begin{bmatrix} \sigma_{yij} \\ \tau_{xyij} \end{bmatrix} = \tilde{\mathbf{P}}_i^T \boldsymbol{\sigma}_{ij} \tag{15}$$

where $\boldsymbol{q}_{ij}$ is the generalised nodal forces vector, l is the length of the joint element, and t_i is the thickness of strip i. (15) also defines $\tilde{\mathbf{P}}_i^T$ implicitly. Due to the linear stress field it is necessary to enforce traction continuity at the ends of the strip.

Internal traction equilibrium for the N strips of the joint element is likewise enforced, which can be stated as:

$$-\tilde{\mathbf{P}}_1^T \boldsymbol{\sigma}_{1j} - \cdots - \tilde{\mathbf{P}}_N^T \boldsymbol{\sigma}_{Nj} = 0, \quad j = 1, 2 \tag{16}$$

where j is the node number. Equilibrium on the element level for an joint element with N adjacent plane stress elements can now be stated as follows:

$$\boldsymbol{q}_{el} = \begin{bmatrix} \tilde{\mathbf{P}}_1^T & & & & & \\ & \tilde{\mathbf{P}}_1^T & & & & \\ & & \ddots & & & \\ & & & \ddots & & \\ & & & & \tilde{\mathbf{P}}_N^T & \\ & & & & & \tilde{\mathbf{P}}_N^T \\ -\tilde{\mathbf{P}}_1^T & & \cdots & \cdots & -\tilde{\mathbf{P}}_N^T & \\ & -\tilde{\mathbf{P}}_1^T & \cdots & \cdots & & -\tilde{\mathbf{P}}_N^T \end{bmatrix} \begin{bmatrix} \boldsymbol{\sigma}_1 \\ \vdots \\ \boldsymbol{\sigma}_N \end{bmatrix} = \mathbf{B}_{el}^T \boldsymbol{\sigma}_{el} \tag{17}$$

where $\mathbf{B}_{el}^T$ is the element equilibrium matrix, and $\boldsymbol{q}_{el}$ contains the contributions to the global equilibrium equations of the joint element. The number of stress variables and equations of the joint element depends on the number of adjacent plane stress elements, N, as seen in (17).

5. Joint model

We now consider a unit section of the joint in the shape of a rectangular box. This unit section is reinforced with U-bar loops from up to four

boundaries which are placed in positions defined by u, u_{y1} and u_{z1} according to Fig. 5. The length of the unit section is s and the widths are given as t_y and t_z. o_y and o_z are the overlap of the U-bars. The distances between the U-bar pairs in the y and z-directions, respectively, are assumed to be identical, i.e. $u = u_{y1} + u_{y2} = u_{z1} + u_{z2}$, which reduce the number of possible stress combinations inside the submodel greatly.

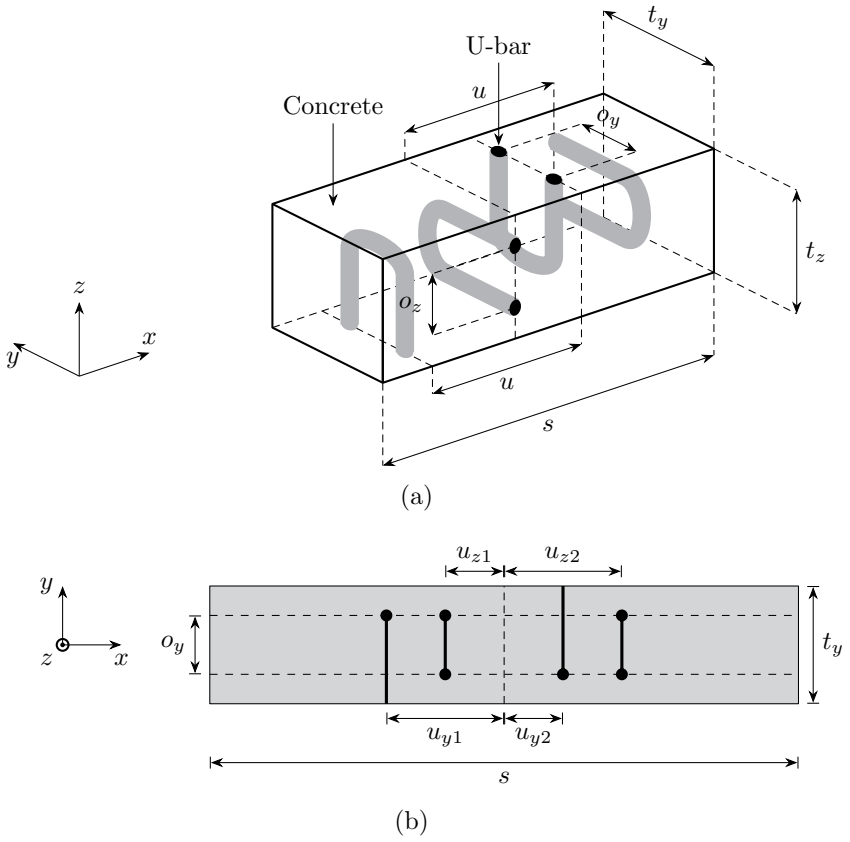

Figure 5: Submodel for the three-dimensional joint element: a) three-dimensional representation of the geometry including U-bar loops, b) two-dimensional sketch of the U-bar placement.

Joints are in practice always reinforced with a so-called locking bar in the longitudinal direction, however, the present model does not consider the behaviour in the longitudinal direction and the locking bar will therefore not affect the capacity and behaviour of the submodel.

Each of the four boundaries reinforced with U-bars can be subjected to a normal stress and a shear stress, σ_y and τ_{xy}, or σ_z and τ_{zx}, depending on the orientation. The stresses on the element level $\boldsymbol{\sigma}_{el}$ are given in the local coordinate systems of the particular strip, hence, a common coordinate system is needed, and all stresses are transformed to the coordinate system of strip 1:

$$\hat{\mathbf{S}}_{ij} = \mathbf{E}_1^T \mathbf{E}_i \mathbf{S}_{ij} \mathbf{E}_i^T \mathbf{E}_1 \tag{18}$$

where $\mathbf{E}_i$ is the transformation matrix of strip i, and $\mathbf{S}_{ij}$ is the stress tensor of strip i at node j, e.g. for strip 1 at node 2 - which is always chosen for the common coordinate system - we have

$$\mathbf{S}_{12} = \begin{bmatrix} 0 & \tau_{xy12} & 0 \\ \tau_{xy12} & \sigma_{y12} & 0 \\ 0 & 0 & 0 \end{bmatrix}$$

Most of the components in $\mathbf{S}_{ij}$ are equal to zero as the strips only have two stress components, which simplifies the calculations. The shear stress component of $\hat{\mathbf{S}}$ is used for the corbels presented in the following section. The equilibrium equations of the element ensures that the normal stress components of $\hat{\mathbf{S}}_{ij}$ are balanced, and the normal stresses are simply added to the final stress field of the submodel, which must satisfy the Mohr-Coulomb criterion.

5.1. Local shear transfer via corbels

A mechanical model for the transfer of shear from one plane to another, e.g. from τ_{xy} to τ_{zx}, is needed. For this purpose a concrete corbel is considered. The corbel utilises the transverse reinforcement of the joint, i.e. the U-bar loops, to transform the shear stress (from $\hat{\mathbf{S}}$) acting on the boundary of the joint to a normal stress in the core of the joint. This is illustrated in Fig. 6(a).

Fig. 6(b) shows a corbel subjected to a shear stress τ_{zx} from the transformed stress state of the particular strip of the macro element. The loop reinforcement is activated and the stringer force T in the reinforcement balances the stress σ_z and the stringer force V. The rectangular panel will have constant shear stress, while the triangle will be in uniaxial compression. For a single corbel, see Fig. 6(b), we have the following variables:

$$\alpha_i = \left[\sigma_x^{(i)}, \quad \sigma_z^{(i)}, \quad \tau_{zx}^{(i)}, \quad T_1^{(i)}, \quad T_2^{(i)}, \quad V^{(i)}\right]^T \tag{19}$$

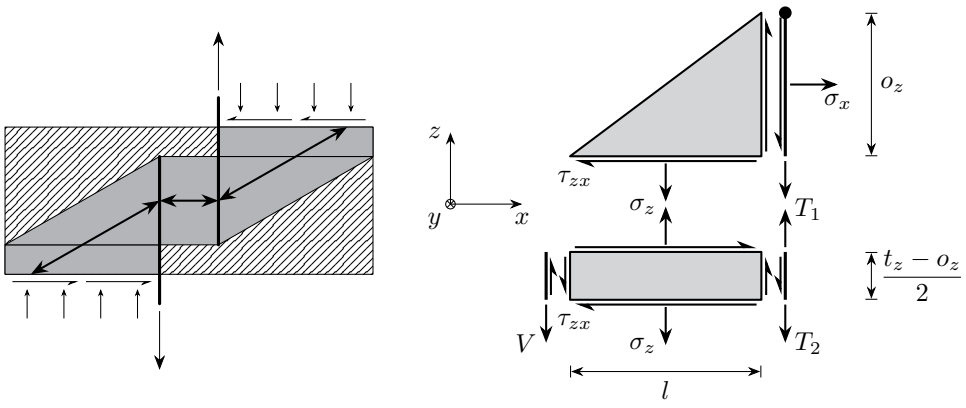

(a) (b)

Figure 6: a) Sketch of two corbel mechanisms working in two-dimensions. b) Two-dimensional representation of a corbel in the xz-plane transforming a shear stress τ_{zx} to a normal stress σ_x. Positive directions of forces and stresses are shown. The panels indicated by gray has a out-of-plane thickness of o_y.

or

$$\alpha_i = \left[\sigma_x^{(i)},\ \ \sigma_y^{(i)},\ \ \tau_{xy}^{(i)},\ \ T_1^{(i)},\ \ T_2^{(i)},\ \ V^{(i)}\right]^T \tag{20}$$

depending on the orientation of the corbel. The following system of equilibrium equations can be derived for a single corbel:

$$\begin{bmatrix} o_z o_y & 0 & -lo_y & 0 & 0 & 0 \\ 0 & -lo_y & 0 & 0 & -1 & -1 \\ 0 & -lo_y & o_z o_y & 0 & 0 & 0 \\ 0 & 0 & -\dfrac{t_z - o_z}{2} o_y & 0 & 0 & -1 \\ 0 & 0 & -\dfrac{t_z - o_z}{2} o_y & 1 & -1 & 0 \\ 0 & 0 & -o_z o_y & -1 & 0 & 0 \end{bmatrix} \begin{bmatrix} \sigma_x \\ \sigma_z \\ \tau_{zx} \\ T_1 \\ T_2 \\ V \end{bmatrix} = \mathbf{0} \tag{21}$$

The first three equations in (21) ensure vertical, horizontal, and moment equilibrium, while the last three ensure equilibrium for the stringers. The stresses σ_x and σ_z will practically always be negative, i.e. compressive, and the same goes for the stringer force V. No reinforcement is located at the

position of the leftmost stringer, hence, the stringer is a so-called compression stringer which cannot take any tension.

A single corbel transforms a shear stress into a normal stress in the core of the joint. Several corbels are therefore needed to transfer shear from one plane to another. Moreover, the corbels are given a predefined length l, see Fig. 6, however, the optimal value of l depends on the reinforcement and loading. Four corbels for each of the four boundaries of the joint is therefore used, thus, the complete submodel features up to 16 corbels, four for each U-bar loop in the considered joint section.

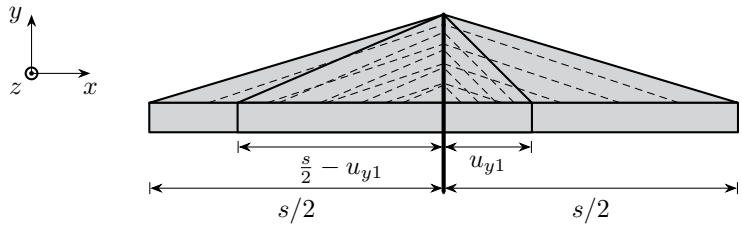

Figure 7: Four corbel models around a single U-bar: The length is fixed at $s/2$ for the two largest, while the length of the two smallest depends on the position of the U-bar in the unit joint section. Dashed lines indicate the load path through the triangular corbels. Some of the corbels overlap and their stress fields are added to obtain the actual stress state.

Fig. 7 shows the four corbels around a U-bar. As shown in Fig. 7, some of the corbels overlap, and it is therefore necessary to add the stress fields together to obtain the actual stress field of the submodel. Each of the corbels can transfer a shear stress to a normal stress in the centre of the joint, which then can be transferred to a shear stress in a different plane via another corbel. This is illustrated schematically in Fig. 8 for two corbels.

Combining the up to 16 corbels requires four equations - one for each U-bar loop - which enforce equilibrium for the normal stresses σ_x according to the positions of the corbels together with four transfer boxes, see Fig. 8.

Fig. 9 shows the transfer of normal stresses σ_x schematically, where each set of arrows is located at the position of an U-bar loop. The four equilibrium

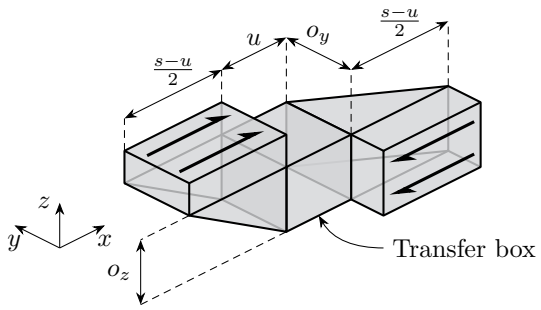

Figure 8: Shear transfer from one plane to another via two corbels. The central transfer box will experience uniaxial compression in the x-direction. Equilibrium of the corbels is ensured by stringer forces and confinement not shown here.

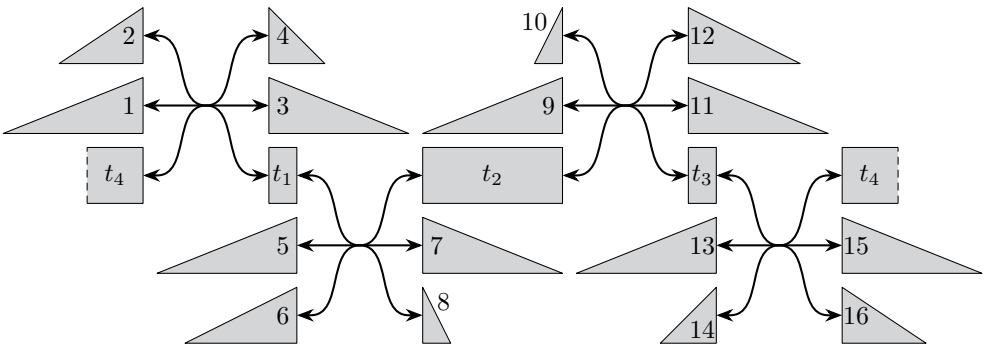

Figure 9: Interaction of the 16 corbels and four transfer boxes illustrated schematically: The triangles represent a corbel mechanism, while the rectangles represent the transfer boxes. Each set of arrows represent an equilibrium equation. The size and locations of corbels are not to scale.

equations are given as

$$\begin{aligned}
&\sigma_x^{(1)} + \sigma_x^{(2)} - \sigma_x^{(3)} - \sigma_x^{(4)} + \sigma_x^{t4} - \sigma_x^{t1} = 0,\\
&\sigma_x^{(5)} + \sigma_x^{(6)} - \sigma_x^{(7)} - \sigma_x^{(8)} + \sigma_x^{t1} - \sigma_x^{t2} = 0,\\
&\sigma_x^{(9)} + \sigma_x^{(10)} - \sigma_x^{(11)} - \sigma_x^{(12)} + \sigma_x^{t2} - \sigma_x^{t3} = 0,\\
&\sigma_x^{(13)} + \sigma_x^{(14)} - \sigma_x^{(15)} - \sigma_x^{(16)} + \sigma_x^{t3} - \sigma_x^{t4} = 0,
\end{aligned} \tag{22}$$

where $\sigma_x^{(i)}$ is the stress in the x-direction associated with the ith corbel, see Fig. 6. The first four corbels are associated with the first U-bar loop, the next four with the second U-bar loop and so on, see Fig. 9 for the numbering. σ_x^{tj} is the normal stress of the jth transfer box. Two corbels associated with

the same U-bar, e.g. the two corbels on the left-hand side in Fig. 7, can work together, each transferring a fraction of the total shear force.

The stress states of the 16 corbels are combined to obtain the actual stress field within the unit joint section. The corbels overlap to some degree, see Fig. 7 where some of the corbels in the same plane overlap, and it is therefore necessary to superimpose the appropriate stress states. Depending on the values of u, u_{y1}, and u_{z1} up to ten triaxial stress states are present inside the unit section. Each of these stress states are given by three normal stresses and two shear stresses.

τ_{yz} is zero for all strips in their local coordinate system. The transformation from the local coordinate system of any strip to the coordinate system of strip 1 is equivalent to rotating the coordinate system about the local x-axis, hence, τ_{yz} will remain zero. The triaxial stress states in the joint concrete must satisfy the Mohr-Coulomb criterion presented in Sec. 2. Moreover, the rectangular panels in the corbels will experience plane stress, which must satisfy the Mohr-Coulomb criterion for plane stress also presented in Sec. 2.

The U-bar loops are subject to tension in order to activate the corbel mechanisms, and the tensile stress must be below the tensile strength:

$$0 \leq T_i \leq f_y A_{su} \tag{23}$$

where f_y is the yield strength and A_{su} is the cross sectional area. It is assumed that the reinforcement only carries tension as seen in (23). The compression stringers illustrated in Fig. 6 must be in compression, i.e. V must be non-positive:

$$V \leq 0$$

The submodel requires second-order constraints as well as semidefinite constraints since the concrete experience both plane stress and triaxial stress. The macro joint element and submodel are implemented in Matlab and the commercial optimisation solver MOSEK [31].

6. Analysis and discussion

6.1. Corner joint subject to shear

First, a corner joint subjected to shear is analysed using a single joint element with the submodel criterion, and the results are compared to the current design criterion of the Eurocode 2. Comparison to experimental

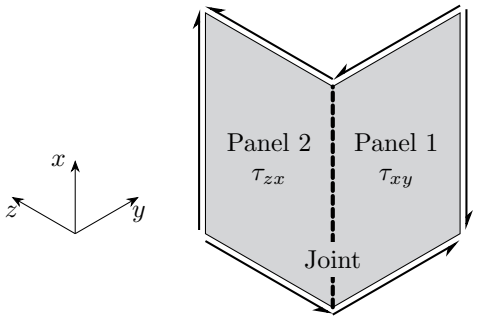

Figure 10: Corner joint connecting two reinforced concrete panels subject to pure shear analysed using a single joint element.

results would be preferable, however, as mentioned experimental results for corner joints have not been published to the best knowledge of the authors.

Fig. 10 shows the corner joint connecting two precast concrete panels as well as the loading, which is applied such that the joint is loaded in pure shear. For the Eurocode 2, the shear capacity of a keyed joint can be calculated as:

$$\tau = c f_t \frac{A_{key}}{A_c} + \mu \rho f_y \leq \frac{1}{2} \nu f_c \frac{A_{key}}{A_c} \tag{24}$$

where $c = 0.5$ is a parameter which relates the tensile strength f_t to the cohesion, and $\mu = 0.9$ is the friction coefficient used for keyed joints. A_{key} is the area of the keys and A_c is the total area of the joint. ρ is defined as

$$\rho = \frac{\sum A_{su}}{A_c}$$

ν is the so-called effectiveness factor, which accounts for microcracking and softening when using a rigid-plastic material model for concrete. An effectiveness factor of $\nu = 0.7 - f_c/200$ (f_c in MPa) is used for the comparison.

The joint is analysed for varying value of u, see Fig. 5, with $u/2 = u_{z1} = u_{y1}$. The following parameters are used:

$$f_t = 0 \text{ MPa},\ t_z = t_y = 50 \text{ mm},\ o_z = o_y = 40 \text{ mm}$$

For the Eurocode 2 design formula (24), $f_t = 0.21 f_c^{2/3}$ and $A_{key}/A_c = 0.5$ are used. Three different types U-bar loops commonly used in practice are analysed using different values of U-bar spacing, s.

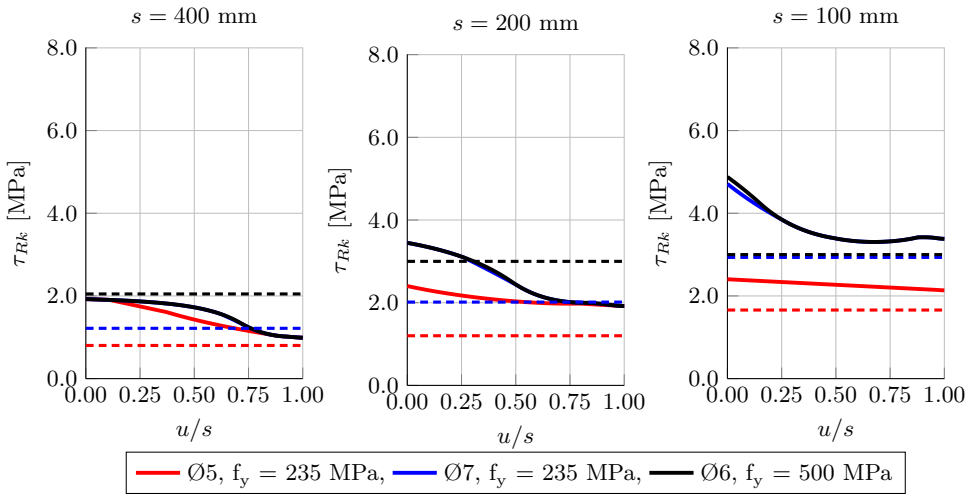

Figure 11: Characteristic shear capacity of the corner joint with $f_c = 20$ MPa and different values of s: The results of the joint element is represented using solid lines, while the capacity predicted using the Eurocode 2 is shown with dashed lines.

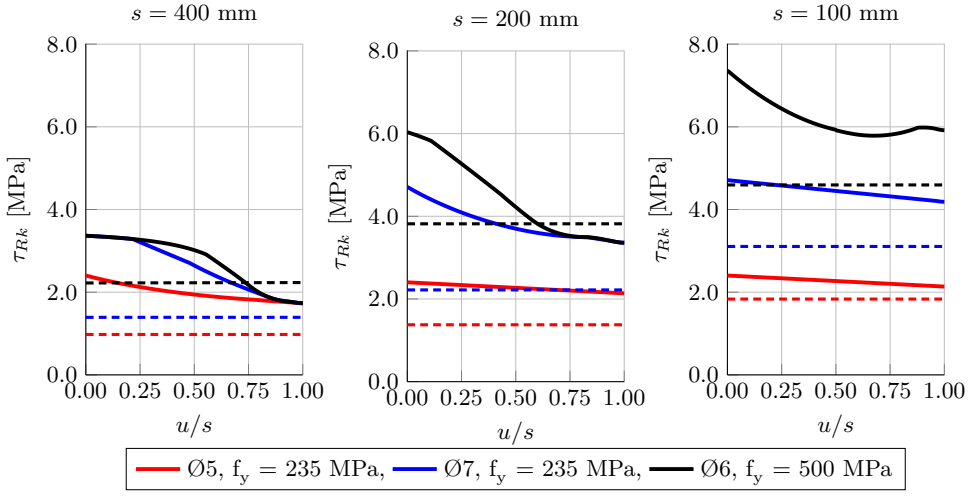

Figure 12: Characteristic shear capacity of the corner joint with $f_c = 35$ MPa and different values of s: The results of the joint element is represented using solid lines, while the capacity predicted using the Eurocode 2 is shown with dashed lines.

Fig. 11 and 12 show the shear capacity of the corner joints for the three types U-bar loops. It is observed that the values of u and s affect the capacity of the joint element and submodel to some degree. Moreover, the concrete strength heavily affects the capacity for the joints with Ø7 and Ø6 U-bars (blue and black lines).

The shear capacity estimated with the Eurocode 2 design equation is somewhat similar to the shear capacity of the joint element, however, for low values of s the Eurocode underestimate the capacity, while it overestimates the capacity for larger values of s depending on u compared to the joint element. Based on the analysis it can be concluded that it is necessary to consider the stress field inside the joint for design.

6.2. Four-storey stairwell with door openings

Herfelt et al. [22] analysed a four-storey stairwell with door openings subjected to shear and torsion using the generalised plane stress element. The stairwell is now considered as a precast concrete structure, and the corners are modelled using the presented joint element.

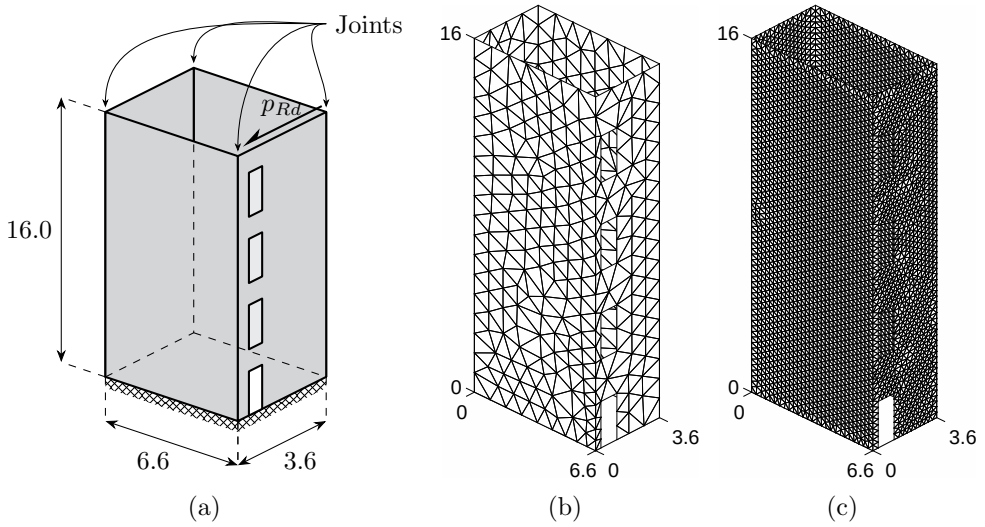

Figure 13: Four-storey stairwell subjected to bending and torsion: a) Sketch showing loading and joints located in the vertical corners are modelled using the joint element[22], b) coarse mesh with 864 triangular elements, c) fine mesh with 11,379. All dimensions are given in metres.

The stairwell including the positions of the joints are seen in Fig. 13. The dimensions of the wall as well as meshes for the model are also given in the figure. The door openings have a height of 2.10 metres and a width of 0.90 metres. The precast concrete panels have a thickness of 180 mm and are reinforced with two layers of Ø8 rebars per 150 mm in both directions. The reinforcement has a design yield strength of $f_{yd} = 458$ MPa, and the concrete has a design compressive strength of $f_{cd} = 21.4$ MPa, while the tensile strength is taken as zero. Considering a single U-bar loop, the reinforcement ratio is given as

$$\Phi = \frac{A_{su} f_y}{s\, t\, f_c}$$

For the joints, a thickness of $t_z = t_y = 180$ mm is used with an overlap of $o_z = o_y = 50$ mm and $s = 300$ mm. $f_{cd} = 21.4$ MPa, $f_t = 0$, and $k = 4$ are used for the joint concrete as well. The reinforcement ratio of the joint is varied and the results are illustrated in Fig. 14 for two meshes generated using GiD v12 [32]; a coarse mesh with 864 plane stress elements, and a fine mesh with 11,379 plane stress element, see Fig. 13(b) and (c). Moreover, the stairwell is analysed for two values of u to assess the effect of the reinforcement layout.

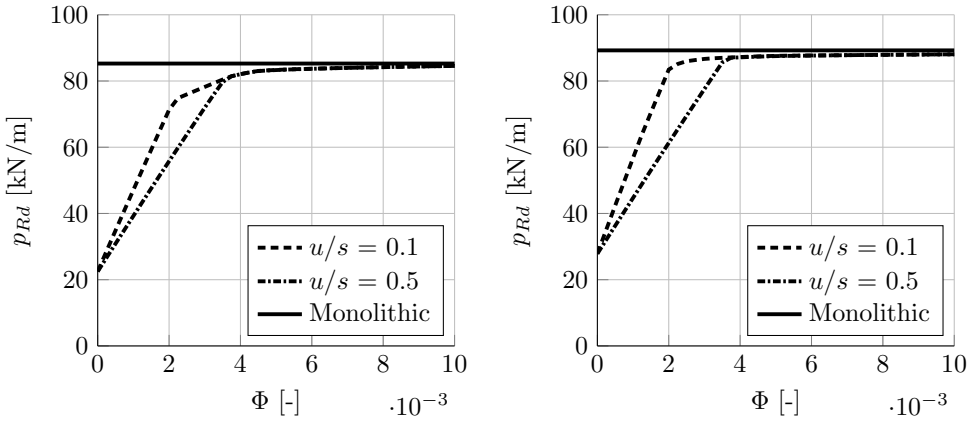

(a) Coarse mesh (b) Fine mesh

Figure 14: Design capacity of the stairwell as a function of the reinforcement ratio of the joints for two different values of u.

Fig. 14 shows that the capacity depends on the joint reinforcement to some degree, however, the joints will hardly affect the capacity provided

sufficient reinforcement, i.e. $\Phi \geq 0.004$ corresponding to Ø5 U-bar loops per 544 mm assuming a design strength of 214 MPa which is far below what is typically used in practice. It is seen that the model with the joint elements approach the capacity of the model without the joint from below, which is to be expected from a lower bound element. It is also seen that the fine mesh predicts a larger capacity.

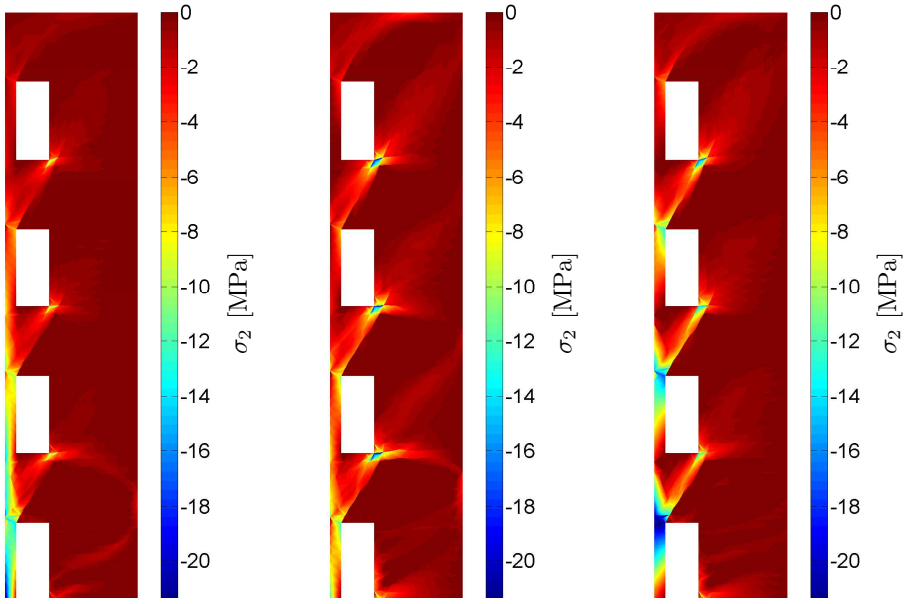

(a) Joints: $\Phi = 0.001$, $p_{Rd} = 47.12$ kN/m

(b) Joints: $\Phi = 0.004$, $p_{Rd} = 87.14$ kN/m

(c) Monolithic: $p_{Rd} = 89.25$ kN/m

Figure 15: Comparison of the smallest principal stress for the wall with the door openings using the fine mesh with and without joints ($u/s = 0.5$).

From Fig. 15 it can be seen that the joints push the structure towards a more evenly distribution of the shear stresses across the corner. For $\Phi = 0.001$ shown in Fig. 15(a), large compressive stresses are observed near the bottom door opening. This is due to the fact that the joints do not have sufficient shear capacity and the stresses have to be transferred to the foundations via the wall itself. Fig. 15(c) shows large compressive stresses above 20 MPa near the bottom door opening which is possible since no criterion is enforced on the stresses in the corner of the structure.

Fig. 16 shows that for $\Phi = 0.001$ and 0.004, the shear stress in the joints

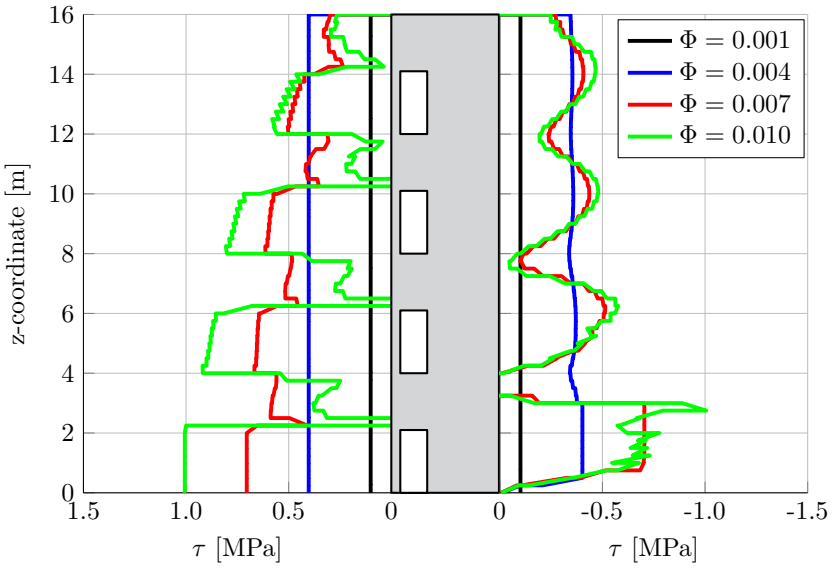

Figure 16: Shear stress distribution over the height of the structure in the joints near adjacent to the slender wall with the door openings. The shear stress is shown for four different reinforcement degrees Φ using the fine mesh and $u/s = 0.5$ for the joints. The wall structure is shown in the centre.

near the door openings will be constant over the entire height. In order to activate the joints over the entire height, significant ductility is needed. Increasing the reinforcement degree means that only a small portion of the joints are utilised fully, hence, the requirement to the ductility is lower, and the structure is more robust. The effect of the door openings on the shear stress is clearly shown in Fig. 16 for $\Phi = 0.007$ and 0.010. The forces are primarily transferred as diagonal compression in the panels, hence, this jagged pattern of shear stresses is generated. The effect of the door openings is also seen to some degree for the joint to the right of the wall, where an almost wave-like distribution is observed for $\Phi = 0.007$ and 0.010.

The analysis has shown that the proposed multiscale joint element makes modelling of real size structures possible. Moreover, the stairwell model using the fine mesh only required a CPU time of approximately 65 seconds on a desktop PC with an Intel Xeon CPU W3565 with 8 CPUs and 3.2 GHz clock frequency. The low computational time is a major advantage over general non-linear finite element models.

7. Conclusion

In practice, design and analysis of precast concrete structure in the ultimate limit state is primarily done using simple manual methods and linear finite element analysis. The manual methods are often based on limit analysis and provide efficient tools for assessment of the capacity. For complex structures, however, it becomes difficult to obtain a decent solution - especially for structures in three dimensions. Moreover, it is rather difficult to account for the behaviour of the in-situ cast joints.

A lower bound multiscale joint element was presented. The element was designed for interaction with a generalised plane stress element with the scope of modelling of real life precast concrete structures. A mechanical submodel was proposed as the yield function of the macro joint element. The submodel used corbels to transfer shear stresses from one plane to another and the resulting triaxial stress field within the joint was checked against the Mohr-Coulomb criterion.

Unfortunately, no experiments of joints in three dimensions have been published, thus, the joint element and submodel was analysed by comparison to the Eurocode criterion. The results of the joint element and the Eurocode design equation were somewhat close and for heavily reinforced joints, the joint element predicted a larger capacity.

A four-storey precast concrete stairwell with door openings was analysed. The precast panels were connected by in-situ cast joints in the corners, and it was observed that the capacity of the joints are crucial to the overall behaviour of the wall. The reinforcement of the joints heavily affects the capacity, especially at low degrees of reinforcement. The joints also affected the stress field considerably, and the shear stresses were distributed more evenly across the corner joint. Higher levels of reinforcement increase the robustness of the structure considerably and lower the requirement to the ductility of the joints and panels.

The proposed multiscale joint model has shown significant potential, however, validation by comparison to experimental results is necessary. It can be concluded that the presented framework and model will enable optimisation of precast concrete structures, and the lower bound property of the model is highly desirable for practical design.

Acknowledgement

The authors would like to thank the ALECTIA Foundation and Innovation Fund Denmark for financial support of the research presented in this paper.

References

[1] J. Fauchart, P. Cortini, Étude expérimentale de joints horizontaux entre panneaux préfabriqués pour murs de batiments, Annales de LInstitut Technique du Batiment et dês Travaux Publics 300 (1972) 86–103.

[2] F. Bljuger, Determination of deformability characteristics of vertical shear joints in precast buildings, Building and Environment 11 (1976) 277–282.

[3] K. Hansen, S. O. Olesen, SBI-Report 97: Keyed Shear Joints, Statens Byggeforskningsinstitut, 1976.

[4] European Committee for Standardization, En 1992-1-1 eurocode 2: Design of concrete structures - part 1-1: General rules and rules for buildings (2005).

[5] M. A. Herfelt, P. N. Poulsen, L. C. Hoang, J. F. Jensen, Numerical limit analysis of keyed shear joints in concrete structures, Structural Concrete 17 (3) (2016) 481–490.

[6] A. A. Gvozdev, The determination of the value of the collapse load for statically indeterminate systems undergoing plastic deformation, International Journal of Mechanical Sciences 1 (4) (1960) 322–335.

[7] W. Prager, The general theory of limit design, in: Proceedings of the 8th International Congress on theoretical and Applied Mechanics, Istanbul, Vol. 19, 1952, pp. 65–72.

[8] D. Drucker, W. Prager, H. Greenberg, Extended limit design theorems for continuous media, Quarterly of Applied Mathematics 9 (1952) 381–389.

[9] K. W. Johansen, Yield-line theory, Cement and Concrete Association, 1962.

[10] B. C. Jensen, On the ultimate load of vertical, keyed shear joints in large panel buildings, in: Symposium on Bearing Walls in Warsaw, Vol. 8, 1975, p. 13th.

[11] J. Christoffersen, Ultimate capacity of joints in precast large panel concrete buildings, Ph.D. thesis, Technical University of Denmark (1997).

[12] M. P. Nielsen, L. C. Hoang, Limit Analysis and Concrete Plasticity, Third Edition, Taylor & Francis, 2010.

[13] fib bulletin 43, Structural connections for precast concrete buildings (2008).

[14] T. Belytschko, P. Hodge, Plane stress limit analysis by finite elements, Journal of the Engineering Mechanics Division 96 (6) (1970) 931–944.

[15] E. Anderheggen, H. Knöpfel, Finite element limit analysis using linear programming, International Journal of Solids and Structures 8 (1972) 1413–1431.

[16] E. Christiansen, On collapse solution in limit analysis, Archive for Rational Mechanics and Analysis.

[17] S. W. Sloan, Lower bound limit analysis using finite elements and linear programming, International Journal for Numerical and Analytical Methods in Geomechanics 12 (1988) 61–77.

[18] S. Krenk, L. Damkilde, O. Høyer, Limit analysis and optimal design of plates with equilibrium elements, Journal of Engineering Mechanics 120 (1994) 1237–1254.

[19] P. N. Poulsen, L. Damkilde, Limit state analysis of reinforced concrete plates subjected to in-plane forces, International Journal of Solids and Structures 37 (2000) 6011–6029.

[20] A. Makrodimopoulos, C. Martin, Lower bound limit analysis of cohesive-frictional materials using second-order cone programming, International Journal for Numerical Methods in Engineering 66 (4) (2006) 604–634.

[21] M. A. Herfelt, P. N. Poulsen, L. C. Hoang, J. F. Jensen, Lower bound equilibrium element and submodel for shear joints in precast concrete structures, Engineering Structures 135 (2017) 1 – 9.

[22] M. A. Herfelt, P. N. Poulsen, L. C. Hoang, J. F. Jensen, Lower bound plane stress element for modelling of 3d structures, Proceedings of the Institution of Civil Engineers - Engineering and Computational Mechanics, submitted for review.

[23] Y. Nesterov, A. Nemirovsky, A general approach to polynomial-time algorithms design for convex programming, report, Central Economical and Mathematical Institute, USSR Academy of Sciences, Moscow (1988).

[24] E. D. Andersen, C. Roos, T. Terlaky, On implementing a primal-dual interior-point method for conic quadratic optimization, Mathematical Programming 95 (2) (2003) 249–277.

[25] M. S. Lobo, L. Vandenberghe, S. Boyd, H. Lebret, Applications of second-order cone programming, Linear algebra and its applications 284 (1) (1998) 193–228.

[26] C. Bisbos, P. Pardalos, Second-order cone and semidefinite representations of material failure criteria, Journal of Optimization Theory and Applications 134 (2) (2007) 275–301.

[27] K. Krabbenhøft, A. Lyamin, S. Sloan, Formulation and solution of some plasticity problems as conic programs, International Journal of Solids and Structures 44 (5) (2007) 1533–1549.

[28] L. Vandenberghe, S. Boyd, Semidefinite programming, SIAM review 38 (1) (1996) 49–95.

[29] K. Krabbenhøft, A. Lyamin, S. Sloan, Three-dimensional mohr–coulomb limit analysis using semidefinite programming, Communications in Numerical Methods in Engineering 24 (11) (2008) 1107–1119.

[30] K. P. Larsen, Numerical limit analysis of reinforced concrete structures, Ph.D. thesis, Technical University of Denmark (2010).

[31] MOSEK ApS, The MOSEK optimization toolbox for MATLAB manual. Version 7.1 (Revision 33) (2015).
URL `https://www.mosek.com/`

[32] R. Ribó, M. Pasenau, E. Escolano, J. Ronda, L. González, Gid reference manual, CIMNE, Barcelona.

o This thesis presents a framework for efficient design and analysis of precast concrete structures based on finite element limit analysis. In-situ cast joints are crucial in precast structures, hence, adequate models for these components are developed and validated by comparison to experimental results. Real size examples illustrate the strength of the framework in both two and three dimensions, and the developed models for the joints make it possible to account for the local behaviour in the global model.

DTU Civil Engineering
Technical University of Denmark

Brovej, Bygning 118
2800 Kongens Lyngby

www.byg.dtu.dk

ISBN 9788778774583
ISSN 1601-2917